Earth-Abundant Metal Oxides for Anodic Reactions in Acidic Electrolytes

Thesis by

Ivan A. Moreno-Hernandez

In Partial Fulfillment of the Requirements for

the Degree of

Doctor of Philosophy

CALIFORNIA INSTITUTE OF TECHNOLOGY

Pasadena, California

2019

(Defended May 15, 2019)

Ivan A. Moreno-Hernandez
ORCID: 0000-0001-6461-9214

ACKNOWLEDGEMENTS

The work that I have done during my doctoral studies would not be possible without the help of many brilliant scientists. My advisor, Nathan Lewis, has inspired me with his deep understanding of all aspects of energy systems and renewable energy technologies, as well as his commitment to creating a friendly and collaborative group culture. Nate, thank you for all of the guidance you have provided throughout the years and for giving me the opportunity to study in your laboratory. You have consistently advocated for me and supported my research efforts, and I feel very fortunate to have studied in your research group.

My committee has provided crucial feedback on my research projects, proposals, and career goals that has allowed me to grow as a scientist. Mitchio Okumura has been a wonderful committee chair, and I am thankful for his advice and commitment to my education. Mitchio, thank you for taking the time to meet with me individually to learn about my work, and for supporting me throughout the years. I have had the opportunity to interact with Harry Gray both through research projects and through outreach activities, and I admire his dedication to encouraging others to do their best. Harry, thank you for always making me feel welcomed into your group. James Heath, thank you for your feedback on my research and your support. Kimberly See has provided great feedback on my work, and I value her expertise on electrochemistry. Kimberly, thank you for taking the time to review my work and for your advice.

The academic staff within the Lewis group has been essential to my studies at Caltech. Bruce Brunschwig helped me with many of the technical aspects of my research, such as finding analog potentiostats, maintaining instruments, and loaning spare parts for equipment

at Jorgensen. I appreciate the feedback that Bruce has provided to my manuscripts. Bruce, thank you for always being willing to help when an instrument is broken and for your advice. Barbara Miralles has assisted me countless of times with the logistics of graduate school, such as arranging room reservations, processing reimbursements, and scheduling meetings. Barbara, thank you for being friendly and for working so hard for the group. Kimberly Papadantonakis has helped the group by assisting with research grants and manuscripts. Kimberly, thank you for all of the thoughtful discussions we have had during group meetings, retreats, and over meals.

I am grateful for all of the assistance the postdoctoral scholars within the Lewis group and collaborators have provided. Ke Sun mentored me during the beginning of my doctoral studies, teaching me many practical lab skills such as how to make electrodes and conduct photoelectrochemical experiments. Ke, thank you for mentoring me during a crucial part of my career and for always being willing to help me. Carlos Read joined the Lewis group just as I started my work on transition metal antimonates, and his expertise on transmission-electron microscopy was essential to this work. Carlos, thank you for taking amazing images of the catalysts I have developed and for your mentorship. Matthias Richter is an expert on x-ray photoelectron spectroscopy, and learning about his projects and discussing the technique with him has been insightful. Matthias, thank you for modifying our XPS to do interesting experiments. I have appreciated my discussions with Miguel Caban-Acevedo about photoelectrochemistry. Miguel, thank you for teaching me about your work on silicon surface chemistry and for the thoughtful discussions. Additionally, I would like to thank the other postdoctoral scholars that I met during my doctoral work: Shu Hu, Robert Coridan,

Mita Dasog, Jimmy John, Jesus Velazquez, Keith Wong, Betar Gallant, James Blakemore, Matt McDowell, Sonja Francis, Burt Simpson, and Fan Yang. You have all brought great expertise into the group and your contributions continuously influence the projects that I and others develop within the group. Carol Garland, thank you for teaching me transmission-electron microscopy and for sharing your stories. Nathan Dalleska, thank you for your assistance with mass spectrometry experiments and for maintaining the instruments in the environmental analysis center.

The graduate students and visiting scholars at Caltech have made the graduate school experience fun, and collectively we have improved our understanding of photoelectrochemical systems. Pai Buabthong, Weilai Yu, and Jingjing Jiang, thank you for teaching me about semiconductor stability in aqueous electrolytes and about piloting aircraft, photography, and martial arts. Xinghao Zhou, thank you for teaching me about your work on protective metal oxides and for keeping me company on late work nights. Sisir Yalamanchili, thank you for collaborating with me on silicon microcones, and for being a cone enthusiast. Jackie Dowling, thank you for collaborating with me on earth-abundant electrocatalysts, and for teaching me about skiing. Harold Fu, thank you for teaching me about polymers, helping with outreach activities, and for our discussions during the drive to Crescenta Valley and over many shared meals. Zach Ifkovits, thank you for teaching me about your experiences in industry and about soccer. Erik Verlage, thank you for mentoring me while I learned how to be a group safety officer and sputterer super-user. Roc Matheu, thank you for teaching me about molecular catalysis, for your advice, and for your continued guidance. Clara MacFarland, thank you for your assistance on crystalline transition metal

antimonates during your summer research experience. Stefan and Cody, thank you for your advice on chlorine evolution experiments. Paul Kempler and Katherine Rinaldi, thanks for keeping Jorgensen G135 fun and for your contributions to the group. Sam Johnson and Sarah Del Ciello, thanks for helping with outreach activities and teaching me about your research. I would also like to thank the rest of the Lewis group for their assistance and motivation to collectively work towards a deeper understanding of electrochemistry and renewable energy technologies.

My friends have supported me during this time and have provided valuable perspective. Jason, thank you for your friendship throughout undergraduate and graduate school and for teaching me about pennycress and plant science. Alex, Alexei, Liz, Denise, Ellen, Abbey, Josh, Agnė, Kim, Marie, Matt, Melissa, Nelson, Rebecca, Red, Yong, Katie, Martín, Celeste, Jeff, Angela, Victoria, Camille, Amrut, Bill, and Delores, thank you for your company and friendship during my doctoral work. I have enjoyed our many adventures together and look forward to more.

My family has helped me become the person that I am today. Mom, thank you for nurturing me and for teaching me about life and always being supportive. You have worked hard to provide opportunities for me and I am thankful for that. Yovanny, Jocelynne, and Alan, thank you for being wonderful siblings and for all of the fun we have had together. I have fond memories of seeing all of you grow up and I look forward to seeing the adults that you will become. Manuel and Olivia, thank you for being wonderful grandparents and for caring for me. Jose and Lily, thank you for being supportive, understanding, and welcoming. Jeff and Stephanie, thank you for your guidance and for accepting me into your family. Your

kindness to me and my family has been extraordinary and your guidance has helped me. Matt, thank you for being the best brother-in-law, and for all of the fun we have had.

Finally, I would like to thank my spouse, Emily Moreno-Hernandez. Meeting Emily in 2011 completely changed my life, and her support and love since then have been unwavering. Emily, I cannot express how thankful I am for you supporting me throughout all of these years, and for always knowing the right thing to say or do. You support me and bring out the best in me, and your kindness to others inspires me every day.

ABSTRACT

The development of electrochemical systems such as electrolyzers and photoelectrochemical devices in corrosive electrolytes has been limited by the lack of earth-abundant materials that are both stable in acidic electrolytes and efficiently utilize energy for electrochemical reactions. Chapter 1 introduces several of the challenges in developing earth-abundant materials for electrochemical systems in acidic electrolytes, such as electrocatalysts for the oxygen and the chlorine evolution reactions, and protective layers for photoanodes. Chapter 2 reports the electrochemical behavior of crystalline transition metal antimonates consisting of solid solutions of $MnSb_2O_6$ with $NiSb_2O_6$ for the oxygen evolution reaction in strongly acidic electrolytes. In Chapter 3, the crystalline transition metal antimonates $NiSb_2O_6$, $CoSb_2O_6$, and $MnSb_2O_6$ are investigated for the chlorine evolution reaction, and $CoSb_2O_6$ is found to exhibit activity and stability comparable to noble metal oxide electrocatalysts. Chapter 4 describes the development of earth-abundant SnO_x coatings as protective heterojunctions for planar Si photoanodes in corrosive electrolytes. Chapter 5 focuses on the development of conformal SnO_x coatings that form protective heterojunctions on Si microcone photoanodes. The work presented herein demonstrates several strategies towards the development of stable earth-abundant materials for efficient electrochemical and photoelectrochemical energy conversion in acidic electrolytes.

PUBLISHED CONTENT AND CONTRIBUTIONS

Chapter II:

1. Moreno-Hernandez, I. A.; MacFarland, C. A.; Read, C. G.; Papadantonakis, K. M.; Brunschwig, B. S.; Lewis, N. S., Crystalline nickel manganese antimonate as a stable water-oxidation catalyst in aqueous 1.0 M H2SO4. *Energy Environ. Sci.* **2017,** *10* (10), 2103-2108. DOI: 10.1039/C7EE01486D

   I.A.M.-H. designed the study, conducted the experiments, and wrote the manuscript.

Chapter III:

2. Moreno-Hernandez, I. A.; Brunschwig, B. S.; Lewis, N. S., Crystalline nickel, cobalt, and manganese antimonates as electrocatalysts for the chlorine evolution reaction. *Energy Environ. Sci.* **2019,** *12* (4), 1241-1248. DOI: 10.1039/C8EE03676D

   I.A.M.-H. designed the study, conducted the experiments, and wrote the manuscript.

Chapter IV:

3. Moreno-Hernandez, I. A.; Brunschwig, B. S.; Lewis, N. S., Tin Oxide as a Protective Heterojunction with Silicon for Efficient Photoelectrochemical Water Oxidation in Strongly Acidic or Alkaline Electrolytes. *Adv. Energy Mater.* **2018**, 8 (24), 1801155. DOI: 10.1002/aenm.201801155

   I.A.M.-H. designed the study, conducted the experiments, and wrote the manuscript.

Chapter V:

4. Moreno-Hernandez, I. A.; Yalamanchili, S.; Atwater, H. A.; Brunschwig, B. S.; Lewis, N. S., *Manuscript in Preparation.*

   I.A.M.-H. designed the study, conducted the experiments, and wrote the manuscript.

TABLE OF CONTENTS

Chapter I

INTRODUCTION

1.1 The Oxygen Evolution Reaction in Acidic Electrolytes

The electrolysis of water is an important reaction for several renewable energy storage technologies.[1-2] Water is electrolyzed by the hydrogen evolution reaction (HER) and the oxygen evolution reaction (OER) in the cathode and the anode of an electrochemical cell, respectively. The HER in acidic electrolytes is a two-electron reaction that reduces protons to form H_2(g). While Pt is currently the most active single-element electrocatalyst for the HER, several earth abundant electrocatalysts for the HER have been developed in acidic electrolytes.[3] For example, transition metal sulfides, selenides, and phosphides have been extensively explored in the literature.[4-5] The most active and stable earth-abundant electrocatalysts for the HER reported in the literature are transition metal phosphides such as NiP_x and CoP_x, with their activity being comparable to Pt.[6-7] While further work is required to improve the stability of earth-abundant HER electrocatalysts under open-circuit conditions, their activity is promising towards the development of earth-abundant electrocatalysts for electrolyzers and photoelectrochemical devices.[8]

The OER is a four-electron reaction that oxidizes two water molecules to form O_2(g) and release four protons and four electrons.[9] While the mechanism for the OER remains an active area of research, a mechanism involving four intermediates has been utilized to understand the activity of metal oxide electrocatalysts.[10] In the first step of this mechanism, a water molecule reacts with the surface of an electrocatalyst and releases a proton and an electron,

forming a bound OH intermediate on the surface of the electrocatalyst.[10] In the second step, another proton and electron are released, forming a bound O intermediate.[10] In the third step, a second water molecule reacts with the O intermediate, releasing another proton and electron and forming an OOH intermediate.[10] In the final step, the OOH intermediate releases another proton and electron, forming O_2(g) and restoring the electrocatalyst surface to the initial state.[10] The released protons and electrons are transferred to the cathode and H_2(g) is formed via the HER. The binding energies of the OH, O, and OOH intermediates can be calculated with quantum mechanical methods, and these binding energies have been used to model the activity of various metal oxide electrocatalysts for the OER.[10] An ideal electrocatalyst surface would exhibit a binding energy of 1.229 eV for each step of the OER.[10] Computational results indicate that the OH and OOH intermediate exhibit a linear binding energy relationship across many electrocatalyst surfaces, indicating that interactions that increase the OH binding energy also increase the OOH binding energy.[10] The linear "scaling" relationship also indicates that OOH binding energies are ~ 3.2 eV stronger than OH binding energies, which leads to a ~1.6 eV energy difference between different reaction intermediates.[10] Unfortunately, this leads to an additional ~0.37 eV required over an ideal electrocatalyst for the OER, leading to a high overpotential for the OER compared to the HER.[10] An important goal of electrocatalyst research is to understand how the "scaling" relationship can be broken in order to improve the activity of electrocatalysts for the OER.

Electrocatalysts for the OER in acidic electrolytes have mostly consisted of scarce noble metal oxides such as IrO_x or RuO_x.[3] Anodes consisting of noble-metal oxides of IrO_x and RuO_x exhibit high activity towards the OER.[11] For example, $SrIrO_x$ exhibits an

overpotential of 270 mV at 10 mA per cm^2 of geometric surface area.[12] The high activity of these electrocatalysts can lead to a high efficiency towards the electrolysis of water. However, the low abundance of Ir and Ru on Earth could lead to shortages of these materials if electrolyzers are implemented to store renewable energy in energy systems relevant to world-wide energy consumption.[13] Thus, there is a need to develop earth-abundant electrocatalysts that exhibit similar activity and stability towards the OER in acidic electrolytes.

The thermodynamic instability of many metal oxides in low pH conditions has limited the discovery of electrocatalysts for the OER in acidic electrolytes. A successful approach for the discovery of electrocatalysts for the OER in alkaline electrolytes has been to utilize first-row transition metal oxides such as NiO_x, CoO_x, and MnO_x as precatalyst films.[3] The oxides convert to transition metal oxyhydroxides under electrochemical operation, with $N_{ix}Fe_{1-x}OOH$ being one of the most active and stable electrocatalysts for the OER in alkaline electrolytes.[3, 14] Unfortunately, many first-row transition metal oxides thermodynamically dissolve in strongly acidic electrolytes, preventing their use as electrocatalysts under these conditions.[15]

Previous work on earth-abundant OER electrocatalysts in acidic electrolytes has focused on modifying established electrocatalysts such as CoO_x or MnO_x by controlling the electrolyte composition and potential applied to obtain improved stability.[16-19] For example, electrodeposited MnO_x has been found to exhibit improved stability under applied bias.[19] The results can be explained by constructing a Pourbaix diagram of Mn in

aqueous electrolytes. The Pourbaix diagram indicates a narrow potential window of stability at potentials relevant for water oxidation.[20] Subsequent studies have verified the stability of MnO_x electrocatalysts at this potential window.[21] CoO_x also exhibits improved stability under electrochemical operation.[16] CoO_x electrocatalysts can be electrodeposited at potentials above the OER.[16] While these results are significant advances in the development of earth-abundant electrocatalysts in acidic electrolytes, the instability at open-circuit and potentials above the narrow stability window can prevent the implementation of these materials in renewable energy systems that are not operated continuously, such as grid-level energy systems that balance variable energy demand.[22]

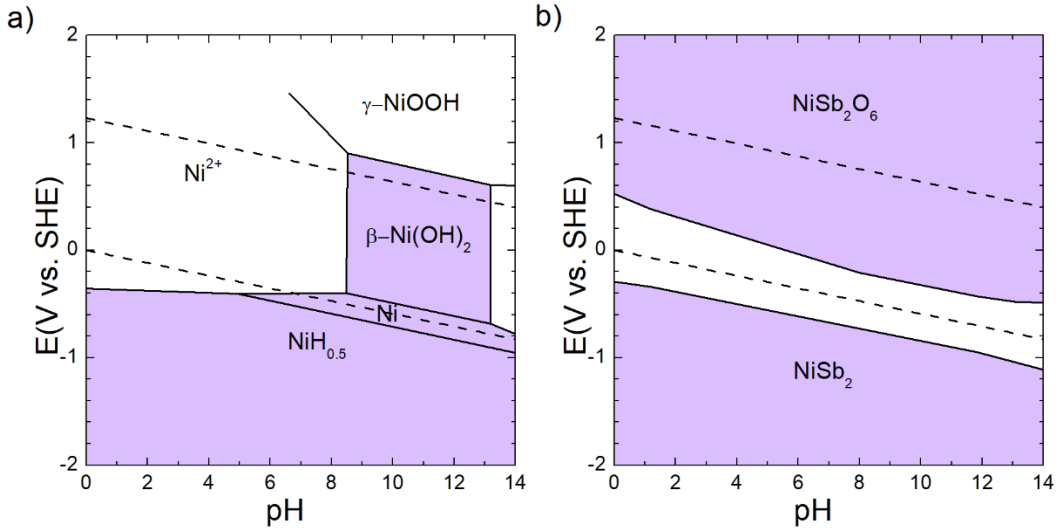

Figure 1. Pourbaix diagrams of representative metal and metal-antimony systems demonstrating the stabilization scheme utilized to develop earth-abundant electrocatalysts for the oxygen evolution reaction. a) Dissolution is spontaneous for Ni in acidic electrolytes and will preferentially occur compared to the oxygen evolution reaction, resulting in electrocatalyst corrosion. b) Formation of a crystalline $NiSb_2O_6$

phase results in a decrease in the Gibbs free energy, which results in corrosion being thermodynamically unfavorable compared to the oxygen evolution reaction. The data used to construct the Pourbaix diagram was obtained from the Materials Project database.[20]

In the work presented in Chapter 2, crystalline transition-metal antimonates are demonstrated to be active and thermodynamically stable electrocatalysts for the OER.[23] The crystallization of transition-metal oxides such as $NiSb_2O_x$ and $MnSb_2O_x$ leads to the formation of a rutile-type MSb_2O_6 phase, which is thermodynamically stable under operation and at open-circuit due to the substantial decrease in Gibbs free energy after crystallization (Figure 1).[23] The results indicate that Mn is required to exhibit high activity towards the OER in acidic electrolytes, and that Mn-containing MSb_2O_x electrocatalysts exhibit reversible redox behavior.[23] The highest activity is obtained with electrocatalysts films consisting of solid solutions of $NiSb_2O_x$ and $MnSb_2O_x$ with a 1:1 Ni:Mn ratio.[23]

1.2 The Chlorine Evolution Reaction in the Acidic Electrolytes

The electrolysis of aqueous sodium chloride solutions is operated at an industrial scale via the chlor-alkali process to generate Cl_2(g), NaOH, and H_2(g) from H_2O(l) and NaCl(aq) (Figure 2).[24] The chemicals generated through this process have important applications for water sanitation, chemical conversions, and renewable fuel technologies.[25] The electrochemical cell for the chlor-alkali process usually consists of an alkaline cathode compartment and an acidic anode compartment separated by a sodium ion exchange

membrane.[24] The cathode reduces two $H_2O(l)$ molecules to form $H_2(g)$ and OH^- via the HER, and the anode oxidizes two $Cl^-(aq)$ anions to form $Cl_2(g)$ via the chlorine evolution reaction (CER).[26] Sodium cations from NaCl are transported through a sodium exchange membrane to form NaOH. The chlor-alkali process requires electrocatalysts for the HER and CER to minimize kinetic losses at high conversion rates.[24] While several earth-abundant electrocatalysts have been developed for the CER in alkaline electrolytes, most electrocatalysts for the CER contain noble-metal elements.[3]

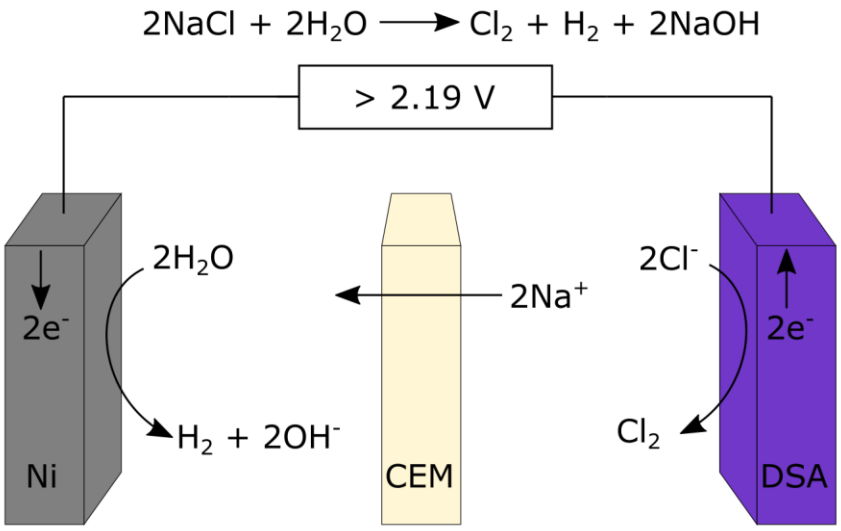

Figure 2. Schematic of electrochemical cell utilized in the chlor-alkali process. A Ni cathode reduces water via the hydrogen evolution reaction to produce hydrogen gas and hydroxide ions, and a dimensionally-stable anode consisting of RuO_2-TiO_2 oxidizes chloride via the chlorine evolution reaction to produce chlorine gas. Sodium is transported across a cation exchange membrane to produce NaOH.

The chlorine evolution reaction is a two-electron reaction that oxidizes chloride from aqueous electrolytes to form $Cl_2(g)$, and has a standard electrochemical potential of 1.36 V vs. NHE.[24] The CER competes with the OER since both H_2O and Cl^- are present in the electrolyte, and OER is thermodynamically favored since it has a standard electrochemical potential of 1.229 V vs. NHE at pH = 0.[24] Selectivity, stability, and activity are important properties of electrocatalysts for the CER.[24] Selectivity for the CER versus the OER is improved as the concentration of chloride and acidity of the electrolyte is increased.[24] High concentrations of chloride improve selectivity by providing more chloride at the electrocatalyst surface for the CER.[24] The selectivity for the CER improves as the pH of the electrolyte decreases since the CER if pH independent, whereas the potential for the OER increases with decreasing pH.[24] The electrolyte for the CER is typically 4.0 M NaCl(aq) with a pH = 2 – 4 in order to obtain >99% selectivity towards the generation of $Cl_2(g)$ versus $O_2(g)$.[24] The electrocatalysts for the CER have to be stable for several years in the commercial chlor-alkali process.[24] The long stability requirements, coupled with the corrosive nature of the electrolyte, have limited the choice of electrocatalysts to noble-metal oxides such as RuO_2 and IrO_2.[24]

A key challenge in the development of electrocatalyst for the CER has been the discovery of materials other than RuO_2 and IrO_2 that exhibit adequate selectivity, stability, and activity. The high oxidizing potential of the CER and the corrosive electrolyte required for selectivity can dissolve many of the typical electrocatalyst used for anodic reactions such as first-row transition metal oxides. While the most stable binary oxide electrocatalysts for the CER consist of RuO_2 and IrO_2, these materials are not thermodynamically stable under the

operating conditions and are susceptible to corrosion.[24] Furthermore, the low elemental abundance of RuO_2 and IrO_2 can prohibit the implementation of the CER in applications that require inexpensive electrocatalysts.

Research on electrocatalysts for the CER has focused on solid solutions of IrO_2 or RuO_2 with abundant metal oxides such as TiO_2.[24] The commercial electrocatalysts for the CER in the chlor-alkali process has consisted of solid solutions of RuO_2 with TiO_2 for over 40 years.[27] The TiO_2 in the electrocatalysts is thermodynamically stable under the operating conditions, but inactive towards the CER. The solid solutions exhibit improved stability compared to pure RuO_2. Addition of TiO_2 lowers the intrinsic activity and the utilization of noble metals in the electrocatalysts. The RuO_2/TiO_2 morphology can be controlled to improve mass transport by creating a mesoporous electrocatalyst film.[28] Metal oxide combinations such as IrO_2 with TaO_x also exhibit improved stability towards the CER in acidic electrolytes.[29] Additionally, conformal TiO_2 coatings have been used to modify the activity of noble-metal oxide electrocatalysts.[30]

In Chapter 3, the properties of crystalline transition-metal antimonates such as $NiSb_2O_x$, $CoSb_2O_x$, and $MnSb_2O_x$ towards the CER are investigated.[31] The research was motivated by the similarities in challenges between the OER in acidic electrolytes and the CER for the chlor-alkali process. In both cases electrocatalysts containing Ir or Ru have been utilized previously, and binary oxides of first-row transition-metals have exhibited limited success due to thermodynamic stability. Crystalline transition-metal antimonates have been demonstrated to be active and stable towards the OER in acidic electrolytes.[23] The results

indicate that $CoSb_2O_x$ is a promising electrocatalyst for the CER since it exhibits high activity and stability that exceeds RuO_2/TiO_2 solid-solutions.[31]

1.3 Semiconductor-Metal Oxide Protective Heterojunctions

Integrated photoelectrochemical devices incorporate semiconductors, electrocatalysts, and membranes to generate fuels via electrochemical reactions with energy from sunlight.[32] Photoelectrochemical devices could be an important component in future renewable energy systems due to the ability to store energy in chemical bonds, which can be utilized to decouple renewable energy availability from energy demand.[33] A proposed design for a photoelectrochemical device integrates two light absorbers, an ion exchange membrane, and electrocatalysts to electrolyze water.[32] The two semiconductors in the integrated device require band gaps close to 1.1 eV and 1.7 eV to optimize efficiency.[34] Additionally, the device must operate in strongly acidic or alkaline electrolytes in order to minimize efficiency losses from pH gradients.[35] Many semiconductors that exhibit the optoelectronic properties for efficient photoelectrochemical operation corrode in aqueous electrolytes.[36-37] For example, under anodic operation in acidic electrolytes silicon will chemically passivate by forming a surface SiO_x layer (Figure 3).[38] The SiO_x layer is insulating and prevents charge transfer between silicon and electrocatalysts. Additionally, in alkaline electrolytes the SiO_x layer and silicon will dissolve and lead to device corrosion (Figure 3).[39]

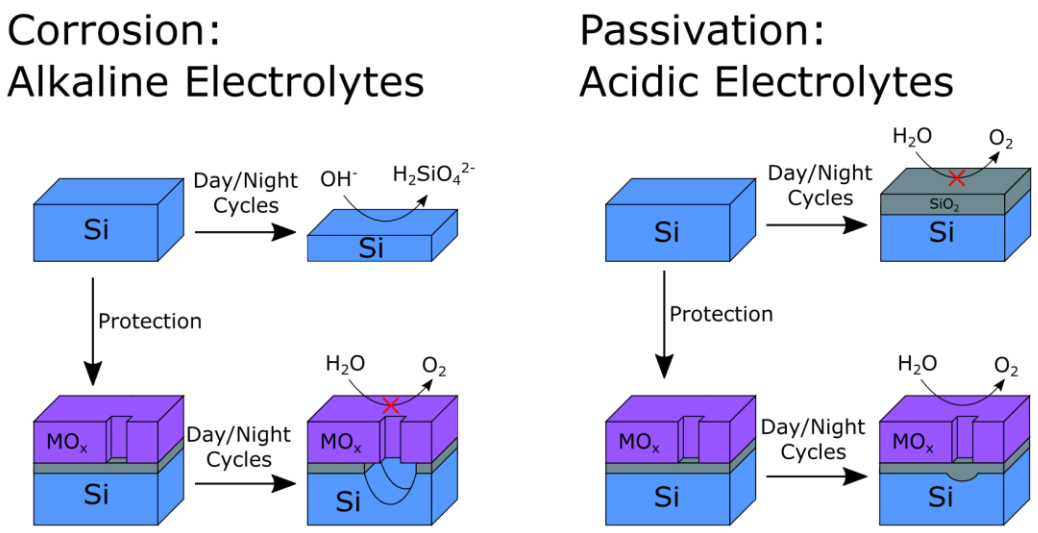

Figure 3. Behavior of Si photoanodes with structurally defective protective layers. In integrated photoelectrochemical devices, Si is exposed to anodic and open-circuit conditions under realistic operating conditions. Since Si and SiO_2 are susceptible to corrosion in alkaline electrolytes, defective layers will lead to eventual corrosion of the Si substrate. In acidic electrolytes, the SiO_2 layer is kinetically stable and will prevent further oxidation of the Si substrate.

Protective heterojunctions can be utilized to prevent semiconductor corrosion and control charge transfer at semiconductor surfaces, which enables stable and efficient photoelectrochemical devices with semiconductors in corrosive electrolytes (Figure 3).[40-41] Photoanodes for the OER typically consist of n-type semiconductors coated with a protective metal oxide coating that is 2 – 200 nm thick.[36-37] The metal oxide coating must be kinetically or thermodynamically stable in the corrosive electrolyte, and should exhibit a large band gap to minimize parasitic light absorption.[42] Additionally, the metal oxide should facilitate charge transfer between the semiconductor and relevant electrocatalysts for the OER. In order to

form a heterojunction, the metal oxide must have a high work function relative to the fermi level of the n-type semiconductor.[43] The high work function requires substantial charge transfer between the n-type semiconductor and the metal oxide, resulting in band bending within the n-type semiconductor.[43] The band bending results in asymmetric charge transfer, which leads to a photovoltage under solar illumination.

A challenge in the development of protective heterojunctions is identifying multifunctional materials that exhibit the protective, electronic, optical and electrocatalytic properties required for photoelectrochemical systems. While there has been substantial progress in the stability of protected silicon photoanodes in alkaline electrolytes, the stability of silicon photoanodes in acidic electrolytes has been limited to ~ 100 h of operation.[36] Silicon photoelectrodes could be more defect-tolerant in acidic electrolytes compared to alkaline electrolytes due to the dissolution of Si and SiO_x in alkaline electrolytes (Figure 3). The electronic properties of silicon/metal oxide interfaces are often poor, exhibiting substantial surface recombination and requiring the use of diffused p-n junctions to separate electron-hole pairs.[42, 44] Protective metal oxides are often opaque, absorbing light in the visible region and reducing the efficiency of photoelectrochemical devices.[45] Additionally, integration of electrocatalyst with protective coatings can lead to unfavorable interactions that result the degradation of device performance, as exemplified by the interface between amorphous TiO_2 and Ir metal.[44] An ideal protective layer would be able to completely suppress semiconductor corrosion, passivate electrical defects at the semiconductor/metal oxide interface, induce band-bending, be optically transparent, act as an anti-reflection layer, and would be electrocatalytic or allow integration of existing electrocatalysts.

Various coatings have been utilized to partially fulfill the desired qualities for protective heterojunctions with silicon photoanodes, such as TiO_2, CoO_x, Ni, MnO_x, CoO_x/NiO_x, and polymer films.[40, 44, 46-47] Conformal layers of TiO_2 deposited with atomic layer deposition have been utilized to protect Si, GaAs, and GaP in alkaline electrolytes. Formation of a SiO_x layer between n-Si and TiO_2 leads to favorable band bending, resulting in a photovoltage of ~ 360 mV under solar illumination.[44] The TiO_2 layer can form conductive contacts to Ni metal precatalyst layers than convert to NiFeOOH under electrochemical operation and molecular catalysts.[44, 48] Unfortunately, deposition of Ir as a precatalyst for the OER in acidic electrolytes leads to unfavorable charge transfer, which prevents TiO_2 from being utilized in acidic electrolytes.[44] Silicon heterojunctions with MnO_x, CoO_x, CoO_x/NiO_x lead to photovoltages < 580 mV, and these metal oxides exhibit electrocatalytic activity towards the OER.[40, 46] However, these films are incompatible with acidic electrolytes.[3] Thus, there is a need to develop a protective metal oxide coating that is compatible with acidic electrolytes.

In Chapter 4, heterojunctions between n-type silicon and tin oxide (SnO_x) are investigated as photoanodes for the OER in corrosive electrolytes.[49] The SnO_x layer exhibits a high work function due to moderate n-type doping, allowing heterojunctions to be formed with n-type silicon with barrier heights > 1.07 eV.[49] The n-Si/SnO_x heterojunction is electrically passivated by an interfacial SiO_x layer that is 1.5 nm thick, allowing photovoltages > 620 mV under simulated sunlight. SnO_x exhibits a 4.2 eV band gap that allows the relevant portion of the solar spectrum to be absorbed by the Si substrate.[49] The SnO_x layer is stable in corrosive electrolytes such as 1.0 M KOH(aq) and 1.0 M H_2SO_4(aq),

and can be coupled to metallic precatalyst Ni, Pt, and Ir films for the OER in these electrolytes.[49] The results indicate that SnO_x is a viable component for photoelectrochemical devices in corrosive electrolytes, and fulfills many of the properties desired for protective heterojunctions.

1.4 Conformal Heterojunctions for Microwire Array Photoelectrochemical Devices

Photoelectrochemical microwire arrays have been proposed as an alternative to planar photoelectrodes.[50] In a silicon microwire array device, high aspect ratio structures with a diameter of approximately 3 μm and a height of 30 μm are embedded in an ion exchange membrane (Figure 4).[51] Integration of the microwires with a membrane allows the construction of flexible devices. [51] The high aspect ratio structure can be used to decouple the light absorption length from the charge-transfer length, which can allow the utilization of semiconductors with short diffusion lengths.[52] The microwires structure also reduces the amount of semiconducting material required to effectively absorb sunlight.[53]

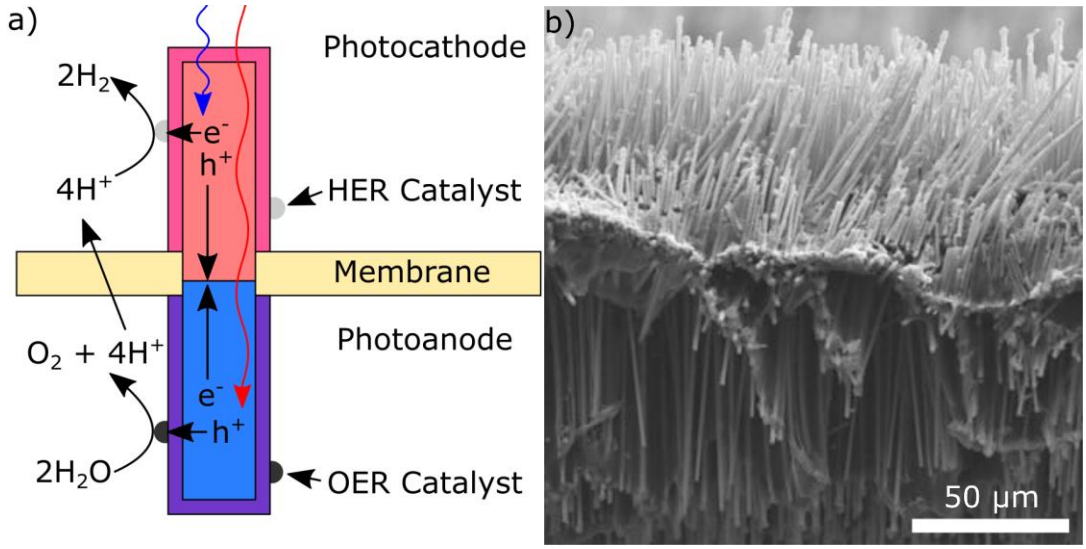

Figure 4. a) Schematic of an integrated photoelectrochemical device consisting of two semiconductors, two protective layers, a cation exchange membrane, and two electrocatalysts for the hydrogen and oxygen evolution reactions. b) Scanning-electron microscopy image of silicon microwires embedded in a Nafion cation-exchange membrane. The image was previous reported in the literature.[51]

The microwire morphology results in several challenges compared to planar photoelectrodes. The higher surface area of microwires compared to planar devices leads to more surface recombination, which can decrease the photovoltage generated by the photoelectrochemical device.[54] Additionally, the microwire morphology exposes several crystal orientations, whereas planar single-crystal substrates only expose one crystal orientation. For example, silicon microcone arrays that exhibit a tapered microwire structure have a rough surface that exposes high index crystal orientations.[53] The exposure of many crystalline facets requires that methods to passivate surface electrical defects that can be generalized to arbitrary crystal orientations. Another challenge is that the microwire array morphology prevents the use of directional deposition methods such as spray pyrolysis, evaporation, or sputtering to deposit uniformly thick protective layers.

Diffused p-n junctions have been utilized to minimize the effect of crystalline orientation on microwire device efficiency and provide enough photovoltage for electrochemical reactions.[54] Radial junctions have been formed on p-type Si microwires by diffusing phosphorous on the surface, allowing the construction of semiconductor wire array devices with a ~ 540 mV photovoltage under solar illumination.[54] Additionally, diffused junctions

have been formed on n-type Silicon microwire arrays for water oxidation, providing ~ 440 mV of photovoltage under solar illumination.[55] While diffused junctions can provide the photovoltage necessary for electrochemical reactions, the diffusion of dopants introduces a high temperature step that increases the energy required to construct a device and could be incompatible with other components in a fully integrated device. An alternative approach toward obtaining a high photovoltage from semiconductor microwire arrays is to utilize a conformal silicon/metal oxide heterojunction to separate electron-hole pairs. While there has been substantial progress in developing metal oxide heterojunctions in single-crystalline substrates for water oxidation, more research is required to demonstrate the efficacy of heterojunctions on microwire array devices.

In Chapter 5, conformal n-Si/SnO_x heterojunctions are developed for silicon microcone arrays. The SnO_x film is deposited with atomic-layer deposition, allowing conformal coatings on mesostructured substrates. The SnO_x film exhibits a high work function, and thickness-dependent morphology changes. Films with thickness < 15 nm are amorphous and conductive, allowing direct electrodeposition of electrocatalysts for the OER. This allows direct integration of electrocatalysts to light absorbers, without the need to deposit metal layers that lead to parasitic light absorption. The n-Si/SnO_x microcone arrays exhibit a photovoltage of 490 mV, which is close to the 520 mV photovoltage expected from the 14 times surface area increase of microcones compared to planar substrates. The SnO_x layer can also be integrated with TiO_2 to form bi-layers that exhibit the heterojunction properties of SnO_x, and the protective properties of TiO_2. These properties indicate that SnO_x is a viable component in integrated microwire array photoelectrochemical devices.

1.5 References

1. Lewis, N. S.; Nocera, D. G., Powering the planet: chemical challenges in solar energy utilization. *Proc Natl Acad Sci U S A* **2006,** *103* (43), 15729-35.
2. Gray, H. B., Powering the planet with solar fuel. *Nat. Chem.* **2009,** *1* (7).
3. McCrory, C. C.; Jung, S.; Ferrer, I. M.; Chatman, S. M.; Peters, J. C.; Jaramillo, T. F., Benchmarking hydrogen evolving reaction and oxygen evolving reaction electrocatalysts for solar water splitting devices. *J. Am. Chem. Soc.* **2015,** *137* (13), 4347-57.
4. Callejas, J. F.; Read, C. G.; Roske, C. W.; Lewis, N. S.; Schaak, R. E., Synthesis, Characterization, and Properties of Metal Phosphide Catalysts for the Hydrogen-Evolution Reaction. *Chem. Mater.* **2016,** *28* (17), 6017-6044.
5. Roger, I.; Shipman, M. A.; Symes, M. D., Earth-abundant catalysts for electrochemical and photoelectrochemical water splitting. *Nature Reviews Chemistry* **2017,** *1* (1).
6. Popczun, E. J.; Read, C. G.; Roske, C. W.; Lewis, N. S.; Schaak, R. E., Highly active electrocatalysis of the hydrogen evolution reaction by cobalt phosphide nanoparticles. *Angew. Chem. Int. Ed.* **2014,** *53* (21), 5427-30.
7. Popczun, E. J.; McKone, J. R.; Read, C. G.; Biacchi, A. J.; Wiltrout, A. M.; Lewis, N. S.; Schaak, R. E., Nanostructured nickel phosphide as an electrocatalyst for the hydrogen evolution reaction. *J. Am. Chem. Soc.* **2013,** *135* (25), 9267-70.
8. Ledendecker, M.; Mondschein, J.; Kasian, O.; Geiger, S.; Gohl, D.; Schalenbach, M.; Zeradjanin, A.; Cherevko, S.; Schaak, R. E.; Mayrhofer, K., Stability and activity of

non-noble based catalysts toward the hydrogen evolution reaction - feasible electrocatalysts in acidic medium? *Angew. Chem. Int. Ed.* **2017**.

9. Dau, H.; Limberg, C.; Reier, T.; Risch, M.; Roggan, S.; Strasser, P., The Mechanism of Water Oxidation: From Electrolysis via Homogeneous to Biological Catalysis. *ChemCatChem* **2010,** *2* (7), 724-761.
10. Man, I. C.; Su, H.-Y.; Calle-Vallejo, F.; Hansen, H. A.; Martínez, J. I.; Inoglu, N. G.; Kitchin, J.; Jaramillo, T. F.; Nørskov, J. K.; Rossmeisl, J., Universality in Oxygen Evolution Electrocatalysis on Oxide Surfaces. *ChemCatChem* **2011,** *3* (7), 1159-1165.
11. McCrory, C. C.; Jung, S.; Peters, J. C.; Jaramillo, T. F., Benchmarking heterogeneous electrocatalysts for the oxygen evolution reaction. *J. Am. Chem. Soc.* **2013,** *135* (45), 16977-87.
12. Seitz, L. C.; Dickens, C. F.; Nishio, K.; Hikita, Y.; Montoya, J.; Doyle, A.; Kirk, C.; Vojvodic, A.; Hwang, H. Y.; Norskov, J. K.; Jaramillo, T. F., A highly active and stable $IrO_x/SrIrO_3$ catalyst for the oxygen evolution reaction. *Science* **2016,** *353* (6303), 1011-1014.
13. Vesborg, P. C. K.; Jaramillo, T. F., Addressing the terawatt challenge: scalability in the supply of chemical elements for renewable energy. *RSC Adv.* **2012,** *2* (21), 7933.
14. Trotochaud, L.; Young, S. L.; Ranney, J. K.; Boettcher, S. W., Nickel-iron oxyhydroxide oxygen-evolution electrocatalysts: the role of intentional and incidental iron incorporation. *J. Am. Chem. Soc.* **2014,** *136* (18), 6744-6753.
15. Beverskog, B.; Puigdomenech, I., Revised Pourbaix Diagrams for Nickel at 25-300 °C. *Corros. Sci.* **1997,** *39* (5), 969-980.

16. Bloor, L. G.; Molina, P. I.; Symes, M. D.; Cronin, L., Low pH electrolytic water splitting using earth-abundant metastable catalysts that self-assemble in situ. *J. Am. Chem. Soc.* **2014,** *136* (8), 3304-11.

17. Frydendal, R.; Paoli, E. A.; Chorkendorff, I.; Rossmeisl, J.; Stephens, I. E. L., Toward an Active and Stable Catalyst for Oxygen Evolution in Acidic Media: Ti-Stabilized MnO_2. *Adv. Energy Mater.* **2015,** *5* (22), 1500991.

18. Mondschein, J. S.; Callejas, J. F.; Read, C. G.; Chen, J. Y. C.; Holder, C. F.; Badding, C. K.; Schaak, R. E., Crystalline Cobalt Oxide Films for Sustained Electrocatalytic Oxygen Evolution under Strongly Acidic Conditions. *Chem. Mater.* **2017**.

19. Huynh, M.; Bediako, D. K.; Nocera, D. G., A functionally stable manganese oxide oxygen evolution catalyst in acid. *J. Am. Chem. Soc.* **2014,** *136* (16), 6002-10.

20. Jain, A.; Ong, S. P.; Hautier, G.; Chen, W.; Richards, W. D.; Dacek, S.; Cholia, S.; Gunter, D.; Skinner, D.; Ceder, G.; Persson, K. A., Commentary: The Materials Project: A materials genome approach to accelerating materials innovation. *APL Mater.* **2013,** *1* (1), 011002.

21. Li, A.; Ooka, H.; Bonnet, N.; Hayashi, T.; Sun, Y.; Jiang, Q.; Li, C.; Han, H.; Nakamura, R., Stable Potential Windows for Long-Term Electrocatalysis by Manganese Oxides Under Acidic Conditions. *Angew. Chem. Int. Ed.* **2019,** *58* (15), 5054-5058.

22. Shaner, M. R.; Davis, S. J.; Lewis, N. S.; Caldeira, K., Geophysical constraints on the reliability of solar and wind power in the United States. *Energy Environ. Sci.* **2018,** *11* (4), 914-925.

23. Moreno-Hernandez, I. A.; MacFarland, C. A.; Read, C. G.; Papadantonakis, K. M.; Brunschwig, B. S.; Lewis, N. S., Crystalline nickel manganese antimonate as a stable water-oxidation catalyst in aqueous 1.0 M H_2SO_4. *Energy Environ. Sci.* **2017,** *10* (10), 2103-2108.

24. Karlsson, R. K.; Cornell, A., Selectivity between Oxygen and Chlorine Evolution in the Chlor-Alkali and Chlorate Processes. *Chem. Rev.* **2016,** *116* (5), 2982-3028.

25. Martinez-Huitle, C. A.; Ferro, S., Electrochemical oxidation of organic pollutants for the wastewater treatment: direct and indirect processes. *Chem. Soc. Rev.* **2006,** *35* (12), 1324-40.

26. Exner, K. S.; Anton, J.; Jacob, T.; Over, H., Full Kinetics from First Principles of the Chlorine Evolution Reaction over a RuO_2 (110) Model Electrode. *Angew. Chem. Int. Ed.* **2016,** *55* (26), 7501-4.

27. Beer, H. B., Method of Making an Electrode Having a Coating Containing a Platinum Metal Oxide Thereon. *U.S. Patent 4052271* **1977**.

28. Jiang, M.; Wang, H.; Li, Y.; Zhang, H.; Zhang, G.; Lu, Z.; Sun, X.; Jiang, L., Superaerophobic RuO_2 -Based Nanostructured Electrode for High-Performance Chlorine Evolution Reaction. *Small* **2017,** *13* (4).

29. Cho, K.; Hoffmann, M. R., $Bi_xTi_{1-x}O_z$ Functionalized Heterojunction Anode with an Enhanced Reactive Chlorine Generation Efficiency in Dilute Aqueous Solutions. *Chem. Mater.* **2015,** *27* (6), 2224-2233.

30. Finke, C. E.; Omelchenko, S. T.; Jasper, J. T.; Lichterman, M. F.; Read, C. G.; Lewis, N. S.; Hoffmann, M. R., Enhancing the activity of oxygen-evolution and chlorine-

evolution electrocatalysts by atomic layer deposition of TiO_2. *Energy Environ. Sci.* **2019,** *12* (1), 358-365.

31. Moreno-Hernandez, I. A.; Brunschwig, B. S.; Lewis, N. S., Crystalline nickel, cobalt, and manganese antimonates as electrocatalysts for the chlorine evolution reaction. *Energy Environ. Sci.* **2019,** *12* (4), 1241-1248.
32. Lewis, N. S., Developing a scalable artificial photosynthesis technology through nanomaterials by design. *Nat. Nanotech.* **2016,** *11* (12), 1010-1019.
33. Lewis, N. S., Research opportunities to advance solar energy utilization. *Science* **2016,** *351* (6271), aad1920.
34. Hu, S.; Xiang, C.; Haussener, S.; Berger, A. D.; Lewis, N. S., An analysis of the optimal band gaps of light absorbers in integrated tandem photoelectrochemical water-splitting systems. *Energy Environ. Sci.* **2013,** *6* (10), 2984.
35. Singh, M. R.; Papadantonakis, K.; Xiang, C.; Lewis, N. S., An electrochemical engineering assessment of the operational conditions and constraints for solar-driven water-splitting systems at near-neutral pH. *Energy Environ. Sci.* **2015,** *8* (9), 2760-2767.
36. Bae, D.; Seger, B.; Vesborg, P. C.; Hansen, O.; Chorkendorff, I., Strategies for stable water splitting via protected photoelectrodes. *Chem. Soc. Rev.* **2017,** *46* (7), 1933-1954.
37. Lichterman, M. F.; Sun, K.; Hu, S.; Zhou, X.; McDowell, M. T.; Shaner, M. R.; Richter, M. H.; Crumlin, E. J.; Carim, A. I.; Saadi, F. H.; Brunschwig, B. S.; Lewis, N. S., Protection of inorganic semiconductors for sustained, efficient photoelectrochemical water oxidation. *Catal. Today* **2016,** *262*, 11-23.

38. Sun, K.; Ritzert, N. L.; John, J.; Tan, H.; Hale, W.; Jiang, J.; Moreno-Hernandez, I. A.; Papadantonakis, K. M.; Moffat, T. P.; Brunschwig, B. S.; Lewis, N., Performance and Failure Modes of Si Anodes Patterned with Thin-Film Ni Catalyst Islands for Water Oxidation. *Sustainable Energy Fuels* **2018,** *2*, 983-998.

39. Nikolaychuk, P. A., The Revised Pourbaix Diagram for Silicon. *Silicon* **2014,** *6* (2), 109-116.

40. Strandwitz, N. C.; Comstock, D. J.; Grimm, R. L.; Nichols-Nielander, A. C.; Elam, J.; Lewis, N. S., Photoelectrochemical Behavior of n-type Si(100) Electrodes Coated with Thin Films of Manganese Oxide Grown by Atomic Layer Deposition. *J. Phys. Chem. C* **2013,** *117* (10), 4931-4936.

41. Zhou, X.; Liu, R.; Sun, K.; Papadantonakis, K. M.; Brunschwig, B. S.; Lewis, N. S., 570 mV photovoltage, stabilized n-Si/CoO_x heterojunction photoanodes fabricated using atomic layer deposition. *Energy Environ. Sci.* **2016**.

42. Sun, K.; McDowell, M. T.; Nielander, A. C.; Hu, S.; Shaner, M. R.; Yang, F.; Brunschwig, B. S.; Lewis, N. S., Stable Solar-Driven Water Oxidation to O_2(g) by Ni-Oxide-Coated Silicon Photoanodes. *J. Phys. Chem. Lett.* **2015,** *6* (4), 592-8.

43. Green, M. A.; Godfrey, R. B., MIS solar cell—General theory and new experimental results for silicon. *Appl. Phys. Lett.* **1976,** *29* (9), 610.

44. Hu, S.; Shaner, M. R.; Beardslee, J. A.; Lichterman, M.; Brunschwig, B. S.; Lewis, N. S., Amorphous TiO_2 coatings stabilize Si, GaAs, and GaP photoanodes for efficient water oxidation. *Science* **2014,** *344* (6187), 1005-9.

45. Sun, K.; Moreno-Hernandez, I. A.; Schmidt, W. C.; Zhou, X.; Crompton, J. C.; Liu, R.; Saadi, F. H.; Chen, Y.; Papadantonakis, K. M.; Lewis, N. S., A Comparison of the

Chemical, Optical and Electrocatalytic Properties of Water-Oxidation Catalysts for Use in Integrated Solar-Fuels Generators. *Energy Environ. Sci.* **2017,** *10*, 987-1002.

46. Zhou, X.; Liu, R.; Sun, K.; Friedrich, D.; McDowell, M. T.; Yang, F.; Omelchenko, S. T.; Saadi, F. H.; Nielander, A. C.; Yalamanchili, S.; Papadantonakis, K. M.; Brunschwig, B. S.; Lewis, N. S., Interface engineering of the photoelectrochemical performance of Ni-oxide-coated n-Si photoanodes by atomic-layer deposition of ultrathin films of cobalt oxide. *Energy Environ. Sci.* **2015,** *8* (9), 2644-2649.
47. Kenney, M. J.; Gong, M.; Li, Y.; Wu, J. Z.; Feng, J.; Lanza, M.; Dai, H., High-performance silicon photoanodes passivated with ultrathin nickel films for water oxidation. *Science* **2013,** *342* (6160), 836-40.
48. Matheu, R.; Moreno-Hernandez, I. A.; Sala, X.; Gray, H. B.; Brunschwig, B. S.; Llobet, A.; Lewis, N. S., Photoelectrochemical Behavior of a Molecular Ru-Based Water-Oxidation Catalyst Bound to TiO_2-Protected Si Photoanodes. *J. Am. Chem. Soc.* **2017,** *139* (33), 11345-11348.
49. Moreno-Hernandez, I. A.; Brunschwig, B. S.; Lewis, N. S., Tin Oxide as a Protective Heterojunction with Silicon for Efficient Photoelectrochemical Water Oxidation in Strongly Acidic or Alkaline Electrolytes. *Adv. Energy Mater.* **2018,** *8* (24), 1801155.
50. Warren, E. L.; Atwater, H. A.; Lewis, N. S., Silicon Microwire Arrays for Solar Energy-Conversion Applications. *J. Phys. Chem. C* **2013,** *118* (2), 747-759.
51. Spurgeon, J. M.; Walter, M. G.; Zhou, J.; Kohl, P. A.; Lewis, N. S., Electrical conductivity, ionic conductivity, optical absorption, and gas separation properties of ionically conductive polymer membranes embedded with Si microwire arrays. *Energy Environ. Sci.* **2011,** *4* (5), 1772.

52. Kayes, B. M.; Atwater, H. A.; Lewis, N. S., Comparison of the device physics principles of planar and radial p-n junction nanorod solar cells. *J. Appl. Phys.* **2005,** *97* (11), 114302.

53. Yalamanchili, S.; Emmer, H. S.; Fountaine, K. T.; Chen, C. T.; Lewis, N. S.; Atwater, H. A., Enhanced Absorption and <1% Spectrum-and-Angle-Averaged Reflection in Tapered Microwire Arrays. *ACS Photonics* **2016,** *3* (10), 1854-1861.

54. Boettcher, S. W.; Warren, E. L.; Putnam, M. C.; Santori, E. A.; Turner-Evans, D.; Kelzenberg, M. D.; Walter, M. G.; McKone, J. R.; Brunschwig, B. S.; Atwater, H. A.; Lewis, N. S., Photoelectrochemical hydrogen evolution using Si microwire arrays. *J. Am. Chem. Soc.* **2011,** *133* (5), 1216-9.

55. Shaner, M. R.; Hu, S.; Sun, K.; Lewis, N. S., Stabilization of Si microwire arrays for solar-driven H_2O oxidation to O_2(g) in 1.0 M KOH(aq) using conformal coatings of amorphous TiO_2. *Energy Environ. Sci.* **2015,** *8* (1), 203-207.

Chapter II

CRYSTALLINE TRANSITION METAL ANTIMONATES FOR THE OXYGEN EVOLUTION REACTION

Moreno-Hernandez, I. A.; MacFarland, C. A.; Read, C. G.; Papadantonakis, K. M.; Brunschwig, B. S.; Lewis, N. S., Crystalline nickel manganese antimonate as a stable water-oxidation catalyst in aqueous 1.0 M H_2SO_4. *Energy Environ. Sci.* **2017,** *10* (10), 2103-2108. DOI: 10.1039/C7EE01486D

2.1 Introduction

Facile conversion of electricity into chemical fuels is an enabling technology for grid-scale energy storage as well as for the production of carbon-neutral transportation fuels.[1] Reductive fuel generation necessitates the oxidation of another molecule. Oxidation of water by the oxygen-evolution reaction (OER) enables release of the oxidized product and the use of atmospheric O_2(g) for oxidation of the fuel. While earth-abundant, low-overpotential electrocatalysts are available for both the hydrogen-evolution and oxygen-evolution reactions in aqueous alkaline media,[2] in acidic electrolytes the only well-established stable OER electrocatalysts are noble metal oxides such as IrO_x and RuO_x.[2-5] The low abundance Ir and Ru presents challenges for global scalability of associated sustainable energy technologies.[6] Efforts to improve the activity and stability of earth-abundant catalysts for the OER in acid have included searches for acid-stable metal-oxide phases;[7-9] anodic electrodeposition of dissolved transition metals to produce phases that are stable in equilibrium with cations in solution at the OER potential;[10] and doping metal oxides using

anions that have high oxidation potentials.[9] Oxides that incorporate two or more metals offer the potential to tune the stability of the material by the formation of new phases that are more stable than the individual metal oxides.[11-12] Synergistic interactions in multimetal electrocatalysts can additionally yield improved activity relative to catalysts formed from the individual metals.[13-14]

According to Pourbaix diagrams, metal oxides of Ni, Mn, and Sb are stable in acidic conditions at OER potentials.[11-12] Furthermore, selected transition-metal antimonates, such as $NiSb_2O_6$, are predicted to be stable at all temperatures with respect to disproportionation to the constituent binary oxides.[15] Thus, Sb was chosen as an element to form ternary or quaternary oxides with Ni and Mn due to the predicted thermodynamic stability under OER conditions in acid and the over 4 orders of magnitude higher annual production of Sb relative to Ir.[6] Accordingly, we report herein the synthesis of solid solutions of crystalline $NiSb_2O_6$ with $MnSb_2O_6$, and report the electrochemical activity and stability of the compounds for the OER in acidic media. The electrochemical behavior was characterized over a range of current densities, with emphasis on the performance at 10 mA cm^{-2}, which is characteristic of the operational current density for an ~10% efficient solar fuels device under 1 Sun, nonconcentrated, peak insolation conditions.[2]

2.2 Results

$Ni_xMn_{1-x}Sb_{1.6-1.8}O_y$ catalysts were prepared by sputter deposition of the precursor metals onto quartz slides that were coated with a conductive film of antimony-doped tin oxide (ATO).[16] The metal film was annealed in air (details provided in Supplementary Information). For compositions with $x > 0.2$, the $Ni_xMn_{1-x}Sb_{1.6-1.8}O_y$ materials obtained by annealing the films at 700 °C contained rutile-type MSb_2O_6 (Figure S1). The bulk composition of the precursor metal films, shown in Table S1, was measured by inductively coupled plasma mass spectrometry (ICP-MS). Figure S2 shows the surface composition of the electrocatalysts as determined by X-ray photoelectron spectroscopy (XPS). The atomic ratios of Ni to the total transition metals (i.e., Ni/(Ni + Mn)), and of Sb to the total transition metals were used to measure their surface segregation. For the as-synthesized material, the ratio of Ni-to-transition metals deduced using XPS (Figure S2A) was similar to the bulk ratio determined using ICP-MS (Table S1). However, deviations from the ratio of Sb-to-transition metals of 1.6-1.8 determined from ICP-MS (Table S1) indicated that the surface was Sb rich for Mn-rich compositions and was transition-metal rich for Ni-rich compositions (Figure S2B). Antimonates generally exhibit surface enrichment of Sb,[17] however modifications in the synthesis temperature can produce Sb-poor surfaces.[18]

The catalytic activity and stability were evaluated via cyclic voltammetry (CV) and chronopotentiometry in 1.0 M H_2SO_4(aq), using methods that closely followed established OER electrocatalyst benchmarking procedures.[2] Figure 1A shows typical cyclic voltammograms obtained for the family of $Ni_xMn_{1-x}Sb_{1.6-1.8}O_y$ materials when the applied potential was scanned at 10 mV s^{-1} within the range of 1.2 to 2.20 V versus a reversible

hydrogen electrode (RHE). Figure 1B summarizes the overpotentials required to produce a current density of 10 mA cm^{-2} (based on the geometric area of the electrodes) for catalysts having the formula $Ni_xMn_{1-x}Sb_{1.6-1.8}O_y$ with a loading of ~0.5 μmol cm^{-2} (Table S1).

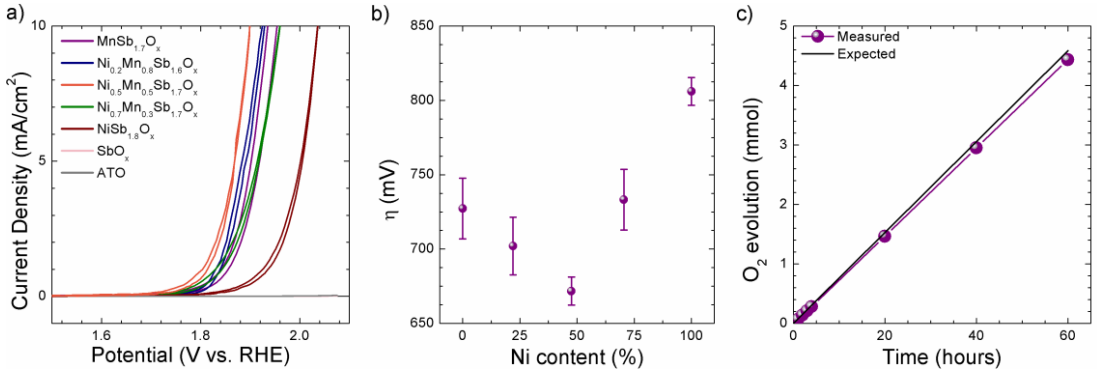

Figure 1. Electrochemical behavior, activity, and faradaic efficiency of $Ni_xMn_{1-x}Sb_{1.6-1.8}O_y$ electrodes in 1.0 M H_2SO_4(aq). (a) Cyclic voltammetry at a scan rate of 10 mV s^{-1} of $Ni_xMn_{1-x}Sb_{1.6-1.8}O_y$, SbO_x, and ATO electrodes. (b) Average overpotential at 10 mA cm^{-2} determined from cyclic voltammetry data at a scan rate of 10 mV s^{-1} for $Ni_xMn_{1-x}Sb_{1.6-1.8}O_y$. Ni content defined as percent of transition metals in the as-synthesized film. The overpotentials for $NiSb_{1.8}O_x$, $MnSb_{1.7}O_x$, and $Ni_{0.5}Mn_{0.5}Sb_{1.7}O_x$ were 806 ± 9 mV, 727 ± 20 mV, and 672 ± 9 mV, respectively. The error bars indicate one standard deviation from at least 3 samples. (c) Faradaic efficiency measurements performed with a eudiometer while a $Ni_{0.5}Mn_{0.5}Sb_{1.7}O_x$ electrode was maintained galvanostatically at 10 mA cm^{-2}. The average faradaic efficiency was 93% from 0 to 4 h and 97% from 20 to 60 h.

The overpotential, η, for $NiSb_{1.8}O_x$ was 806 ± 9 mV, while $MnSb_{1.7}O_x$ exhibited η = 727 ± 20 mV. Films incorporating both Ni and Mn showed the highest activity (i.e., lowest overpotentials) and $Ni_{0.5}Mn_{0.5}Sb_{1.7}O_x$ had the lowest initial overpotential (η = 672 ± 9 mV) of the materials prepared. Resistance compensation had a minimal effect on the measured

overpotentials, with all electrodes being corrected less than 15 mV at 10 mA cm^{-2} (Figure S3A). The overpotentials at a current density of 0.1 mA cm^{-2} based on the electrochemically active surface areas of the electrodes (as determined from the double-layer capacitance, see SI) indicated that films containing both Ni and Mn showed higher activity than antimonate films containing only Ni or Mn (Figure S3B). The series resistance of $Ni_xMn_{1-x}Sb_{1.6-1.8}O_y$ increased for x = 0.2 and 0.5, indicating a decrease in conductivity of the electrocatalyst film (Figure S3C). The slope in the linear region of the Tafel plot for $NiSb_{1.8}O_x$ was 105 ± 2 mV/dec, while $MnSb_{1.7}O_x$ exhibited a slope of 96 ± 7 mV/dec and $Ni_{0.2}Mn_{0.8}Sb_{1.6}O_x$ exhibited the lowest slope measured among the materials, of 60 ± 3 mV/dec, (Figure S4A). Electrodes made from bare ATO or SbO_x did not exhibit substantial activity for water oxidation in this potential range in 1.0 M H_2SO_4(aq) (Figure 1B). Faradaic efficiency measurements using electrodes coated with $Ni_{0.5}Mn_{0.5}Sb_{1.7}O_x$ indicated > 97% efficiency for O_2(g) production during 60 h of operation (Figure 1C). The current density at a fixed potential increased with catalyst loading, indicating that increasing the loading of $Ni_{0.5}Mn_{0.5}Sb_{1.7}O_x$ increased the catalytic activity (Figure S4B). The capacitance of the electrode also increased with loading, suggesting that the catalyst film remained permeable to the electrolyte for the film thicknesses studied herein (Figure S4C). The initial turnover frequency at 0.65 V vs. RHE was 0.03 s^{-1} based on the loading of the catalyst and was 0.67 s^{-1} based on the surface area determined by the measured differential capacitance.

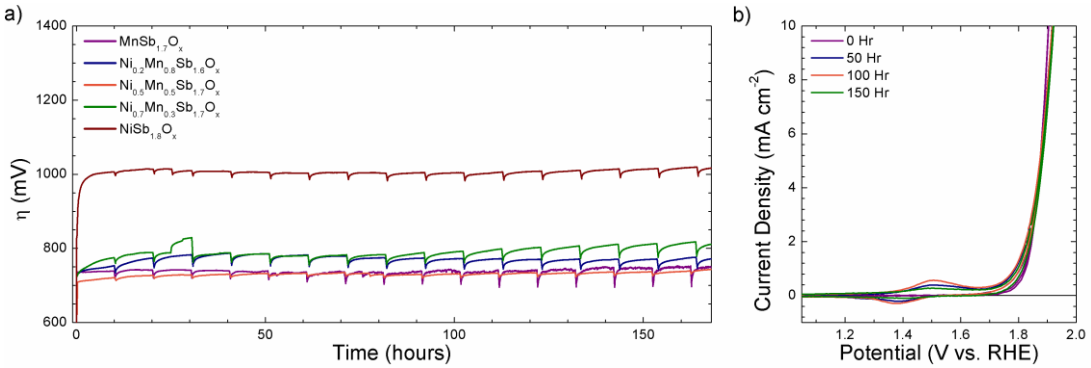

Figure 2. Chronopotentiometric stability of $Ni_xMn_{1-x}Sb_{1.6-1.8}O_y$ electrodes. (a) Chronopotentiometry at 10 mA cm^{-2} of the $Ni_xMn_{1-x}Sb_{1.6-1.8}O_y$ family in 1.0 M H_2SO_4(aq). (b) Cyclic voltammetry at 10 mV s^{-1} of $Ni_{0.5}Mn_{0.5}Sb_{1.7}O_x$ in between chronopotentiometry.

Figure 2A shows chronopotentiometric stability data for the $Ni_xMn_{1-x}Sb_{1.6-1.8}O_y$ family during galvanostatic control at 10 mA cm^{-2}. A transient decrease in the overpotential was observed when cyclic voltammograms were collected, as well as when the experiment was paused every 1-3 days to replenish the electrolyte. No substantial loss of activity was observed after placing the electrodes in fresh electrolyte. $Ni_{0.7}Mn_{0.3}Sb_{1.7}O_x$ showed an increase in overpotential from 25-30 h due to the electrode being partially blocked by a bubble after electrolyte replenishment. For all of the materials, the overpotentials at 10 mA cm^{-2} varied over the course of the test by less than 5% from the average value for that electrode. The overpotential for $Ni_{0.5}Mn_{0.5}Sb_{1.7}O_x$ initially increased from ~670 mV to ~735 mV but then remained at 735 ± 10 mV for 168 h. Based on the 168 h of continuous operation at 10 mA cm^{-2}, the turnover number of $Ni_{0.5}Mn_{0.5}Sb_{1.7}O_x$ exceeded 33,000 (by loading) and 120,000 (by capacitance). Holding $Ni_{0.5}Mn_{0.5}Sb_{1.7}O_x$ at open circuit for 16 h had little effect on the overpotential (Figure S5), demonstrating that the stability of $Ni_{0.5}Mn_{0.5}Sb_{1.7}O_x$ does not depend upon application of a potential positive of the thermodynamic potential required

for water oxidation. Cyclic voltammetry measurements performed at intervals during chronopotentiometry on $Ni_{0.5}Mn_{0.5}Sb_{1.7}O_x$ electrodes exhibited the development of redox peaks centered at 1.46 V versus RHE (Figure 2B). The development of similar redox peaks was observed for $MnSb_{1.7}O_x$ samples, but not for $NiSb_{1.8}O_x$ (Figure S6A). $Ni_{0.5}Mn_{0.5}O_x$ electrodes without Sb, as well as ATO and SbO_x electrodes exhibited $\eta > 1{,}300$ mV after < 10 min at 10 mA cm^{-2} (Figure S6B), consistent with previous reports of the OER behavior of NiO_x and MnO_x in 1 M acid.[2]

ICP-MS was used to determine the concentration of dissolved metals in the electrolyte at different times during the chronopotentiometric stability test (details provided in SI). Approximately 56, 17, and 11 percent of the Mn, Ni, and Sb, respectively, from a $Ni_{0.5}Mn_{0.5}Sb_{1.7}O_x$ electrode had leached into the electrolyte after 144 h at 10 mA cm^{-2} (Figure S7). For all elements measured, the leach rate decreased with time and after 120 h was zero within the error of the ICP-MS technique. The capacitance of the electrode also increased during chronopotentiometry at 10 mA cm^{-2} (Figure S6C), which is consistent with increased porosity arising from the dissolution of electrode material during electrolysis.

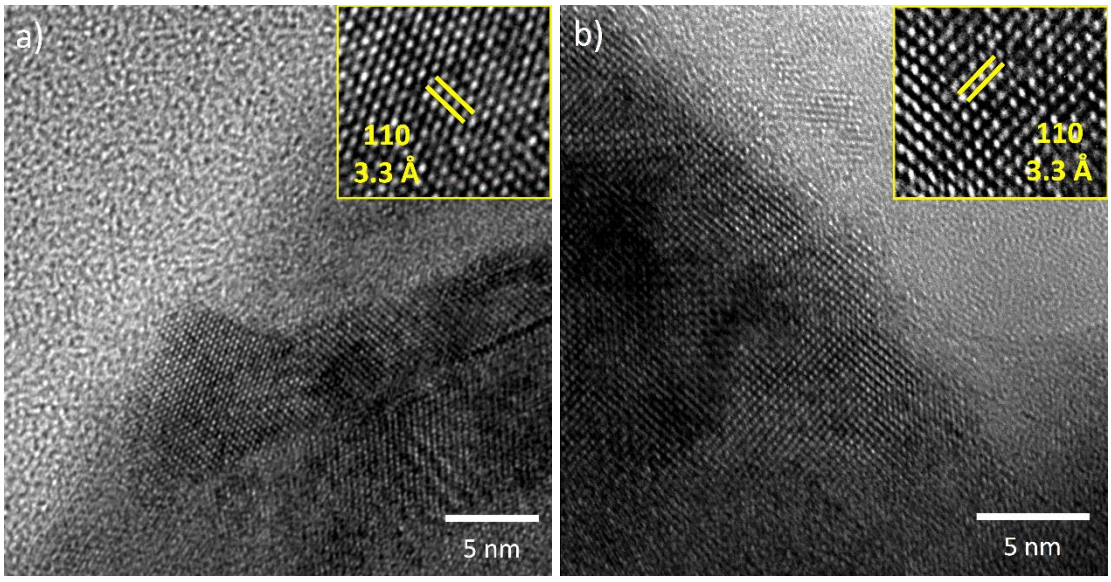

Figure 3. Structural characterization of $Ni_{0.5}Mn_{0.5}Sb_{1.7}O_x$ electrocatalyst. Transmission-electron microscopy of $Ni_{0.5}Mn_{0.5}Sb_{1.7}O_x$ (a) before and (b) after chronopotentiometry for 144 h at 10 mA cm^{-2} of geometric area, highlighting the 3.3 Å lattice fringes that correspond to the (110) planes. The dark areas represent the catalyst and the dark/light interface is the part of the samples that was in contact with the electrolyte.

Figure 3 compares high-resolution transmission electron microscope images (HRTEM) of the surface of $Ni_{0.5}Mn_{0.5}Sb_{1.7}O_x$ before and after operation for 144 h at 10 mA cm^{-2} in 1.0 M H_2SO_4(aq). The observed lattice spacing of ~3.3 Å closely matches the (110) planes of the rutile-type MSb_2O_6,[19] and is consistent with X-ray diffraction data collected after electrochemical operation (Figure S8). The HRTEM images showed no crystalline or amorphous impurities at the surface of the as-synthesized electrodes. High-angle annular dark-field (HAADF) images did not show substantial changes in the ~300 nm thickness of an electrocatalyst film (corresponding to a catalyst loading of 0.48 μmol cm^{-2}) after operation for 144 h (Figure S9). Scanning electron microscopy (SEM) images of $Ni_{0.5}Mn_{0.5}Sb_{1.7}O_x$ -

coated electrodes before and after electrochemical operation were consistent with the presence of polycrystalline surfaces (Figure S10). The STEM-EDS spectrum of the as-synthesized $Ni_{0.5}Mn_{0.5}Sb_{1.7}O_x$ film further confirmed the presence of Ni, Mn, and Sb, with no other observable impurities (Figure S11). No Ir or Ru was detectable by high-resolution XPS after electrochemical operation of the catalyst film (Figure S12).

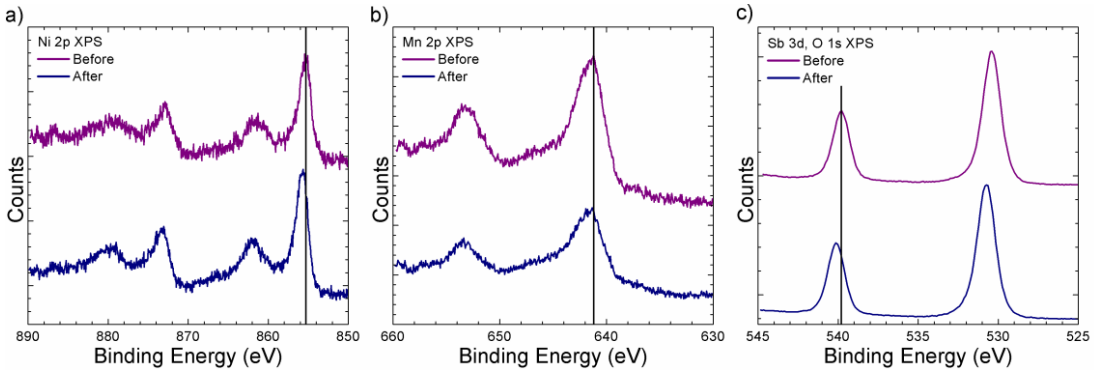

Figure 4. Chemical characterization of $Ni_{0.5}Mn_{0.5}Sb_{1.7}O_x$ electrocatalyst. High-resolution XPS data of $Ni_{0.5}Mn_{0.5}Sb_{1.7}O_x$ before and after chronopotentiometry for 144 h at 10 mA cm^{-2}. The spectral regions are: (a) Ni 2p, (b) Mn 2p, (c) Sb 3d and O 1s. The spectra were normalized so that the integrated signals of the Ni 2p, Mn 2p, and Sb 3d peaks were the same for both samples.

Figure 4 presents high-resolution Mn 2p, Ni 2p, and Sb 3d XPS spectra of a $Ni_{0.5}Mn_{0.5}Sb_{1.7}O_x$-coated electrode before and after electrochemical operation, respectively. After electrolysis, the Ni 2p and Sb 3d peaks shifted towards higher binding energies by 0.39 ± 0.10 eV and 0.33 ± 0.09 eV, respectively. The surface composition determined via XPS for $Ni_{0.5}Mn_{0.5}Sb_{1.7}O_x$ was 1:0.98:4.15 ± 0.05 Ni:Mn:Sb before electrochemical operation and was 1:0.48:3.67 ± 0.03 Ni:Mn:Sb after electrochemical operation. The surface composition determined via XPS for $Ni_{0.7}Mn_{0.3}Sb_{1.7}O_x$ was 1:0.50 ± 0.16 Ni:Mn and 1:2.98 ± 0.93 Ni:Sb

after electrochemical operation. The bulk composition determined by EDS for $Ni_{0.5}Mn_{0.5}Sb_{1.7}O_x$ was 1:1.10:3.57 ± 0.03 Ni:Mn:Sb before electrochemical operation and was 1:1.03:4.44 ± 0.03 Ni:Mn:Sb after electrochemical operation.

Figure S13 shows the effect of the annealing temperature on the electrochemical stability of $Ni_{0.5}Mn_{0.5}Sb_{1.7}O_x$. For films annealed at 500 °C, the overpotential increased to $\eta > 1{,}000$ mV in < 1 min, whereas films annealed at 700 °C exhibited $\eta \sim 745$ mV for 168 h (Figures S13, 1B). XRD of these films indicated that the MSb_2O_6 phase formed at and above 700 °C but not at 500 °C (Figure S14). $NiSb_2O_x$ and $MnSb_2O_x$ undergo a transformation from amorphous to crystalline material at ~ 615 °C and ~715 °C, respectively.[20] Films annealed at 900 °C could not be evaluated, due to the high resistance (> 10 kΩ) as determined from impedance measurements of the resulting electrodes, compared to the resistance exhibited by films annealed at 700 °C (< 150 Ω). The ATO sheet resistance as determined by four-point probe measurements changed little with temperature, and was 17.2 ± 0.9 Ω sq^{-1} for the as-prepared films, 17.2 ± 1.0 Ω sq^{-1} for films annealed at 700 °C, and 21.4 ± 1.0 Ω sq^{-1} for films that had been annealed 900 °C.

2.3 Discussion

The activity of the $Ni_xMn_{1-x}Sb_{1.6-1.8}O_y$ family of electrocatalysts was highest when both Ni and Mn were initially present at equal concentrations in the film. The enhanced activity is not primarily due to changes in film resistance because a higher resistance was observed for x = 0.2 and 0.5 (~ 100 Ω) electrodes compared to x = 0, 0.7, 1 (< 50 Ω) electrodes (Figure S3C). Similar synergistic interactions have been observed for other water-oxidation catalysts, such as $Ni_{1-x}Fe_xOOH$ in alkaline media.[21] The rutile crystal phase appears to favorably affect the electrochemical stability of $Ni_xMn_{1-x}Sb_{1.6-1.8}O_y$ materials for use as oxygen-evolving electrocatalysts in strongly acidic electrolytes. The formation of $NiSb_2O_6$ from NiO and Sb_2O_5 is more favorable than decomposition of $NiSb_2O_6$ to Sb_2O_5 accompanied by subsequent dissolution of NiO to produce Ni^{2+} in pH 0 solution.[15, 22] Hence, the dissolution of Ni is inhibited by the formation of the more stable Ni-containing antimonate phase. Together these results suggest a strategy for discovery of acid-stable water-oxidation catalysts through identification of thermodynamically stable crystalline ternary oxides followed by tuning the electrocatalytic activity and stability of the oxides by altering the ratio between the transition metals in the oxides.

Preferential leaching of Mn from the $Ni_{0.5}Mn_{0.5}Sb_{1.7}O_x$ material is evidenced by Mn detected by ICP-MS in the electrolyte after electrolysis, resulting in the surface enrichment of Ni observed by XPS. Surface enrichment of Sb increases with an increase of Mn in the film, which may be due to the poor crystallization kinetics of $MnSb_2O_6$ at 700 °C. Other OER electrocatalysts, such as $SrIrO_3$ and $Fe_1Co_{1.02}W_{0.7}$ oxyhydroxides, also leach initially under operation, thereby forming a more stable catalyst.[5, 13] The leaching of Mn from a

$Ni_xMn_{1-x}Sb_{1.6-1.8}O_y$ structure with $x > 0.5$ could produce a film that does not have the same surface structure as one obtained directly by annealing metal films of the same final composition. Formation of amorphous, active phases throughout the catalyst film cannot be excluded. Alternatively, the leaching of Mn could be due to the dissolution of materials that did not form a ternary rutile-type oxide with Sb, thus exposing the stable crystalline phase. The capacitance increased by a factor of ~ 6 after electrochemical operation (Figure S6C), with minimal changes in thickness (Figure S9), indicating an increase in porosity of the catalyst film.

The Ni 2p, Mn 2p, and Sb 3d spectra all indicated that before electrochemical operation Ni, Mn, and Sb were in 2+, 2+ and 3+ oxidation states, respectively, at the surface (Table S2, see Supplementary Information).[23-24] The shift of the peaks in the XPS data suggest that the surface oxidation states for small amounts of Ni and large amounts of Sb increase during electrochemical operation. The Ni and Sb signals exhibited a shift towards higher binding energies by 0.39 and 0.33 eV, respectively. Before electrochemistry, the XPS spectra in the Ni 2p and Mn 2p regions closely resembled spectra reported for Ni^{2+} and Mn^{2+} (Table S2).[23] The ~1 eV shift of the XPS Ni $2p_{3/2}$ maximum between NiO and NiOOH suggests that Ni is partially oxidized.[23] The surfaces of transition metal antimonates usually consist of a mixture of Sb^{3+} and Sb^{5+}. The observed 0.33 eV shift of the Sb $3d_{3/2}$ peak suggests that after electrochemistry the surface Sb was oxidized, indicating that the surface changed from having a substantial Sb^{3+} component to adopting more Sb^{5+} character, which could be due to the removal of an Sb-rich surface layer that did not form a rutile-type structure. The Sb^{5+} component is consistent with the rutile-type bulk structure. The increase in the oxidation state of surfacial Sb and the small initial loss of Sb during electrolysis as

measured by ICP-MS (Figure S7) suggest that the surface was initially partially covered by oxides that did not form a rutile-type structure and dissolved over time. The ability of transition metals to accept various oxidation states within a material is often required in proposed mechanisms of the oxygen-evolution reaction.[25]

The most active OER catalysts in acidic electrolytes, such as $IrO_x/SrIrO_3$, exhibit η = 270-290 mV at 10 mA cm^{-2} of current density.[5] Molecular oxygen-evolving catalysts based on Ru and other precious metals exhibit turnover numbers of < 43,000 in acidic media, and their stability is limited to a few hours.[26-27] Electrodeposited Fe-Ni oxyhydroxide exhibits η = 286-340 mV in 1.0 M KOH(aq),[2, 28] whereas deposition of Fe-Ni oxyhydroxide by pulsed-laser ablation yields η = 280 mV at these same geometric electrode current densities.[29] Co oxide prepared in phosphate- or borate-buffered aqueous solutions exhibits η = 390-410 mV at 10 mA cm^{-2},[30] and is unstable after 10 min of water oxidation at current densities of 10 mA cm^{-2} in pH < 12 electrolytes.[31] CoFe Prussian blue compounds exhibit η < 820 mV at 10 mA cm^{-2} for 2 h in pH 2.2 electrolyte.[32] MnO_x exhibits η ~ 500 mV at 2 μA cm^{-2} in pH 1 electrolyte, with a projected η = 1.96 V at 10 mA cm^{-2} based on the reported Tafel slope, and has a turnover number for water oxidation of < 1 and is unstable at open circuit.[3] $Ni_{0.5}Mn_{0.5}Sb_{1.7}O_x$ exhibits η ~ 745 mV at 10 mA cm^{-2} in pH 0 electrolyte with a turnover number > 33,000.

Although the overpotentials of the reported $Ni_xMn_{1-x}Sb_{1.6-1.8}O_y$ family are 300–450 mV higher than state-of-the-art catalysts, their stability is at least comparable to the noble metal oxides, which are known to corrode under operation.[4, 33] Crystalline antimonates have not been thoroughly optimized or explored for water oxidation. For the $Ni_xMn_{1-x}Sb_2O_6$ family, further improvements could be made by optimizing the synthesis method to improve

the conductivity of the catalyst, incorporate more Mn without dissolution, identify the active sites of the catalyst, and increase the catalytic active site density. Furthermore, many other earth-abundant transition metals form rutile-type oxides with antimony, and their stability and activity towards water oxidation in acid is unknown. Further studies on the activity and stability of the transition metal antimonates, along with a mechanistic understanding of the electrocatalyst enhancement, could thus potentially lead to development of earth-abundant catalysts with activities comparable to noble metal oxides.

The long-term activity of $Ni_{0.5}Mn_{0.5}Sb_{1.7}O_x$ is sufficient to construct an electrolyzer that is 57% efficient (see SI). Electrolyzers and integrated solar-fuels devices that use strongly acidic or alkaline media allow for the efficient evolution of H_2(g) and O_2(g) in intrinsically safe systems, while also producing H_2(g) under pressure to facilitate beneficial separation and collection of the evolved gases.[34] The 745 mV OER overpotential is also sufficient to construct solar-fuels devices that have energy-conversion efficiencies of >20%, in conjunction with optimized, compatible, acid-stable light absorbers and membranes.[35] Further improvements in OER performance will require development of more active, stable, non-precious non-noble metal electrocatalysts for water oxidation, perhaps building upon the ternary metal oxide approach to obtain stability and OER activity in oxidizing aqueous acidic media.

2.4 Conclusion

$Ni_xMn_{1-x}Sb_{1.7}O_x$ acts as a stable water-oxidation electrocatalyst for > 168 h of continuous operation in aqueous 1.0 M sulfuric acid. The stability of the electrocatalyst was related to the formation of a crystalline MSb_2O_6 rutile-type phase. The activity was optimized when both Ni and Mn were present in approximately equal amounts. Anodic exposure in 1.0 M H_2SO_4(aq) resulted in preferential leaching of Mn and oxidation of the surface Ni and Sb. The observations suggest further development of crystalline ternary or quaternary oxides consisting of earth-abundant elements for water oxidation in aqueous acidic media.

2.5 Acknowledgements

This work is supported through the Office of Science of the U.S. Department of Energy (DOE) under award no. DE-SC0004993 to the Joint Center for Artificial Photosynthesis, a DOE Energy Innovation Hub. I.M.H acknowledges a National Science Foundation Graduate Research Fellowship under Grant No. DGE-1144469. This work was also supported by the Gordon and Betty Moore Foundation under Award No. GBMF1225. C.G.R acknowledges the Resnick Sustainability Institute for a post-doctoral fellowship. We thank N. Dalleska and P. Buabthong for assistance with mass spectroscopy measurements and x-ray photoelectron spectroscopy measurements, respectively.

2.6 Supplementary Information

2.6.1 Chemicals

All chemicals were used as received, including sulfuric acid (H_2SO_4, Fisher Scientific, TraceMetal Grade, 93-98%), antimony(III) chloride ($SbCl_3$, Alfa Aesar, ACS, 99.0% min), tin(IV) chloride hydrate ($SnCl_4 \cdot xH_2O$, Alfa Aesar, 98%), antimony standard for ICP (Sigma Aldrich, TraceCERT), multielement standard solution 1 for ICP (Sigma Aldrich, TraceCERT), potassium sulfate (K_2SO_4, Macron Chemicals, ACS), and gallium-indium eutectic (Alfa Aesar, 99.99%). A Millipore deionized water system was used to obtain water with resistivity of 18.2 MΩ cm.

2.6.2 Sample Preparation

A conductive film of antimony-doped tin oxide (ATO) was deposited onto quartz slides via a spray pyrolysis procedure.[16] Briefly, the process consisted of heating a quartz slide at 550 °C on a hot plate, and using a spray gun to spray a 0.24 M ethanolic solution of $SnCl_4$ doped with 3 mol% $SbCl_3$ onto the quartz slide. The thickness of the ATO film was controlled by changing the duration of the spray. Films with a sheet resistance of 13-20 Ω sq^{-1} were used for this study.

Sputter depositions were performed with an AJA Orion sputtering system. To make a direct contact to the ATO after film preparation, prior to depositing metal films the ATO-coated quartz slides were partially covered with Kapton tape. Multi-metal films were co-sputtered from three metal targets in an Ar plasma: Antimony (ACI Alloys, 99.95%), Nickel (ACI Alloys, 99.95%), and Manganese (ACI Alloys, 99.95%). An Ar flow rate of 20 sccm

was used to sustain the plasma, and the power applied to the three metal targets was varied to obtain films that had different compositions. The chamber pressure was 5 mTorr during the deposition, and the base pressure of the chamber was < 10^{-7} Torr prior to use. The sample was not heated intentionally during the deposition process. The stoichiometry reported in the sample name was obtained by dissolving the deposited unannealed metal films in 1.0 M H_2SO_4(aq), followed by determination of the concentration of dissolved ions using ICP-MS.

After metal film deposition, the films were annealed in a muffle furnace (Thermolyne F48020-80) to form the oxides. The temperature was increased at a ramp rate of 10 °C min^{-1} until the temperature set point was reached. The temperature was then held for 6 h and allowed to return to room temperature. The temperature set point was 700 °C unless otherwise specified. Samples were cleaved into pieces, and In-Ga eutectic (Aldrich) was scribed on the ATO. Tinned Cu wire was threaded through a glass tube that had been cleaned with aqua regia, which consisted of a 3:1 v/v solution of concentrated hydrochloric acid and nitric acid, respectively. Ag paint (SPI, Inc.) was used to bond the wire to the portion of ATO that had been covered with In-Ga. The contact was allowed to dry for at least 2 h at room temperature or for 15 min at 85 °C in an oven. Hysol 9460 epoxy was used to insulate the contact and define the electrode area, and the epoxy was allowed to cure for at least 12 h at room temperature. An optical scanner (Epson perfection V360) was used to image the electrode area and ImageJ was used to quantify the area. Electrode areas were between 1 and 11 mm^2 unless otherwise specified.

2.6.3 Materials Characterization

X-ray diffraction (XRD) analysis was performed with a Bruker D8 Discover instrument equipped with a 2-dimensional Vantec-500 detector. Copper Kα radiation (1.54 Å) was generated with a tube voltage of 50 kV and a tube current of 1000 μA. The incident beam was focused with a 0.5 mm diameter mono-capillary collimator. An aligned laser beam was used to ensure that the sample was placed at the correct depth for diffraction measurements. Coupled theta/two theta mode was used, with a θ angle that was half of the 2θ angle. The scattered x-ray radiation was collected by the Vantec-500 detector with an angular resolution < 0.04°, which enabled the collection of diffraction from a 2θ range of 20°. Four scans were performed in the range of 25° to 85° 2θ, and radiation was counted for a total duration of 4 h to obtain the XRD profile. The collected data were analyzed using Bruker EVA software. The peaks were indexed to reference patterns of SnO_2 and $CoSb_2O_6$.[19, 36] The preferred orientation of the ATO crystals was not controlled during the ATO fabrication process, thus XRD data were not used for quantitative analysis. Transmission-electron microscopy (TEM) samples of the films were prepared using a focused Ga-ion beam (FIB) on a FEI Nova-600 Nanolab FIB/FESEM, with Pt and C protection layers being applied before being exposed to the FIB. High-resolution TEM (HRTEM) and scanning-transmission electron microscopy energy-dispersive X-ray spectroscopy (STEM-EDS) data were obtained using a Tecnai Polara (F30) TEM at an accelerating voltage of 300 keV.

2.6.4 X-ray Photoelectron Spectroscopy

X-ray photoelectron spectroscopy (XPS) data were collected using a Kratos Axis NOVA (Kratos Analytical, Manchester, UK) at a background pressure of 10^{-9} Torr. A monochromatic Al Kα source at 1486.6 eV was used for excitation. Survey scans were collected at 1 eV resolution, whereas 0.05 eV resolution was used for high-resolution scans. The peak energies were calibrated against the binding energy of the adventitious C 1s peak, which was set at 284.8 eV.

The XPS $2p_{3/2}$ spectra of transition metal oxides are fit by multiple peaks, often 6, with the intensity of the individual peaks varying with the compound. Thus the energy for the intensity maximum of the observed spectra can significantly shift without a change in metal oxidation state. For example, both NiO and $Ni(OH)_2$ are formally Ni(II) but the observed peak maxima differ by more than 1.5eV.[37] The Ni2p3/2 spectra taken for $Ni_{0.5}Mn_{0.5}Sb_{1.7}O_x$ before electrochemistry (Figure 4A) are similar to XPS spectra of $Ni(OH)_2$ and dissimilar to those of γ-NiOOH or β-NiOOH which have a maxima at ~ 856 eV.[23] Also no sharp low energy peak for Ni metal was observed in $Ni_{0.5}Mn_{0.5}Sb_{1.7}O_x$ (Figure 4A).[23] The peak maximum observed for $Ni(OH)_2$ is ~855.3 eV compared to a maximum observed here of 855.3 eV.[37] NiO has an observed maximum at 853.8 eV with a side peak at ~855.8,[37] two peaks of almost equal height at 853.7 and 855.4 eV are used to fit these lines.[38] The higher energy peak has an area of about 3 times that of the lower energy peak but the narrow width of the lower energy peak is responsible for the maximum in the observed spectra. Thus we assign the Ni in the $Ni_{0.5}Mn_{0.5}Sb_{1.7}O_x$ compound to Ni(II). The Mn spectra taken before electrochemical operation qualitatively looked more like MnO then the higher oxides

(Mn_2O_3, MnOOH, or MnO_2).[23] The peak maximum observed here is 641.3 eV while that of MnO is ~ 641.5 eV. All the other Mn oxides have peak maxima close to 642 eV and have a sharp feature in the spectra at low energy. Thus we assign the Mn as Mn(II). The XP spectrum of Sb $3d_{5/2}$ overlaps with that of the O 1s. The $3d_{3/2}$ XP spectra of the oxides of Sb shows peak maxima at 539.7, 540.3, and 540.6 eV for Sb_2O_3, Sb_2O_4, and Sb_2O_5, respectively.[39] The $Ni_{0.5}Mn_{0.5}Sb_{1.7}O_x$ had a $3d_{3/2}$ maxima at 539.7 eV and was assigned as Sb(III).

After electrochemical operation the Ni and Sb signals exhibited a shift towards higher binding energies by 0.39 and 0.33 eV, respectively.[23] The shift of the Ni $2p_{3/2}$ maximum suggests that Ni near the surface is partially oxidized.[23] The surfaces of transition metal antimonates usually consist of a mixture of Sb^{3+} and Sb^{5+}. The observed 0.33 eV shift of the Sb $3d_{3/2}$ peak suggests that the surface Sb was oxidized, indicating that the surface changed from having a substantial Sb(III) component to adopting more Sb(V) character.

2.6.5 Electrochemical Testing

Sulfuric acid (TraceMetal grade, Fisher Chemical) was used to make 1.0 M solutions, unless otherwise indicated. Digital potentiostats (MPG-2, Bio-Logic Science Instruments) were used to acquire electrochemical data. (Mercury/mercury sulfate electrodes (MSEs) were calibrated with a reversible hydrogen electrode (RHE). The RHE consisted of a platinum disk (CH Instruments) submerged in hydrogen-saturated 1.0 M sulfuric acid, with H_2(g) bubbled underneath the Pt disk. The potentials of the MSEs were between 0.676 V and 0.691 V vs. RHE. Glass electrochemical cells were cleaned with aqua regia prior to use. The working, reference, and counter electrodes consisted of the sample, a calibrated MSE,

and a carbon rod (Strem) separated from the main compartment by a glass frit, respectively. Approximately 25 mL of 1.0 M H_2SO_4(aq) was used as the electrolyte, unless otherwise specified. The solution resistance was determined to be ~ 10 Ohm from impedance measurements on a platinum disk, and the electrochemical data were corrected for the solution resistance (i.e., 10 Ohm). Cyclic voltammetric data were collected at 10 mV s^{-1} unless otherwise specified.

The electrochemically active surface area (ECSA) was determined using a previously reported procedure.[2] After cyclic voltammetry, the electrodes were held at open circuit for 1 min, and subsequently cyclic voltammetry scans were collected at ± 50 mV from open circuit at scan rates of 100, 75, 25, and 10 mV s^{-1}. The current steps for the cyclic voltammetry were 100 uV and 100% of the current was acquired during each time step. The anodic and cathodic currents at the center of the cyclic voltammetry scans were plotted versus scan rate, and a linear fit was used to determine the capacitance. For all linear fits the R^2 value was greater than 0.99. Atomic-force microscopy was used to determine the roughness factor of the ATO (RF = 1.32), and the geometric area-normalized capacitance of ATO (0.0254 mF cm^{-2}) was divided by the roughness factor to determine the capacitance normalized to the electrochemical surface area (0.0192 mF cm^{-2}). The roughness factor for antimonates was calculated by dividing the electrochemical surface area determined by capacitance measurements by the geometric area of the electrode. Impedance measurements were performed in a static electrolyte of 1.0 M H_2SO_4 (aq) in the frequency range of 50 kHz – 50 Hz. A potential of 1.63 V vs. RHE was applied and the amplitude of the sinusoidal wave amplitude was 10 mV.

2.6.6 Inductively-coupled Plasma Mass Spectrometry

Inductively coupled plasma mass spectrometry (ICP-MS) data were collected using an Agilent 8800 Triple Quadrupole ICP-MS system. Calibration solutions were prepared by diluting the multielement and antimony standard solutions for ICP with 18.2 MΩ cm resistivity water. To determine the loading of the catalysts, metal films were sputter deposited on glass slides and cut into ~ 1 cm^2 pieces, and the geometric area of the pieces was measured with an optical scanner (Epson perfection V360) and ImageJ. The unannealed metal films on glass were placed in 10 mL of 1.0 M H_2SO_4(aq), and the films were allowed to dissolve for several days. The total amount of Ni, Mn, and Sb in solution was determined from ICP-MS measurements, and the results were normalized to the geometric area of the pieces used.

A two-compartment electrolysis cell with a Nafion membrane separating the reference electrode and working electrode (~ 0.9 cm^2) from the counter electrode was used to determine the amount of Ni, Mn, and Sb from the working compartment (25 mL) in the electrolyte during chronopotentiometry at 10 mA cm^{-2}. At various time intervals 1 mL of electrolyte was taken from the working compartment, and immediately replenished with 1 mL of fresh electrolyte. The concentration of Ni, Mn, and Sb in the working compartment was determined for every time interval, and was corrected for the dilution that occurred each time a sample was taken.

2.6.7 Electrolyzer Efficiency Calculation and Solar Fuel Device Efficiency Discussion

The expected efficiency of an electrolyzer was calculated with equation 1. The overpotential for the hydrogen-evolution reaction (HER) was taken to be 80 mV (for example, Ni_2P and CoP),[40] and the voltage drop from solution resistance was taken to be 100 mV. The efficiency for $Ni_{0.5}Mn_{0.5}Sb_{1.7}O_x$ (~ 745 mV overpotential) was 57.7%, and for IrO_x (~350 mV) the efficiency was 69.9%.

The maximum efficiency expected when an optimized tandem cell is coupled with a set of electrocatalysts has been determined previously.[35] Briefly, the procedure consists of determining the overall overpotential of the water splitting reaction, in this case 825 mV at 10 mA cm^{-2} (745 mV for $Ni_{0.5}Mn_{0.5}Sb_{1.7}O_x$ and 80 mV for an HER catalyst) and finding a combination of semiconductors operating at the Shockley-Queisser limit that maximize the efficiency of the device. For semiconductors operating at the Shockley-Queisser limit an efficiency above 20% can be obtained for devices with overall overpotentials and resistance losses < 960 mV.[35]

$$Efficiency = \frac{1.229\,V}{1.229\,V+\eta_{OER}+\eta_{HER}+\eta_{iR}} \quad (1)$$

2.6.8 Turnover Frequency and Turnover Number Calculations

The turnover frequency and turnover number of $Ni_{0.5}Mn_{0.5}Sb_{1.7}O_x$ were determined by calculating the amount of catalyst with the total number of transition-metal atoms in the film or by estimating the number of exposed transition metals based on the electrochemically active surface area (ECSA). The ECSA should give an upper bound to the values, and the total number of transition metals should give a lower bound. An estimate for the surface

atom density ($4.6x10^{14}$ atoms cm^{-2}) based on the crystal structure of transition-metal antimonates was used to convert the ECSA to the number of transition-metal atoms exposed.

2.7 Supplementary Figures

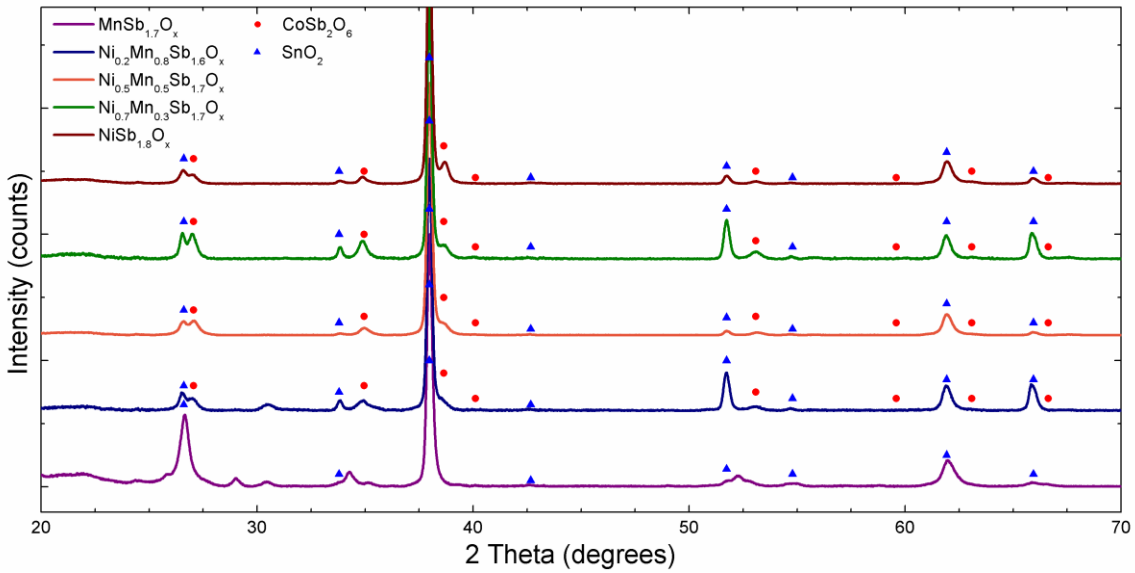

Figure S1. X-ray diffraction pattern for $Ni_xMn_{1-x}Sb_{1.6-1.8}O_y$ thin films on an ATO substrate. The peaks were indexed to reference patterns of SnO_2 and $CoSb_2O_6$.[19, 36]

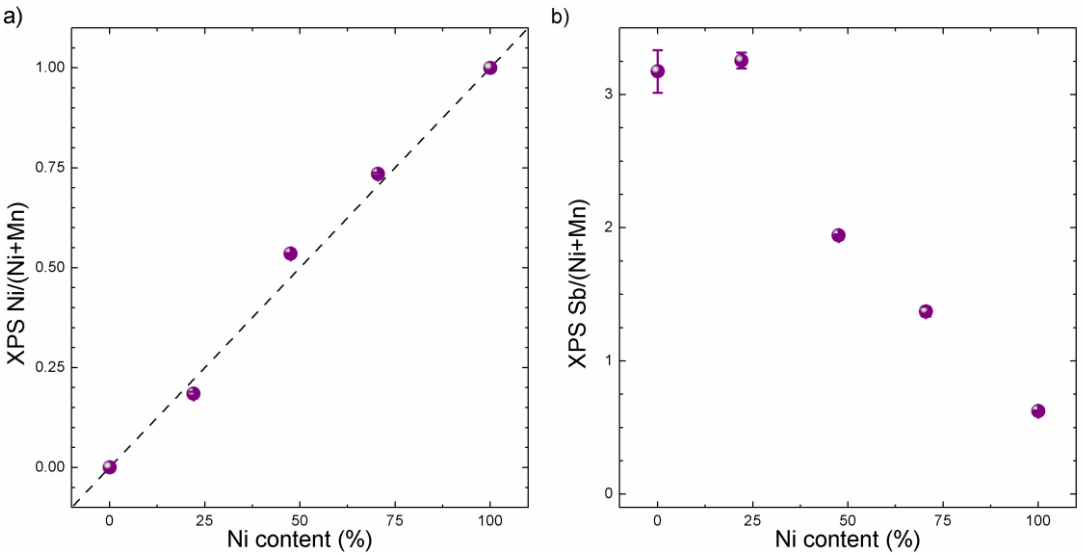

Figure S2. (a) Surface nickel-to-transition metal ratio and (b) surface antimony-to-transition metal ratio, as determined by XPS measurements, as a function of the bulk composition determined by ICP-MS. Error bars are included in each data point and are one standard deviation from at least 3 samples.

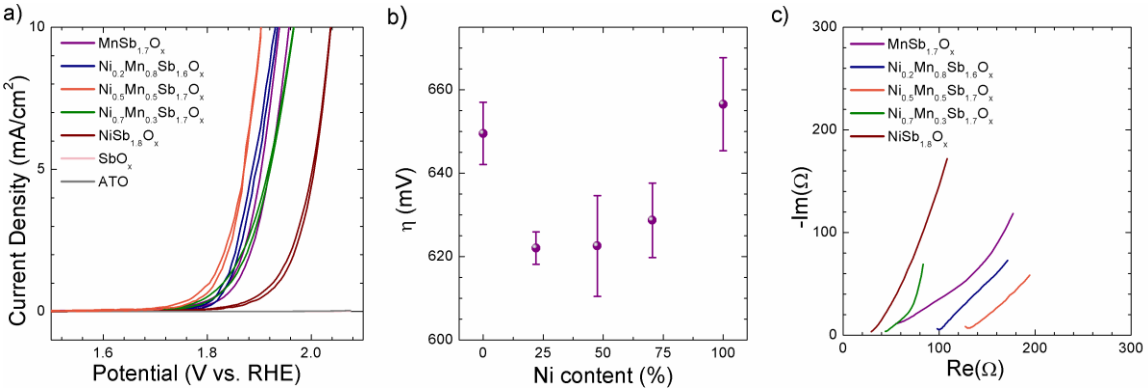

Figure S3. (a) Cyclic voltammetry of $Ni_xMn_{1-x}Sb_{1.7}O_x$, SbO_x, and ATO electrodes without resistance compensation. (b) Overpotential at 0.1 mA cm^{-2} of electrochemically active surface area for $Ni_xMn_{1-x}Sb_{1.7}O_x$. (c) Impedance measurements of $Ni_xMn_{1-x}Sb_{1.7}O_x$, SbO_x in the frequency range of 50 Hz – 50 kHz, 10 mV amplitude in contact with 1.0 M H_2SO_4 (aq) at 1.63 V vs. RHE. Electrode areas were ~0.2 cm^2 for impedance measurements. Impedance data were fit to a model (insert) that consisted of the series resistance (R_s) associated with the electrode and electrolyte resistance, in series with a constant-phase element (CPE) in parallel with the contact resistance (R_{ct}) associated with the OER kinetics.

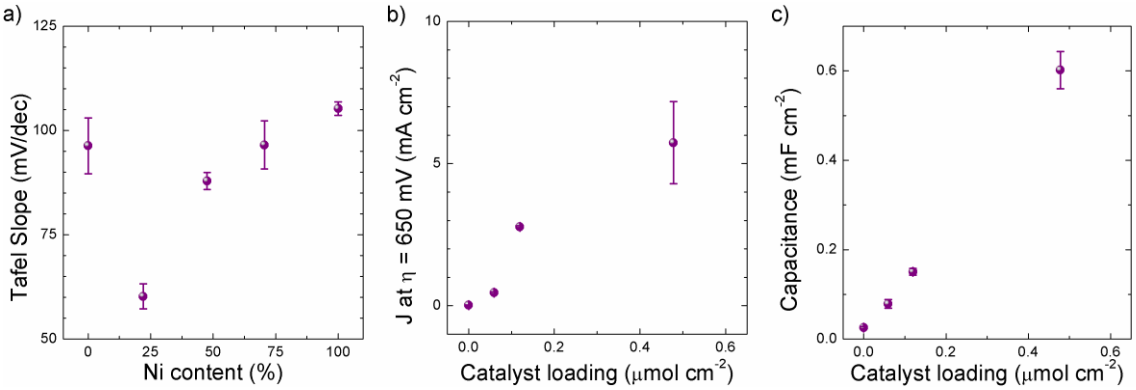

Figure S4. (a) Tafel slopes determined from cyclic voltammetry in the current density range of 0.3-3 mA cm^{-2}. (b) Current density (*J*) at η = 650 mV for $Ni_{0.5}Mn_{0.5}Sb_{1.7}O_x$ at various loadings determined by calibration of the deposition rate of the sputterer. The loading is defined as the amount of Ni and Mn present in the as-synthesized film. A loading of 0.48 μmol cm^{-2} corresponded to a film thickness of ~ 300 nm. Error bars are one standard deviation from at least 3 samples. (c) Area-normalized electrode differential capacitance at various loadings. Higher differential capacitance indicates more electrochemically active surface area.

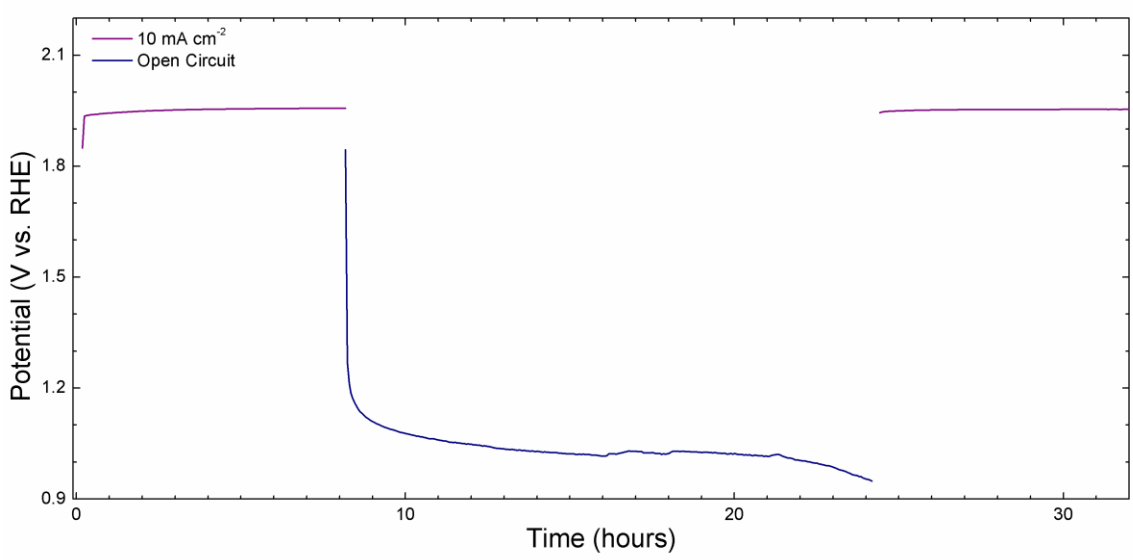

Figure S5. Potential of a $Ni_{0.5}Mn_{0.5}Sb_{1.7}O_x$ electrode being held at 10 mA cm^{-2} for 8 h, followed by 16 h at open circuit and subsequently being held at 10 mA cm^{-2} for 8 h.

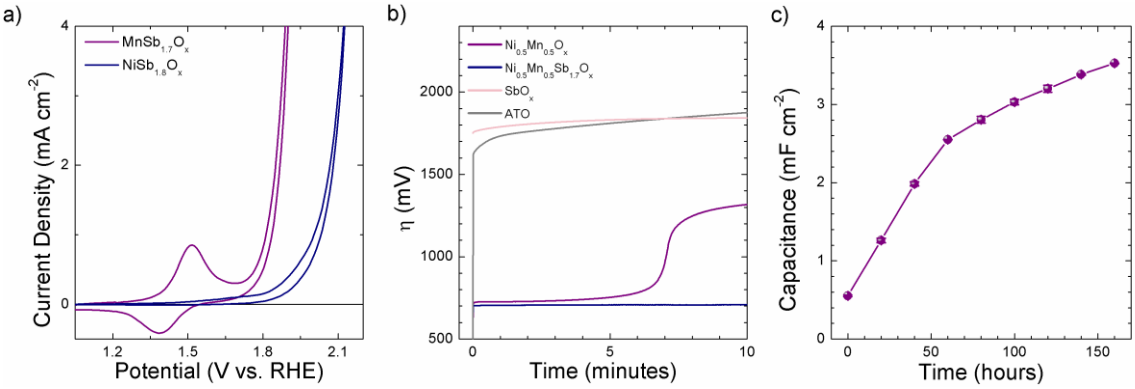

Figure S6. (a) Cyclic voltammetry of $NiSb_{1.8}O_x$ and $MnSb_{1.7}O_x$ after 50 h of chronopotentiometry at 10 mA cm^{-2} based on the electrode geometric area. (b) Chronopotentiometry of $Ni_{0.5}Mn_{0.5}O_x$, SbO_x, ATO, and $Ni_{0.5}Mn_{0.5}Sb_{1.7}O_x$ at 10 mA cm^{-2} based on the electrode geometric area. (c) Area-normalized differential capacitance of a $Ni_{0.5}Mn_{0.5}Sb_{1.7}O_x$ electrode determined between chronopotentiometry tests at 10 mA cm^{-2} of geometric area.

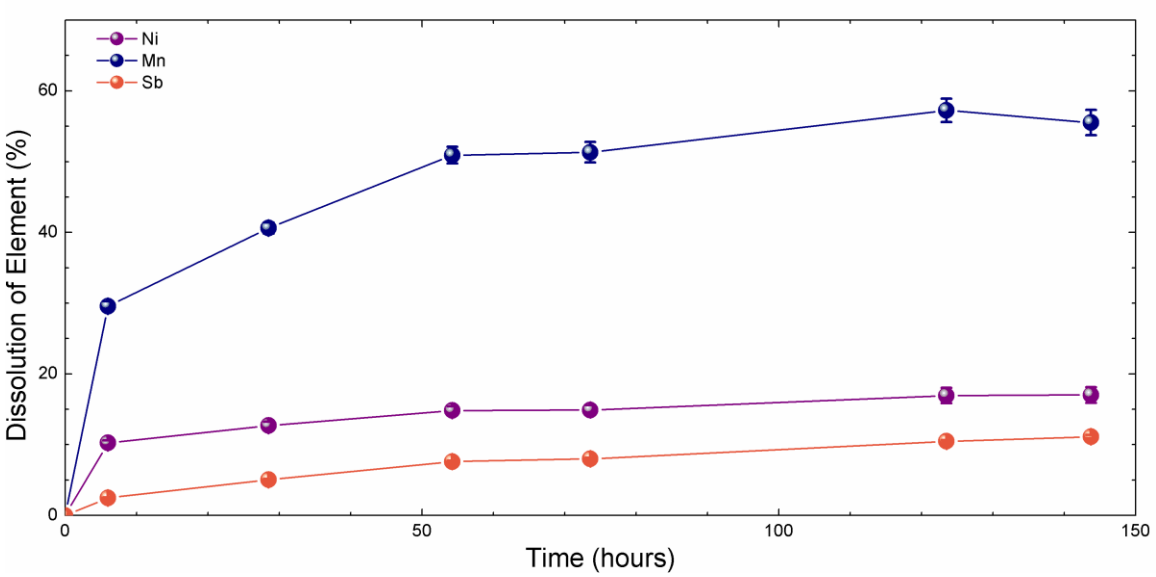

Figure S7. Cumulative dissolution of a $Ni_{0.5}Mn_{0.5}Sb_{1.7}O_x$ electrode during chronopotentiometry at 10 mA cm^{-2}. The active electrode geometric area was 0.920 cm^2.

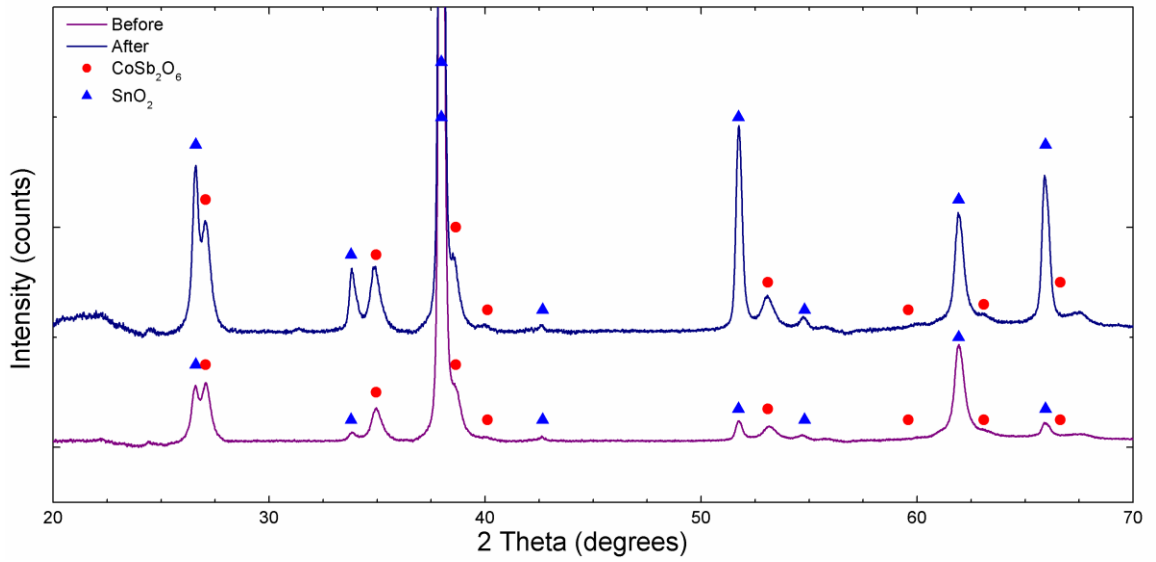

Figure S8. Diffraction pattern of $Ni_{0.5}Mn_{0.5}Sb_{1.7}O_x$ before and after chronopotentiometry for 144 h at 10 mA cm^{-2} of geometric area. The peaks were indexed to reference patterns of SnO_2 and $CoSb_2O_6$.[19, 36]

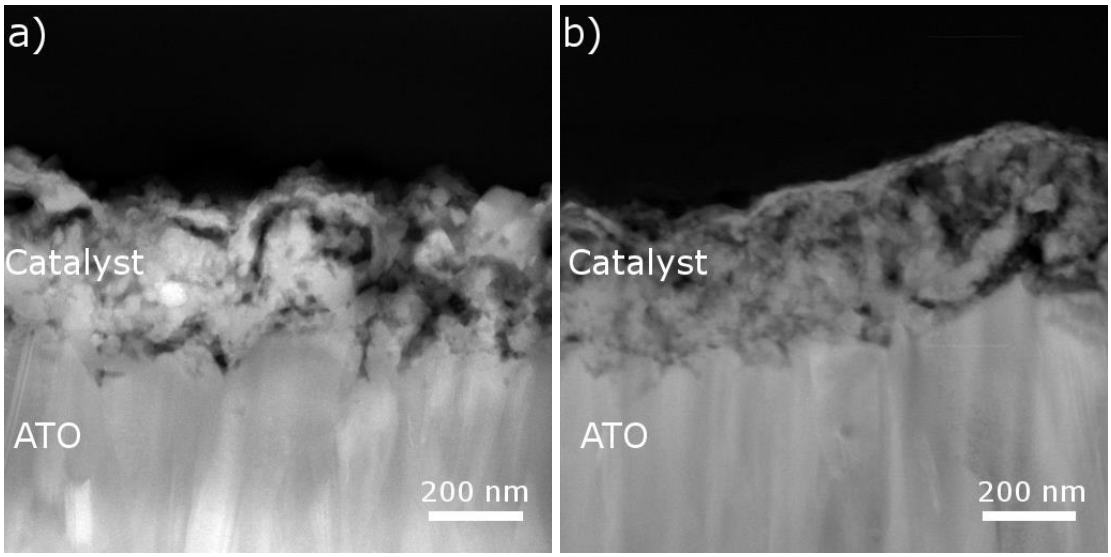

Figure S9. High-angle annular dark-field (HAADF) images of (a) $Ni_{0.5}Mn_{0.5}Sb_{1.7}O_x$ before electrochemical operation, and (b) $Ni_{0.5}Mn_{0.5}Sb_{1.7}O_x$ after chronopotentiometry for 144 h at 10 mA cm^{-2}. The lower portion of the image was identified as the ATO support, and a porous film on top of the ATO was identified as the catalyst film. The film thickness for each image was measured as the distance between the compact ATO layer and the dark portion of the image corresponding to regions without material.

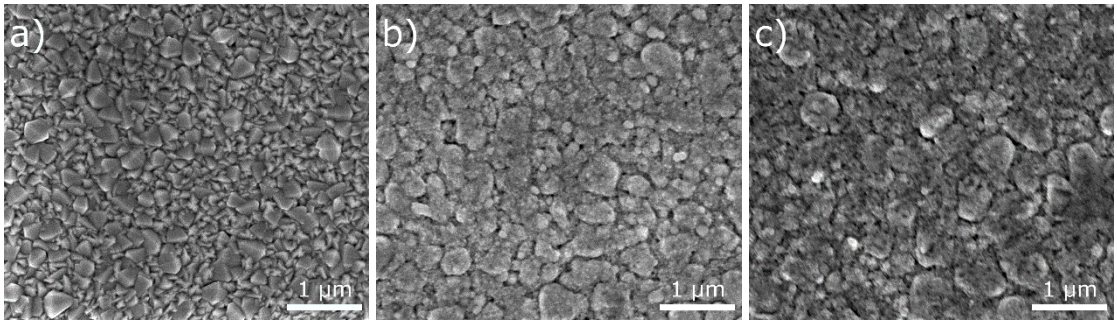

Figure S10. SEM images of (a) ATO substrate,(b) $Ni_{0.5}Mn_{0.5}Sb_{1.7}O_x$ before electrochemical operation, and (c) $Ni_{0.5}Mn_{0.5}Sb_{1.7}O_x$ after chronopotentiometry for 144 h at 10 mA cm^{-2}.

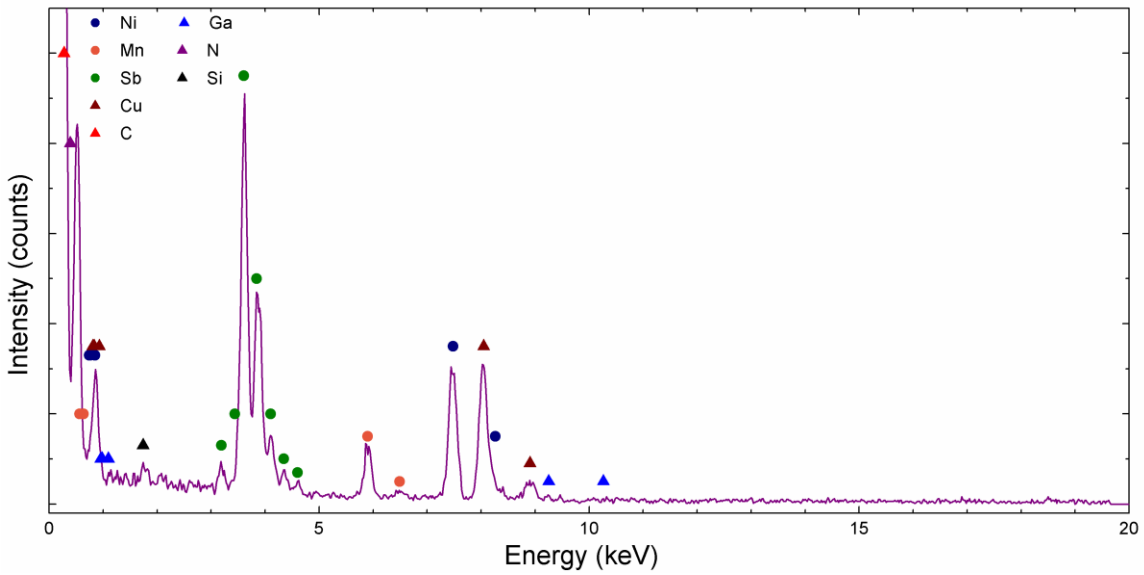

Figure S11. STEM-EDS data of as-synthesized $Ni_{0.5}Mn_{0.5}Sb_{1.7}O_x$ showing that only Ni, Mn, Sb were detectable in the film. Cu, C, Ga, N, and Si are from the TEM grid and TEM sample preparation.

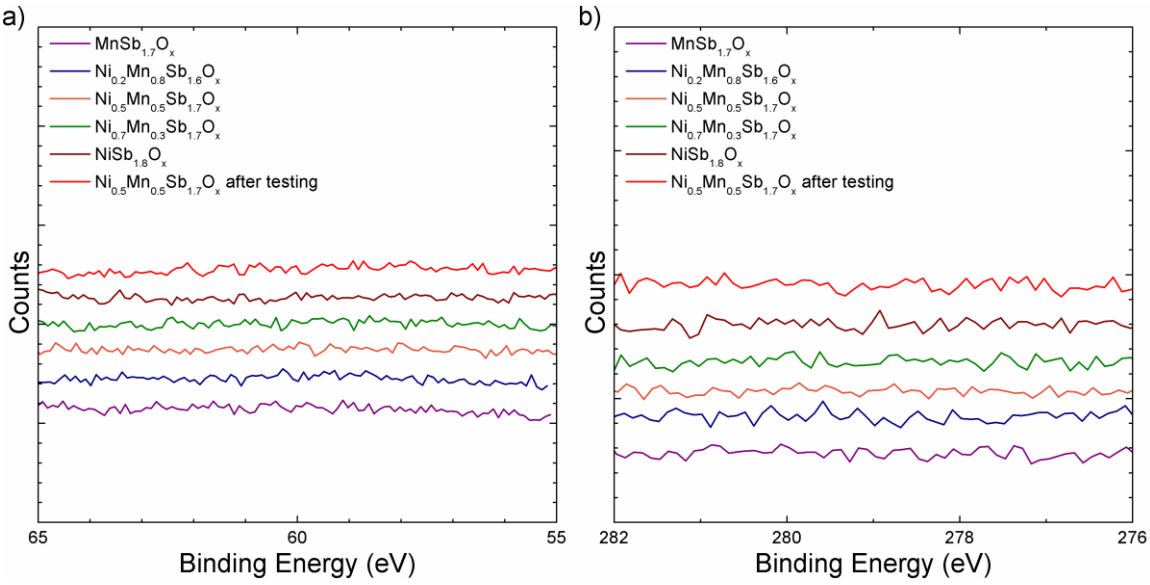

Figure S12. High-resolution XPS data of as-synthesized $Ni_xMn_{1-x}Sb_{1.6-1.8}O_y$ and $Ni_{0.5}Mn_{0.5}Sb_{1.7}O_x$ after chronopotentiometry for 144 h at 10 mA cm^{-2}. The spectral regions are: (a) Ir 4f and (b) Ru 3d. No Ir or Ru was detected on the surface by XPS.

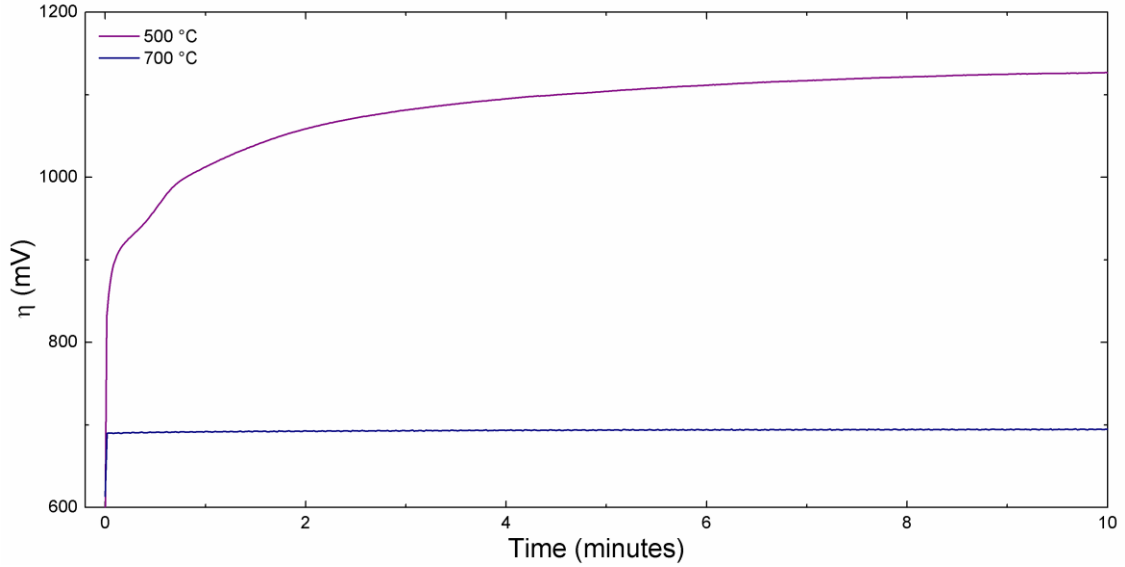

Figure S13. Chronopotentiometry at 10 mA cm^{-2} of $Ni_{0.5}Mn_{0.5}Sb_{1.7}O_x$ films annealed at 500 °C and 700 °C.

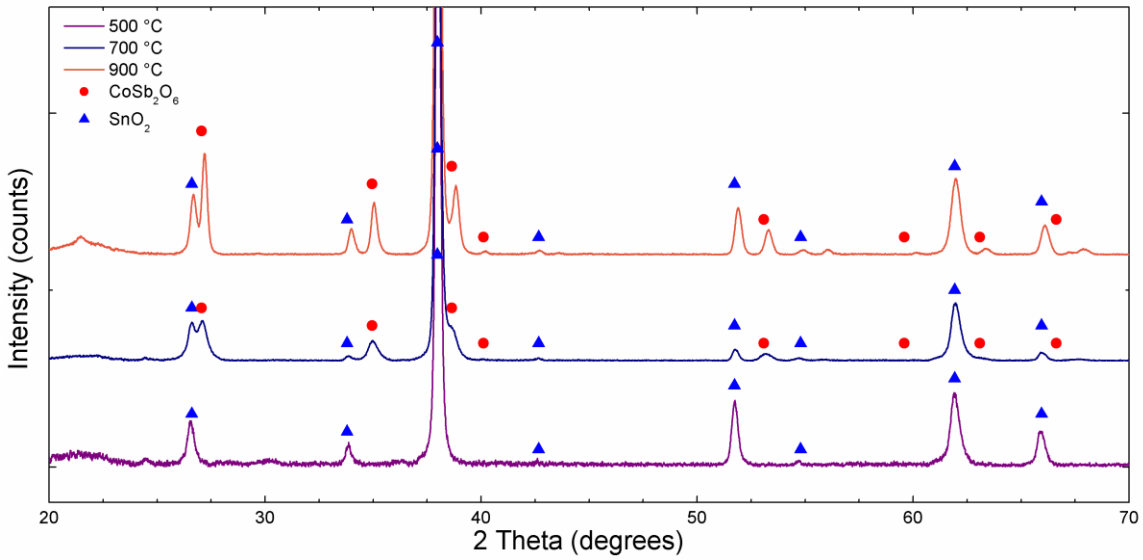

Figure S14. X-ray diffraction of $Ni_{0.5}Mn_{0.5}Sb_{1.7}O_x$ films annealed at 500 °C, 700 °C, and 900 °C. Reference patterns are SnO_2 (red circles) and $CoSb_2O_6$ (blue triangles).

Table S1. Composition of electrocatalysts determined with ICP-MS and initial roughness factor (RF) determined from capacitance measurements.

Sample	Ni (μmol cm^{-2})	Mn (μmol cm^{-2})	Sb (μmol cm^{-2})	RF
$MnSb_{1.7}O_x$	0.000	0.475 ± 0.007	0.797 ± 0.005	18 ± 4
$Ni_{0.2}Mn_{0.8}Sb_{1.6}O_x$	0.111 ± 0.003	0.392 ± 0.005	0.808 ± 0.012	17 ± 2
$Ni_{0.5}Mn_{0.5}Sb_{1.7}O_x$	0.228 ± 0.004	0.251 ± 0.004	0.813 ± 0.008	29 ± 2
$Ni_{0.7}Mn_{0.3}Sb_{1.7}O_x$	0.342 ± 0.003	0.143 ± 0.002	0.819 ± 0.012	12 ± 1
$NiSb_{1.8}O_x$	0.470 ± 0.005	0.000	0.830 ± 0.003	4 ± 1

Table S2. Comparison of X-Ray Photoelectron spectroscopy peak positions for various samples.

Sample	Ni $2p_{3/2}$ (eV)	Mn $2p_{3/2}$ (eV)	Sb $3d_{3/2}$ (eV)	Reference
$Ni_{0.5}Mn_{0.5}Sb_{1.7}O_x$ Before	855.3 ± 0.1	641.3 ± 0.1	539.7 ± 0.1	
$Ni_{0.5}Mn_{0.5}Sb_{1.7}O_x$ After	855.6 ± 0.1	641.5 ± 0.1	540.0 ± 0.1	
$Ni(OH)_2$	855.3 ± 0.1	-	-	[37]
NiO	853.8 ± 0.1	-	-	[37]
γ-NiOOH	856.2 ± 0.2	-	-	[37]
β-NiOOH	856.1 ± 0.1	-	-	[37]
MnO	-	641.5 ± 0.1	-	[23]
Sb_2O_3	-	-	539.7 ± 0.1	[39]
Sb_2O_4	-	-	540.3 ± 0.1	[39]
Sb_2O_5	-	-	540.6 ± 0.1	[39]

2.8 References

1. Lewis, N. S., Research opportunities to advance solar energy utilization. *Science* **2016,** *351* (6271), aad1920.
2. McCrory, C. C.; Jung, S.; Ferrer, I. M.; Chatman, S. M.; Peters, J. C.; Jaramillo, T. F., Benchmarking hydrogen evolving reaction and oxygen evolving reaction electrocatalysts for solar water splitting devices. *J. Am. Chem. Soc.* **2015,** *137* (13), 4347-57.
3. Huynh, M.; Bediako, D. K.; Nocera, D. G., A functionally stable manganese oxide oxygen evolution catalyst in acid. *J. Am. Chem. Soc.* **2014,** *136* (16), 6002-10.
4. Danilovic, N.; Subbaraman, R.; Chang, K. C.; Chang, S. H.; Kang, Y. J.; Snyder, J.; Paulikas, A. P.; Strmcnik, D.; Kim, Y. T.; Myers, D.; Stamenkovic, V. R.; Markovic, N. M., Activity-Stability Trends for the Oxygen Evolution Reaction on Monometallic Oxides in Acidic Environments. *J. Phys. Chem. Lett.* **2014,** *5* (14), 2474-8.
5. Seitz, L. C.; Dickens, C. F.; Nishio, K.; Hikita, Y.; Montoya, J.; Doyle, A.; Kirk, C.; Vojvodic, A.; Hwang, H. Y.; Norskov, J. K.; Jaramillo, T. F., A highly active and stable $IrO_x/SrIrO_3$ catalyst for the oxygen evolution reaction. *Science* **2016,** *353* (6303), 1011-1014.
6. Vesborg, P. C. K.; Jaramillo, T. F., Addressing the terawatt challenge: scalability in the supply of chemical elements for renewable energy. *RSC Adv.* **2012,** *2* (21), 7933.
7. Frydendal, R.; Paoli, E. A.; Chorkendorff, I.; Rossmeisl, J.; Stephens, I. E. L., Toward an Active and Stable Catalyst for Oxygen Evolution in Acidic Media: Ti-Stabilized MnO_2. *Adv. Energy Mater.* **2015,** *5* (22), 1500991.

8. Shinde, A.; Jones, R. J. R.; Guevarra, D.; Mitrovic, S.; Becerra-Stasiewicz, N.; Haber, J. A.; Jin, J.; Gregoire, J. M., High-Throughput Screening for Acid-Stable Oxygen Evolution Electrocatalysts in the (Mn–Co–Ta–Sb)O_x Composition Space. *Electrocatalysis* **2014,** *6* (2), 229-236.
9. Patel, P. P.; Datta, M. K.; Velikokhatnyi, O. I.; Kuruba, R.; Damodaran, K.; Jampani, P.; Gattu, B.; Shanthi, P. M.; Damle, S. S.; Kumta, P. N., Noble metal-free bifunctional oxygen evolution and oxygen reduction acidic media electro-catalysts. *Sci. Rep.* **2016,** *6*, 28367.
10. Bloor, L. G.; Molina, P. I.; Symes, M. D.; Cronin, L., Low pH electrolytic water splitting using earth-abundant metastable catalysts that self-assemble in situ. *J. Am. Chem. Soc.* **2014,** *136* (8), 3304-11.
11. Jain, A.; Ong, S. P.; Hautier, G.; Chen, W.; Richards, W. D.; Dacek, S.; Cholia, S.; Gunter, D.; Skinner, D.; Ceder, G.; Persson, K. A., Commentary: The Materials Project: A materials genome approach to accelerating materials innovation. *APL Mater.* **2013,** *1* (1), 011002.
12. Jain, A.; Hautier, G.; Ong, S. P.; Moore, C. J.; Fischer, C. C.; Persson, K. A.; Ceder, G., Formation enthalpies by mixing GGA and GGA+U calculations. *Phys. Rev. B* **2011,** *84* (4).
13. Zhang, B.; Zheng, X.; Voznyy, O.; Comin, R.; Bajdich, M.; García-Melchor, M.; Han, L.; Xu, J.; Liu, M.; Zheng, L.; García de Arquer, F. P.; Dinh, C. T.; Fan, F.; Yuan, M.; Yassitepe, E.; Chen, N.; Regier, T.; Liu, P.; Li, Y.; De Luna, P.; Janmohamed, A.; Xin, H. L.; Yang, H.; Vojvodic, A.; Sargent, E. H., Homogeneously dispersed, multimetal oxygen-evolving catalysts. *Science* **2016**, 10.1126/science.aaf1525.

14. Smith, R. D. L.; Prévot, M. S.; Fagan, R. D.; Zhang, Z.; Sedach, P. A.; Siu, M. K. J.; Trudel, S.; Berlinguette, C. P., Photochemical Route for Accessing Amorphous Metal Oxide Materials for Water Oxidation Catalysis. *Science* **2013,** *340*, 60-63.

15. Swaminathan, K.; Sreedharan, O. M., Potentiometric determination of stabilities of $NiSb_2O_4$ and $NiSb_2O_6$. *J. Alloys Compd.* **1999,** *292*, 100–106.

16. Bisht, H.; Eun, H.-T.; Mehrtens, A.; Aegerter, M. A., Comparison of spray pyrolyzed FTO, ATO and ITO coatings for flat and bent glass substrates. *Thin Solid Films* **1999,** *351*, 109-114.

17. Straguzzi, G. I.; Bischoff, K. B.; Koch, T. A.; Schuit, G. C. A., Selective Oxidation Catalysts Containing Antimony for the Conversion of I-Butene to Butadiene. *J. Catal.* **1987,** *103*, 357-365.

18. Burriesci, N.; Garbassi, F.; Petrera, M.; Petrini, G., Influence of the Bulk and Surface Properties on the Performance of Iron-Antimony Catalysts. *J. Chem. Soc. Faraday Trans. 1* **1982,** *78*, 817-833.

19. Reimers, J. N.; Greedan, J. E.; Stager, C. V.; Kremer, R., Crystal Structure and Magnetism in $CoSb_2O_6$ and $CoTa_2O_6$. *J. Solid State Chem.* **1989,** *83*, 20-30.

20. Westin, G.; Nygren, M., Sol-Gel Preparation of M-Sb Oxides from Sb $(OBu'')_3$-M-Acetate Precursors with M = Mn, Co, Ni. *J. Mater. Chem.* **1993,** *3* (4), 367-371.

21. Friebel, D.; Louie, M. W.; Bajdich, M.; Sanwald, K. E.; Cai, Y.; Wise, A. M.; Cheng, M. J.; Sokaras, D.; Weng, T. C.; Alonso-Mori, R.; Davis, R. C.; Bargar, J. R.; Norskov, J. K.; Nilsson, A.; Bell, A. T., Identification of Highly Active Fe Sites in (Ni,Fe)OOH for Electrocatalytic Water Splitting. *J. Am. Chem. Soc.* **2015,** *137* (3), 1305-13.

22. Beverskog, B.; Puigdomenech, I., Revised Pourbaix Diagrams for Nickel at 25-300 °C. *Corros. Sci.* **1997,** *39* (5), 969-980.

23. Biesinger, M. C.; Payne, B. P.; Grosvenor, A. P.; Lau, L. W. M.; Gerson, A. R.; Smart, R. S. C., Resolving surface chemical states in XPS analysis of first row transition metals, oxides and hydroxides: Cr, Mn, Fe, Co and Ni. *Appl. Surf. Sci.* **2011,** *257* (7), 2717-2730.

24. Delobel, R.; Baussart, H.; Leroy, J.-M.; Grimblot, J.; Gengembre, L., X-ray Photoelectron Spectroscopy Study of Uranium and Antimony Mixed Metal-oxide Catalysts. *J. Chem. Soc. Faraday Trans. 1* **1983,** *79*, 879-891.

25. Reier, T.; Nong, H. N.; Teschner, D.; Schlögl, R.; Strasser, P., Electrocatalytic Oxygen Evolution Reaction in Acidic Environments - Reaction Mechanisms and Catalysts. *Adv. Energy Mater.* **2016**, 1601275.

26. Jiang, Y.; Li, F.; Zhang, B.; Li, X.; Wang, X.; Huang, F.; Sun, L., Promoting the activity of catalysts for the oxidation of water with bridged dinuclear ruthenium complexes. *Angew. Chem. Int. Ed.* **2013,** *52* (12), 3398-401.

27. Karkas, M. D.; Verho, O.; Johnston, E. V.; Akermark, B., Artificial photosynthesis: molecular systems for catalytic water oxidation. *Chem. Rev.* **2014,** *114* (24), 11863-2001.

28. Sun, K.; Moreno-Hernandez, I. A.; Schmidt, W. C.; Zhou, X.; Crompton, J. C.; Liu, R.; Saadi, F. H.; Chen, Y.; Papadantonakis, K. M.; Lewis, N. S., A Comparison of the Chemical, Optical and Electrocatalytic Properties of Water-Oxidation Catalysts for Use in Integrated Solar-Fuels Generators. *Energy Environ. Sci.* **2017,** *10*, 987-1002.

29. Hunter, B. M.; Blakemore, J. D.; Deimund, M.; Gray, H. B.; Winkler, J. R.; Muller, A. M., Highly active mixed-metal nanosheet water oxidation catalysts made by pulsed-laser ablation in liquids. *J. Am. Chem. Soc.* **2014,** *136* (38), 13118-21.

30. Surendranath, Y.; Dinca, M.; Nocera, D. G., Electrolyte-Dependent Electrosynthesis and Activity of Cobalt-Based Water Oxidation Catalysts. *J. Am. Chem. Soc.* **2009,** *131*, 2615-2620.

31. Minguzzi, A.; Fan, F.-R. F.; Vertova, A.; Rondinini, S.; Bard, A. J., Dynamic potential–pH diagrams application to electrocatalysts for wateroxidation. *Chem. Sci.* **2012,** *3* (1), 217-229.

32. Han, L.; Tang, P.; Reyes-Carmona, A.; Rodriguez-Garcia, B.; Torrens, M.; Morante, J. R.; Arbiol, J.; Galan-Mascaros, J. R., Enhanced Activity and Acid pH Stability of Prussian Blue-type Oxygen Evolution Electrocatalysts Processed by Chemical Etching. *J. Am. Chem. Soc.* **2016,** *138* (49), 16037-16045.

33. Cherevko, S.; Zeradjanin, A. R.; Topalov, A. A.; Kulyk, N.; Katsounaros, I.; Mayrhofer, K. J. J., Dissolution of Noble Metals during Oxygen Evolution in Acidic Media. *ChemCatChem* **2014,** *6* (8), 2219-2223.

34. Xiang, C.; Papadantonakis, K. M.; Lewis, N. S., Principles and implementations of electrolysis systems for water splitting. *Mater. Horiz.* **2016,** *3* (3), 169-173.

35. Chen, Y.; Hu, S.; Xiang, C.; Lewis, N. S., A sensitivity analysis to assess the relative importance of improvements in electrocatalysts, light absorbers, and system geometry on the efficiency of solar-fuels generators. *Energy Environ. Sci.* **2015,** *8* (3), 876-886.

36. Baur, W. H.; Khan, A. A., Rutile-Type Compounds. IV. SiO_2, GeO_2 and a Comparison with other Rutile-Type Structures. *Acta Cryst.* **1971,** *B27*, 2133-2139.

37. Grosvenor, A. P.; Biesinger, M. C.; Smart, R. S. C.; McIntyre, N. S., New interpretations of XPS spectra of nickel metal and oxides. *Surf. Sci.* **2006,** *600* (9), 1771-1779.

38. Biesinger, M. C.; Payne, B. P.; Lau, L. W. M.; Gerson, A.; Smart, R. S. C., X-ray photoelectron spectroscopic chemical state quantification of mixed nickel metal, oxide and hydroxide systems. *Surf. Interface Anal.* **2009,** *41* (4), 324-332.

39. Izquierdo, R.; Sacher, E.; Yelon, A., X-Ray Photoelectron Spectra of Antimony Oxides. *Appl. Surf. Sci.* **1989,** *40*, 175-177.

40. Callejas, J. F.; Read, C. G.; Roske, C. W.; Lewis, N. S.; Schaak, R. E., Synthesis, Characterization, and Properties of Metal Phosphide Catalysts for the Hydrogen-Evolution Reaction. *Chem. Mater.* **2016,** *28* (17), 6017-6044.

Chapter III

CRYSTALLINE TRANSITION METAL ANTIMONATES FOR THE CHLORINE EVOLUTION REACTION

Moreno-Hernandez, I. A.; Brunschwig, B. S.; Lewis, N. S., Crystalline nickel, cobalt, and manganese antimonates as electrocatalysts for the chlorine evolution reaction. *Energy Environ. Sci.* **2019**. DOI: 10.1039/C8EE03676D

3.1 Introduction

The chlor-alkali process entails the electrochemical oxidation of chloride to Cl_2(g) by the chlorine-evolution reaction (CER) in conjunction with the production of caustic soda (i.e., NaOH) and H_2. The process is performed at industrial scale globally and consumes over 150 TWh of electricity annually. Dimensionally stable anodes, consisting of noble metal oxides of Ir or Ru, are the predominantly used CER anode electrocatalysts.[1-3] The scarcity of Ir and Ru has the potential to constrain industrial use of the chlor-alkali process and limit chlorine use in applications such as water sanitation.[4] Solid solutions of these metal oxides with TiO_2, SnO_2, CoO_x, or SbO_x have been explored to decrease the amount of Ir and Ru used in CER catalysts.[5-11] The resulting RuO_2-TiO_2 anodes exhibit low corrosion rates and are operationally stable for several years. However, Ru is susceptible to the formation of thermodynamically stable species such as soluble Ru chlorides or gaseous Ru oxides, contributing eventually to catalyst degradation.[12-13] Electrocatalysts for the CER that do not contain noble metals include Co_3O_4 and mixed first-row transition metal oxides, but these

materials show limited stability under the corrosive conditions required to obtain selectivity for the CER relative to the oxygen-evolution reaction (OER).[1, 10]

Crystalline transition metal antimonates (TMAs) have recently been reported to be active and stable electrocatalysts for water oxidation in acidic electrolytes.[14] Pourbaix diagrams predict that crystalline TMAs such as $NiSb_2O_6$, $CoSb_2O_6$, and $MnSb_2O_6$ should be stable under acidic conditions as well as in the presence of $Cl_2(g)$.[15] Accordingly, we report herein the synthesis of metal oxide films containing crystalline MSb_2O_6 (M = Ni, Co, Mn), and report the electrochemical activity and stability of these materials for the CER in acidic NaCl(aq). A primary focus is the electrochemical stability at 100 mA cm^{-2} of anodic current density, due to the relevance of this current density for the commercially practiced chlor-alkali process.[1] The structural, chemical, and dissolution behaviors of crystalline MSb_2O_6 for the CER have been evaluated by scanning-electron microscopy, x-ray photoelectron spectroscopy, and inductively coupled plasma mass spectrometry.

3.2 Results

Films of $NiSb_2$, $CoSb_2$, and $MnSb_2$ were prepared by co-sputtering Sb and M (M = Ni, Co, or Mn) onto conductive antimony-doped tin oxide (ATO) substrates.[16] The catalyst loading and stoichiometry of the sputtered metallic films were determined by dissolving the films in 1.0 M H_2SO_4(aq) and measuring the amount of dissolved ions by inductively coupled plasma mass spectrometry (ICP-MS). The loading of transition metal was 375 – 483 nmol cm^{-2} whereas the Sb loading was 709 – 820 nmol cm^{-2}, indicating a bulk M:Sb atomic ratio of ~1:2 (Table S1). To obtain MSb_2O_x films, the Ni, Co, and Mn metal/Sb films were annealed at 750 °C in air.[14, 17] X-ray diffraction (XRD) data indicated that the $NiSb_2O_x$ and

$CoSb_2O_x$ films both contained the tri-rutile MSb_2O_6 structure (Figure S1, S2). $MnSb_2O_x$ films contained $MnSb_2O_6$, orthorhombic Sb_2O_4, and monoclinic Sb_2O_4 (Figure S3). $RuTiO_x$ films deposited on ATO and annealed at 500 °C exhibited diffraction peaks consistent with a solid solution of rutile-type RuO_2 and TiO_2 (Figure S4). Scanning-electron microscopy (SEM) images of the catalyst films indicated that the morphology was different for each film (Figure S5-S8).

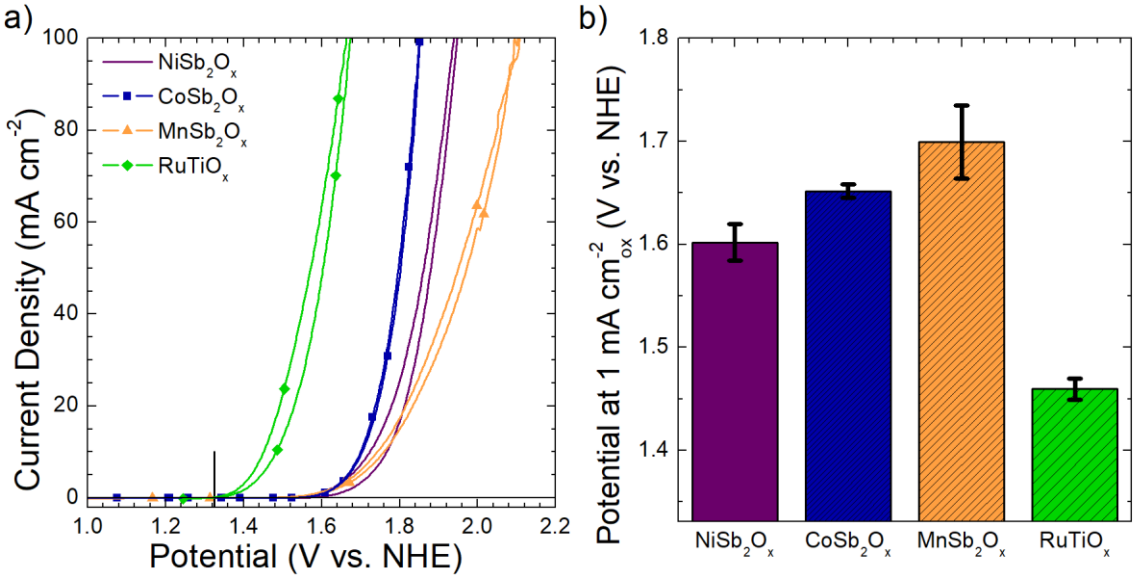

Figure 1. Initial electrochemical behavior of $NiSb_2O_x$, $CoSb_2O_x$, $MnSb_2O_x$, and $RuTiO_x$ in pH = 2.0, 4.0 M NaCl(aq) electrolyte. (a) Cyclic voltammetry of $NiSb_2O_x$, $CoSb_2O_x$, $MnSb_2O_x$, and $RuTiO_x$ at a scan rate of 10 mV s^{-1}. (b) Intrinsic potential of $NiSb_2O_x$, $CoSb_2O_x$, $MnSb_2O_x$, and $RuTiO_x$ determined from cyclic voltammetry data at 1 mA cm^{-2} of electrochemically active surface area. The vertical black line indicates the thermodynamic potential for chlorine evolution in 4.0 M NaCl(aq).

The electrochemical behavior of the TMAs was evaluated by cyclic voltammetry (CV), impedance spectroscopy, and chronopotentiometry in 4.0 M NaCl(aq) that was adjusted to

pH = 2 with 1.0 M HCl(aq). The equilibrium potential for $Cl^-/Cl_2(g)$ was determined to be 1.331 V vs. the normal hydrogen electrode (NHE) under these experimental conditions. For comparison to the behavior of the TMA's, dimensionally stable $RuTiO_x$ anodes were also evaluated (details in Supporting Information). Figure 1a shows typical cyclic voltammograms for $NiSb_2O_x$, $CoSb_2O_x$, $MnSb_2O_x$, and $RuTiO_x$ at a scan rate of 10 mV s^{-1} in the potential range of 1.0 to 2.1 V vs. NHE. Impedance measurements yielded electrode resistances in the range of 20 – 200 Ω for $NiSb_2O_x$, $CoSb_2O_x$, $MnSb_2O_x$, and $RuTiO_x$ films, hence compensation of 85% of the electrode resistance for electrodes with a geometric area of 0.01 – 0.1 cm^2 resulted in < 30 mV of voltage compensation at j_{geo} = 10 mA cm^{-2} for most of the catalysts studied herein.

Measurements of the electrochemically active surface area (ECSA) by impedance spectroscopy of the TMAs indicated that $NiSb_2O_x$, $CoSb_2O_x$, $MnSb_2O_x$, and $RuTiO_x$ films initially had roughness factors of 1.1 ± 0.1, 6.6 ± 2.5, 9.0 ± 5.2, and 8.8 ± 3.9, respectively (Table S2). The initial intrinsic activity of the electrocatalyst films was evaluated by determining the potential required to obtain 1 mA per cm^2 of ECSA from the backward scan, as shown on Figure 1b. The potential at 1 mA cm^{-2} of ECSA, which corresponds to a geometric current density of 1 – 15 mA cm^{-2} for roughness factors of 1 – 15 as observed herein, is referred to as the intrinsic potential (E_i). The $NiSb_2O_x$, $CoSb_2O_x$, $MnSb_2O_x$, and $RuTiO_x$ films exhibited a 1 mA cm^{-2} initial intrinsic potential of 1.602 ± 0.018, 1.652 ± 0.006, 1.699 ± 0.036, and 1.460 ± 0.010 V vs. NHE, respectively (Figure 1b, Table S3). The initial E_i measurements thus indicated that $RuTiO_x$ was the most active electrocatalyst at this current density, followed by $NiSb_2O_x$, $CoSb_2O_x$, and $MnSb_2O_x$.

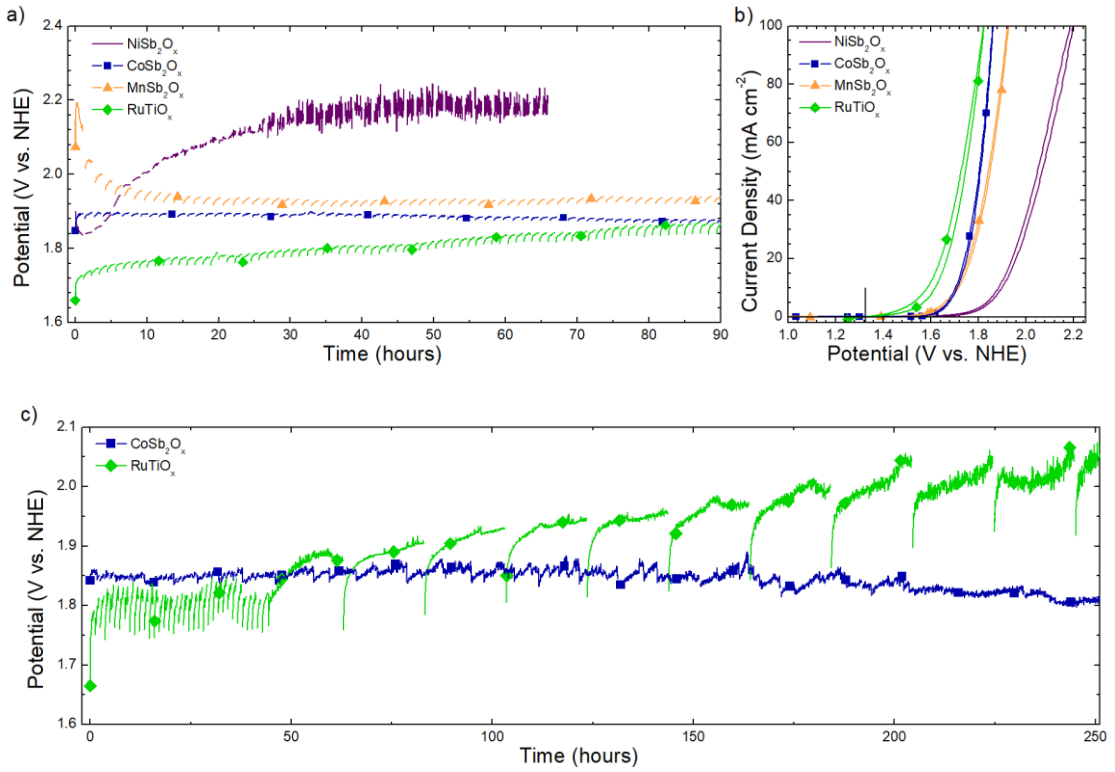

Figure 2. a) Chronopotentiometry of MSb_2O_x films and $RuTiO_x$, at j_{geo} = 100 mA cm^{-2} in 4.0 M NaCl(aq), pH = 2.0 electrolyte. b) Cyclic voltammetry of MSb_2O_x films and of $RuTiO_x$, after the chonopotentiometry stability experiments, at j_{geo} =100 mA cm^{-2} in 4.0 M NaCl(aq), pH = 2.0 electrolyte. The cyclic voltammetry data shown were recorded after operation for 65 h for $NiSb_2O_x$ and 90 h for $MnSb_2O_x$, $CoSb_2O_x$ and $RuTiO_x$. c) Chronopotentiometry of $CoSb_2O_x$ and $RuTiO_x$ at j_{geo} = 100 mA cm^{-2} in 4.0 M NaCl(aq), pH = 2.0 electrolyte for 250 h. Cyclic voltammetry scans were collected at 1 h intervals for the first ~ 45 h, then collected at 20 h intervals from 45 – 250 h.

Figure 2a shows the electrochemical stability of the TMAs under galvanostatic control at j_{geo} = 100 mA cm^{-2}. Cyclic voltammetry data were obtained before at 1 h intervals after the chronopotentiometry data were collected (Figure 2b). The potential increased slowly during the 1 h of chronopotentiometry with an abrupt decrease after cyclic voltammograms

and impedance data were collected. High frequency transient increases in potential were also observed due to partial blockage of the catalyst film as a result of $Cl_2(g)$ evolution. Figure 3a shows a comparison between the potential obtained from cyclic voltammetry and chronopotentiometry at 100 mA cm^{-2} after 85 h of operation for $CoSb_2O_x$ and $RuTiO_x$. In general, the potential observed during extended chronopotentiometry was 10 – 50 mV larger than the potential determined by cyclic voltammetry.

3.2.1 $NiSb_2O_x$

For $NiSb_2O_x$, the potential at j_{geo} = 100 mA cm^{-2} under galvanostatic control averaged 1.874 ± 0.015 V vs. NHE during the first 30 min of operation, after which the galvanostatic potential decreased to a minimum value of 1.842 ± 0.002 V vs. NHE for 1 - 2 h of operation (Figure 2a). Then the galvanostatic potential gradually increased and stabilized after 40 h, with an average value of 2.184 ± 0.022 V from 50 – 65 h of operation at j_{geo} = 100 mA cm^{-2} (Figure 2a). The fluctuation in potential observed for $NiSb_2O_x$ after 30 h was due to a periodic decrease in the potential every 5-10 min associated with bubble detachment. Impedance measurements collected after 1 h intervals of galvanostatic control indicated substantial changes in the capacitance and series resistance of the $NiSb_2O_x$-coated electrode. The series resistance of the $NiSb_2O_x$ catalyst increased from 101 Ω to 165 Ω over 50 h of chronopotentiometry at j_{geo} = 100 mA cm^{-2}. The increase in series resistance accounted for ~ 88 mV of the observed increase in potential for this film. Impedance data collected at 1 h intervals indicated that $NiSb_2O_x$ exhibited an increase in ECSA from ~1 to ~11 after 50 h of chronopotentiometry (Figure S9a).

The appearance of Ni and Sb in the electrolyte was measured using ICP-MS (Figure S10a). After 50 h of operation, 380 nmol cm^{-2} of Ni and 45 nmol cm^{-2} of Sb were present in the electrolyte. The detected concentration corresponded to 79 ± 6% of the Ni and 6 ± 1% of the Sb in the original catalyst film, indicating substantial loss of the catalyst layer. XRD of the electrode after electrochemical operation for 50 h indicated that crystalline $NiSb_2O_6$ remained in the catalyst film, and that the mean crystalline size was 39 ± 9 nm before operation and 11 ± 1 nm after operation (Figure S1). The XRD and ICP-MS data of $NiSb_2O_x$ indicate that dissolution leads to a decrease in the mean crystalline size. SEM images indicated a loss of catalyst loading from the surface, while also indicating that the substrate remained coated with a conformal layer of catalyst (Figure S5).

3.2.2 $CoSb_2O_x$

At j_{geo} = 100 mA cm^{-2}, the galvanostatic potential of $CoSb_2O_x$ initially increased from ~ 1.851 to ~1.891 V vs. NHE during the first 1 h of operation, and subsequently remained at ~1.876 V vs. NHE after 90 h (Figure 2a). Figure 3a shows the comparison between the potential obtained from cyclic voltammetry and chronopotentiometry between 85 – 90 h of operation. The potential from cyclic voltammetry was ~ 1.864 V vs. NHE, which was ~ 12 mV lower than the galvanostatic potential of ~ 1.876 V vs. NHE measured immediately preceding the cyclic voltammetry scans. Impedance measurements collected after the 1 h galvanostatic intervals indicated minor changes in the ECSA (Figure S9b). The series resistance of $CoSb_2O_x$ remained in the range of 30 - 34 Ω during the chronopotentiometric experiment, accounting for < 10 mV in the observed variation of the potential. The roughness factor increased from ~ 4 to ~8 after 50 h of operation. Less than 2 nmol cm^{-2} of

Co and 3 nmol cm^{-2} of Sb dissolved into the electrolyte after 50 h of operation (Figure S10b), corresponding to a loss of ~ 0.6 nm and ~ 0.3 nm of catalyst or 0.5 ± 0.1% Co and 0.3 ± 0.1% Sb, respectively. After electrochemical operation for 50 h, XRD data indicated that crystalline $CoSb_2O_6$ remained on the $CoSb_2O_x$ catalyst film, and that the mean crystalline size was 29 ± 5 nm before operation and 41 ± 13 nm after operation (Figure S2). SEM images indicated that the morphology of $CoSb_2O_x$ films tested for 50 h at j_{geo} = 100 mA cm^{-2} was similar to the morphology of as-synthesized films (Figure S6). Figure 2c shows the galvanostatic potential for $CoSb_2O_x$ at j_{geo} = 100 mA cm^{-2} for 250 h. Cyclic voltammetry data was collected at 1 h intervals for the first 45 h, then at 20 h intervals to observe the effect of long-term chronopotentiometry. The activity of $CoSb_2O_x$ was not substantially affected by the duration between cyclic voltammetry scans. The galvanostatic potential for $CoSb_2O_x$ at j_{geo} = 100 mA cm^{-2} was 1.804 V vs. NHE after 250 h of operation.

3.2.3 $MnSb_2O_x$

Over the first 0.3 h of operation at j_{geo} = 100 mA cm^{-2}, the galvanostatic potential of $MnSb_2O_x$ initially increased to ~ 2.191 V vs. NHE, followed by a gradual decrease to ~ 1.936 V vs. NHE over 20 h, followed by an average potential of 1.926 ± 0.006 V vs. NHE from 20 to 90 h of operation (Figure 2a). The series resistance of the $MnSb_2O_x$ was between 144 – 168 Ω during the stability test, accounting for ~ 40 mV in the observed variability in potential. The roughness factor of the $MnSb_2O_x$ film gradually increased from ~3 to ~ 25 over 50 h of chronopotentiometry (Figure S9c). ICP-MS of the electrolyte indicated that 192 nmol cm^{-2} and 185 nmol cm^{-2} of Mn and Sb dissolved in the electrolyte, corresponding to 46 ± 3% of Mn and 26 ± 1% of Sb in the catalyst film (Figure S10c). After electrochemical

operation, XRD confirmed that crystalline $MnSb_2O_6$, monoclinic Sb_2O_4, and orthorhombic Sb_2O_4 remained in the catalyst film, and that the mean crystalline size of $MnSb_2O_x$ was 3.4 ± 0.1 nm before operation and 3.7 ± 0.1 nm after operation (Figure S3). After electrochemical operation, SEM images showed a loss of catalyst loading as well as an increase in film porosity (Figure S7).

3.2.4 $RuTiO_x$

Figure 2a shows chronopotentiometry data for $RuTiO_x$ at j_{geo} = 100 mA cm^{-2}. The initial galvanostatic potential was ~ 1.661 V vs. NHE and then increased to ~1.871 V vs. NHE after 90 h of operation. Figure 3a shows the comparison between the potential obtained from cyclic voltammetry and chronopotentiometry between 85 – 90 h of operation. The potential from cyclic voltammetry was ~1.828 V vs. NHE, whereas the potential was ~ 1.871 V vs. NHE from chronopotentiometry immediately preceding the cyclic voltammetry scans. The roughness factor of $RuTiO_x$ remained essentially constant throughout the chronopotentiometry experiment (Figure S9d). The series resistance of $RuTiO_x$ electrodes was 17 - 18 Ω and remained within this range for the duration of the stability test. XRD indicated that RuO_2 and TiO_2 remained in the catalyst film after electrochemical testing, and that the crystalline size was 17 ± 1 nm before operation and 25 ± 1 nm after operation (Figure S4). SEM images indicated an increase in the porosity of the $RuTiO_x$ films after electrochemical operation (Figure S8). Figure 2c shows the galvanostatic potential for $RuTiO_x$ at j_{geo} = 100 mA cm^{-2} for 250 h. Cyclic voltammetry data was collected at 1 h intervals for the first 42 h, and then at 20 h intervals to observe the effect of long-term chronopotentiometry. The galvanostatic potential substantially increased during the 20 h

chronopotentiometry intervals. The galvanostatic potential at j_{geo} = 100 mA cm^{-2} for $RuTiO_x$ was 2.051 V vs. NHE after 250 h of operation.

3.2.5 TMA-free electrodes

To serve as controls, SbO_x on ATO and ATO electrodes were prepared without TMA electrocatalyst coatings. These electrodes exhibited a galvanostatic potential > 2.331 V vs. NHE at j_{geo} = 100 mA cm^{-2} under galvanostatic control. The electrochemical stability of the transition metal oxides NiO_x, CoO_x, and MnO_x was determined using electrocatalyst films that were prepared by the same procedure and transition-metal loading as the MSb_2O_x films, except that Sb was not co-sputtered during the metal deposition. Electrodes consisting of NiO_x or MnO_x were unstable for chlorine evolution at j_{geo} = 100 mA cm^{-2} under galvanostatic control (Figure S11b). CoO_x electrodes exhibited a potential of ~ 1.801 V vs. NHE at j_{geo} = 100 mA cm^{-2} under galvanostatic control during the first 6 h of operation, but then the potential increased to > 2.051 V vs. NHE after 8 h of operation (Figure S11b).

3.2.6 Intrinsic activity of the electrocatalysts

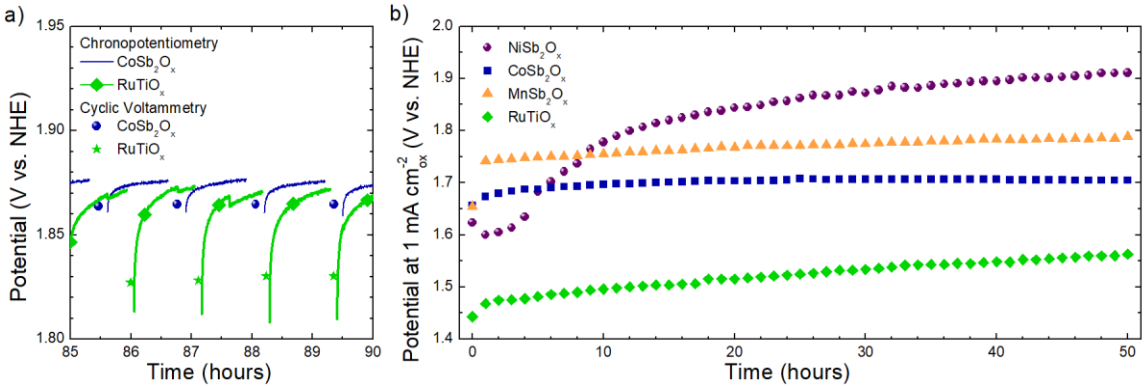

Figure 3. a) Comparison between potential after extended operation obtained from cyclic voltammetry and chronopotentiometry at j_{geo} = 100 mA cm^{-2} for $CoSb_2O_x$ and $RuTiO_x$. b) Intrinsic potential, E_i, at 1 mA cm^2 of electrochemically active surface area determined from cyclic voltammetry and impedance measurements, collected at 1 h intervals in between chronopotentriometry measurements at j_{geo} = 100 mA cm^{-2}, for $NiSb_2O_x$, $CoSb_2O_x$, $MnSb_2O_x$, and $RuTiO_x$.

The intrinsic activity of the electrocatalyst films was obtained by calculating the intrinsic potential after 1 h intervals of galvanostatic control. After each 1 h interval of chronopotentiometry at j_{geo} = 100 mA cm^{-2}, cyclic voltammetry and impedance measurements were collected to determine the ECSA, E_{cv}, series resistance, and E_i of the catalyst films. Each intrinsic potential was corrected at 85% of the series resistance determined for each time interval. Figure 3b shows the values of E_i at 1 mA cm^{-2} of ECSA for $NiSb_2O_x$, $CoSb_2O_x$, $MnSb_2O_x$, and $RuTiO_x$ obtained from these measurements. In general, the qualitative changes in both the potential (Figure 2) and the intrinsic potential (Figure 3b) were similar during operation for most of the electrocatalyst films. Figure 3b

shows the intrinsic potential for representative electrodes, whereas Table S3 shows the average and standard deviation for the electrocatalysts studied herein. Figure 3b shows that $NiSb_2O_x$ exhibited an E_i of 1.624 V vs. NHE initially, that decreased to a minimum value of 1.600 V vs. NHE after 1 h of operation and subsequently increased gradually, to 1.911 V vs. NHE after 50 h of operation. $CoSb_2O_x$ initially exhibited an E_i of 1.656 V vs. NHE, that gradually increased to 1.704 V vs. NHE over 20 h, followed by a stable E_i of 1.704-1.707 V vs. NHE from 20 to 50 h of operation. $MnSb_2O_x$ initially exhibited E_i = 1.655 V vs. NHE, that then increased to 1.741 V vs. NHE after 1 h of operation, followed by a gradual increase to E_i = 1.789 V vs. NHE after 50 h of operation. $RuTiO_x$ exhibited an initial E_i of 1.443 V vs. NHE, followed by a gradual increase to 1.561 V vs. NHE after 50 h of operation. Table S3 summarizes the changes in intrinsic potential vs. time for MSb_2O_x and $RuTiO_x$.

3.2.7 Faradaic Efficiency for Cl_2 Production

The faradaic efficiency towards the CER was determined using iodometric titration of Cl_2(aq) generated at a galvanostatic current density of 100 mA cm^{-2}. The iodometric measurements indicated that $CoSb_2O_x$ had the highest faradaic efficiency for the CER (97.4 ± 3.0%), with $NiSb_2O_x$ (96.0 ± 3.7%), $RuTiO_x$ (94.8 ± 0.9%), and $MnSb_2O_x$ (89.9 ± 0.8%) having a slightly lower faradaic efficiency towards the CER but still predominantly evolving Cl_2(g) preferentially relative to oxidizing water (Table S2). The production of chlorine was also confirmed with colorimetric measurements using N,N-diethyl-p-phenylenediamine. Cyclic voltammograms collected in pH = 2.0 H_2SO_4(aq), with current solely attributable to the OER, further confirmed minimal activity towards the OER for $CoSb_2O_x$ in the potential range relevant to the CER (Figure S13).

3.2.8 Surface Composition as probed by XPS

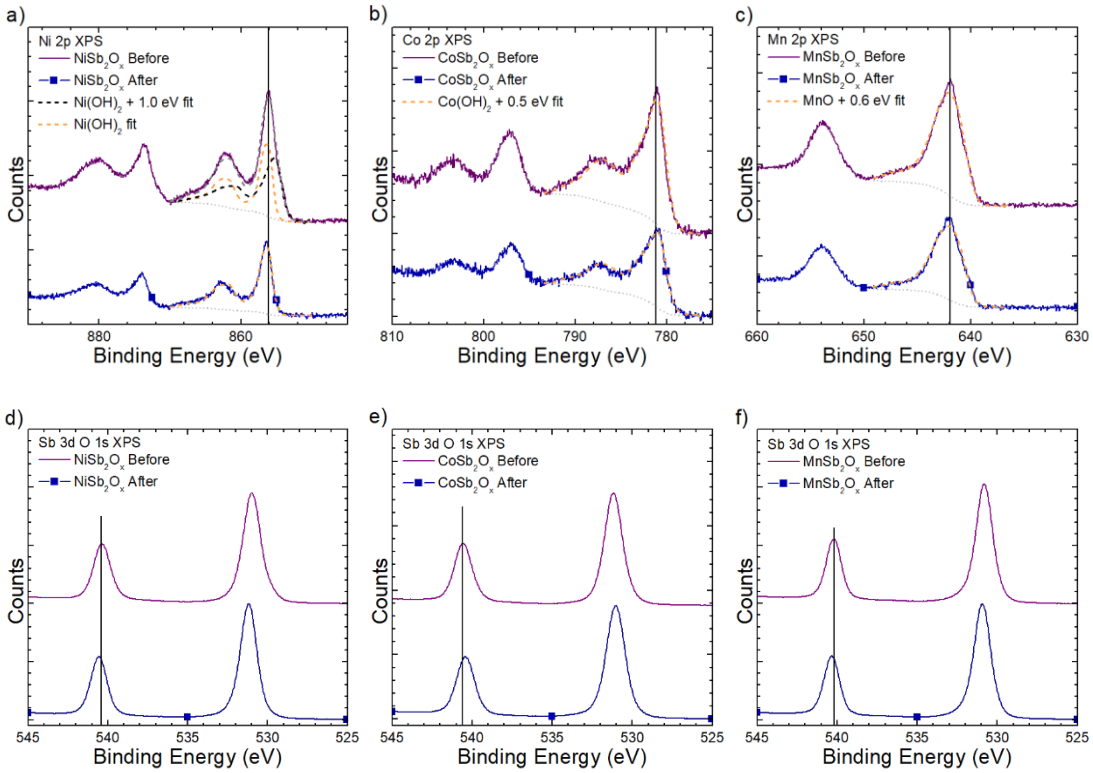

Figure 4. X-ray photoelectron spectra of TMAs before and after electrochemical operation: a) $NiSb_2O_x$ Ni 2p spectra, b) $CoSb_2O_x$ Co 2p spectra, c) $MnSb_2O_x$ Mn 2p spectra, and Sb 3d and O 1s spectra of d) $NiSb_2O_x$, e) $CoSb_2O_x$, and f) $MnSb_2O_x$.

Figure 4 shows high-resolution XP spectra of $NiSb_2O_x$, $CoSb_2O_x$, and $MnSb_2O_x$ before and after chronopotentiometry at j_{geo} =100 mA cm^{-2}. The Ni 2p spectra of $NiSb_2O_x$ exhibited a peak at ~ 856.1 eV. The peak shapes of $NiSb_2O_x$ were fitted to two Ni(II) components, $Ni(OH)_2$ and a peak shape similar to $Ni(OH)_2$ but with a 1.0 eV more positive binding energy. The observed binding energy for the more positive contribution is intermediate to that of Ni(II) in $NiCl_2$ and $Ni(OH)_2$.[18] In general, the M 2p spectra of TMAs exhibited peak shapes similar to that of the $M(OH)_2$ or MO species, but with more positive binding energies.

$NiSb_2O_6$ is chemically different than Ni oxides and hydroxides, so the Ni 2p peak binding energy can be different while remaining in the 2+ oxidation state. Thus, we assign the more positive contribution to Ni(II) in the $NiSb_2O_6$ lattice. After electrochemical operation, $NiSb_2O_x$ samples exhibited a narrower Ni $2p_{3/2}$ peak at 856.3 ± 0.1 eV compared to $NiSb_2O_x$ before electrochemical operation. The peak shape of $NiSb_2O_x$ after electrochemical operation could be adequately fit with a peak shape similar to $Ni(OH)_2$ but shifted positively by 1.0 eV. XP spectra in the Cl, Ir, and Ru regions revealed no detectable Cl, Ir, and Ru before or after electrochemical operation. Mutually similar Sb $3d_{3/2}$ binding energies were observed for $NiSb_2O_x$ before (540.4 ± 0.1 eV) and after (540.5 ± 0.1 eV) electrochemical operation. The Sb binding energy is consistent with the samples containing Sb^{5+} as well as minor contributions from Sb^{3+}.[19] The surface stoichiometry of the $NiSb_2O_x$ was 1:1.8 ± 0.1 Ni:Sb prior to electrochemical operation and was 1:3.2 ± 0.1 Ni:Sb after electrochemical operation, indicating that the surface became Sb rich. The catalyst surface coverage was determined by comparing the catalyst metal signal (Ni + Sb) to the overall metal signal of the catalyst and the substrate (Ni+ Sb + Sn), with the signals corrected using the respective relative sensitivity factors. The catalyst coverage was 100% of the surface in both cases.

Before and after electrochemical operation, $CoSb_2O_x$ samples exhibited a narrow Co $2p_{3/2}$ XPS peak at 781.2 ± 0.1 eV. The peak shape of Co in $CoSb_2O_x$ was similar to that of Co in $Co(OH)_2$, but with a ~ 0.5 eV higher binding energy.[20] The observed binding energy is between that of hydrated $CoCl_2$ and $Co(OH)_2$, indicating that Co is in the 2+ oxidation state at the surface of the $CoSb_2O_x$ films.[20] The XPS measurements indicate that the oxidation state of Co did not irreversibly change as a result of electrochemical operation. Wide scan XP spectra showed no detectable Cl, Ir, or Ru on the electrodes. The Sb $3d_{3/2}$ binding energy

was 540.6 ± 0.1 eV prior to electrochemical operation and 540.3 ± 0.1 eV after electrochemical operation. The XPS measurements indicate that Sb was present in the 5+ oxidation state prior to electrochemical operation and was in a mixed 5+/3+ oxidation state after electrochemical operation.[19] The surface stoichiometry of $CoSb_2O_x$ was 1:4.0 ± 0.1 Co:Sb prior to electrochemical operation and was 1:4.5 ± 0.1 Co:Sb after electrochemical operation, indicating enrichment of Sb at the surface. The $CoSb_2O_x$ surface catalyst coverage was 100% before and after electrochemical operation.

The $MnSb_2O_x$ samples exhibited a Mn $2p_{3/2}$ XPS peak at a binding energy of 641.9 ± 0.1 eV before electrochemical operation and 642.0 ± 0.1 eV after electrochemical operation. The binding energies are comparable to Mn in the 2+ oxidation state in $MnCl_2$, and the peak shape was similar to MnO but shifted 0.5 eV more positive.[20-21] Wide scan XP spectra indicated no detectable Cl, Ir, or Ru on the surface. The Sb $3d_{3/2}$ peak exhibited a binding energy of 540.2 ± 0.1 eV prior to electrochemical operation and 540.3 ± 0.1 eV after electrochemical operation. The Sb 3d spectra indicated that Sb was present in both the 5+ and 3+ oxidation states before and after electrochemical operation. The surface stoichiometry of $MnSb_2O_x$ was 1:2.0 ± 0.1 Mn:Sb prior to electrochemical operation and 1:2.7 ± 0.2 Mn:Sb after electrochemical operation, indicating surface enrichment of Sb after chlorine evolution. The surface coverage of $MnSb_2O_x$ was 98.8 ± 0.4% prior to electrochemical operation and 96.8 ± 0.1% after electrochemical operation, indicating partial exposure of the electrocatalyst substrate after chlorine evolution. Table S4 summarizes the observed binding energies of the MSb_2O_x samples and also presents a comparison of the binding energies to literature values. Figure S14 summarizes the roughness factor, potential, stoichiometry, and crystalline size of the catalysts studied herein after different durations of galvanostatic operation.

3.3 Discussion

3.3.1 Trends in Catalyst Intrinsic Activity

The initial intrinsic activity measurements of TMAs under chlorine evolution indicate an activity trend of $NiSb_2O_x$ > $CoSb_2O_x$ > $MnSb_2O_x$. Previous studies of the intrinsic OER activity of MSb_2O_x in acidic electrolytes indicated an OER activity trend of $NiSb_2O_x$ ≈ $MnSb_2O_x$, while $CoSb_2O_x$ was not previously examined for the OER.[14] Further improvements in the activity of TMAs towards chlorine evolution could possibly be achieved via solid solutions, as has been demonstrated for OER electrocatalysts and/or by use of other transition metals in the SbO_x framework.[14] Notably, $CoSb_2O_x$ had the highest CER activity after extended operation (Figure 2, Figure S13). While the $CoSb_2O_x$ catalyst had an initial intrinsic potential that was ~ 190 mV higher than $RuTiO_x$, this difference decreased to ~ 140 mV after 50 h of chronopotentiometry, due to the intrinsic potential of $RuTiO_x$ increasing (~ 1.3 mV h^{-1}) while the $CoSb_2O_x$ intrinsic potential remained constant after an initial increase (Figure 3b). The high stability of the electrochemical activity of $CoSb_2O_x$ relative to $RuTiO_x$ suggests that $CoSb_2O_x$ electrodes could have active electrocatalytic CER lifetimes exceeding those of $RuTiO_x$.

During chlorine evolution, the surface composition of the TMAs changed, and correlated with changes in the intrinsic activity of the catalyst films. As indicated by XPS, $NiSb_2O_x$ and $MnSb_2O_x$ exhibited surface compositions that were very similar to their bulk composition (~1:2 M:Sb), but $CoSb_2O_x$ exhibited substantial initial surface enrichment of Sb (1:4 Co:Sb) despite having a bulk composition of ~ 1:2 M:Sb (Figure 4, Table S1). The surface enrichment of $CoSb_2O_x$ is consistent with previous reports for cobalt antimony oxides.[22]

The intrinsic potential of $NiSb_2O_x$ films initially decreased by 32 mV during operation, followed by an increase of 300 mV (Figure 3). While the Ni 2p spectra indicate that Ni is in the 2+ oxidation state before and after electrochemical operation, Ni(II) compounds such as NiO, $Ni(OH)_2$, $NiCl_2$, and $NiSb_2O_6$ have different peak binding energies despite having the same formal oxidation state. Fitting of the Ni 2p peak shape can reveal which species are present on the surface.[23] The spectrum of $NiSb_2O_x$ could not be adequately fit with the fitting parameters of previously reported species, so $NiSb_2O_x$ was fit by using the peak shape of $Ni(OH)_2$ shifted positively by 1.0 eV. The observed contributions at 1.0 eV more positive binding energies could correspond to Ni(II) in the $NiSb_2O_6$ lattice. Fitting the Ni 2p data of $NiSb_2O_x$ before electrochemical operation with the proposed $NiSb_2O_6$ fit revealed low binding energy contributions that are consistent with Ni hydroxide species (Figure 4a). The surface composition of the $NiSb_2O_x$ was similar to its bulk composition (~1:2 M:Sb), but the XPS data suggest that the surface was covered by multiple Ni(II) species, such as $NiSb_2O_6$, NiO_x, and $Ni(OH)_2$ (Figure 4a). NiO_x and $Ni(OH)_2$ are expected to be readily removed from the surface due to thermodynamically favored dissolution processes under the operating conditions, and NiO_x is unstable towards the CER (Figure S11b). Loss of NiO_x and $Ni(OH)_2$ in the first hour of operation could explain the initial improvement in catalytic activity, if these species had a detrimental effect on the activity. After 50 h of operation, $NiSb_2O_x$ exhibited substantial surface enrichment of Sb, as indicated by the ~ 80% increase of Sb relative to Ni (Figure 4a, 4d). The Ni in $NiSb_2O_x$ exhibited a 2+ oxidation state before and after electrochemical operation. Contributions from $Ni(OH)_2$ or NiO_x decreased after electrochemical operation as indicated by the Ni 2p XPS data, suggesting that the surface Ni

either dissolved or is in a $NiSb_2O_6$ lattice and did not undergo conversion to stable Ni oxides or (oxy)hydroxides.

The intrinsic potential of $MnSb_2O_x$ increased by ~ 85 mV in the first hour of operation but increased by only another 20 mV in the next 50 h. The oxidation states of both Mn and Sb did not change substantially after electrochemical operation (Figure 4b, 4e). However, the surface of the $MnSb_2O_x$ became Sb rich, as indicated by the ~ 39% increase in Sb at the surface compared to Mn as measured by XPS. The increase in Sb at the surface, without a substantial change in binding energy, suggests that Sb remained in the 5+ oxidation state. The substantially smaller change in potential after 50 h for $MnSb_2O_x$ (ΔE_i = 134 mV) as compared to $NiSb_2O_x$ (ΔE_i = 287 mV) might be due to a lower surface coverage of SbO_x species (Figure 3, 4).

The surface of $CoSb_2O_x$ differed substantially from the surface of $NiSb_2O_x$ or $MnSb_2O_x$. $CoSb_2O_x$ exhibited substantial initial surface enrichment of Sb (1:4 Co:Sb) prior to electrochemical operation in contrast to both $NiSb_2O_x$ and $MnSb_2O_x$ that had an initial surface M:Sb ratio close to their bulk stoichiometry of ~1:2. The $CoSb_2O_x$ exhibited an increase in surface Sb (1:4.5 Co:Sb) after electrochemical operation (~ 13%), again in contrast to $NiSb_2O_x$ and $MnSb_2O_x$ whose Sb surface enrichment after electrochemical operation increased ~ 80%, and ~ 39%, respectively, However, in all cases after electrochemical operation the surfaces were significantly enriched in Sb relative to the transition metal. As opposed to the $NiSb_2O_x$ and $MnSb_2O_x$ electrodes, the $CoSb_2O_x$ electrode exhibited a minimal change in intrinsic potential after 50 h (ΔE_i = 48 mV), which correlates with the minimal change in Sb enrichment at the surface. The initial oxidation states of Co and Sb at the surface were 2+ and 5+, in accord with expectations for stoichiometric $CoSb_2O_6$

(Figure 4). After electrochemical testing, $CoSb_2O_x$ exhibited a decrease of 0.3 eV in Sb $3d_{5/2}$ binding energy, whereas $NiSb_2O_x$ and $MnSb_2O_x$ both exhibited an increase in the binding energy of Sb $3d_{5/2}$ ($\Delta E = 0.1$ eV). The decrease in binding energy of Sb in $CoSb_2O_x$ could be related to the Sb-rich layer on the surface of $CoSb_2O_x$, which is not present in the nearly stoichiometric surface of the $NiSb_2O_x$ and $MnSb_2O_x$ films before electrochemical operation. Cyclic voltammetry data were collected at more negative potentials than thermodynamic potential for chlorine evolution, and cathodic current was observed at such potentials (Figure 2b). Further studies to determine the catalytically active site of TMAs could allow more detailed elucidation of the electrocatalytic role of the Sb oxidation state.

3.3.2 Comparison of Activity to Other CER Electrocatalysts

Previous studies of chlorine evolution catalysts have included Co_3O_4, which exhibits $\eta \sim 1.951$ V vs. NHE at j_{geo} =100 mA cm^{-2}, with an estimated catalyst roughness factor of > 3,000.[24] Nanostructured RuO_2-TiO_2 electrodes exhibit $\eta \sim 2.041$ V vs. NHE at j_{geo} =250 mA cm^{-2}, with an estimated roughness factor of ~ 390.[25] $Ir_{0.7}Ta_{0.3}O_y$ films exhibit $\eta > 2.331$ V vs. NHE at j_{geo} =30 mA cm^{-2} in pH = 7, 50 mM NaCl(aq) electrolyte.[26] Mesoporous Ru/TiO_2 dimensionally stable anodes exhibit $\eta \sim 1.981$ V vs. NHE at j_{geo} =100 mA cm^{-2} in 4.0 M NaCl(aq), pH = 3.0 electrolyte.[8] The ~ 1.871 V vs. NHE galvanostatic potential at j_{geo} =100 mA cm^{-2} reported herein for $RuTiO_x$ between 85 – 90 h of operation is comparable to previous reports of noble metal oxides for chlorine evolution (Figure 2a). $CoSb_2O_x$ exhibits a galvanostatic potential of ~ 1.804 V vs. NHE at j_{geo} =100 mA cm^{-2} after 250 h, which is lower than some previous reports for noble metal oxides and is lower than the potential observed herein for $RuTiO_x$ after extended operation (Figure 2c). The catalyst loading and

roughness factor used herein were both relatively low, to facilitate determination of the intrinsic properties of the electrocatalysts. Consequently, the potential of the TMAs could be improved further by increasing the catalyst loading and roughness, to expose additional catalytically active sites without changing the geometric area of the electrode. Due to the deactivation of $RuTiO_x$ during chronopotentiometry and the comparatively high electrochemical stability of $CoSb_2O_x$, after 250 h of operation $CoSb_2O_x$ exhibited a galvanostatic potential ~ 247 mV lower than that of $RuTiO_x$ (~ 2.051 V vs. NHE). This behavior suggests that $CoSb_2O_x$ may constitute a promising alternative to $RuTiO_x$ for the chlor-alkali process and other processes that require the CER. Co and Sb are substantially more abundant than Ru, and their annual molar production rates are over 5,000 times higher than Ru.[27] The high abundance of both Co and Sb relative to Ru is reflected in the market price of these elements, which reflects a substantially lower price per mole of metals for $CoSb_2O_x$ (~ 2 USD mol^{-1}) compared to the price per mol for the commercially used $Ru_{0.3}Ti_{0.7}O_x$ (~153 USD mol^{-1}) catalyst.[27]

3.3.3 Trends in Catalyst Stability

Under CER conditions, the chemical stability of the TMA's decreased in the order $CoSb_2O_x > MnSb_2O_x > NiSb_2O_x$. $CoSb_2O_x$ exhibited the lowest dissolution rate, with < 0.6 nm of Co (~ 2 nmol cm^{-2}) and < 0.3 nm of Sb lost (~ 3 nmol cm^{-2}) from the surface after 50 h of operation (Figure S10b). Possible explanations for the appearance of M and Sb in the electrolyte include dissolution of oxide species that did not form the stable MSb_2O_6 phase, and/or chemically or electrochemically driven dissolution processes. Additionally, mechanical detachment of MSb_2O_6 particles could lead to changes in the catalyst loading

that cannot be detected with ICP-MS. The small amount of dissolved Co and Sb (~ 4×10^{-9} mol cm^{-2}) for $CoSb_2O_x$, compared to the charge passed during the stability experiments (~ 1.8×10^4 C cm^{-2}), suggests a turnover number of > 2×10^7 based on the dissolution observed per charge passed, indicating that faradaic dissolution pathways are unlikely to be dominant. After 250 h at j_{geo} =100 mA cm^{-2}, the $CoSb_2O_x$ electrocatalyst has thus turned-over ~10^6 equivalents of Cl_2 without substantial degradation. While the dissolution studies indicate that $CoSb_2O_x$ has high electrochemical stability, industrial applications will require toxicology studies to determine possible exposure routes to Co and Sb. Similar studies have been conducted for polyethylene terephthalate bottles used for water consumption containing an antimony trioxide polymerization catalyst.[28] The high turnover number suggest that Sb could be present at ~0.05 ppm concentrations in the products of the chlor-alkali process utilizing a $CoSb_2O_x$ electrocatalysts. However, since chlorine is usually used in the 1 - 3 ppm range to disinfect water, the dilution of chlorine would also lead to the dilution of Sb, which could lead to an Sb concentration of ~0.15 parts-per-trillion. Antimony is limited to 5 - 6 ppb in drinkable water in the United States and the European Union, which is ~ 3×10^4 greater than the concentration expected for water treated with diluted chlorine generated with a $CoSb_2O_x$ catalyst under the specific experimental conditions evaluated in this work. The high chemical and electrochemical stability of $CoSb_2O_x$, as indicated by minimal changes in catalyst morphology, intrinsic potential, and surface oxidation, suggest that $CoSb_2O_x$ and possibly other TMAs could be viable materials for chlorine evolution in devices requiring abundant and stable electrocatalysts under industrially relevant operational conditions.

3.4 Conclusion

$NiSb_2O_x$, $CoSb_2O_x$, and $MnSb_2O_x$ were found to be moderately active chlorine evolution catalysts for > 60 h at j_{geo} = 100 mA cm^{-2} in 4.0 M NaCl(aq), pH = 2.0 electrolyte. $CoSb_2O_x$ exhibited the highest stability and selectivity among the TMAs tested herein, with < 1 nm of metals lost after extended electrochemical operation. After 250 h of operation, the galvanostatic potential of $CoSb_2O_x$ at j_{geo} = 100 mA cm^{-2} was lower than that of dimensionally stable $RuTiO_x$. The results suggest that TMAs could be further modified to potentially yield stable catalysts for chlorine evolution with lifetimes and selectivity comparable to or greater than that of dimensionally stable anodes such as $RuTiO_x$.

3.5 Acknowledgements

This work was supported through the Office of Science of the U.S. Department of Energy (DOE) under award no. DE-SC0004993 to the Joint Center for Artificial Photosynthesis, a DOE Energy Innovation Hub. I.A.M.-H. acknowledges a National Science Foundation Graduate Research Fellowship under Grant No. DGE-1144469. We thank Dr. K. Papadantonakis for assistance with editing the manuscript, and C. Finke for assistance with iodometric measurements.

3.6 Supplementary Information

3.6.1 Chemicals

All chemicals were used as received, including antimony(III) chloride ($SbCl_3$, Alfa Aesar, ACS, 99.0% min), tin(IV) chloride hydrate ($SnCl_4 \cdot xH_2O$, Alfa Aesar, 98%), sodium chloride (NaCl, Macron Chemicals, ACS grade), potassium iodide (KI, EMD Millipore, ACS grade), sodium thiosulfate pentahydrate ($Na_2S_2O_3$, Alfa Aesar, ACS grade), 1.0 M hydrochloric acid (1.0 M HCl(aq), Fluka Analytical), multielement standard solution 1 for ICP (Sigma Aldrich, TraceCERT), sulfuric acid (H_2SO_4(aq), Fischer Scientific, TraceMetal grade, 93-98%), sodium hydroxide (NaOH, Macron Chemicals, ACS grade), antimony standard for ICP (Sigma Aldrich, TraceCERT), potassium chloride (KCl, Macron Chemicals, ACS grade), and gallium-indium eutectic (Alfa Aesar, 99.99%). Deionized water with a resistivity of 18.2 MΩ-cm was obtained from a Millipore deionized water system.

3.6.2 Sample Preparation

A previously described spray pyrolysis procedure was used to deposit conductive films of antimony-doped tin oxide (ATO).[14, 16] The process consisted of spraying a 0.24 M $SnCl_4$ solution in ethanol doped with 3 mol% $SbCl_2$ onto a quartz microscope slide heated at 550 °C on a hot plate. The thickness of the ATO film was adjusted by controlling the duration of the spray. ATO films with a sheet resistance of 5- 10 Ω sq^{-1}, as determined from four-point probe measurements, were used for subsequent experiments.

Metallic films of Ni, Co, Mn, Sb, $NiSb_2$, $CoSb_2$, and $MnSb_2$ were deposited onto the ATO substrates with an AJA Orion sputtering system. The ATO substrates were partially

covered with Kapton tape to prevent complete coverage of the ATO with the catalyst films, to form a direct contact between the ATO and the working electrode wire. The metallic films were co-sputtered from four metallic targets in an Ar plasma: Antimony (ACI Alloys, 99.95%), Nickel (ACI Alloys, 99.95%), Cobalt (ACI Alloys, 99.95%), and Manganese (ACI Alloys 99.95%). The chamber pressure was < 10^{-7} Torr prior to the depositions. A chamber pressure of 5 mTorr was sustained during the depositions with an Ar flow rate of 20 sccm. The samples were not intentionally heated during the deposition process. The power applied to the metal targets was varied to obtain similar transition metal loadings and a stoichiometry close to 2:1 Sb:M in MSb_x samples. The actual stoichiometry and loading of Ni, Co, Mn, and Sb was determined by dissolving in 1.0 M H_2SO_4(aq) films deposited on glass, and then using the concentration of the metals as determined by ICP-MS, the areas of the samples dissolved, and the amount of H_2SO_4(aq) used during the dissolution to obtain the total loading.

After the metal films were deposited on ATO, the films were annealed in a muffle furnace (Thermolyne F48020-80) to form the crystalline oxides.[14] Unless otherwise specified, the temperature was increased to 750 °C at a ramp rate of 10 °C min^{-1}, was held at 750 °C for 6 h, and then allowed to return to room temperature without active cooling. $RuTiO_x$ films with the same molar loading (~ 1.5 μmol cm^{-2}) as the MSb_2O_x films were prepared by drop casting 4 μL cm^{-2} of a 0.11 M $RuCl_3$ and 0.26 M $TiCl_4$ solution in ethanol onto ATO, followed by drying on a hot plate at 400 °C.[8] The $RuTiO_x$ was annealed at 500 °C for 1 h in a muffle furnace.[8] The samples were cleaved into pieces that had exposed ATO regions, and In-Ga eutectic was scribed on the ATO. The electrode support consisted of a tinned Cu wire that was threaded through a glass tube. The Cu wire was coiled and bonded to the ATO substrate

by use of Ag paint (SPI, Inc). The contact was allowed to dry for at least 2 h at room temperature or for 15 min at 85 °C in an oven. Hysol 9460 epoxy was used to insulate the Cu, ATO, and In-Ga from the electrolyte and to define the geometric electrode area. The epoxy was allowed to cure for > 12 h at room temperature or for 2 h at 85 °C in an oven. The electrode area and a calibration ruler was imaged with an optical scanner (Epson Perfection V360), and the electrode area was quantified with ImageJ software. Electrode areas were between 1 and 40 mm^2 unless otherwise specified.

3.6.3 Materials Characterization

X-ray diffraction (XRD) data were collected with a Bruker D8 Discover instrument. The Cu Kα (1.54 Å) x-ray beam was generated with a tube current of 1000 μA and a tube voltage of 50 kV, and was detected with a Vantec-500 2-dimensional detector. The incident beam was collimated with a 0.5 mm diameter mono-capillary collimator. A calibrated visible laser was used to align the sample with the x-ray beam. XRD data were collected in coupled θ-2θ mode, with four scans collected every 20° from a 2θ theta range of 20° – 80°. The x-ray radiation was collected for 1 h for each scan, corresponding to 4 h per sample. The 2-dimensional signal was integrated to obtain a 1-dimensional scan with an angular resolution of 0.01° 2θ. The x-ray diffraction peaks were analyzed using Bruker EVA software with reference patterns of SnO_2 for the ATO substrate, in addition to reference patterns for monoclinic Sb_2O_4, orthorhombic Sb_2O_4, $NiSb_2O_6$, $CoSb_2O_6$, $MnSb_2O_6$, RuO_2, and TiO_2 obtained from the Crystallography Open Database or literature.[29-30] Scanning-electron microscopy (SEM) images were collected using immersion mode with an accelerating voltage of 10 kV on a Nova nanoSEM 450 (FEI) instrument.

3.6.4 X-ray Photoelectron Spectroscopy

X-ray photoelectron spectroscopy (XPS) scans were collected using a Kratos Axis NOVA (Kratos Analytical, Manchester, UK) at a background pressure of $<10^{-9}$ Torr. The x-ray source consisted of a monochromatic Al kα beam with an energy of 1486.6 eV. Survey scans were collected at 1.0 eV resolution, and high-resolution scans were collected at 0.05 eV resolution. The binding energy of the scans was corrected against the adventitious C 1s peak with a constant offset to obtain an adventitious C 1s peak energy of 284.8 eV. The M 2p spectra of Ni, Co, and Mn were fit using previously reported fitting parameters.[20] The reported peak separations, FWHM ratios, and relative peak areas were used to fit the collected M 2p spectra. However, in most cases the peak shapes could not be fit adequately without shifting the peaks towards more positive binding energies. Since MSb_2O_x samples are chemically different than MO_x or $M(OH)_2$ samples, we tentatively assign the shifted peak shapes to M(II) in a MSb_2O_6 lattice. For example, while the peak position of $NiSb_2O_x$ is similar to other Ni(II) species, the peak shape could not be adequately fit with Ni 2p spectra of Ni oxide or hydroxide species. We introduced an addition peak shape that consisted of the $Ni(OH)_2$ spectra shifted 1.0 eV more positive.[23] We tentatively assign this peak shape to Ni(II) in the $NiSb_2O_6$ lattice. The XP spectrum of Sb $3d_{3/2}$ was used to determine the oxidation state of the surface Sb on MSb_2O_x samples. Literature values of Sb $3d_{3/2}$ peak binding energies for oxidation states of 3^+, $3^+/5^+$, and 5^+ are 539.5 eV, 540.1 eV, and 540.4 eV respectively, for a C 1s peak binding energy of 284.8 eV.[19]

3.6.5 Electrochemical Testing

NaCl was used to make 4.0 M aqueous solutions, and 1 M HCl(aq) was used to adjust the pH to 2 as measured by a pH probe. A saturated calomel electrode (SCE) was calibrated with a normal hydrogen electrode (NHE). The NHE consisted of a platinum disk (CH Instruments) submerged in a H_2 saturated 1.0 M sulfuric acid electrolyte, with H_2(g) bubbled underneath the Pt disk to ensure saturation. The potential of the SCE was 0.244 V vs. NHE. Electrochemical measurements were collected in a two-compartment cell with the compartments separated using a Nafion N424 membrane. The cathode compartment was filled with 0.1 M NaOH(aq), and the anode compartment was filled with 4.0 M NaCl(aq) adjusted to pH = 2 with HCl(aq). After 48 h chronopotentiometry experiments, the pH of the electrolyte was usually 2.05 – 2.10. The OER acidifies solutions, and the observations are consistent with the observed increase in pH arising from minor leakage of NaOH through the Nafion N424 membrane. The electrolyte was replaced after 48 h to prevent the pH from increasing. The working and reference electrodes were placed in the anode compartment, and the counter electrode was placed in the cathode compartment. The working, reference, and counter electrodes consisted of the sample, an SCE, and a carbon rod or Ni wire, respectively. The anode compartment was saturated with Cl_2(aq) by applying ~ 10 V for at least 30 min between the counter electrode and a second working electrode that consisted of a graphite rod. The saturation of the electrolyte with Cl_2(aq) did not substantially affect the activity of the electrocatalysts or the pH of the electrolyte. However, this step was implemented to establish and maintain a well-defined potential based on the Nernst equation, which requires that Cl_2(aq) is present in the electrolyte. Cyclic voltammograms were

collected at a scan rate of 10 mV s^{-1} unless otherwise specified. Electrochemical data were collected using a digital potentiostat (SP-200, Bio-Logic). The thermodynamic potential for chlorine evolution was calculated to be 1.331 V vs. NHE in 4.0 M NaCl(aq).[31]

The roughness factor (RF) of the TMAs was determined by comparing the electrochemically active surface area of bare ATO substrates and TMAs, as determined from impedance measurements. Impedance measurements were collected in 4.0 M NaCl(aq) adjusted to pH = 2 with the electrolyte additionally saturated with Cl_2(aq). Electrodes were held at 1.660 V vs. NHE for 15 s prior to impedance measurements, which were collected at the same potential with a frequency range of 20 Hz – 20 kHz, with a sinusoidal wave amplitude of 10 mV. The impedance data were fit with a circuit model consisting of a resistor in series with a parallel component consisting of a constant phase element and another resistor.[32] The capacitance was obtained by using a formula previously reported for the analysis of this circuit.[32] The formula is shown below:

$$C_{DL} = \left[Q_0 \left(\frac{1}{R_s} + \frac{1}{R_{CT}} \right)^{(a-1)} \right]^{\frac{1}{a}}$$

where Q_0 and a are the parameters associated with the constant phase element, R_s is the series resistance, R_{ct} is the charge-transfer resistance, and C_{DL} is the determined double-layer capacitance. The impedance data were fit using EC-Lab software by constraining all variables to positive values, and using the Randomize + Simplex method for at least 10,000 iterations. The fitting process was repeated at least four times to ensure that the best fit was obtained. Table S5 shows examples of impedance data collected for the electrocatalysts studied herein. ATO substrates prepared by a spray deposition method have previously been

determined from atomic force microscopy measurements to have a RF = 1.32.[14] The capacitance of ATO electrodes was determined with impedance measurements, and divided by the projected area of the electrodes to determine the geometric-area normalized capacitance. The geometric-area normalized capacitance of ATO was 14.4 ± 1.6 μF cm^{-2}, which corresponds to an electrochemical surface area normalized capacitance of 11 ± 1 μF cm_{ox}^{-2} after dividing by the RF = 1.32 of ATO. The roughness factor of the TMAs was determined by dividing the geometric-area normalized capacitance of the TMAs by the electrochemical surface area normalized capacitance of ATO (11 μF cm_{ox}^{-2}).

3.6.6 Inductively-coupled plasma mass spectrometry

An Agilent 8000 Triple Quadrupole Inductively Coupled Plasma Mass Spectrometer (ICP-MS) system was used to determine the concentration of various ions in aqueous samples. Calibration solutions were prepared by diluting antimony and multielement standard solutions (Sigma Aldrich) with 18.2 MΩ cm resistivity water. The concentration of various ions was determined from a linear fit of the counts per second of each standard solution versus the known concentration. The mass loading of the TMAs was determined by depositing the MSb_2 (M = Ni, Co, Mn) layers on glass slides that were then cut into ~ 1 cm^2 pieces. The projected area of the pieces was determined with a calibrated optical scanner and ImageJ software. The MSb_2 layers were dissolved in 10 mL of 1.0 M H_2SO_4(aq) for > 100 h, and samples from these solutions were diluted with water and analyzed with ICP-MS. The loading of the catalyst layer was determined using the concentration of M and Sb, the volume of 1.0 M H_2SO_4(aq), and the projected area of the MSb_2 layers. The dissolution of species from TMAs films under chlorine evolution conditions was determined by collecting 40 μL

samples of electrolyte from a cell operating at 100 mA cm^{-2} with an initial 5 mL volume of 4.0 M NaCl(aq), pH = 2 electrolyte in the anode compartment, and diluting these samples to 5 mL with 18.2 MΩ cm resistivity water. For $RuTiO_x$ samples, 1 mL of the electrolyte was collected from a 7 mL cell, and electrolyte was replenished after every sample was taken. The 1 mL samples were diluted to 10 mL with 18.2 MΩ cm resistivity water. The dissolution studies for $RuTiO_x$ could only be conducted for ~ 20 h, because the expected Ru dissolution product, RuO_4, is a volatile compound that escapes the anode compartment in conjunction with the evolved $Cl_2(g)$, resulting in an underestimate of the Ru dissolution rate.[33] ICP-MS measurements of Ru in the collected samples after 48 h of the initial measurements verified the volatility of the dissolved Ru. The amount of M and Sb lost was determined from the concentration, volume of the cell, and electrode area. The amount of M and Sb removed from the cell after each sample was collected was taken into account when determining the amount of metals lost over time during chronopotentiometry measurements.

3.6.7 Chlorine Faradaic Efficiency and Oxygen Evolution Reaction Activity

The faradaic efficiency towards chlorine evolution was determined using an established iodometric titration technique.[25, 34-35] A two-compartment cell separated by a Nafion N424 membrane and with an 8 mL anode compartment was used for this study. The anode compartment was completely filled with 4.0 M NaCl(aq), pH = 2 electrolyte. Electrodes consisting of $RuTiO_x$ or TMAs were operated at 100 mA cm^{-2} for 10 minutes. The electrolyte was transferred to a 25 mL Erlenmeyer flask containing 0.3 g of KI, and 0.2 mL of glacial acetic acid was added to the solution. The resulting yellow solution was titrated with 0.01 M

NaS_2O_3(aq) using a 10 mL burette, and starch solution was added near the endpoint. This titration method requires 2 mol of NaS_2O_3(aq) per mol of Cl_2(aq). The moles of Cl_2 expected was calculated using the charge passed during the galvanostatic measurement, Faraday's constant (F, 96485.3389 C mol^{-1}), and the electrons required to obtain Cl_2 (2 mol e^- per mol Cl_2). The faradaic efficiency was determined by comparing the moles of Cl_2(aq) detected to the moles of Cl_2 expected. Measurements were also collected for 4.0 M NaCl(aq), pH =2 electrolyte that had not been used for electrochemical measurements as a blank. At least three measurements were collected per electrode. In these experiments, some minor nucleation of bubbles on the epoxy used to encapsulate the electrodes and the Teflon adapter used seal the electrochemical cell was observed. Since only dissolved species are detected by the iodometric technique, the faradaic efficiency measurements represent a lower limit on the Faradaic efficiency of the electrocatalysts studied herein. The generation of Cl_2(aq) was also verified with colorimetric measurements using N,N-diethyl-p-phenylenediamine. The high activity towards chlorine evolution relative to oxygen evolution was also verified by collecting cyclic voltammograms of $RuTiO_x$ and TMAs in pH = 2 H_2SO_4(aq) electrolyte.

3.7 Supplementary Figures

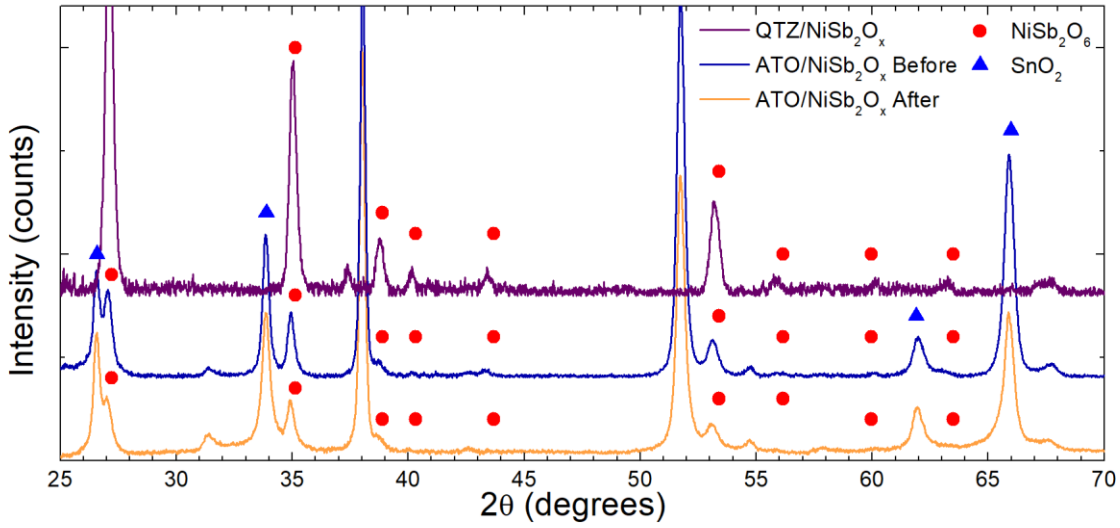

Figure S1. X-ray diffraction of as-synthesized $NiSb_2O_x$ films on quartz and ATO, and $NiSb_2O_x$ films after electrochemical operation in 4.0 M NaCl(aq), pH = 2.0 electrolyte at 100 mA cm^{-2} for 65 h.

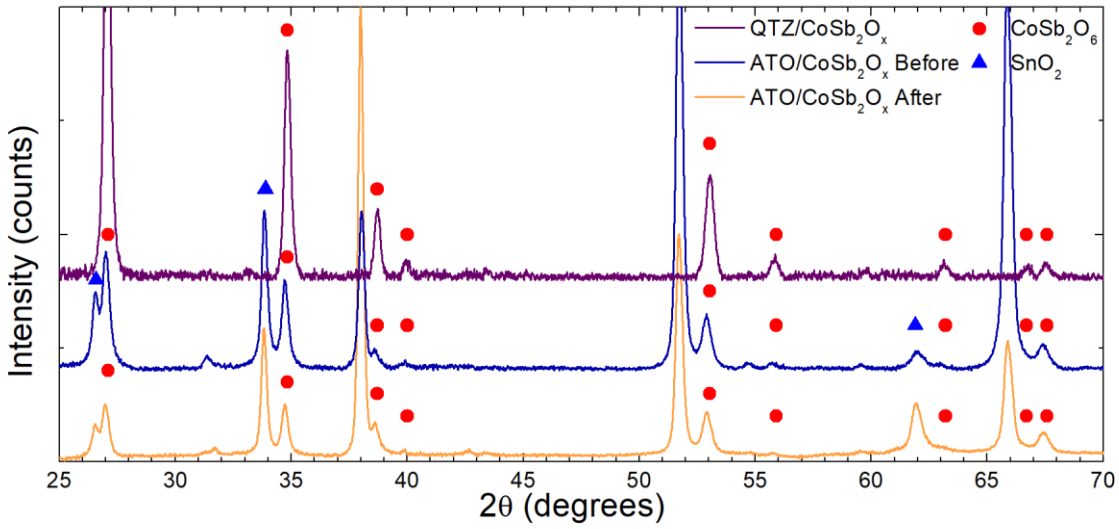

Figure S2. X-ray diffraction of as-synthesized $CoSb_2O_x$ films on quartz and ATO, and $CoSb_2O_x$ films after electrochemical operation in 4.0 M NaCl(aq), pH = 2.0 electrolyte at 100 mA cm^{-2} for 90 h.

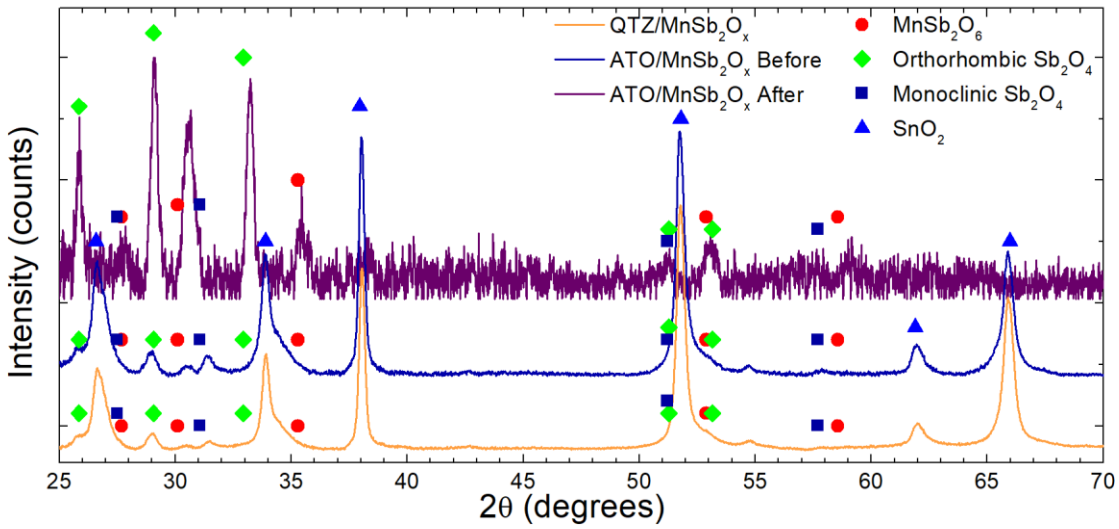

Figure S3. X-ray diffraction of as-synthesized $MnSb_2O_x$ films on quartz and ATO, and $MnSb_2O_x$ films after electrochemical operation in 4.0 M NaCl(aq), pH = 2.0 electrolyte at 100 mA cm^{-2} for 90 h.

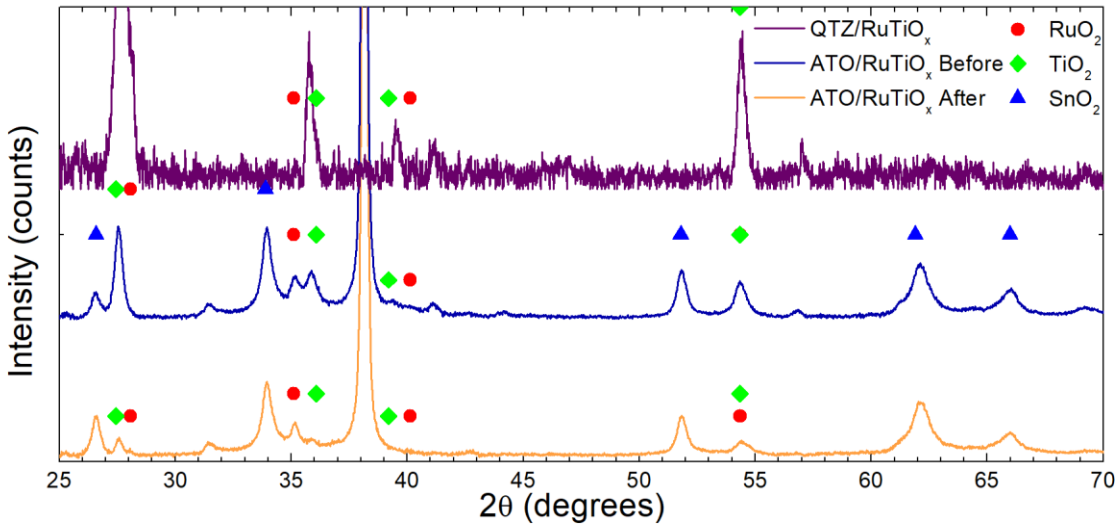

Figure S4. X-ray diffraction of as-synthesized $RuTiO_x$ films on ATO, and $RuTiO_x$ films after electrochemical operation in 4.0 M NaCl(aq), pH = 2.0 electrolyte at 100 mA cm^{-2} for 90 h.

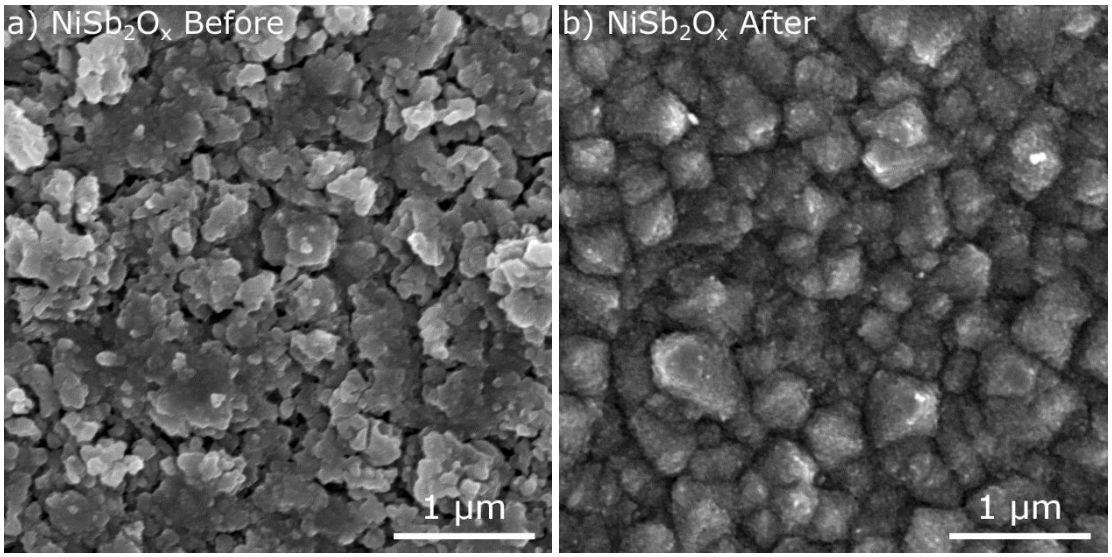

Figure S5. Scanning-electron microscope image of $NiSb_2O_x$: a) before operation, b) after 65 h at 100 mA cm^{-2} in 4.0 M NaCl(aq), pH = 2.0 electrolyte.

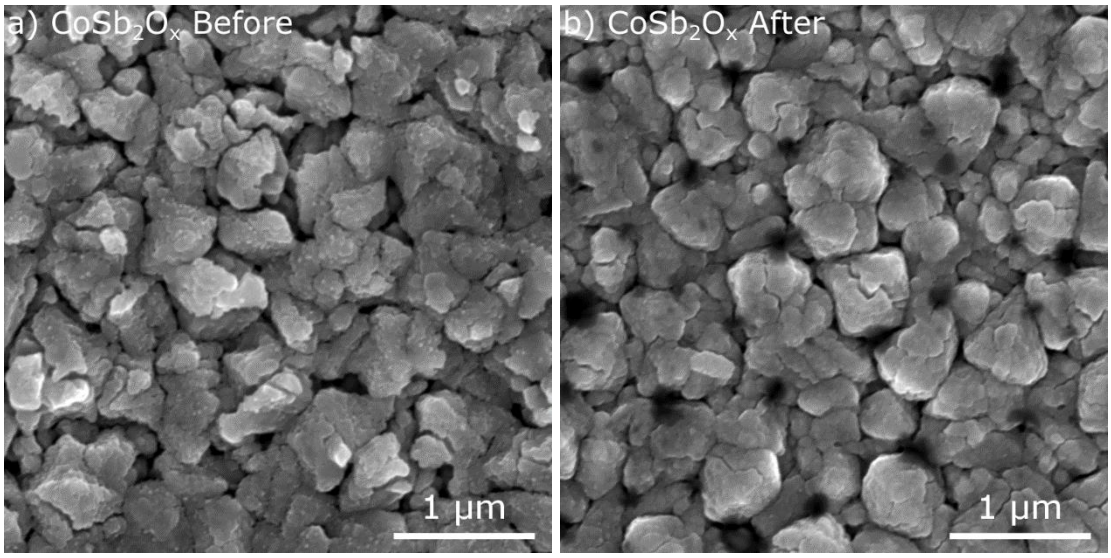

Figure S6. Scanning-electron microscope image of $CoSb_2O_x$: a) before operation, b) after 90 h at 100 mA cm^{-2} in 4.0 M NaCl(aq), pH = 2.0 electrolyte.

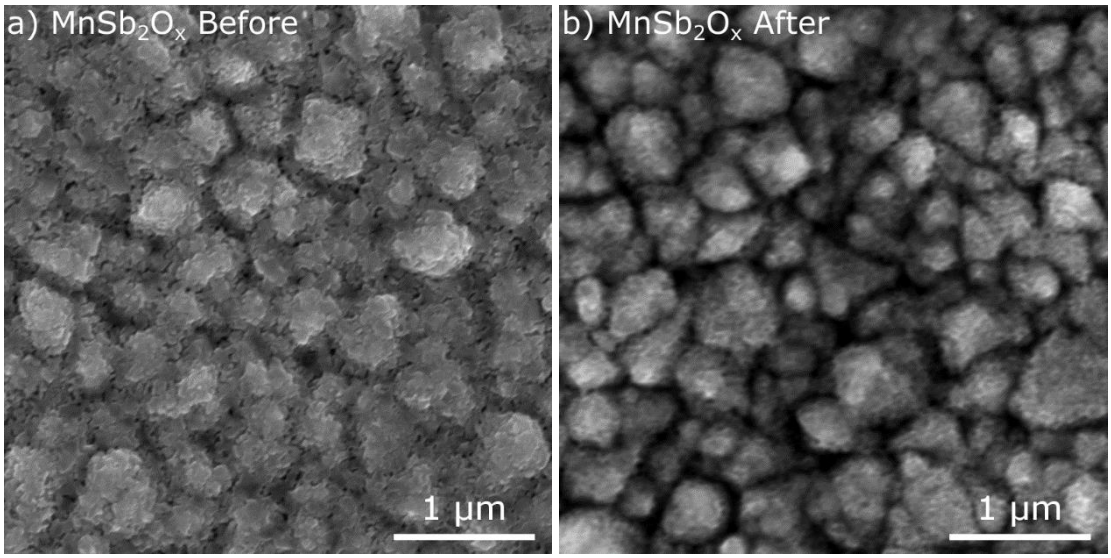

Figure S7. Scanning-electron microscope image of $MnSb_2O_x$: a) before operation, b) after 90 h at 100 mA cm^{-2} in 4.0 M NaCl(aq), pH = 2.0 electrolyte.

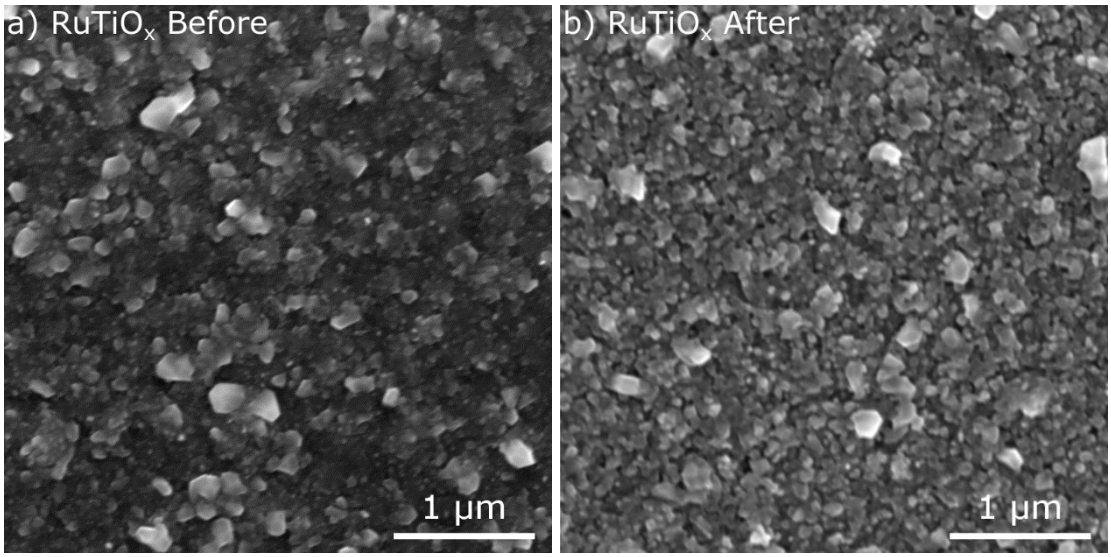

Figure S8. Scanning-electron microscope image of $RuTiO_x$: a) before operation, b) after 90 h at 100 mA cm^{-2} in 4.0 M NaCl(aq), pH = 2.0 electrolyte.

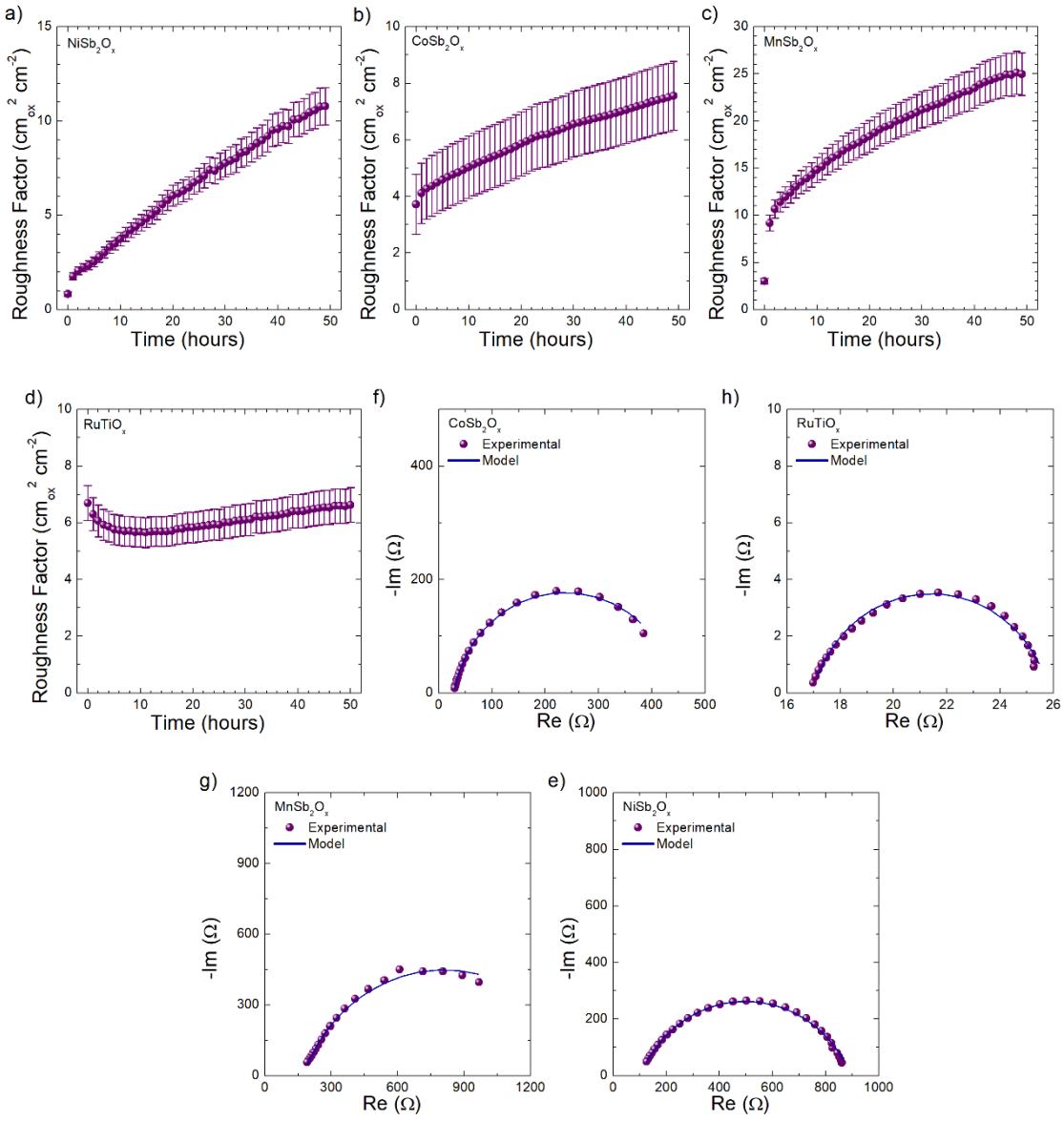

Figure S9. Roughness factor determined from impedance data collected at 1 h intervals between chronopotentiomery stability tests at 100 mA cm^{-2} for a) $NiSb_2O_x$, b) $CoSb_2O_x$, c) $MnSb_2O_x$, and d) $RuTiO_x$. Comparison between initial impedance data and impedance model fit for e) $NiSb_2O_x$, f) $CoSb_2O_x$, g) $MnSb_2O_x$, and h) $RuTiO_x$.

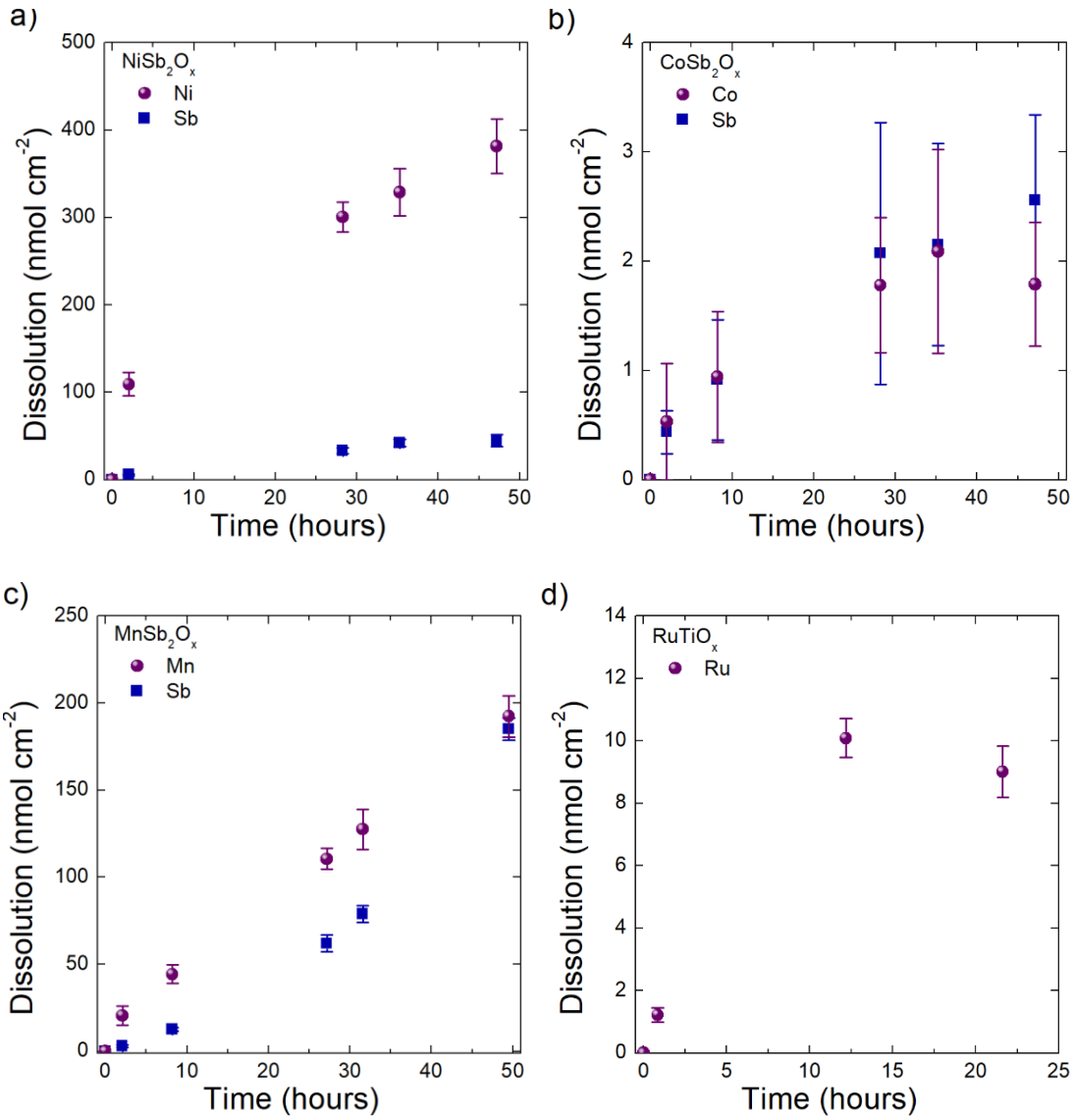

Figure S10. Amount of elements dissolved from MSb_2O_x and $RuTiO_x$ electrodes operated at 100 mA cm^{-2} in 4.0 M NaCl, pH = 2.0 electrolyte: a) $NiSb_2O_x$, b) $CoSb_2O_x$, c) $MnSb_2O_x$, d) $RuTiO_x$.

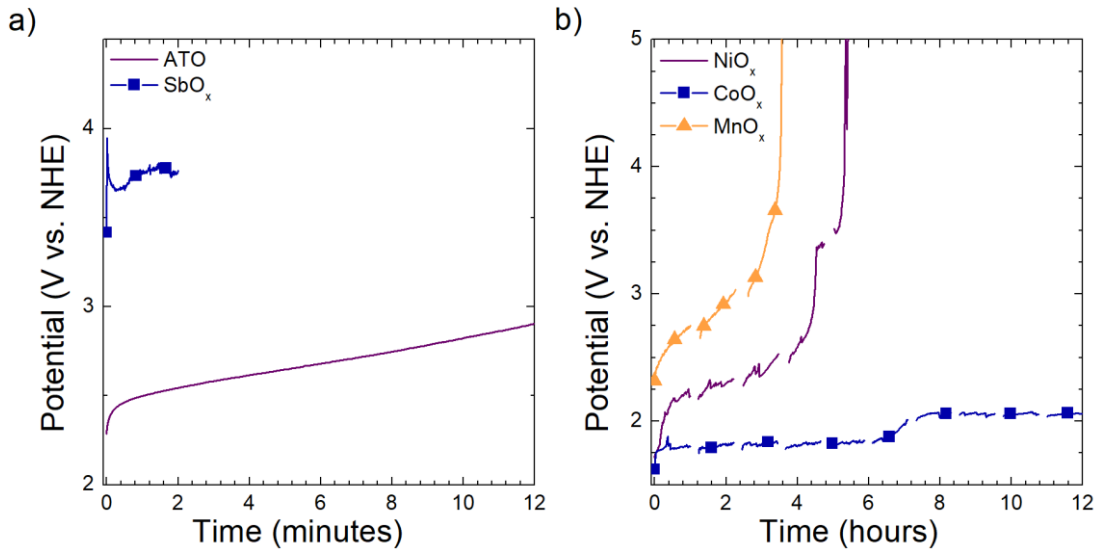

Figure S11. a) Chronopotentiometry of ATO and SbO_x at 100 mA cm^{-2}. b) Chronopotentiometry of NiO_x, CoO_x, and MnO_x at 100 mA cm^{-2}.

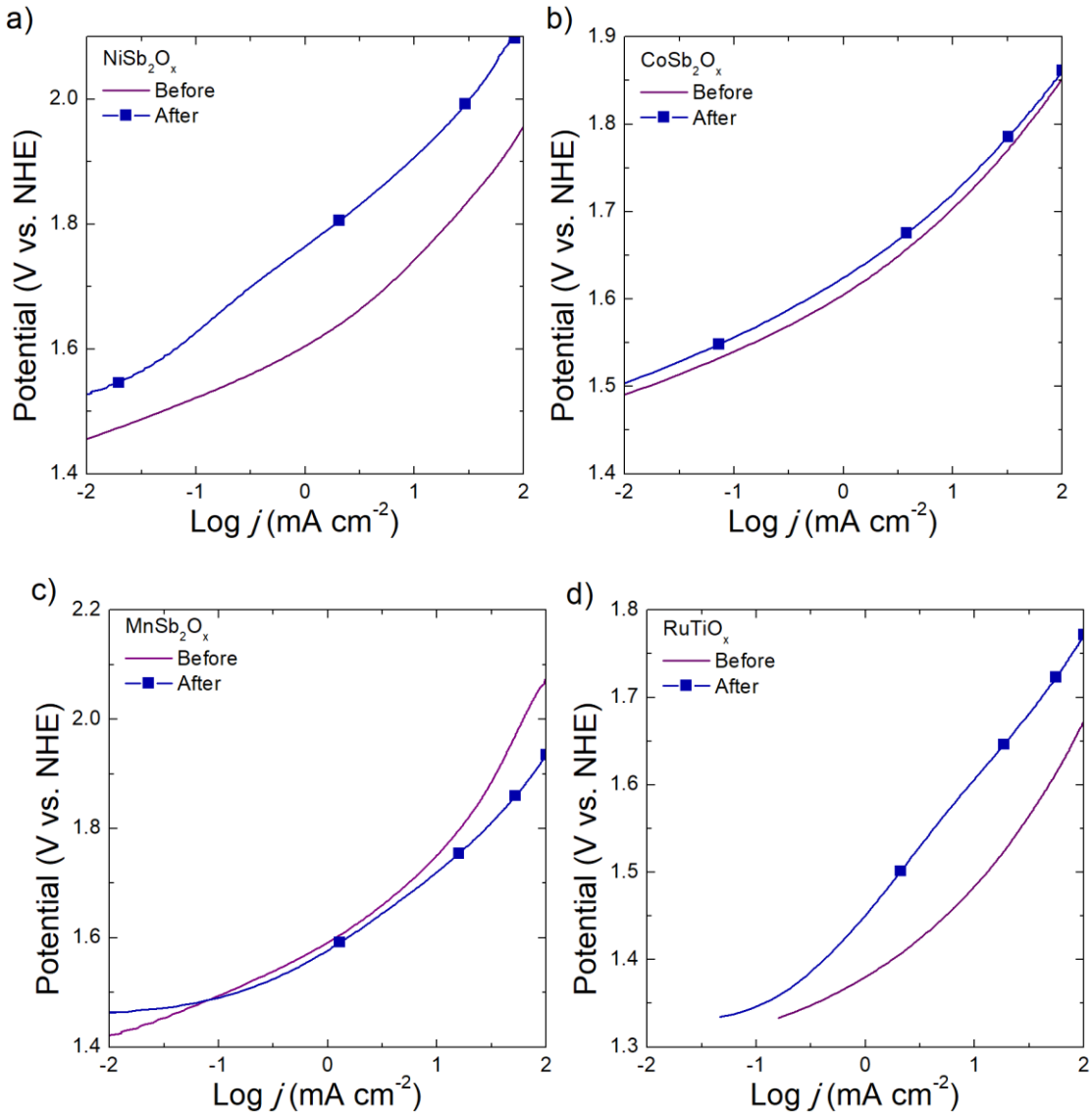

Figure S12. Tafel plots from 10^{-2} to 10^{2} mA cm^{-2} before and after 50 h at 100 mA cm^{-2} for a) $NiSb_2O_x$, b) $CoSb_2O_x$, c) $MnSb_2O_x$, d) $RuTiO_x$. The current-voltage data was collected from cyclic voltammograms.

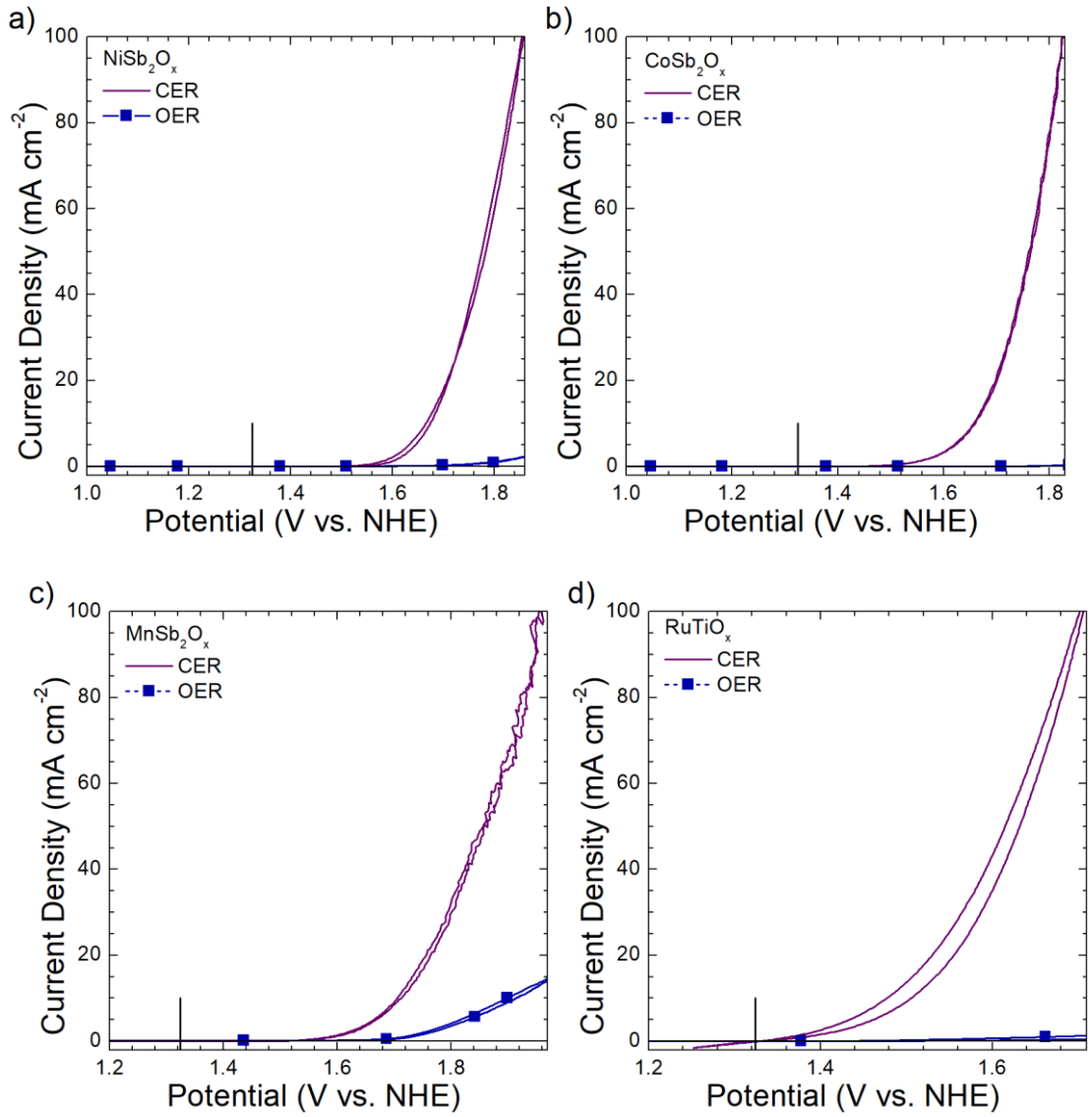

Figure S13. Cyclic voltammograms collected under chlorine evolution conditions [4.0 M NaCl(aq), pH = 2.0] and oxygen evolution conditions [pH = 2.0 H_2SO_4(aq)] for a) $NiSb_2O_x$, b) $CoSb_2O_x$, c) $MnSb_2O_x$, and d) $RuTiO_x$.

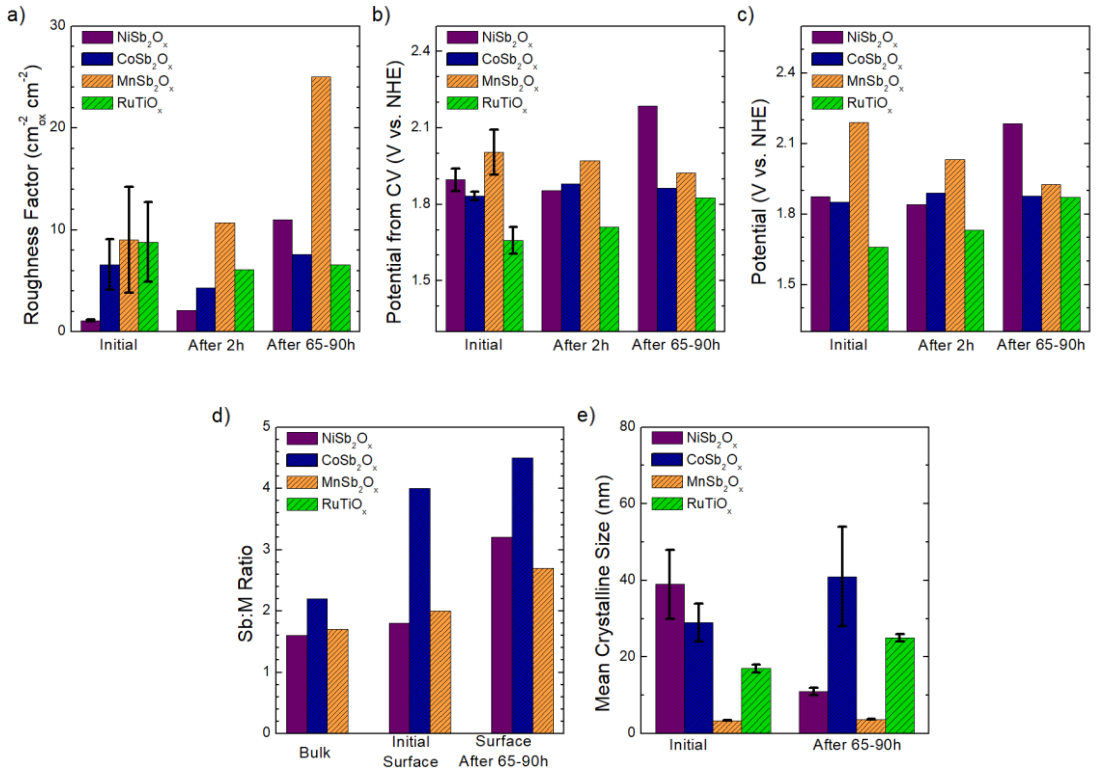

Figure S14. Summary of a) roughness factor, b) potential at 100 mA cm^{-2} from cyclic voltammetry, c) potential at 100 mA cm^{-2} from chronopotentiometry, d) bulk and surface composition, and e) mean crystalline size for $NiSb_2O_x$, $CoSb_2O_x$, $MnSb_2O_x$, and $RuTiO_x$. Final data is at 90 h for $CoSb_2O_x$, $MnSb_2O_x$, and $RuTiO_x$, and at 65 h for $NiSb_2O_x$.

Table S1. Catalyst loading of MSb_2O_x (M = Ni, Co, or Mn) films determined from ICP-MS measurements of MSb_2 films dissolved in 1.0 M H_2SO_4(aq).

Catalyst	M Loading (nmol cm^{-2})	Sb Loading (nmol cm^{-2})
$NiSb_2O_x$	483 ± 3	763 ± 5
$CoSb_2O_x$	375 ± 4	820 ± 5
$MnSb_2O_x$	417 ± 9	709 ± 8

Table S2. Potentials vs. NHE of MSb_2O_x films and $RuTiO_x$ determined from cyclic voltammetry data prior to galvanostatic operation at geometric current densities of 100 mA cm^{-2} in pH = 2.0, 4.0 M NaCl(aq). Roughness factors (RF) were determined from impedance data at 1.660 V vs. NHE. Faradaic efficiency (FE) towards the chlorine evolution reaction at a geometric current density of 100 mA cm^{-2} determined by iodometric titration. The faradaic efficiency experimental details such as the electrode areas, charge passed, amounts of Cl_2 expected, and amount of Cl_2 detected are included.

Catalyst	Potential at 100 mA cm^{-2} (V)	RF	FE Area (mm^{-2})	FE Charge Passed (C)	FE Cl_2 Expected (μmol)	FE Cl_2 Detected (μmol)	FE (%)
$NiSb_2O_x$	1.896 ± 0.045	1.1 ± 0.1	1.91	1.14	5.93	5.43, 5.83, 5.80	96.0 ± 3.7
$CoSb_2O_x$	1.833 ± 0.016	6.6 ± 2.5	3.49	2.09	10.8	10.3, 10.9, 10.5	97.4 ± 3.0
$MnSb_2O_x$	2.005 ± 0.088	9.0 ± 5.2	1.97	1.18	6.10	5.46, 5.47, 5.55	89.9 ± 0.8
$RuTiO_x$	1.659 ± 0.053	8.8 ± 3.9	11.76	7.05	36.5	35.0, 34.6, 34.3	94.8 ± 0.9

Table S3. Intrinsic Potential (E_i) vs. NHE at 1.0 mA cm^{-2} of ECSA and Tafel slope (b) of MSb_2O_x films and $RuTiO_x$ prior to and after 50 h of galvanostatic operation at 100 mA cm^{-2}. The Tafel slope was determined from a linear fit of a plot of η vs. $\log_{10}(J)$ between geometric current densities of 0.2 to 2.0 mA cm^{-2}. All Tafel slopes had an R-squared value greater than 0.99.

Catalyst	E_i at 0 h (V)	E_i at 50 h (V)	b at 0 h (mV dec^{-1})	b at 50 h (mV dec^{-1})
$NiSb_2O_x$	1.602 ± 0.018	1.911	94	131
$CoSb_2O_x$	1.652 ± 0.006	1.705	73	74
$MnSb_2O_x$	1.699 ± 0.036	1.789	110	110
$RuTiO_x$	1.460 ± 0.010	1.563	69	134

Table S4. Summary of XPS binding energies observed for MSb_2O_x samples before and after electrochemical operation and literature values for various M and Sb compounds.

Material	M $2p_{3/2}$ Binding Energy (eV)	Sb $3d_{5/2}$ Binding Energy (eV)	Reference
$NiSb_2O_x$ (before)	856.1 ± 0.1	540.4 ± 0.1	–
$NiSb_2O_x$ (after)	856.3 ± 0.1	540.5 ± 0.1	–
$CoSb_2O_x$ (before)	781.2 ± 0.1	540.6 ± 0.1	–
$CoSb_2O_x$ (after)	781.2 ± 0.1	540.3 ± 0.1	–
$MnSb_2O_x$ (before)	641.9 ± 0.1	540.2 ± 0.1	–
$MnSb_2O_x$ (after)	642.0 ± 0.1	540.3 ± 0.1	–
$NiCl_2$	856.77	–	[18]
$Ni(OH)_2$	855.80	–	[18]
$CoCl_2 \cdot (H_2O)_6$	782.1	–	[36]
$Co(OH)_2$	780.65	–	[20]
$MnCl_2$	642.0	–	[21]
Sb_2O_3	–	539.7	[19]
Sb_2O_4	–	540.3	[19]
Sb_2O_5	–	540.6	[19]

Table S5. Example of impedance data collected and ECSA determined for MSb_2O_x and $RuTiO_x$ films.

Catalyst	Area (cm^{-2})	R_s (Ω)	Q_0 $\mu F\ s^{(a-1)}$	a	R_{ct} (Ω)	C_{DL} (μF)	ECSA (cm^{-2})	RF
$NiSb_2O_x$	0.0179	110.2	6.87	0.714	343.3	0.341	0.0316	1.76
$CoSb_2O_x$	0.0282	29.29	2.87	0.912	396.6	1.15	0.1049	3.72
$MnSb_2O_x$	0.0179	153.1	21.0	0.704	1,522	1.81	0.1645	9.19
$RuTiO_x$	0.2030	16.91	49.9	0.871	8.790	14.9	1.355	6.67

3.8 References

1. Karlsson, R. K.; Cornell, A., Selectivity between Oxygen and Chlorine Evolution in the Chlor-Alkali and Chlorate Processes. *Chem. Rev.* **2016,** *116* (5), 2982-3028.
2. Hansen, H. A.; Man, I. C.; Studt, F.; Abild-Pedersen, F.; Bligaard, T.; Rossmeisl, J., Electrochemical chlorine evolution at rutile oxide (110) surfaces. *Phys. Chem. Chem. Phys.* **2010,** *12* (1), 283-90.
3. Exner, K. S.; Anton, J.; Jacob, T.; Over, H., Controlling selectivity in the chlorine evolution reaction over RuO_2-based catalysts. *Angew. Chem. Int. Ed.* **2014,** *53* (41), 11032-5.
4. Martinez-Huitle, C. A.; Ferro, S., Electrochemical oxidation of organic pollutants for the wastewater treatment: direct and indirect processes. *Chem. Soc. Rev.* **2006,** *35* (12), 1324-40.
5. Nanni, L.; Polizzi, S.; Benedetti, A.; Battisti, A. D., Morphology, Microstructure, and Electrocatalytic Properties of RuO_2-SnO_2 Thin Films. *J. Electrochem. Soc.* **1999,** *146* (1), 220-225.
6. Karlsson, R. K. B.; Hansen, H. A.; Bligaard, T.; Cornell, A.; Pettersson, L. G. M., Ti atoms in $Ru_{0.3}Ti_{0.7}O_2$ mixed oxides form active and selective sites for electrochemical chlorine evolution. *Electrochim. Acta* **2014,** *146*, 733-740.
7. Xiong, K.; Deng, Z.; Li, L.; Chen, S.; Xia, M.; Zhang, L.; Qi, X.; Ding, W.; Tan, S.; Wei, Z., Sn and Sb co-doped RuTi oxides supported on TiO_2 nanotubes anode for selectivity toward electrocatalytic chlorine evolution. *J. Appl. Electrochem.* **2013,** *43* (8), 847-854.

8. Menzel, N.; Ortel, E.; Mette, K.; Kraehnert, R.; Strasser, P., Dimensionally Stable Ru/Ir/TiO_2-Anodes with Tailored Mesoporosity for Efficient Electrochemical Chlorine Evolution. *ACS Catal.* **2013,** *3* (6), 1324-1333.
9. Cao, H.; Lu, D.; Lin, J.; Ye, Q.; Wu, J.; Zheng, G., Novel Sb-doped ruthenium oxide electrode with ordered nanotube structure and its electrocatalytic activity toward chlorine evolution. *Electrochim. Acta* **2013,** *91*, 234-239.
10. Trasatti, S., Electrocatalysis in the Anodic Evolution of Oxygen and Chlorine. *Electrochim. Acta* **1984,** *29* (11), 1503-1512.
11. Zeradjanin, A. R.; Menzel, N.; Schuhmann, W.; Strasser, P., On the faradaic selectivity and the role of surface inhomogeneity during the chlorine evolution reaction on ternary Ti-Ru-Ir mixed metal oxide electrocatalysts. *Phys. Chem. Chem. Phys.* **2014,** *16* (27), 13741-7.
12. Loucka, T., The potential-pH diagram for the Ru-H_2O-Cl^- system at 25° C. *J. Appl. Electrochem.* **1990,** *20*, 522-523.
13. Beer, H. B., Method of Making an Electrode Having a Coating Containing a Platinum Metal Oxide Thereon. *U.S. Patent 4052271* **1977**.
14. Moreno-Hernandez, I. A.; MacFarland, C. A.; Read, C. G.; Papadantonakis, K. M.; Brunschwig, B. S.; Lewis, N. S., Crystalline nickel manganese antimonate as a stable water-oxidation catalyst in aqueous 1.0 M H_2SO_4. *Energy Environ. Sci.* **2017,** *10* (10), 2103-2108.
15. Jain, A.; Ong, S. P.; Hautier, G.; Chen, W.; Richards, W. D.; Dacek, S.; Cholia, S.; Gunter, D.; Skinner, D.; Ceder, G.; Persson, K. A., Commentary: The Materials

Project: A materials genome approach to accelerating materials innovation. *APL Mater.* **2013,** *1* (1), 011002.

16. Bisht, H.; Eun, H.-T.; Mehrtens, A.; Aegerter, M. A., Comparison of spray pyrolyzed FTO, ATO and ITO coatings for flat and bent glass substrates. *Thin Solid Films* **1999,** *351*, 109-114.
17. Westin, G.; Nygren, M., Sol-Gel Preparation of M-Sb Oxides from Sb $(OBu'')_3$-M-Acetate Precursors with M = Mn, Co, Ni. *J. Mater. Chem.* **1993,** *3* (4), 367-371.
18. Biesinger, M. C.; Lau, L. W.; Gerson, A. R.; Smart, R. S., The role of the Auger parameter in XPS studies of nickel metal, halides and oxides. *Phys. Chem. Chem. Phys.* **2012,** *14* (7), 2434-42.
19. Izquierdo, R.; Sacher, E.; Yelon, A., X-Ray Photoelectron Spectra of Antimony Oxides. *Appl. Surf. Sci.* **1989,** *40*, 175-177.
20. Biesinger, M. C.; Payne, B. P.; Grosvenor, A. P.; Lau, L. W. M.; Gerson, A. R.; Smart, R. S. C., Resolving surface chemical states in XPS analysis of first row transition metals, oxides and hydroxides: Cr, Mn, Fe, Co and Ni. *Appl. Surf. Sci.* **2011,** *257* (7), 2717-2730.
21. Aoki, A., X-Ray Photoelectron Spectroscopic Studies on ZnS: MnF_2 Phosphors. *Jpn. J. Appl. Phys* **1976,** *15* (2), 305-311.
22. Straguzzi, G. I.; Bischoff, K. B.; Koch, T. A.; Schuit, G. C. A., Selective Oxidation Catalysts Containing Antimony for the Conversion of I-Butene to Butadiene. *J. Catal.* **1987,** *103*, 357-365.

23. Biesinger, M. C.; Payne, B. P.; Lau, L. W. M.; Gerson, A.; Smart, R. S. C., X-ray photoelectron spectroscopic chemical state quantification of mixed nickel metal, oxide and hydroxide systems. *Surf. Interface Anal.* **2009,** *41* (4), 324-332.

24. Zhu, X.; Wang, P.; Wang, Z.; Liu, Y.; Zheng, Z.; Zhang, Q.; Zhang, X.; Dai, Y.; Whangbo, M.; Huang, B., Co_3O_4 nanobelt arrays assembled with ultrathin nanosheets as high efficient and stable electrocatalyst for chlorine evolution reaction. *J. Mater. Chem. A* **2018,** *6*, 12718-12723.

25. Jiang, M.; Wang, H.; Li, Y.; Zhang, H.; Zhang, G.; Lu, Z.; Sun, X.; Jiang, L., Superaerophobic RuO_2 -Based Nanostructured Electrode for High-Performance Chlorine Evolution Reaction. *Small* **2017,** *13* (4).

26. Cho, K.; Hoffmann, M. R., $Bi_xTi_{1-x}O_z$ Functionalized Heterojunction Anode with an Enhanced Reactive Chlorine Generation Efficiency in Dilute Aqueous Solutions. *Chem. Mater.* **2015,** *27* (6), 2224-2233.

27. Vesborg, P. C. K.; Jaramillo, T. F., Addressing the terawatt challenge: scalability in the supply of chemical elements for renewable energy. *RSC Adv.* **2012,** *2* (21), 7933.

28. Aghaee, E. M.; Alimohammadi, M.; Nabizadeh, R.; khaniki, G. J.; Naseri, S.; Mahvi, A. H.; Yaghmaeian, K.; Aslani, H.; Nazmara, S.; Mahmoudi, B.; Ghani, M., Effects of storage time and temperature on the antimony and some trace element release from polyethylene terephthalate (PET) into the bottled drinking water. *J. Environ. Health Sci. Eng.* **2014,** *12*, 133.

29. Grazulis, S.; Chateigner, D.; Downs, R. T.; Yokochi, A. F.; Quiros, M.; Lutterotti, L.; Manakova, E.; Butkus, J.; Moeck, P.; Le Bail, A., Crystallography Open Database - an

open-access collection of crystal structures. *J. Appl. Crystallogr.* **2009,** *42* (Pt 4), 726-729.

30. Donaldson, J. D.; Kjekshus, A.; Nicholson, D. G.; Rakke, T., Properties of Sb-compounds with Rutile-like Structures. *Acta Chem. Scand. A* **1975,** *29*, 803-809.
31. Partanen, J. I.; Covington, A. K., Re-Evaluation of the Thermodynamic Activity Quantities in Aqueous Sodium and Potassium Chloride Solutions at 25 °C. *J. Chem. Eng. Data* **2009,** *54*, 208-219.
32. McCrory, C. C.; Jung, S.; Peters, J. C.; Jaramillo, T. F., Benchmarking heterogeneous electrocatalysts for the oxygen evolution reaction. *J. Am. Chem. Soc.* **2013,** *135* (45), 16977-87.
33. Wohlfhart-Mehrens, M.; Heitbaum, J., Oxygen Evolution on Ru and RuO_2 Electrodes Studied Using Isotope Labelling and On-Line Mass Spectrometry. *J. Electroanal. Chem.* **1987,** *237*, 251-260.
34. 4500-Cl Chlorine (Residual) (2017). In *Standard Methods For the Examination of Water and Wastewater*.
35. Finke, C. E.; Omelchenko, S. T.; Jasper, J. T.; Lichterman, M. F.; Read, C. G.; Lewis, N. S.; Hoffmann, M. R., Enhancing the activity of oxygen-evolution and chlorine-evolution electrocatalysts by atomic layer deposition of TiO_2. *Energy Environ. Sci.* **2019,** *12* (1), 358-365.
36. Brown, D. G.; Weser, U., XPS Spectra of Spin-Triplet Cobalt(III) Complexes. *Z. Naturforsch. (B)* **1979,** *34*, 1468-1470.

CHAPTER IV

TIN OXIDE PROTECTIVE HETEROJUNCTIONS FOR SILICON PHOTOANODES

Moreno-Hernandez, I. A.; Brunschwig, B. S.; Lewis, N. S., Tin Oxide as a Protective Heterojunction with Silicon for Efficient Photoelectrochemical Water Oxidation in Strongly Acidic or Alkaline Electrolytes. *Adv. Energy Mater.* **2018,** *8* (24), 1801155. DOI: 10.1002/aenm.201801155

4.1 Introduction

In conjunction with a fuel-forming cathodic reaction, the oxidation of water to O_2(g) is a key component in the production of sustainable fuels by photoelectrosynthetic cells.[1] Protective coatings that prevent physical contact between the electrolyte and the semiconductor can stabilize semiconductor photoanodes against passivation or corrosion.[2-6] Buried p-n junctions in a photovoltaic-electrochemical type photoelectrochemical cell can yield photovoltages close to the theoretical bulk-recombination limit,[7] but high quality p-n junctions cannot readily be formed on many semiconductor photoanode materials. Moreover, the protective coatings must form a low resistance electrical contact to the electrocatalysts needed for the multi-electron oxidation of water to O_2(g).

Semiconductors have been protected and operated as photoanodes for water oxidation by formation of Schottky barriers, metal-insulator-semiconductor contacts, or mixed barriers between semiconductors and metals/oxides/liquids.[8-14] When a < 2 nm thick

interfacial SiO_x layer is formed on the Si substrate, heterojunctions formed between n-type silicon (n-Si) and metal oxides provide efficient photoelectrochemical devices if the heterojunctions are protected with materials such as TiO_2, CoO_x, or MnO_x.[7, 9, 15] The SiO_x electrically passivates the underlying Si and allows a high tunnel current. The SiO_x layer can be formed either incidentally during the deposition of the metal oxide or intentionally by various oxidation methods.[16] Such protected photoanodes are of limited utility for water oxidation in acidic electrolytes, due to the Pourbaix instability of metal oxides such as MnO_x and CoO_x in acidic media, as well as the non-ohmic contact between the protection layers and water oxidation catalysts, as exemplified by the rectifying behavior observed between amorphous TiO_2 and Ir/IrO_x.[15]

Tin oxides have been previously used as protective layers for photocathodes and photoanodes in corrosive environments.[8, 14, 17-18] Previous studies involving tin oxide protective layers have relied on semiconductor p-n junctions to obtain high photovoltages or have been severely limited in efficiency by slow charge transfer to water oxidation catalysts. Moreover, the stability of photoanodes in acid with stable photocurrents has been limited to 60 h of operation.[3, 12] Without a p-n junction, protected n-Si photoanodes have exhibited ideal regenerative solar-to-O_2(g) efficiencies < 2.3% in alkaline electrolytes and < 2.6% in acidic electrolytes under 100 mW cm^{-2} of simulated solar illumination.[19-20] Herein we report that n-Si photoanodes that have been chemically oxidized prior to deposition of a protective SnO_x layer form a semiconductor-insulator-semiconductor n-$Si/SiO_x/SnO_x$ heterojunction that exhibits a photovoltage of 620 ± 3 mV, and moreover forms low resistance, ohmic contacts to a variety of metal electrocatalysts. These properties allow the construction of silicon photoanodes with ideal regenerative solar-to-O_2(g)

efficiencies of 4.1% in 1.0 M KOH(aq) and 3.7% in 1.0 M H_2SO_4(aq), respectively. Further, silicon photoanodes with a protective SnO_x layer coating and a patterned catalyst layer can effect the efficient photoanodic oxidation of water to O_2(g) in either alkaline or acidic aqueous electrolytes for over 100 h of operation.

4.2 Results

Prior to deposition of a SnO_x layer, Si wafers were etched in buffered HF(aq), and a Si oxide layer (SiO_x) was grown by placing the wafers in H_2O_2/HCl(aq) for 10 min (details provided in Experimental Section). The SnO_x coatings were deposited on the chemically oxidized Si substrates via a spray-deposition process. The SnO_x films contained rutile SnO_2, with an average crystalline size of 3 nm (Figure S1), as indicated by X-ray diffraction. High-resolution transmission-electron microscope (HRTEM) images of the n-Si/SiO_x/SnO_x interface indicated the presence of a 1.5 ± 0.2 nm thick SiO_x layer between the SnO_x and n-Si layers **(Figure 1a)**. Nanocrystals of SnO_2 were detected near the SiO_x layer (Figure 1a). The SnO_x film thickness varied between 90 and 130 nm, with an average thickness of 113 ± 10 nm (Figure 1b), as revealed by transmission-electron microscopy. Dark-field imaging indicated that the crystallite size increased near the surface of the SnO_x film (Figure S2). Scanning-electron microscopy revealed closely packed 50–200 nm diameter polycrystalline grains that covered the n-Si/SiO_x/SnO_x surface (Figure S2c).

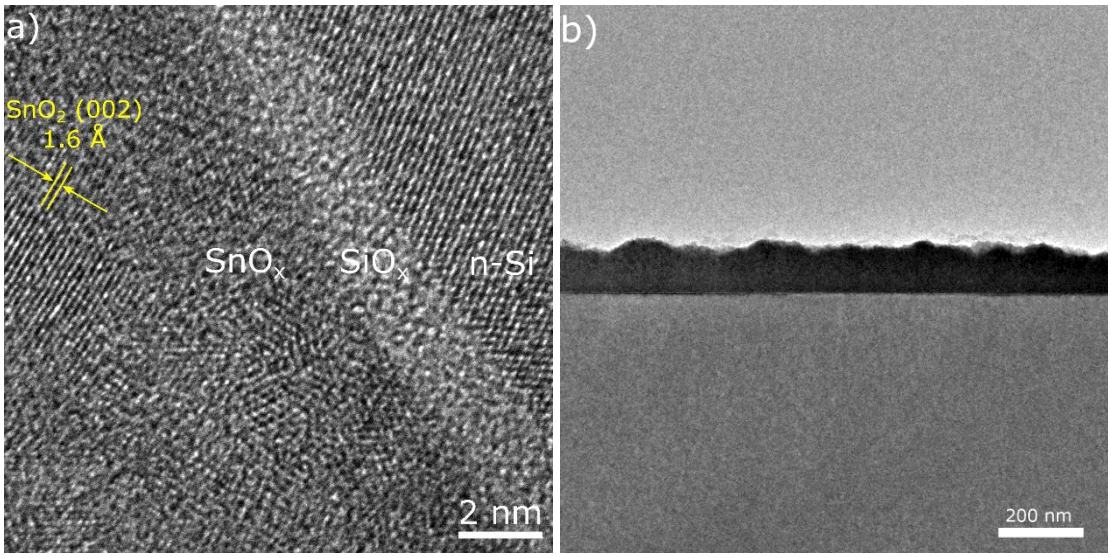

Figure 1. Structural characterization of n-Si/SiO_x/SnO_x heterojunction. (a) High-resolution transmission-electron microscopy image of representative n-Si/SiO_x/SnO_x interface. The interfacial SiO_x layer had a thickness of 1.5 ± 2 nm. (b) Transmission-electron microscopy image of n-Si/SiO_x/SnO_x film.

UV-Vis spectroscopy measurements indicated that the SnO_x film had a direct band gap of 4.2 eV (**Figure 2a**). X-ray photoelectron spectroscopy measurements indicated that the Fermi level at the SnO_x surface was ≥ 4.7 ± 0.1 eV below the vacuum level, and the valence-band edge at the SnO_x surface was 3.2 ± 0.1 eV below the Fermi level. A weak defect band centered at the Fermi level (Figure 2b, 2c) with a FWHH of ~ 0.8 eV was observed.

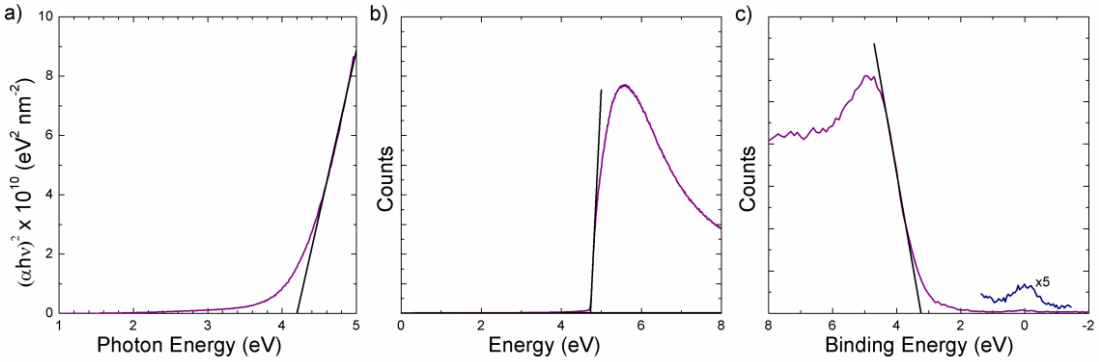

Figure 2. (a) Direct band-gap determination of SnO_x on a quartz slide from UV-Vis spectroscopy using the Tauc plot method. (b) Determination of the Fermi level of SnO_x from the secondary-electron energy cut-off collected with an XPS from an n-Si/SiO_x/SnO_x sample under bias. (c) Valence-band spectrum of n-Si/SiO_x/SnO_x relative to the Fermi level, and higher-resolution spectrum near the Fermi level, indicating the presence of defect states.

The photoelectrochemical current density vs potential (*J*-*E*) behavior of the n-Si/SiO_x/SnO_x structure was evaluated using a reversible, one-electron redox couple (0.35 M $K_4Fe(CN)_6$/0.050 M $K_3Fe(CN)_6$ in 0.50 M KCl(aq)) (Table S1). For n-Si/SiO_x/SnO_x photoanodes coated with 2 nm Pt, under 100 mW cm^{-2} of simulated solar illumination, a maximum photovoltage of 595 ± 1 mV was observed for n-Si wafers with a resistivity of 0.45 Ω-cm when SnO_x deposition was performed using substrate temperatures of 375–400 °C (Table 1, Figure S3a, S3b). When the deposition temperature was 400 °C, a maximal barrier height of 1.00 ± 0.02 eV was observed for the n-Si/SiO_x/SnO_x/Pt photoanodes (Figure S3c). Photoanodes that did not contain a chemically formed SiO_x layer exhibited a photovoltage that was ~ 65 mV lower than that of the n-Si/SiO_x/SnO_x heterojunctions at a photocurrent density of 30 mA cm^{-2} (Figure 3a). The n-Si/SiO_x/SnO_x

photoanodes prepared at 400 °C without a metal film and with less resistive Si (0.21 Ω-cm) exhibited photovoltages of 620 ± 3 mV under these test conditions, and n-Si/SiO_x/SnO_x photoanodes coated with 2 nm Ni, 1 nm Ir, or 1 nm Pt metal films exhibited photovoltages between 600 and 615 mV (Figure 3b). The barrier height measured by Mott-Schottky analysis of n-Si/SiO_x/SnO_x electrodes prepared with 0.21 Ω-cm Si was 1.07 ± 0.02 eV, whereas n-Si/SiO_x/SnO_x electrodes coated with Ni, Ir, and Pt had barrier heights of 1.03 ± 0.04 eV, 0.99 ± 0.01 eV, and 1.02 ± 0.03 eV, respectively (Figure 3c). Between 20 and 60 mA cm^{-2} of short-circuit current density, the n-Si/SiO_x/SnO_x/Pt photoanodes exhibited a diode quality factor, n ~ 1.19, and an extrapolated diode saturation current density, J_o, of 3.47×10^{-11} A cm^{-2}, whereas at short-circuit current densities of < 3 mA cm^{-2}, these photoanodes exhibited an n of ~3.26 and an extrapolated J_o of 7.40×10^{-6} A cm^{-2} (Figure S4a). The metal layers improved the charge-transfer kinetics of the $Fe(CN)_6^{3-/4-}$ redox reactions, with diffusion-limited anodic current densities of > 100 mA cm^{-2} observed for p^+-Si/SiO_x/SnO_x electrodes coated with Ni, Ir, or Pt metal films (Figure S4b). The results are consistent with the improved fill factor observed for metallized n-Si photoanodes (Figure 3b), indicating that metallization improves the charge-transfer kinetics at the SnO_x surface. Impedance measurements indicated that p^+-Si/SiO_x/SnO_x electrodes exhibited n-type behavior in contact with $Fe(CN)_6^{3-/4-}$ with V_{bi} = 0.17 V and N_d = 3.3×10^{17} cm^{-3}, whereas metallized p^+-Si/SiO_x/SnO_x electrodes exhibited highly doped p-type behavior consistent with expectations for a p^+-Si substrate (Figure S4c).

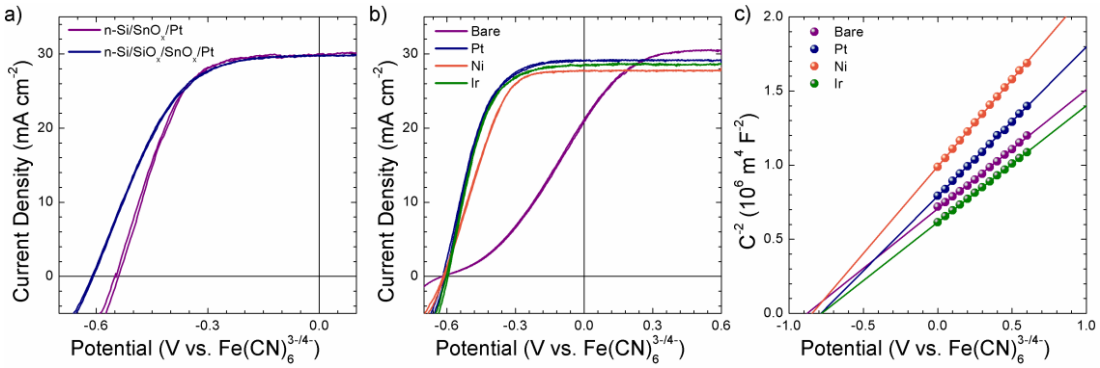

Figure 3. *J-E* behavior of n-Si photoelectrodes in contact with a one-electron $Fe(CN)_6^{3-/4-}$ redox couple in 0.50 M KCl(aq). (a) *J-E* behavior of n-Si and n-Si/SiO_x electrodes coated with SnO_x at a deposition temperature of 400 °C and metallized with ~ 2 nm Pt under simulated solar illumination adjusted to obtain 30 mA cm^{-2} of photocurrent density. (b) *J-E* behavior of n-Si/SiO_x/SnO_x electrodes prepared at 400 °C with 0.21 Ω-cm Si and metallized with 2 nm Ni, 1 nm Ir, or 1 nm Pt under 100 mW cm^{-2} of simulated solar illumination. (c) Representative C_d^{-2} vs *E* plot for n-Si/SiO_x/SnO_x electrodes metallized with 2 nm Ni, 1 nm Ir, or 1 nm Pt in the dark.

The photoelectrochemical oxygen-evolution *J-E* behavior of optimized n-Si/SiO_x/SnO_x heterojunctions with a 1–2 nm film of Ni, Ir, or Pt catalysts was evaluated under 100 mW cm^{-2} of simulated sunlight in 1.0 M KOH(aq) for Ni films and in 1.0 M H_2SO_4(aq) for Ir and Pt films (Table S2). In 1.0 M KOH(aq), photoanodes with Ni films exhibited an increase in catalytic activity that stabilized after ten *J-E* scans, consistent with the incorporation of Fe from the electrolyte into the oxy-hydroxide catalytic layer.[21] The n-Si/SiO_x/SnO_x/Ni photoanodes exhibited a photocurrent density of 30.8 mA cm^{-2} at the formal potential for the OER (1.229 V vs. the reversible hydrogen electrode, RHE) and a

light-limited photocurrent density of 31.5 mA cm^{-2} at potentials, E > 1.32 V vs. RHE **(Figure 4a)**.

External quantum yield (Φ_{ext}) measurements of n-Si/SiO_x/SnO_x/Ni photoanodes in contact with 1.0 M KOH(aq) indicated Φ_{ext} > 0.8 in the 570 to 930 nm wavelength range, with an expected photocurrent density of 31.8 mA cm^{-2} for excitation with 100 mW cm^{-2} of an Air Mass (AM) 1.5G spectrum (Figure 4b). UV-Vis spectroscopy measurements indicated that the SnO_x had an average transmittance of 88% in the 570–930 nm wavelength range (Figure 2a), with additional losses expected due to the optical properties of the water oxidation catalysts.[22] Compared to a Si wafer coated with a 1.5 nm SiO_x layer, which had an average reflective of 40% (570-930 nm), the SnO_x film acted as an anti-reflection layer and reduced the optical reflection at normal incidence at all wavelengths in the range of 300 –1300 nm (Figure S5).

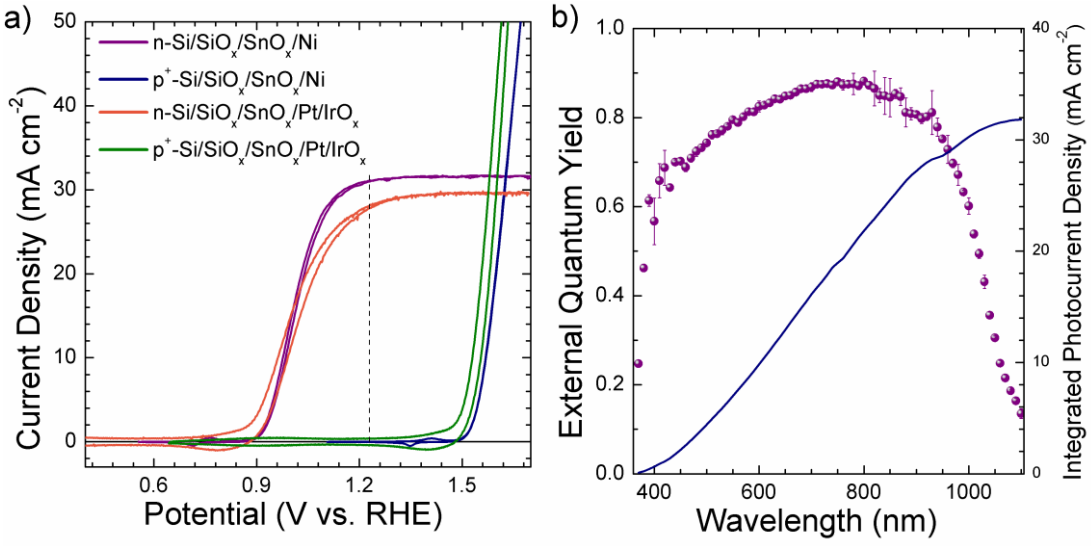

Figure 4. (a) *J-E* behavior of n-Si/SiO_x/SnO_x and p^+-Si/SiO_x/SnO_x junctions under water oxidation conditions in 1.0 M KOH(aq) (Ni catalyst films) and 1.0 M H_2SO_4(aq) (Pt/IrO_x catalyst films) under 100 mW cm^{-2} of simulated solar illumination and in the dark,

respectively. (b) Wavelength-dependent external quantum yield (purple points) of an n-Si/SiO_x/SnO_x heterojunction with 2 nm Ni and Pt in 1.0 M KOH(aq), held at 2.0 V vs RHE and cumulative photocurrent density obtained from integrating the product of the external quantum yield with the spectral photon flux of the AM 1.5G solar spectrum.

The overpotential (η) for the oxygen-evolution reaction (OER) at 1 mA cm^{-2} was compared for n-Si/SiO_x/SnO_x/M under 100 mW cm^{-2} of simulated sunlight and p^+-Si/SiO_x/SnO_x/M in the dark. For an illuminated n-Si/SiO_x/SnO_x/Ni electrode, η was -318 mV, whereas similarly coated p^+-Si/SiO_x/SnO_x/Ni electrodes exhibited η = +287 mV in the dark, indicating a -605 mV voltage shift for the n-Si/SiO_x/SnO_x heterojunction towards the OER in 1.0 M KOH(aq) (Figure 4a). At 1 mA cm^{-2} in 1.0 M H_2SO_4(aq), the n-Si/SiO_x/SnO_x/Ir photoanodes exhibited η = -187 mV, whereas similarly coated p^+-Si/SiO_x/SnO_x/Ir electrodes exhibited η = +400 mV (Figure S6a). n-Si/SiO_x/SnO_x/Pt electrodes with 1 nm Pt were subsequently coated by a photoelectrochemical procedure with IrO_x (details in Experimental Section), and exhibited η = -322 mV at 1 mA cm^{-2}. Analogous p^+-Si/SiO_x/SnO_x/Pt/IrO_x electrodes exhibited η = +272 mV, indicating a -594 mV photovoltage produced by the n-Si/SiO_x/SnO_x heterojunction towards the OER in 1.0 M H_2SO_4(aq) (Figure 4a). In the absence of an IrO_x film, n-Si/SiO_x/SnO_x/Pt photoanodes exhibited η = +58 mV, and p^+-Si/SiO_x/SnO_x/Pt electrodes exhibited η = +719 mV at 1 mA cm^{-2} in 1.0 M H_2SO_4(aq) (Figure S6a).

In 1.0 M KOH(aq), the n-Si/SiO_x/SnO_x/Ni 2 nm photoanodes produced stable photocurrents at 1.51 V vs RHE for > 25 h under 100 mW cm^{-2} of simulated solar illumination (Figure S6b) and retained their efficiency for > 20 h of continuous operation

(Figure S6d). In 1.0 M H_2SO_4(aq) under 100 mW cm^{-2} of simulated solar illumination, n-Si/SiO_x/SnO_x photoanodes with 1 nm film of Pt showed stable photocurrents for < 2 h (Figure S6b, S6c) while photoanodes with Pt/IrO_x or Ir were stable for <2 min. The n-Si/SiO_x/SnO_x electrodes with films of Ir, Pt, or Pt/IrO_x had high overpotentials for the water oxidation reaction after extended electrochemical operation (Figure S6d). SEM images indicated that the SnO_x films remained on the surface after electrochemical operation (Figure S7).

Figure 5a shows high-resolution Ni 2p x-ray photoelectron spectroscopy (XPS) data for n-Si/SiO_x/SnO_x electrodes coated with 2 nm Ni, with the data collected before and after electrochemical operation in 1.0 M KOH(aq). The Ni 2p peaks indicated the presence of a mixture of Ni metal, NiO, and $Ni(OH)_2$ with a composition of 9, 38, and 53%, respectively, before electrochemical operation, and > 96% $Ni(OH)_2$ after electrochemical operation (Figure 5a). The initial NiO and $Ni(OH)_2$ components can be attributed to oxidation and hydration of the Ni film during exposure to the atmosphere during electrode preparation. The decrease in Ni metal after electrochemical operation is consistent with the conversion of Ni to $Ni(OH)_2$/NiOOH under anodic conditions.

Figure 5b shows high-resolution Ir 4f XPS data for n-Si/SiO_x/SnO_x/Ir photoanodes before and after photoelectrochemical operation in 1.0 M H_2SO_4(aq). The Ir 4f peaks indicated the presence of a mixture of Ir metal (Ir $4f_{7/2}$ B.E. = 61.4 ± 0.1 eV) and IrO_x (Ir $4f_{7/2}$ B.E. = 62.5 ± 0.1 eV). The Ir film was 7 ± 1 % IrO_x before and 96 ± 2 % IrO_x after photoelectrochemical operation, indicating substantial conversion to IrO_x under these conditions. The Pt 4f peaks (Figure S8a) of n-Si/SiO_x/SnO_x/Pt photoanodes indicated the presence of a mixture of Pt metal (Pt $4f_{7/2}$ B.E. = 71.4 ± 0.1 eV), PtO (Pt $4f_{7/2}$ B.E. = 73.3

± 0.1 eV), and PtO_2 (Pt $4f_{7/2}$ B.E. = 75.5 ± 0.1 eV). The composition of the Pt film was 100% Pt before and 22% PtO and 78% PtO_2 after photoelectrochemical operation, indicating conversion of Pt to PtO/PtO_2 under anodic conditions.

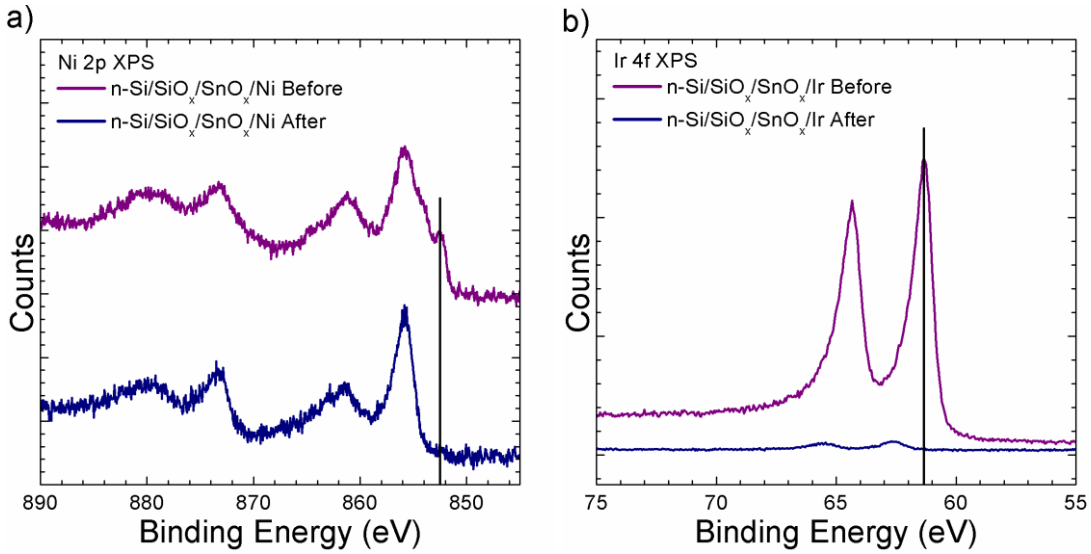

Figure 5. Chemical characterization of n-Si/SiO_x/SnO_x photoanodes coated with 2 nm Ni or 1 nm Ir. High-resolution XPS data were collected before and after photoelectrochemical operation under 100 mW cm^{-2} of simulated solar illumination in 1.0 M KOH (aq) or 1.0 M H_2SO_4 (aq) for n-Si/SiO_x/SnO_x/Ni and n-Si/SiO_x/SnO_x/Ir electrodes, respectively. The spectral regions are (a) Ni 2p, (b) Ir 4f, and (c) Sn 3d. The spectra were normalized so that the integrated Sn $3d_{3/2}$ signal was the same for all samples.

The Sn 3d spectra of n-Si/SiO_x/SnO_x films showed a sharp Sn $3d_{3/2}$ peak at a binding energy of 486.9 ± 0.1 eV (Figure S8b). This peak could not be deconvoluted from signals ascribable to SnO_2 and SnO. The Sn $3d_{3/2}$ peak binding energy shifted to 486.5 ± 0.1 eV, 487.0 ± 0.1 eV, and 487.2 ± 0.1 eV for n-Si/SiO_x/SnO_x samples coated with 2 nm Ni, 1 nm Ir, and 1 nm Pt metal, respectively (Figure 5c, Figure S8b). After photoelectrochemical

operation, the Sn $3d_{3/2}$ peak binding energy was 486.5 ± 0.1 eV, 487.2 ± 0.1 eV, and 487.3 ± 0.1 eV for n-Si/SiO_x/SnO_x samples coated with 2 nm Ni, 1 nm Ir, and 1 nm Pt metal (Figure 5c), respectively. The O/Sn ratio of the SnO_x film was 1.50 ± 0.03 based on the integrated Sn $3d_{3/2}$ and O 1s signals corrected by their relative sensitivity factors, which is lower than the 1.7 ± 0.1 O/Sn ratio measured for a F-doped SnO_2 plate (FTO) (Figure S8b, S8c). The catalyst/Sn ratio was 2.4 ± 0.1, 2.2 ± 0.1, and 1.3 ± 0.1 for Ni, Ir, and Pt before and 1.8 ± 0.2, 0.08 ± 0.01, and 0.19 ± 0.01 after photoelectrochemical operation, indicating a 25%, 96%, and 85% loss in Ni, Ir, and Pt signal after operation, respectively (Figure 5, Figure S8).

The amount of Ni-based catalyst on the surface of SnO_x did not substantially change under water oxidation conditions in 1.0 M KOH(aq), but in 1.0 M H_2SO_4(aq), the amount of Ir and Pt catalysts on the SnO_x surface decreased by 97% and 86%, respectively, after water oxidation. Additionally, the remaining Ni, Ir, or Pt from the original 1–2 nm thick metal deposit was oxidized to oxides, hydroxides, or oxyhydroxides (Figure 5, Figure S8). Loss of Ir and Pt from the electrode surface can occur by corrosion of the metal during water oxidation or by detachment of the catalytic layers during oxygen evolution. At a chronopotentiometric current density of 5 mA cm^{-2}, Ir and Pt corrode at ~0.30 and ~ 0.04 ng cm^{-2} s^{-1}, respectively.[23] These corrosion rates correspond to film thickness loss rates of ~ 0.48 and ~0.07 nm h^{-1} for Ir and Pt, respectively, indicating that 1–2 nm thick catalyst layers are expected to persist for only a few hours at light-limited current densities of ~ 30 mA cm^{-2}.

Patterning the metallic films of Ni, Ir, or Pt catalysts into microdisk arrays allowed for increased loading of the catalysts while blocking little of the exciting solar radiation (details

in Experimental Section).[24] Metal microdisk arrays consisted of 2–3 μm diameter metal disks with an ~ 7 μm pitch, and covered ~ 9% of the electrode area (Figure S9). Additionally, IrO_2 particles were loaded onto n-Si/SiO_x/SnO_x/Pt electrodes to obtain efficient photoanodes for water oxidation in acid with enhanced stability compared to photoanodes coated with thin Ir films (details in Experimental Section).

In contact with $Fe(CN)_6^{3-/4-}$(aq), photovoltages of 600–610 mV were observed under 100 mW cm^{-2} of simulated sunlight for n-Si/SiO_x/SnO_x electrodes coated with metallic microdisks (Figure S10a, Table S1). In contact with 1.0 M KOH(aq), photoanodes coated with Ni microdisk arrays (μNi) exhibited less hydroxide/oxyhydroxide sites than electrodes coated with Ni films, as determined by the charge contained in the integrated cathodic peaks (0.40 mC cm^{-2} and 0.14 mC cm^{-2} for Ni and μNi, respectively) in the $Ni(OH)_2$/NiOOH region (Figure 4a, Figure S10b). The OER kinetics for μNi electrodes were improved by electrodeposition of additional NiFeOOH catalyst (e-NiFeOOH).[22] The electrodeposited NiFeOOH catalyst decreased the photocurrent density at the formal potential for OER from 29.8 mA cm^{-2} to 27.9 mA cm^{-2} but improved η at 1 mA cm^{-2} from η = -283 mV to η = -351 mV (Figure S11a).

Photoanodes coated with μNi/e-NiFeOOH showed stable photocurrents for > 100 h in 1.0 M KOH(aq) **(Figure 6, Table S2)**. Photoanodes coated with Ir microdisk arrays (μIr) had ~ 13 times more Ir loading than the Ir film electrodes, and were stable for 4 min (Figure S10c). Photoanodes with drop-cast IrO_2 particles had ~160 times more Ir loading than the Ir film electrodes, and were stable for 5 h (Figure S10d) of operation. In contrast, photoanodes coated with Pt microdisk arrays (μPt) exhibited a stable photocurrent for > 30 h in contact with 1.0 M H_2SO_4(aq) (Figure S10d). Electrodeposition of additional Pt (e-Pt) on the μPt

yielded a stable photocurrent for > 100 h (Figure 6, S11b). Inductively coupled plasma mass spectrometry (ICP-MS) was used to determined the amount of Sn in the 1.0 M KOH(aq) or 1.0 M H_2SO_4(aq) electrolyte while p^+-Si/SiO_x/SnO_x electrodes were held at η = 300 mV. The ICP-MS data indicates that an equivalent of 29 nm and 14 nm of SnO_2 had dissolved after 42 h of electrochemical operation in 1.0 M KOH(aq) and 1.0 M H_2SO_4(aq), respectively (Figure S11c). Faradaic efficiency measurements of n-Si/SiO_x/SnO_x with μNi in contact with 1.0 M KOH(aq) indicated that > 97% of the photocurrent contributed to water oxidation (Figure S11d).

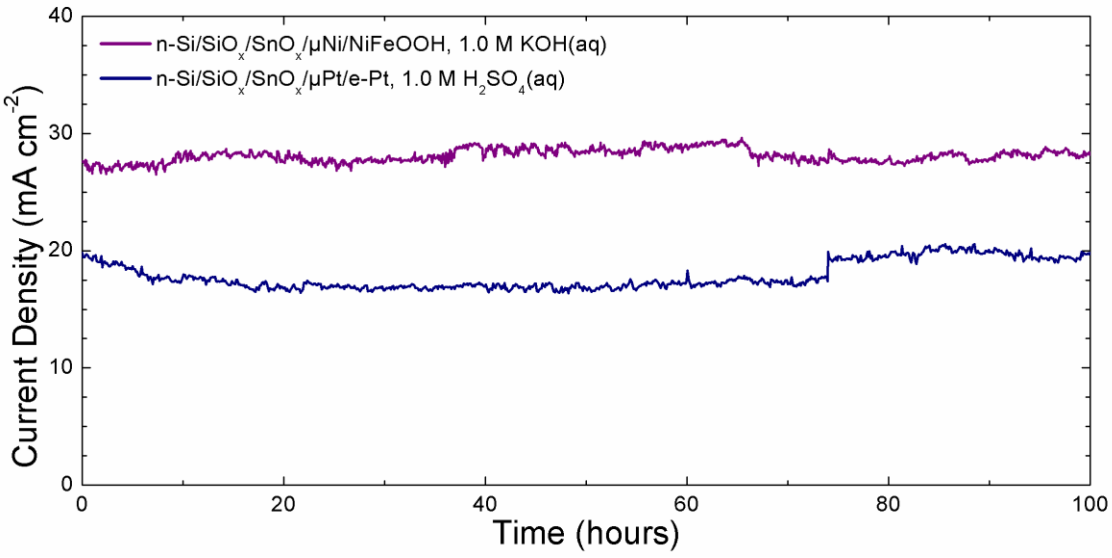

Figure 6. Chronoamperometry of n-Si/SiO_x/SnO_x photoanodes at 1.61 V vs. RHE and 1.94 V vs. RHE in 1.0 M KOH(aq) and 1.0 M H_2SO_4(aq), respectively, under 100 mW cm^{-2} of simulated sunlight. Photoelectrodes in contact with 1.0 M KOH(aq) had a patterned Ni microdisk array coating with an electrodeposited NiFeOOH catalyst, and photoelectrodes in

contact with 1.0 M H_2SO_4(aq) had a patterned Pt microdisk array coating with an electrodeposited Pt catalyst.

4.3 Discussion

The 620 mV photovoltage provided by the n-Si/SiO_x/SnO_x heterojunction provides slightly in excess of 50% of the thermodynamic potential required for the water-splitting reaction. The n-Si/SiO_x/SnO_x heterojunction exhibited a diode current ~ 10^5 greater than the diode current expected for a 1.12 eV band gap semiconductor based on the Shockley-Queisser limit (Figure S4a), indicating that a 20% efficient, intrinsically safe, solar-driven water-splitting device could be constructed from this heterojunction by appropriate integration with catalysts, a top light absorber, and suitable membranes.[25] The demonstrated stability of the n-Si/SiO_x/SnO_x photoanodes in both strongly acidic and alkaline electrolytes allows for device configurations that minimize the resistance due to solution transport losses. Furthermore, the ability to make ohmic contacts to various metals might allow integration with highly active heterogeneous or immobilized molecular catalysts.[22, 26]

The n-Si/SiO_x/SnO_x photoanodes that did not contain deposited metal exhibited barrier heights of 1.07 ± 0.02 eV (Figure 3c), whereas metal deposition reduced the barrier height, possibly due to direct metal contact to the SiO_x layer through pinholes or cracks in the SnO_x film (Figure S7). Formation of a controlled SiO_x layer improved the photovoltage observed in heterojunctions between n-Si and SnO_x (Figure 3a), possibly due to improved passivation of surface defects at the n-Si/SiO_x interface that unpins the Si Fermi level and allows higher barrier heights to be obtained. At barrier height values close to the Si band

gap, bulk recombination and recombination at the back contact limits the photovoltage. The use of electron-selective back contacts and/or the formation of an n^+ back-surface field may further increase the photovoltage.

Previous photoanodes containing heterojunctions between n-Si and tin oxides have exhibited barrier heights < 0.95 eV with highly doped tin oxides.[8, 14] Doped tin oxides generally exhibit a donor concentration of ~ 10^{20} cm^{-3}, whereas the SnO_x film studied herein had a donor concentration of ~10^{17} cm^{-3} (Figure S4c).[27] Generally, as the donor concentration decreases the work function of a material increases, and the depletion width for a given built-in voltage increases. The heterojunction formed between n-Si and SnO_x exhibits an improved barrier height of ~ 1.07 eV compared to other heterojunctions due to the moderate doping of the SnO_x film but exhibits a contact resistance associated with the built-in voltage at the SnO_x/electrolyte interface. The contact resistance was minimized by sputtering metallic films of Ni, Ir, or Pt onto the SnO_x film (Figure S4b, S4c). The decrease in contact resistance could be due to appropriate band alignment between the metals and SnO_x, or electronic changes at the SnO_x surface caused by sputter damage. Charge transport through the SnO_x film could be through the defect states observed at the Fermi level energy of the SnO_x film (Figure 2c), which would be close to the energy of the holes from the Si substrate after equilibration between Si and SnO_x.

Sn is expected to be predominantly SnO_2 under anodic conditions in 1.0 M H_2SO_4(aq), with an equilibrium concentration of dissolved Sn^{4+} species of ~ 21 nM.[28] Consequently, SnO_x should provide a long-term, durable protection layer for devices operating in acidic electrolytes. The SnO_x layer studied herein produced electrolyte concentrations of Sn approximately 24 times higher than expected for soluble Sn^{4+} formed from SnO_2 (Figure

S11c). One possible mechanism for this high concentration is the detachment of nanocrystalline SnO_2 particles to form a colloidal dispersion which cannot be differentiated from soluble Sn species by ICP-MS. Alternatively, highly soluble Sn^{2+} species can be formed from SnO, which could be present in the film based on the O/Sn stoichiometry < 2 observed with XPS.[28]

In 1.0 M KOH(aq), Sn is expected to be predominantly $Sn(OH)_6^{2-}$ under anodic conditions.[28] Methods of suppressing any residual SnO_x dissolution in alkaline electrolytes include deposition of additional protection layers such as TiO_2, or decreasing the local pH at the SnO_x surface via oxygen evolution. Devices operating under real conditions will experience periods of time without illumination, which might affect the stability of the semiconducting, protective, and catalytic components. For SnO_x protective layers in acidic electrolytes, retaining the electrolyte under a Nernstian condition with dissolved oxygen could prevent cathodic dissolution of the SnO_x film. Adhesion between SnO_x nanocrystals must be controlled to prevent loss of SnO_x through mechanisms, such as the formation of colloidal nanocrystal suspensions. Additionally, minimizing the amount of SnO in the SnO_x film would enhance the stability in acidic electrolytes.

The effect of catalyst corrosion on photoanode stability can be minimized by patterning the catalyst layer to allow an increase in catalyst loading without substantial decreases in the transmission of light to the absorber. However, at low catalyst loadings, further improvements in the stability of photoanodes in acid will require the development of water oxidation catalysts with inherently lower corrosion rates in acid than those of Pt or Ir.[29]

The photovoltage obtained from the n-Si/SiO_x/SnO_x heterojunction is close to the bulk-recombination limit for these n-type Si wafers. The reported conduction band-edge positions

of SnO, SnO_2, and Si are -3.59, -4.5, and -4.05 eV versus the vacuum energy, respectively, with band gaps of 4.2, 3.5, and 1.12 eV, and valence band-edge positions of 7.79, 8.0, and -5.17 eV, respectively.[30] The large band gaps of the SnO and SnO_2 suggest that moderately n-type tin oxide will have its Fermi level substantially below its conduction band edge, yielding work functions in the range of 3.59 to 6.25 eV based on the mid-gap Fermi level position for undoped SnO_2. Thus the Fermi level of the SnO_x near the n-Si/SiO_x interface is expected to be close to, or more negative than, the valence band of Si, and close to the Fermi level of the metal contact (Figure S12). Thus, equilibration of n-Si with n-SnO_x could lead to barrier heights with values close to the 1.12 eV band gap of Si. The surface work function of SnO_x is at least 4.7 eV, and structural changes throughout the SnO_x film could affect the work function of SnO_x near the n-Si/SiO_x/SnO_x interface (Figure 1a, S2b, 2b).

4.4 Conclusion

The n-Si/SiO_x/SnO_x heterojunction provides 620 mV of photovoltage under 100 mW cm^{-2} of simulated solar illumination, while facilitating ohmic contact to Ni, Ir, or Pt films that convert to oxygen-evolving catalysts under anodic conditions. Water oxidation in 1.0 M H_2SO_4(aq) resulted in corrosion of the Ir or Pt catalytic films. Patterning of the catalyst layer to increase the loading of the catalysts allowed the construction of photoanodes that exhibited stable photocurrents for > 100 h of continuous operation in either 1M H_2SO_4 or 1.0 M KOH The observations suggest that n-Si/SiO_x/SnO_x heterojunctions are a viable component for the construction of efficient, stable, intrinsically safe, solar-driven fuel-forming devices.

4.5 Acknowledgements

This work was supported through the Office of Science of the U.S. Department of Energy (DOE) under award no. DE-SC0004993 to the Joint Center for Artificial Photosynthesis, a DOE Energy Innovation Hub. I.M.H. acknowledges a National Science Foundation Graduate Research Fellowship under Grant No. DGE-1144469. We thank C. Garland for assistance with transmission-electron microscopy measurements.

4.6 Supplementary Information

4.6.1 Chemicals

All chemicals were used as received, including tin(IV) chloride hydrate ($SnCl_4 \cdot xH_2O$, Alfa Aesar, 98%), sulfuric acid (H_2SO_4, Fisher Scientific, TraceMetal Grade, 93-98%), potassium hydroxide (KOH, Sigma-Aldrich, Semiconductor Grade, 99.99%), potassium chloride (KCl, Macron Chemicals, 99.6%), potassium ferrocyanide trihydrate ($K_4Fe(CN)_6 \cdot 3H_2O$, Acros Organics, > 99%), potassium ferricyanide ($K_3Fe(CN)_6$, Fisher Scientific, Certified ACS), ethyl acetate (EMD Millipore Co., HPLC Grade), hydrogen peroxide (H_2O_2, EMD Millipore Co., 30% aqueous solution), hydrochloric acid (HCl, EMD Millipore Co., 36-38% aqueous solution), nickel(II) nitrate hexahydrate ($Ni(NO_3)_2 \cdot 6H_2O$, Sigma-Aldrich, 99.999%), iron(II) sulfate heptahydrate ($FeSO_4 \cdot 7H_2O$, Sigma-Aldrich, ACS >99.0%), potassium hexachloroiridate(IV) (K_2IrCl_6, Sigma-Aldrich, Technical Grade), dihydrogen hexachloroplatinate(IV) hydrate ($H_2PtCl_6 \cdot xH_2O$, Alfa Aesar, 99.9%), iridium(IV) oxide (IrO_2, Alfa Aesar, 99.99%), and gallium-indium eutectic (Alfa Aesar, 99.99%). Deionized water with a resistivity of 18.2 MΩ cm was obtained from a Barnsted Millipore system.

4.6.2 Chemical Oxidation of Silicon

Silicon wafers of n-type conductivity (n-Si, ρ = 0.1-1 Ω cm) or degenerately doped p-type conductivity (p^+-Si, $\rho < 0.005$ Ω cm) were etched in a buffered HF(aq) solution for 1 min to remove the native oxide, then rinsed with deionized water and dried under a flow of N_2(g). A controlled silicon oxide layer (SiO_x) was formed by placing the wafers in a 5:1:1

by volume $H_2O/H_2O_2/HCl$ solution at 75 °C for 10 min. The samples were then rinsed with deionized water and dried under $N_2(g)$.

4.6.3 Sample Preparation

SnO_x was deposited by a spray deposition process onto Si wafers. A 45 mg mL^{-1} $SnCl_4 \cdot xH_2O$ solution was prepared with ethyl acetate. Silicon wafers were placed on a hot plate set between 350-475 °C and were allowed to warm for 30 s prior to metal oxide deposition. SnO_x was deposited onto the Si wafers by spraying the $SnCl_4 \cdot xH_2O$ solution from a plastic spray gun. The SnO_x thickness was controlled by changing duration of the spray deposition. SnO_x films were deposited at 400 °C unless otherwise specified.

Metallic films were deposited using an AJA Orion sputtering system. Ni, Ir, and Pt were sputtered from an Ar plasma with Ni (ACI Alloys), Ir (ACI Alloys), or Pt (ACI Alloys) metal targets. During the sputter depositions, the Ar plasma was maintained at a chamber pressure of 5 mTorr with a 20 sccm Ar flow rate. Target powers of 150 W, 150 W, and 100 W were used for Ni, Ir, and Pt depositions, respectively. Prior to the depositions, the chamber pressure was < 10^{-7} Torr. Deposition rates were determined via profilometry (DektakXT Stylus profilometer) measurements. The thickness of the metal films was controlled by the duration of the sputtering, and no intentional heating of the sample occurred during deposition.

For some experiments, metal disk arrays (μM, M = Ni, Ir, Pt) were patterned onto the $Si/SiO_x/SnO_x$ wafers. The SnO_x-coated wafers were cut into ~ 3x3 cm pieces and cleaned with flowing $N_2(g)$ prior to being loaded onto a spin-coater. Subsequent layers of MCC Primer (Microchem Corp.) and S1813 photoresist (Dow Chemical Co.) were spin-coated

onto the samples at 3,000 rpm for 1 min. The coated samples were prebaked at 110 °C on a hotplate for 1 min. Ultraviolet-light photolithography was used to transfer a 3 μm diameter hole array with a 7 μm pitch pattern onto the samples, and the samples were developed for 2 min in MF 319 developer (Dow Chemical Co.). The samples were rinsed with deionized H_2O to remove excess developer and were dried under N_2(g). Metal disk arrays were sputter deposited with the same sputter parameters as for the metallic films, expect for the duration of the sputter deposition. The photoresist was removed by soaking the samples in acetone for 1-4 h. Excess photoresist and metal were removed by sonicating the samples in acetone, then rinsing with deionized H_2O and drying with N_2(g).

Electrodes were prepared with methods similar to those used previously.[26] Electrodes were prepared by cleaving the Si wafers into ~ 0.25 cm^2 pieces, and In-Ga eutectic (Aldrich) was scribed on the back to form an ohmic contact. Glass tubes were cleaned with aqua regia (3:1 v/v HCl: HNO_3) prior to use, and tinned Cu wire was threaded through the tubes. Ag paint (SPI, Inc.) was used to make an electrical contact between the In-Ga and Cu wire, as well as to provide mechanical stability to the contact. The Ag paint was dried for at least 2 h at room temperature. Hysol 9460 epoxy was used to insulate the back contact and to define the sample area. The epoxy was cured at room temperature for at least 12 h prior to use. The electrode areas were determined by imaging the electrodes with an optical scanner (Epson Perfection V360) and quantifying the area with ImageJ software. Electrode areas were between 3 and 20 mm^2, unless otherwise specified.

For some electrodes, IrO_2 was deposited via a drop-casting method that has been described previously.[31] A dispersion of IrO_2 powder (80 mg), deionized water (3.8 mL), 2-propanol (1.0 mL), and 5 wt% Nafion 117 solution (40 μL) was sonicated for at least 30

min prior to use. The dispersion was drop-cast onto the electrodes at a loading of 25 μL cm^{-2} and allowed to dry for at least 5 min in air. The electrodes were heated at 85 °C for 5 min in an oven, and then cooled to room temperature prior to electrochemical testing.

4.6.4 Materials Characterization

X-ray diffraction (XRD) analysis was performed with a Bruker D8 Discover instrument equipped with a Vantec-500 2-dimensional detector. Cu Kα radiation (1.54 Å) was generated at a tube current of 1000 μA and a tube voltage of 50 kV. The incident radiation was focused with a 0.5 mm diameter mono-capillary collimator. An aligned laser beam was used to ensure that the sample was placed at the correct position for diffraction measurements. The theta angle was fixed at 5 degrees. The scattered radiation was collected with a Vantec-500 detector with an angular resolution < 0.04 °, which enabled the collection of diffraction from a 2θ range of 20°. Four scans were performed in the range of 20° to 80° 2θ, and radiation was counted for a total duration of 4 h to obtain the XRD profile. The collected data were analyzed using Bruker EVA software. The peaks were indexed to reference patterns of SnO_2.[32]

Scanning-electron microscopy (SEM) images were collected with a Nova nanoSEM 450 (FEI) instrument at an accelerating voltage of 5 keV. Cross-sectional samples for transmission-electron microscopy (TEM) were prepared with conventional mechanical polishing and ion milling techniques. Samples consisting of n-Si/SiO_x/SnO_x were cleaved and glued on the SnO_x side with M-bond 610 adhesive. The glued pieces were cut with a diamond saw into ~ 1 mm samples, and then polished and glued to Mo TEM slot grids (SPI Supplies) with M-bond 610. The pieces were polished with sandpaper, and then thinned

with progressively finer diamond lapping film disks (Allied High Tech Products Inc.) until the cross section of the sample was ~ 20 μm thick. The samples were placed on a dimpler (Fischione Instruments Inc., Model 2000) and polished down to an appropriate thickness before ion milling. The samples were then milled with Ar ions (Fischione Instruments Inc.) until the sample was thin enough for TEM imaging. An FEI Tecnai F30ST transmission electron microscope with an accelerating voltage of 300 kV was used for imaging.

Wavelength-dependent transmission measurements were collected with a Cary 5000 UV/vis/NIR equipped with an integrating sphere. SnO_x was deposited at 400 °C onto a quartz substrate supported by a Si wafer during the deposition. Ellipsometry measurements were used to determine the thickness of the SnO_x film on Si, which had the same thickness as the film on the quartz substrate. Transmission measurements were normalized to 100% with a clean quartz substrate and to 0% by blocking the beam with an opaque metal plate. Data were collected at 1 nm intervals with a scan rate of 600 nm per min.

4.6.5 X-ray Photoelectron Spectroscopy

X-ray photoelectron spectroscopic (XPS) data were collected using a Kratos Axis NOVA (Kratos Analytical, Manchester, UK) at a background pressure of < 10^{-9} Torr. A monochromatic Al Kα source at 1486.6 eV was used for excitation. Survey scans were collected at 1 eV resolution, and a resolution of 0.05 eV was used for high-resolution scans. The peak energies, valence-band spectra, and work function measurements were calibrated against the binding energy of the adventitious C 1s peak, which was set at 284.8 eV. For peak energies and valence band spectra, the bias of the sample was controlled internally by

the XPS instrument, whereas for work function measurements the bias was controlled by an external power supply. The Ni 2p spectra were fit using a previously reported procedure to determine the amount of Ni, NiO, and $Ni(OH)_2$ in the Ni film.[33] The reported FWHM ratios, peak separations, and relative peak areas of standard samples of Ni, NiO, and $Ni(OH)_2$ were used to fit the collected Ni $2p_{3/2}$ spectra for 2 nm thick Ni films on n-Si/SiO_x/SnO_x before and after electrochemical operation. Contributions from Ni, NiO, and $Ni(OH)_2$ were required to fit the observed Ni $2p_{3/2}$ spectra for Ni films before electrochemical operation, whereas only $Ni(OH)_2$ was required to adequately fit the observed Ni $2p_{3/2}$ spectra of Ni after electrochemical operation. The cyclic voltammetry data of Ni films suggests that $Ni(OH)_2$ was oxidized to NiOOH under operation (Figure 4a). However, NiOOH was not required to fit the observed Ni $2p_{3/2}$ spectra, which could result from the conversion of NiOOH to $Ni(OH)_2$ without an applied potential. The Ir 4f and Pt 4f spectra were fit based on previously reported experiments on Ir and Pt electrodes in sulfuric acid.[34-35] The Ir 4f spectra were fit with a spin-orbit coupling separation of 2.98 eV, and a 3:4 peak area ratio for the Ir $4f_{5/2}$ and Ir $4f_{7/2}$ peaks. Ir metal was fit with two asymmetric peaks with equal FWHM values and an Ir $4f_{7/2}$ peak position of 61.4 ± 0.1 eV. IrO_x species were fit with two symmetric peaks with equal FWHM values and an Ir $4f_{7/2}$ peak position of 62.5 ± 0.1 eV. The Pt 4f spectra were fit with a spin-orbit coupling separation of 3.33 eV, and a 3:4 peak area ratio for the Pt $4f_{5/2}$ and Pt $4f_{7/2}$ peaks. Pt metal was fit with two asymmetric peaks with equal FWHM values and a Pt $4f_{7/2}$ peak position of 71.4 ± 0.1 eV. PtO was fit with two symmetric peaks with equal FWHM values and a Pt $4f_{7/2}$ peak position of 73.3 ± 0.1 eV. PtO_2 was fit with two symmetric peaks with equal FWHM values and a Pt $4f_{7/2}$ peak position of 75.5 ± 0.1 eV. Energy cut-offs for the valence band and work function measurements were determined by

fitting two lines to each spectra, with one line defining the background signal and another defining the signal rise. The background signal rise has been omitted from the graphs for clarity, but the signal rise line is included in all figures depicting data obtained by this technique.

4.6.6 Electrochemical Testing

Potassium hydroxide pellets (Sigma-Aldrich, Semiconductor Grade, 99.99%) and sulfuric acid (Fisher Scientific, TraceMetal Grade, 93-98%) were used to make 1.0 KOH(aq) and 1.0 M H_2SO_4(aq) solutions, respectively, with deionized water (18.2 MΩ cm). Potassium ferrocyanide trihydrate, potassium ferricyanide, and potassium chloride were used to make a 0.35 M $K_4Fe(CN)_6$/ 0.050 M $K_3Fe(CN)_6$/ 0.50 M KCl solution ($Fe(CN)_6^{3-/4-}$) with deionized water. Electrochemical data were acquired with digital potentiostats (MPG-2 or SP-200, Bio-Logic Science Instruments). Mercury/mercury oxide (Hg/HgO, CH Instruments) and mercury/mercury chloride (SCE, CH Instruments) reference electrodes were calibrated with a reversible hydrogen electrode (RHE) in 1.0 M KOH(aq) or 1.0 M H_2SO_4(aq), respectively. The RHE consisted of a Pt disk electrode (CH Instruments) submerged in either 1.0 M KOH(aq) or 1.0 M H_2SO_4(aq), with hydrogen gas (H_2) being bubbled constantly underneath the Pt disk. The potentials of the Hg/HgO and SCE reference electrodes were 0.906 V and 0.244 V vs. RHE, respectively. Aqua regia was used to clean the electrochemical cells prior to use. For electrochemical experiments, the working, reference, and counter electrodes consisted of the sample, a calibrated Hg/HgO electrode in 1.0 M KOH(aq) or a calibrated SCE in 1.0 M H_2SO_4(aq), and a Pt mesh separated from the other compartment by a porous frit. Electrochemical experiments

in $Fe(CN)_6^{3-/4-}$ used the sample, a Pt disk, and a Pt mesh as working, reference, and counter electrodes, respectively. The electrolyte volume was ~ 40 mL for most experiments. Cyclic voltammetric data were collected at 40 mV s^{-1} unless otherwise specified.

Dissolution studies were conducted with two-comparement cells that seperated the counter from the working and reference electrodes with an anion-exchange membrane (Fumasep FAA-3-PK-130) or a cation-exchange membrane (Nafion 117). The working and counter compartment were filled with 1.0 M KOH(aq) (45 mL) or 1.0 M H_2SO_4(aq) (40 mL). Electrodes consisting of p^+-Si/SiO_x/SnO_x with an area of appoximately 0.3 cm^2 were held at η = 300 mV and 200 μL samples were collected throughout the test. The samples were diluted to 5.0 mL with 1.0 M H_2SO_4(aq) (1.0 mL) and H_2O (3.8 mL). The amount of Sn in the solution was determined using an inductively-coupled plasma mass spectrometer (ICP-MS) (Agilent 800 Triple Quadrupole ICP-MS system). Calibration solutions were prepared with a multielement standard (Semi Metals Plasma Standard Solution, Specpure, Alfa Aesar).

4.6.7 Electrochemical Depositions

For some experiments, additional catalyst was electrodeposited on the working electrodes. $NiFe(OH)_2$ was cathodically deposited from a stirred aqueous solution of 5 mM $Ni(NO_3)_2 \cdot 6H_2O$ (Sigma Aldrich) and 5 mM $FeSO_4 \cdot 6H_2O$ (Sigma Aldrich).[22] Precipitation of Fe was prevented by purging the Ni solution with N_2(g) prior to the addition of Fe to the solution as well as during the electrodepositions. Depositions were conducted with a one-compartment cell that consisted of the working electrode, an SCE reference electrode, and a

Pt mesh counter electrode. $NiFe(OH)_2$ films were electrodeposited at a current density of -10 mA cm^{-2} for 20 s on n-Si/SiO_x/SnO_x/μNi electrodes in the dark, and excess catalyst was removed by sonicating the electrode in deionized water. IrO_x was anodically deposited with a modified procedure that has been reported previously.[36] Solutions of 2 mM K_2IrCl_6(Sigma) were prepared in 10 mM KOH(aq) to produce a dark-brown solution. The solution was heated at 70 °C under 600 rpm of stirring until the solution became light-brown and slightly turbid. The solution was immediately placed in an ice bath to limit precipitation of aqueous Ir species. Electrodepositions were performed with a one-compartment cell with a SCE as the reference electrode and a Pt mesh as the counter electrode. IrO_x was electrodeposited on p^+-Si/SiO_x/SnO_x/Pt electrodes with two cyclic voltammetry scans from 0.3 V to 2.1 V vs. SCE. IrO_x was photoelectrochemically deposited on n-Si/SiO_x/SnO_x/Pt electrodes under 100 mW cm^{-2} of simulated solar illumination with two cyclic voltammetry scans from -0.3 V to 1.5 V vs. SCE. The potential range for the electrodepositions on n-Si/SiO_x/SnO_x/Pt was modified due to the ~ 0.6 V photovoltage from the n-Si/SiO_x/SnO_x heterojunction. Pt was cathodically deposited from 10 mM H_2PtCl_6/1.0 M HCl aqueous solutions with the working, reference, and counter electrodes being n-Si/SiO_x/SnO_x/μPt, SCE, and a Pt mesh, respectively. A cathodic current density of 10 mA cm^{-2} was applied for 5 min in the dark to electrodeposit Pt on n-Si/SiO_x/SnO_x/μPt, and excess catalyst was removed by sonicating the electrode in deionized water.

4.6.8 Impedance Measurements

The potential range for the impedance measurements in $Fe(CN)_6^{3-/4-}$ were collected in the frequency range of 20 kHz to 20 Hz at a sinusoidal wave amplitude of 10 mV, with an

electrode bias of 0.0 to 0.6 V vs. $Fe(CN)_6^{3-/4-}$ in the dark. The impedance measurements were fit with a circuit consisting of a resistor in series with an additional component consisting of a resistor and a capacitor in parallel. The capacitance determined from the impedance measurements was attributed to the differential capacitance of the depletion-region of the semiconductor, and the voltage dependence was analyzed with the Mott-Schottky relationship:

$$C_d^{-2} = \frac{2}{qA^2\varepsilon_0\varepsilon_r N_d}\left(V_{app} + V_{bi} - \frac{k_B T}{q}\right)$$

where C_d^{-2} is the differential capacitance, q is the unsigned charge of an electron, A is the electrode area, ε_0 is the vacuum permittivity, ε_r is the relative permittivity of Si or SnO_x, N_d is the donor impurity concentration of Si or SnO_x, V_{app} is the potential difference relative to $E(Fe(CN)_6^{3-/4-})$ in the dark, V_{bi} is the built-in voltage, and T is the absolute temperature of the device during testing. The slope of the Mott-Schottky plot was used to determine N_d for each electrode, which agreed with the dopant density expected for Si wafers with 0.1 – 1.0 Ω cm resistivity and predicted a resistivity within ±0.3 Ω cm of the resistivity determined by four-point probe measurements. The Fermi level position for Si relative to the Si conduction band minimum was determined using the following relationship:

$$\boldsymbol{E}_C - \boldsymbol{E}_F = k_B T \, ln\left(\frac{N_c}{N_d}\right)$$

where $\mathbf{E}_C$ is the energy of the conduction band minimum for Silicon, $\mathbf{E}_F$ is the Fermi level position, and N_c is the effective density of states in the conduction band. The barrier height (ϕ_B) was determined with the following relationship:

$$\phi_B = qV_{bi} + \frac{\boldsymbol{E}_C - \boldsymbol{E}_F}{q}$$

For photoelectrochemical experiments, illumination was provided by a 50 W ENH-type W-halogen lamp. The light passed through a 4 cm diameter x 7 cm long metallic tube and was directed to the photoelectrode surface using a mirror tilted at 45 degrees. The light intensity was adjusted prior to addition of electrolyte to the electrochemical cell, by measuring the photocurrent of a calibrated Si diode (FDS100, Thor Labs) placed in the same position as the photoelectrode. The photocurrent of the calibrated Si diode was determined at 100 mW cm^{-2} illumination with a calibrated solar simulator (Sun 3000 Solar Simulator, ABET Technologies).

4.7 Supplementary Figures

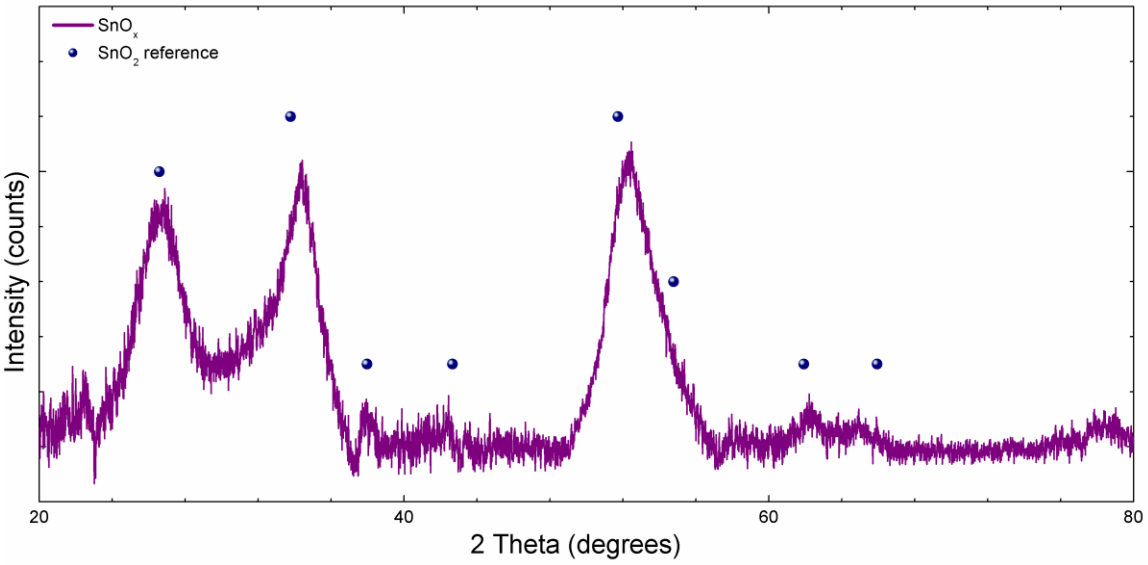

Figure S1. X-ray diffraction pattern for SnO_x film prepared at a deposition temperature of 400 °C on a Si(100) substrate. The diffraction peaks were indexed to a reference pattern of SnO_2.[32]

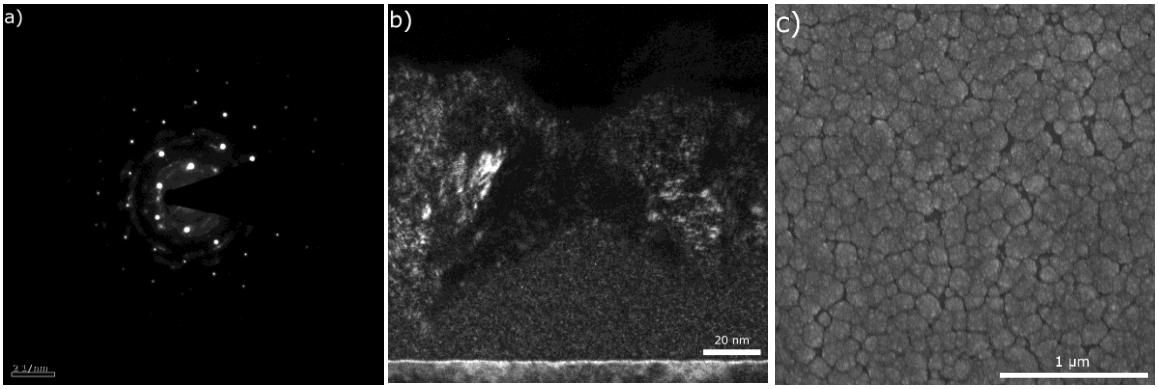

Figure S2. (a) Electron diffraction pattern of n-Si/SiO_x/SnO_x interface collected at an accelerating voltage of 300 kV. (b) Dark-field image of n-Si/SiO_x/SnO_x collected with a 10 µm selective area diffraction aperture centered on the SnO_2 (002) diffraction ring. (c) Scanning-electron microscopy image of n-Si/SiO_x/SnO_x surface.

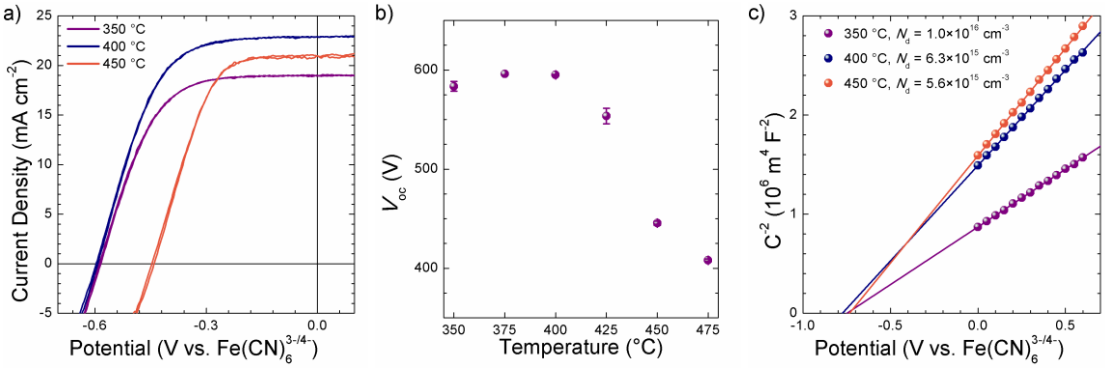

Figure S3. *J-E* behavior of n-Si/SiO_x/SnO_x electrodes made with 0.45 Ω-cm Si and coated with ~ 2 nm Pt in contact with a one-electron $Fe(CN)_6^{3-/4-}$ redox couple in 0.50 M KCl(aq). (a) *J-E* behavior of n-Si/SiO_x/SnO_x/Pt electrodes under 100 mW cm^{-2} of simulated solar illumination. (b) Open-circuit voltage of n-Si/SiO_x/SnO_x/Pt electrodes under 100 mW cm^{-2} of simulated solar illumination of as a function of substrate temperature during SnO_x deposition. (c) Mott-Schottky plot of the inverse square of the differential capacitance (Cd^{-2}) of the electrode, as determined from impedance measurements, vs applied potential for n-Si/SiO_x/SnO_x/Pt electrodes in the dark. Barrier height values were obtained from the values of the built-in voltage and dopant concentrations determined from the Mott-Schottky plots. The deduced N_d values are shown in the figure legend, and are within the range expected for 0.1-1.0 Ω-cm resistivity Si wafers.

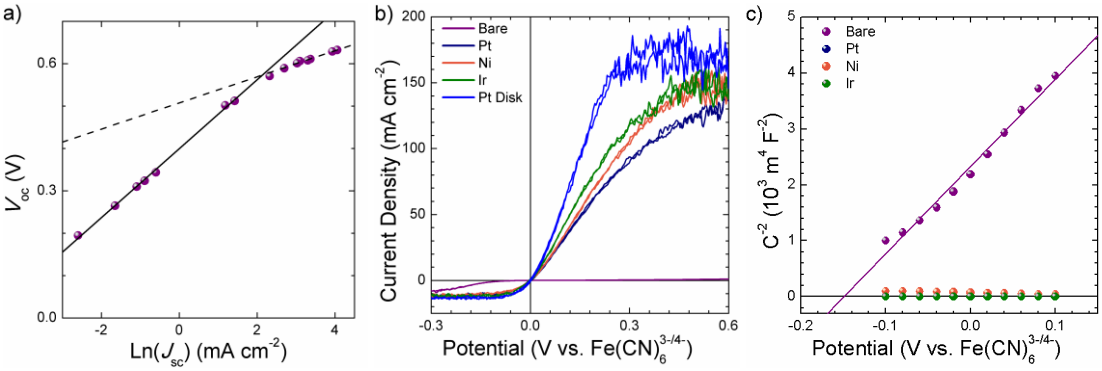

Figure S4. (a) Short-circuit current density and photovoltage obtained for n-Si/SiO_x/SnO_x/Pt photoelectrodes in contact with $Fe(CN)_6^{3-/4-}$ in 0.50 M KCl(aq) under simulated solar illumination attenuated with neutral density filters to obtain an irradiance in the range of 0.2 – 200 mW cm^{-2}. (b) Voltammetry in contact with $Fe(CN)_6^{3-/4-}$(aq) of p^+-Si/SiO_x/SnO_x electrodes metallized with 2 nm Ni, 1 nm Ir, or 1 nm Pt. (c) Representative C_d^{-2} vs E plot for p^+-Si/SiO_x/SnO_x electrodes metallized with 2 nm Ni, 1 nm Ir, or 1 nm Pt in the dark. Data points for Pt and Ir metallized electrodes overlap.

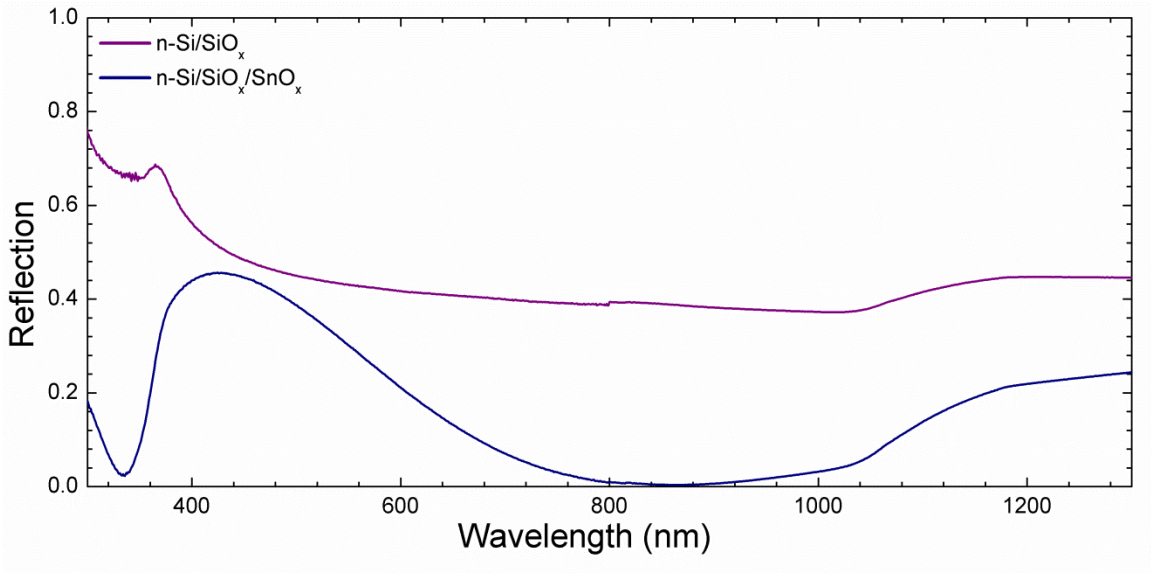

Figure S5. Optical reflectivity at normal incidence of an n-Si(100) wafer coated with ~1.5 nm SiO_x formed via chemical oxidation and of n-Si/SiO_x coated with ~ 100 nm SnO_x deposited at 400 °C.

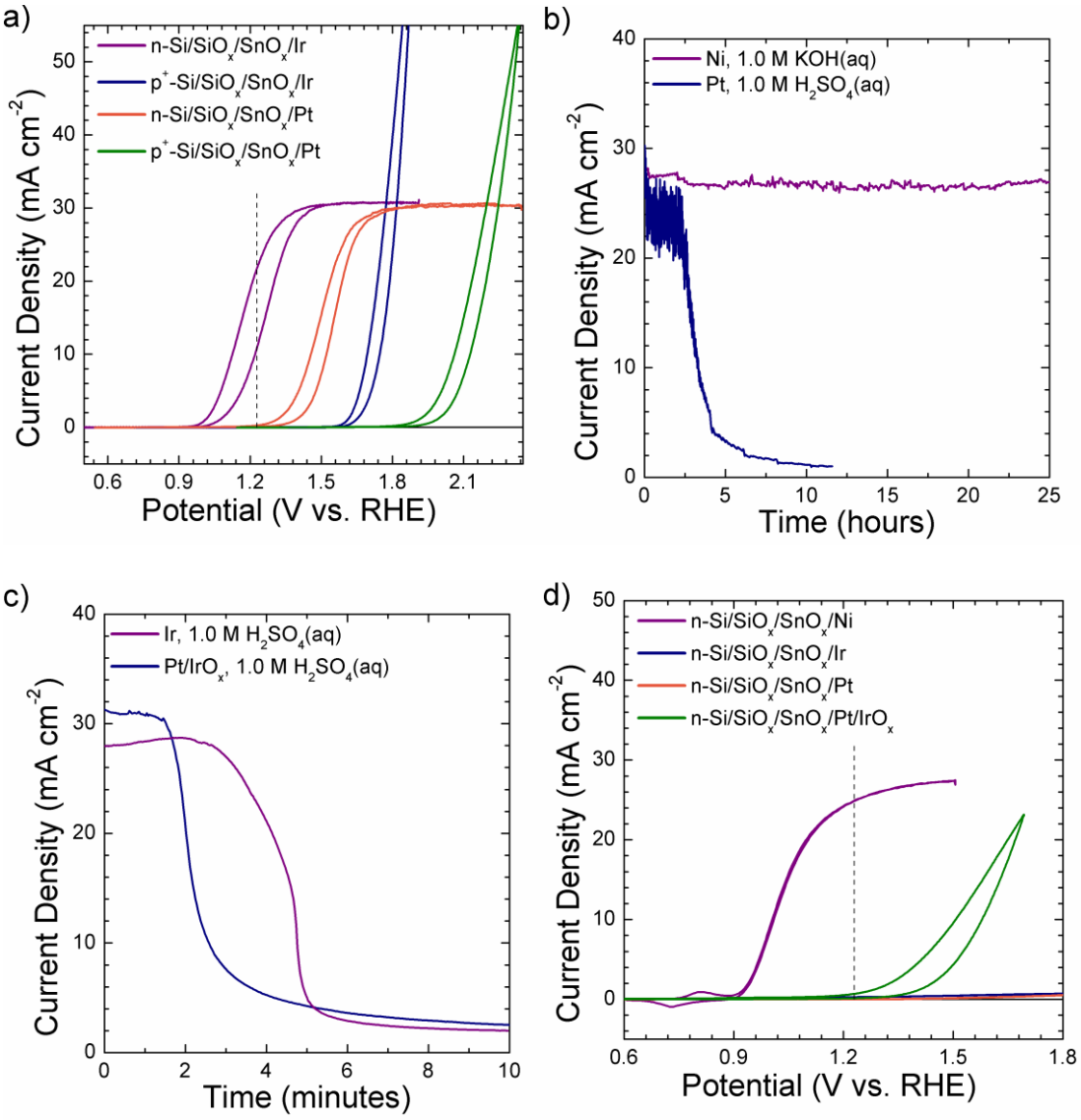

Figure S6. Photoelectrochemical behavior of n-Si/SiO_x/SnO_x and p^+-Si/SiO_x/SnO_x electrodes towards water oxidation under 100 mW cm^{-2} of simulated solar illumination. (a) Photoelectrodes with 1 nm Ir or Pt in contact with 1.0 M H_2SO_4(aq). (b) Stability of photoelectrodes coated with 2 nm Ni in contact with 1.0 M KOH(aq) at 1.51 V vs. RHE and with 1 nm Pt in contact with 1.0 M H_2SO_4(aq) at 2.04 V vs. RHE. (c) Stability of photoelectrodes coated with 1 nm Ir or Pt/IrO_x in contact with 1.0 M H_2SO_4(aq) at 1.54 V

vs. RHE. (d) Photoelectrodes with Ni in contact with 1.0 M KOH(aq) and 1 nm Ir, Pt, or Pt/IrO_x in contact with 1.0 M H_2SO_4(aq) after stability experiments.

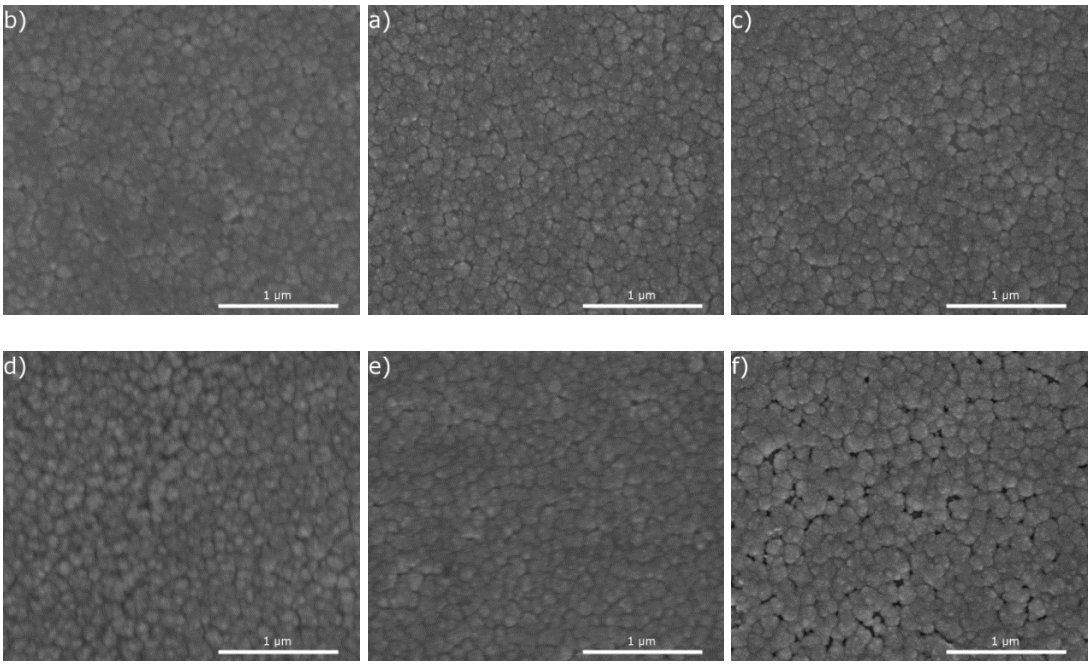

Figure S7. Scanning-electron microscopy images of n-Si/SiO_x/SnO_x photoelectrodes before and after electrochemical operation. (a) n-Si/SiO_x/SnO_x/Ni (b) n-Si/SiO_x/SnO_x/Ir, (c) n-Si/SiO_x/SnO_x/Pt, (d) n-Si/SiO_x/SnO_x/Ni after 25 h in 1.0 M KOH(aq) at 1.51 V vs. RHE, (e) n-Si/SiO_x/SnO_x/Ir after 3 h in 1.0 M H_2SO_4(aq) at 1.54 V vs. RHE, (f) n-Si/SiO_x/SnO_x/Pt after 12 h in 1.0 M H_2SO_4(aq) at 2.04 V vs. RHE.

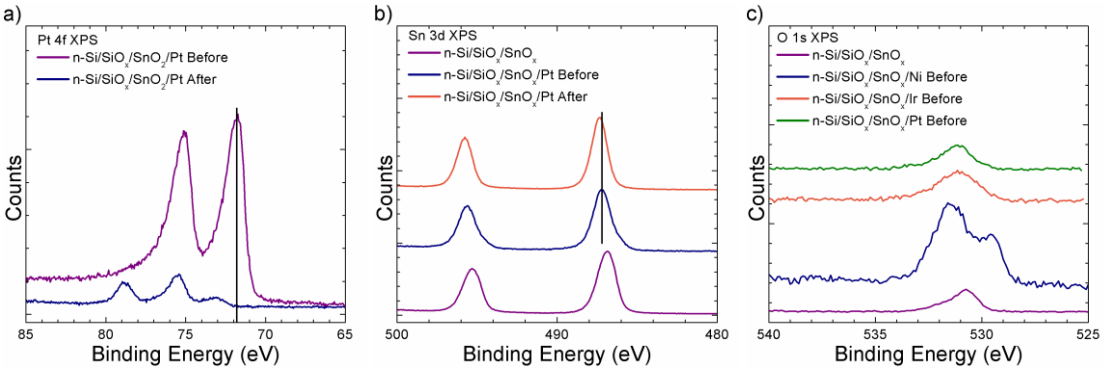

Figure S8. Chemical characterization of n-Si/SiO_x/SnO_x photoanodes. (a) High-resolution XPS spectra in the Pt 4f region of n-Si/SiO_x/SnO_x/Pt photoanodes before and after electrochemical operation in 1.0 M H_2SO_4(aq). (b) High-resolution XPS spectra in the Sn 3d region of n-Si/SiO_x/SnO_x and n-Si/SiO_x/SnO_x/Pt photoanodes before and after electrochemical operation in 1.0 M H_2SO_4(aq). (c) High-resolution XPS spectra in the O 1s region of n-Si/SiO_x/SnO_x with 2 nm Ni, 1 nm Ir, or 2 nm Pt coatings before electrochemical operation in 1.0 M KOH(aq) for Ni and in 1.0 M H_2SO_4(aq) for Ir and Pt. All spectra were normalized so that the integrated Sn 3d7/5 signal was the same for all samples.

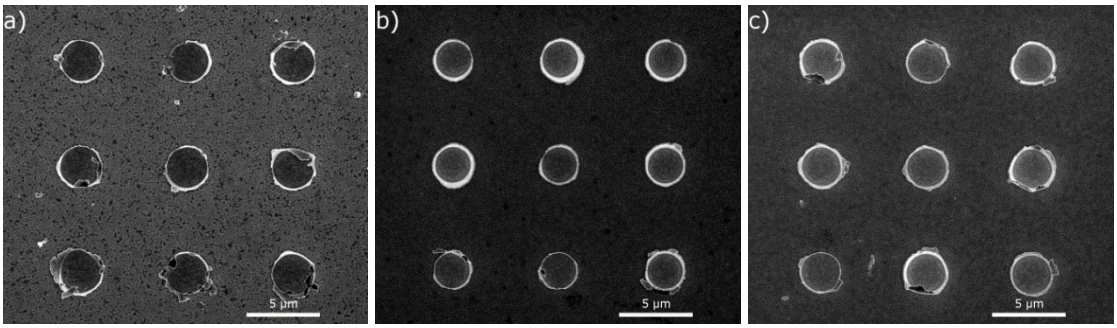

Figure S9. Scanning-electron microscopy images of n-Si/SiO_x/SnO_x photoelectrodes with patterned 100 – 130 nm thick (a) Ni, (b) Ir, or (c) Pt microdisk metallic arrays. The 3x3

array consisted of metallic circles that obstructed ~ 9% of the area, with SnO_x exposed on the remaining area.

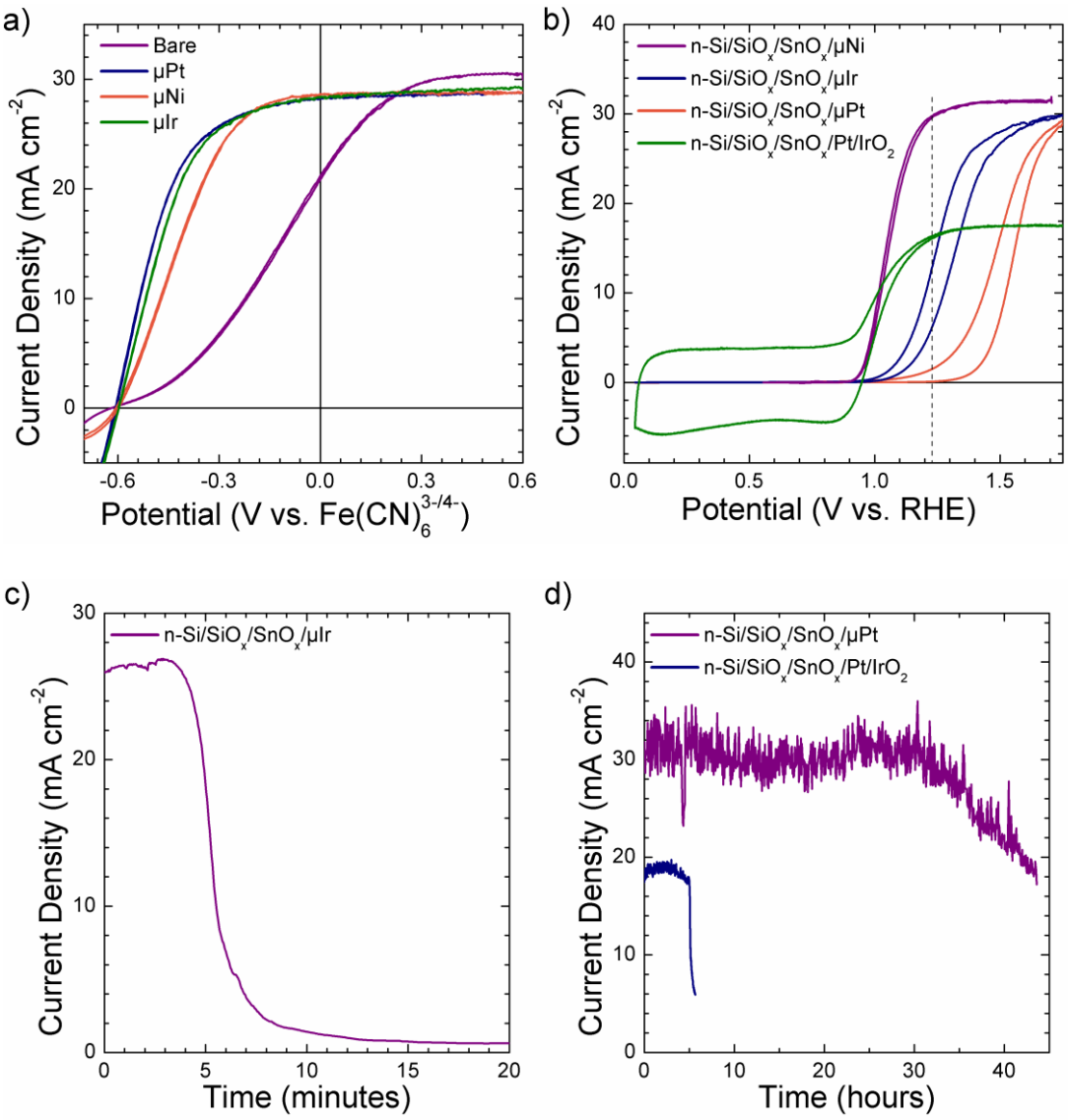

Figure S10. (a) Photoelectrochemical behavior of n-Si/SiO_x/SnO_x electrodes prepared at 400 °C with 100–130 nm thick Ni, Ir, or Pt microdisk arrays in contact with $Fe(CN)_6^{3-/4-}$ in 0.50 M KCl(aq) under 100 mW cm^{-2} of simulated solar illumination. (b) Photoelectrochemical behavior of n-Si/SiO_x/SnO_x towards water oxidation with 100–130 nm thick Ni, Ir, or Pt microdisk arrays patterned to cover ~ 9% of the electrode area, or 2

nm thick Pt coating with drop-casted IrO_2 particles. Ni-covered electrodes were in contact with 1.0 M KOH(aq), and Ir- or Pt-covered electrodes were in contact with 1.0 M H_2SO_4(aq). (c) Photocurrent stability under 100 mW cm^{-2} of simulated solar illumination of n-Si/SiO_x/SnO_x electrodes coated μIr in contact with 1.0 M H_2SO_4(aq) at 1.54 V vs. RHE. (d) Photocurrent stability under 100 mW cm^{-2} of simulated solar illumination of n-Si/SiO_x/SnO_x electrodes coated with μPt in contact with 1.0 M H_2SO_4(aq) at 2.04 V vs. RHE, or coated with 2 nm thick Pt with drop-casted IrO_2 particles in contact with 1.0 M H_2SO_4(aq) at 1.54 V Vs. RHE.

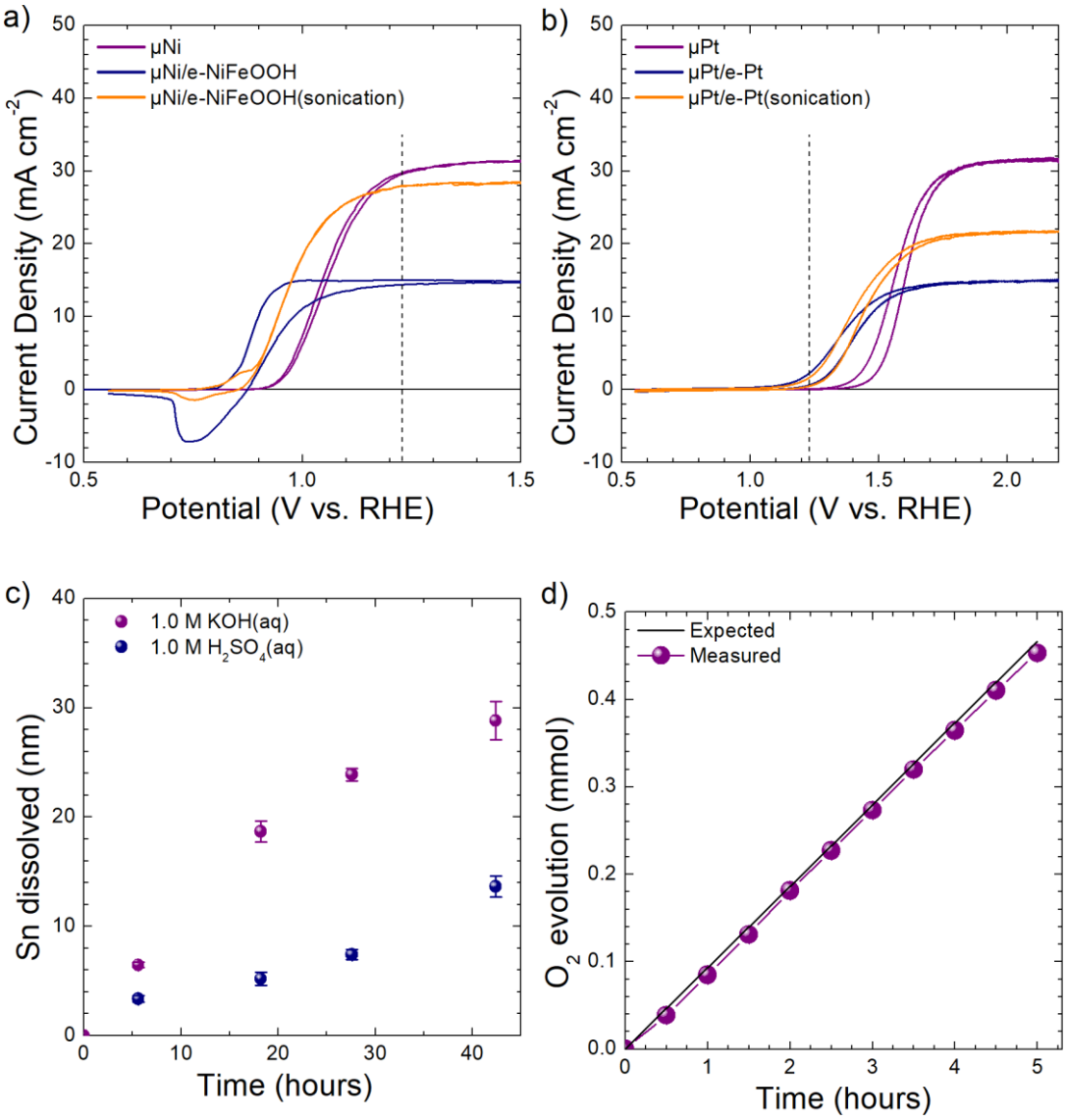

Figure S11. (a) *J-E* behavior of n-Si/SiO_x/SnO_x/μNi electrodes in 1.0 M KOH(aq) under 100 mW cm^{-2} of simulated solar illumination before electrodeposition of NiFeOOH, after electrodeposition of NiFeOOH, and after removal of excess catalyst via sonication. (b) *J-E* behavior of n-Si/SiO_x/SnO_x/μPt electrodes in 1.0 M H_2SO_4(aq) under 100 mW cm^{-2} of simulated solar illumination before electrodeposition of Pt, after electrodeposition of Pt, and after removal of excess catalyst via sonication. (c) Equivalent nm of SnO_2 detected in the electrolyte during polarization of a p^+-Si/SiO_x/SnO_x electrode at η = 300 mV in 1.0 M

KOH(aq) or 1.0 M H_2SO_4(aq). (d) Comparison between the O_2(g) production measured via an eudiometer and the O_2(g) production calculated assuming 100% faradaic efficiency for water oxidation in 1.0 M KOH(aq), for n-Si/SiO_x/SnO_x electrodes coated with Ni microdisk arrays under 100 mW cm^{-2} of simulated sunlight. O_2(g) was generated with a chronopotentiometric current of 10 mA.

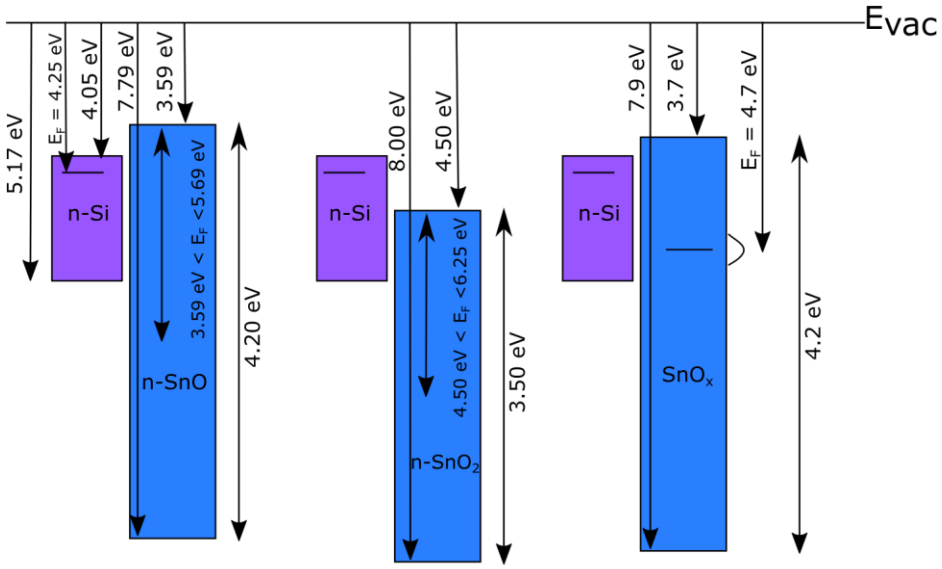

Figure S12. Band diagram of n-type Si, bulk n-type SnO, bulk n-type SnO_2, and surface of the SnO_x films studied in this work. The Si band edges and Fermi level position displayed in this figure are equal to the energetics of the n-type Si used in this work. The band edges of bulk SnO and SnO_2 are from a previous report.[30] Surface properties of SnO_x were determined from experiments in Figure S3.

Table S1. Photoelectrochemical properties of n-Si/SiO_x/SnO_x/M devices with a $Fe(CN)_6^{4-/3-}$ redox couple.

Device	Wafer Resistivity [Ω-cm]	Metal Thickness [nm]	Deposition Temperature [°C]	Photovoltage [mV]	Barrier Height [eV]
n-Si/SiO_x/SnO_x/Pt	0.45	2	350	384	0.98
n-Si/SiO_x/SnO_x/Pt	0.45	2	450	445	0.97
n-Si/SiO_x/SnO_x/Pt	0.45	2	400	595	1.00
n-Si/SnO_x/Pt	0.45	2	400	525	-
n-Si/SiO_x/SnO_x	0.21	0	400	620	1.07
n-Si/SiO_x/SnO_x/Ni	0.21	2	400	606	1.03
n-Si/SiO_x/SnO_x/Ir	0.21	1	400	605	0.99
n-Si/SiO_x/SnO_x/Pt	0.21	1	400	612	1.02
n-Si/SiO_x/SnO_x/μNi	0.21	100-130	400	601	-
n-Si/SiO_x/SnO_x/μIr	0.21	100-130	400	596	-
n-Si/SiO_x/SnO_x/μPt	0.21	100-130	400	610	-

Table S2. Photoelectrochemical water oxidation properties of n-Si/SiO_x/SnO_x/M and p^+-Si/SiO_x/SnO_x/M devices in 1.0 M KOH(aq) or 1.0 M H_2SO_4(aq).

Catalyst	Electrolyte [1.0 M]	η_{light} (n-Si) [mV]	η_{dark} (p^+-Si) [mV]	Photovoltage (η_{dark} - η_{light}) [mV]	Lifetime (n-Si) [hr]
Ni	KOH(aq)	-318	287	605	>25
μNi	KOH(aq)	-283	-	-	-
μNi/e-NiFeOOH	KOH(aq)	-351	-	-	>100
Pt/IrO_x	H_2SO_4(aq)	-322	272	594	$<10^{-3}$
Pt/IrO_2	H_2SO_4(aq)	-269	-	-	>5
Ir	H_2SO_4(aq)	-187	400	587	$<10^{-3}$
μIr	H_2SO_4(aq)	-159	-	-	$<10^{-3}$
Pt	H_2SO_4(aq)	58	719	661	>2
μPt	H_2SO_4(aq)	181	-	-	>30
μPt/e-Pt	H_2SO_4(aq)	8	-	-	>100

4.8 References

1. Lewis, N. S., Research opportunities to advance solar energy utilization. *Science* **2016,** *351* (6271), aad1920.
2. Lichterman, M. F.; Sun, K.; Hu, S.; Zhou, X.; McDowell, M. T.; Shaner, M. R.; Richter, M. H.; Crumlin, E. J.; Carim, A. I.; Saadi, F. H.; Brunschwig, B. S.; Lewis, N. S., Protection of inorganic semiconductors for sustained, efficient photoelectrochemical water oxidation. *Catal. Today* **2016,** *262*, 11-23.
3. Bae, D.; Seger, B.; Vesborg, P. C.; Hansen, O.; Chorkendorff, I., Strategies for stable water splitting via protected photoelectrodes. *Chem. Soc. Rev.* **2017,** *46* (7), 1933-1954.
4. Yang, J.; Walczak, K.; Anzenberg, E.; Toma, F. M.; Yuan, G.; Beeman, J.; Schwartzberg, A.; Lin, Y.; Hettick, M.; Javey, A.; Ager, J. W.; Yano, J.; Frei, H.; Sharp, I. D., Efficient and sustained photoelectrochemical water oxidation by cobalt oxide/silicon photoanodes with nanotextured interfaces. *J. Am. Chem. Soc.* **2014,** *136* (17), 6191-4.
5. Mei, B.; Seger, B.; Pedersen, T.; Malizia, M.; Hansen, O.; Chorkendorff, I.; Vesborg, P. C., Protection of p^+-n-Si Photoanodes by Sputter-Deposited Ir/IrO_x Thin Films. *J. Phys. Chem. Lett.* **2014,** *5* (11), 1948-52.
6. Bae, D.; Mei, B. T.; Fryndendal, R.; Pedersen, T.; Seger, B.; Hansen, O.; Vesborg, P. C. K.; Chorkendorff, I., Back-illuminated Si based photoanode with nickel cobalt oxide catalytic protection layer. *ChemElectroChem* **2016,** *3*, 1546.

7. Scheuermann, A. G.; Lawrence, J. P.; Kemp, K. W.; Ito, T.; Walsh, A.; Chidsey, C. E.; Hurley, P. K.; McIntyre, P. C., Design principles for maximizing photovoltage in metal-oxide-protected water-splitting photoanodes. *Nat. Mater.* **2016,** *15* (1), 99-105.
8. Hodes, G.; Thompson, L.; DuBow, J.; Rajeshwar, K., Heterojunction Silicon/Indium Tin Oxide Photoelectrodes: Development of Stable Systems in Aqueous Electrolytes and Their Applicability to Solar Energy Conversion and Storage. *J. Am. Chem. Soc.* **1983,** *105*, 324-330.
9. Strandwitz, N. C.; Comstock, D. J.; Grimm, R. L.; Nichols-Nielander, A. C.; Elam, J.; Lewis, N. S., Photoelectrochemical Behavior of n-type Si(100) Electrodes Coated with Thin Films of Manganese Oxide Grown by Atomic Layer Deposition. *J. Phys. Chem. C* **2013,** *117* (10), 4931-4936.
10. Laskowski, F. A. L.; Nellist, M. R.; Venkatkarthick, R.; Boettcher, S. W., Junction behavior of n-Si photoanodes protected by thin Ni elucidated from dual working electrode photoelectrochemistry. *Energy Environ. Sci.* **2017,** *10* (2), 570-579.
11. Chen, L.; Yang, J.; Klaus, S.; Lee, L. J.; Woods-Robinson, R.; Ma, J.; Lum, Y.; Cooper, J. K.; Toma, F. M.; Wang, L. W.; Sharp, I. D.; Bell, A. T.; Ager, J. W., p-Type Transparent Conducting Oxide/n-Type Semiconductor Heterojunctions for Efficient and Stable Solar Water Oxidation. *J. Am. Chem. Soc.* **2015,** *137* (30), 9595-603.
12. Mei, B.; Pedersen, T.; Malacrida, P.; Bae, D.; Frydendal, R.; Hansen, O.; Vesborg, P. C. K.; Seger, B.; Chorkendorff, I., Crystalline TiO_2: A Generic and Effective Electron-Conducting Protection Layer for Photoanodes and -cathodes. *J. Phys. Chem. C* **2015,** *119* (27), 15019-15027.

13. Kenney, M. J.; Gong, M.; Li, Y.; Wu, J. Z.; Feng, J.; Lanza, M.; Dai, H., High-performance silicon photoanodes passivated with ultrathin nickel films for water oxidation. *Science* **2013,** *342* (6160), 836-40.

14. Yao, T.; Chen, R.; Li, J.; Han, J.; Qin, W.; Wang, H.; Shi, J.; Fan, F.; Li, C., Manipulating the Interfacial Energetics of n-type Silicon Photoanode for Efficient Water Oxidation. *J. Am. Chem. Soc.* **2016,** *138* (41), 13664-13672.

15. Hu, S.; Shaner, M. R.; Beardslee, J. A.; Lichterman, M.; Brunschwig, B. S.; Lewis, N. S., Amorphous TiO_2 coatings stabilize Si, GaAs, and GaP photoanodes for efficient water oxidation. *Science* **2014,** *344* (6187), 1005-9.

16. Bae, D.; Pedersen, T.; Seger, B.; Iandolo, B.; Hansen, O.; Vesborg, P. C. K.; Chorkendorff, I., Carrier-selective p- and n-contacts for efficient and stable photocatalytic water reduction. *Catal. Today* **2017,** *290*, 59-64.

17. Kast, M. G.; Enman, L. J.; Gurnon, N. J.; Nadarajah, A.; Boettcher, S. W., Solution-deposited F:SnO_2/TiO_2 as a base-stable protective layer and antireflective coating for microtextured buried-junction H_2-evolving Si photocathodes. *ACS Appl. Mater. Interfaces* **2014,** *6* (24), 22830-7.

18. Azevedo, J.; Tilley, S. D.; Schreier, M.; Stefik, M.; Sousa, C.; Araújo, J. P.; Mendes, A.; Grätzel, M.; Mayer, M. T., Tin oxide as stable protective layer for composite cuprous oxide water-splitting photocathodes. *Nano Energy* **2016,** *24*, 10-16.

19. Zhou, X.; Liu, R.; Sun, K.; Friedrich, D.; McDowell, M. T.; Yang, F.; Omelchenko, S. T.; Saadi, F. H.; Nielander, A. C.; Yalamanchili, S.; Papadantonakis, K. M.; Brunschwig, B. S.; Lewis, N. S., Interface engineering of the photoelectrochemical

performance of Ni-oxide-coated n-Si photoanodes by atomic-layer deposition of ultrathin films of cobalt oxide. *Energy Environ. Sci.* **2015,** *8* (9), 2644-2649.

20. Azarpira, A.; Schedel-Niedrig, T.; Lewerenz, H. J.; Lublow, M., Sustained Water Oxidation by Direct Electrosynthesis of Ultrathin Organic Protection Films on Silicon. *Adv. Energy Mater.* **2016,** *6* (10), 1502314.
21. Trotochaud, L.; Young, S. L.; Ranney, J. K.; Boettcher, S. W., Nickel-iron oxyhydroxide oxygen-evolution electrocatalysts: the role of intentional and incidental iron incorporation. *J. Am. Chem. Soc.* **2014,** *136* (18), 6744-6753.
22. Sun, K.; Moreno-Hernandez, I. A.; Schmidt, W. C.; Zhou, X.; Crompton, J. C.; Liu, R.; Saadi, F. H.; Chen, Y.; Papadantonakis, K. M.; Lewis, N. S., A Comparison of the Chemical, Optical and Electrocatalytic Properties of Water-Oxidation Catalysts for Use in Integrated Solar-Fuels Generators. *Energy Environ. Sci.* **2017,** *10*, 987-1002.
23. Cherevko, S.; Zeradjanin, A. R.; Topalov, A. A.; Kulyk, N.; Katsounaros, I.; Mayrhofer, K. J. J., Dissolution of Noble Metals during Oxygen Evolution in Acidic Media. *ChemCatChem* **2014,** *6* (8), 2219-2223.
24. Sun, K.; Ritzert, N. L.; John, J.; Tan, H.; Hale, W.; Jiang, J.; Moreno-Hernandez, I. A.; Papadantonakis, K. M.; Moffat, T. P.; Brunschwig, B. S.; Lewis, N., Performance and Failure Modes of Si Anodes Patterned with Thin-Film Ni Catalyst Islands for Water Oxidation. *Sustainable Energy Fuels* **2018,** *2*, 983-998.
25. Chen, Y.; Hu, S.; Xiang, C.; Lewis, N. S., A sensitivity analysis to assess the relative importance of improvements in electrocatalysts, light absorbers, and system geometry on the efficiency of solar-fuels generators. *Energy Environ. Sci.* **2015,** *8* (3), 876-886.

26. Matheu, R.; Moreno-Hernandez, I. A.; Sala, X.; Gray, H. B.; Brunschwig, B. S.; Llobet, A.; Lewis, N. S., Photoelectrochemical Behavior of a Molecular Ru-Based Water-Oxidation Catalyst Bound to TiO_2-Protected Si Photoanodes. *J. Am. Chem. Soc.* **2017,** *139* (33), 11345-11348.

27. Bisht, H.; Eun, H.-T.; Mehrtens, A.; Aegerter, M. A., Comparison of spray pyrolyzed FTO, ATO and ITO coatings for flat and bent glass substrates. *Thin Solid Films* **1999,** *351*, 109-114.

28. House, C. I.; Kelsall, G. H., Potential-pH Diagrams for the Sn/H_2O-Cl System. *Electrochim. Acta* **1984,** *29* (10), 1459-1464.

29. Moreno-Hernandez, I. A.; MacFarland, C. A.; Read, C. G.; Papadantonakis, K. M.; Brunschwig, B. S.; Lewis, N. S., Crystalline nickel manganese antimonate as a stable water-oxidation catalyst in aqueous 1.0 M H_2SO_4. *Energy Environ. Sci.* **2017,** *10* (10), 2103-2108.

30. Xu, Y.; Schoonen, M. A. A., The absolute energy positions of conduction and valence bands of selected semiconducting minerals. *Am. Mineral.* **2000,** *85*, 543-556.

31. Jung, S.; McCrory, C. C. L.; Ferrer, I. M.; Peters, J. C.; Jaramillo, T. F., Benchmarking nanoparticulate metal oxide electrocatalysts for the alkaline water oxidation reaction. *J. Mater. Chem. A* **2016,** *4* (8), 3068-3076.

32. Baur, W. H.; Khan, A. A., Rutile-Type Compounds. IV. SiO_2, GeO_2 and a Comparison with other Rutile-Type Structures. *Acta Cryst.* **1971,** *B27*, 2133-2139.

33. Biesinger, M. C.; Payne, B. P.; Lau, L. W. M.; Gerson, A.; Smart, R. S. C., X-ray photoelectron spectroscopic chemical state quantification of mixed nickel metal, oxide and hydroxide systems. *Surf. Interface Anal.* **2009,** *41* (4), 324-332.

34. Hall, H. Y.; Sherwood, P. M. A., X-Ray Photoelectron Spectroscopic Studies of the Iridium Electrode System. *J. Chem. Soc., Faraday Trans. 1* **1984,** *80*, 135-152.

35. Peuckert, M.; Coenen, F. P.; Bonzel, H. P., XPS Study of the Electrochemical Surface Oxidation of Platinum in 1 N H_2SO_4 Acid Electrolyte. *Electrochim. Acta* **1984,** *29* (10), 1305-1314.

36. Zhao, Y.; Vargas-Barbosa, N. M.; Hernandez-Pagan, E. A.; Mallouk, T. E., Anodic deposition of colloidal iridium oxide thin films from hexahydroxyiridate(IV) solutions. *Small* **2011,** *7* (14), 2087-93.

Chapter V

CONFORMAL TIN OXIDE HETEROJUNCTIONS FOR SILICON MICROWIRE ARRAYS

5.1 Introduction

High aspect-ratio structures are promising for photoelectrochemical water splitting due to the minimal use of semiconducting material; the potential to obtain high efficiencies with defective materials, due to decoupling of the paths of light absorption and charge-carrier collection; and the ability to use high catalyst loadings while minimizing parasitic light absorption.[1-3] Silicon microwire array photoanodes generally utilize diffused p-n junctions to obtain the large photovoltages necessary to drive electrochemical reactions.[1, 4-5] Si microcone (μcn) arrays have been proposed as an alternative to Si microwire arrays, because microcones can maximize light absorption via enhanced coupling of broadband light to available waveguide modes, and thus increase device efficiencies while maintaining the advantages associated with the microwire array morphology.[6-8] However, high aspect-ratio structures introduce additional challenges such as non-standard surface terminations, as well as additional surface area that can increase surface recombination and limit device performance.

The oxidation of water to O_2(g) is a key reaction in photoelectrochemical systems that produce sustainable fuels.[9] Without a protective coating, most efficient semiconductors passivate or corrode while performing solar-driven O_2(g) evolution in contact with highly acidic or alkaline aqueous electrolytes.[10-11] Optimal metal oxide protective coatings provide

a conductive pathway to catalytically active sites, and can moreover provide additional functionality such as anti-reflection, intrinsic catalytic activity without additional catalyst deposition, and an appropriate work function to form a high photovoltage semiconductor/metal-oxide heterojunction.[10-11] TiO_2, Ni, NiO_x, CoO_x, MnO_x, ITO, and SnO_x have been used to protect semiconductors in strongly alkaline electrolytes, and oxides such as TiO_2, Ir/IrO_x, and SnO_x have been used as protection layers in strongly acidic electrolytes.[10-20]

SnO_x can act as a protective heterojunction in strongly alkaline or acidic electrolytes, providing 620 mV of photovoltage on planar n-Si photoanodes, with a solar-to-O_2(g) ideal regenerative cell photoelectrode efficiency, η_{IRC}, of 3.7-4.0%.[12] Herein we report the growth of conformal SnO_x layers by atomic-layer deposition as well as use of such films as heterojunctions, protective layers, and electrocatalyst integration layers on both planar Si and Si microcone array electrodes.

5.2 Results

5.2.1 Chemical Composition, Structure, and Stability of SnO_x Films on Si

Conformal coatings of SnO_x were deposited by atomic-layer deposition (ALD) at > 200 °C using tetrakis-dimethylamine tin and ozone (details in Supplementary Information) on oxidized planar Si(100) wafers.[21] Microwave conductivity decay measurements indicated that intrinsically doped, 300 μm thick, double-side-polished, float-zone Si(100) wafers (with a bulk lifetime > 1.5 ms) that were coated with a chemically formed SiO_x layer and 100 ALD cycles of SnO_x at 210 °C had a charge-carrier lifetime of 37 μs, implying a surface recombination velocity of ~ 400 cm s^{-1}.

In contact with $Fe(CN)_6^{3-/4-}$(aq), n-Si(100)/SiO_x/SnO_x electrodes with SnO_x deposited at 210-220 °C (Figure S1) exhibited photovoltages of 620 ± 2 mV under 100 mW cm^{-2} of simulated solar illumination, with barrier heights of 1.01 ± 0.02 eV as determined by differential capacitance vs potential measurements (Figure S1c). Between 15 – 60 mA cm^{-2} of light-limited photocurrent density, the n-Si(100)/SiO_x/SnO_x photoanodes exhibited a diode quality factor of n = 1.07 and a saturation current density of $J_0 = 1.3\times10^{-11}$ A cm^{-2}, whereas between 0.3 - 8 mA cm^{-2} of light-limited photocurrent density, n-Si(100)/SiO_x/SnO_x photoanodes exhibited n = 2.44 and $J_0 = 8.1\times10^{-7}$ A cm^{-2} (Figure S1d).

Transmission-electron microscopy (TEM) data of the n-Si(100)/SiO_x/SnO_x interface indicated that the SiO_x layer was 1.5 ± 0.1 nm thick and SnO_x was amorphous near the interface (Figure 1A). The SnO_x films deposited with 850 ALD cycles were 90 ± 3 nm thick, corresponding to a growth rate of 1.06 ± 0.04 Å $cycle^{-1}$ (Figure 1b). Dark-field imaging and high-resolution TEM images of the SnO_x layer indicated that the SnO_x film transitioned from amorphous to crystalline after ~ 18 nm of growth, and was terminated at the surface by polycrystalline SnO_2 (Figure 1a, S3). X-ray diffraction and electron diffraction data indicated that the SnO_x layer contained nanocrystals of SnO_2 (Figure S4, S4b).

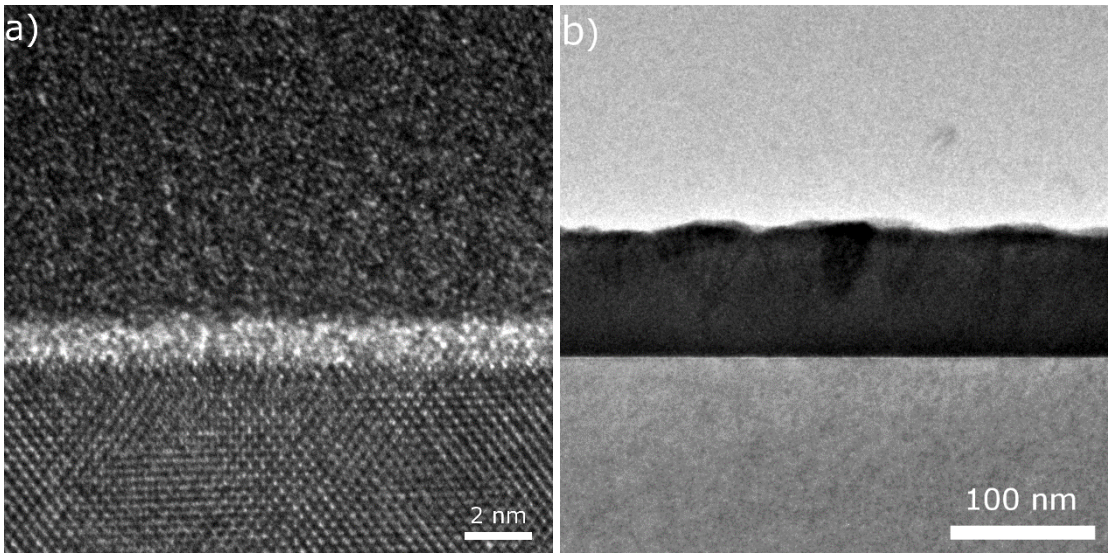

Figure 1. a) High-resolution transmission electron miscroscopy (HRTEM) of the n-Si/SiO_x/SnO_x interface. b) Transmission electron microscopy image of n-Si/SiO_x/SnOx cross-section.

The electrochemical stability of the ALD-deposited SnO_x was determined by measuring the concentration of dissolved Sn species produced in 1.0 M KOH(aq) or 1.0 H_2SO_4(aq) using a p^+-Si(100)/SiO_x/SnO_x anode held at 1.53 V vs. the reversible hydrogen electrode, RHE (Figure S2). Prior to electrochemical testing, ~ 3-12 μg L^{-1} of Sn was observed in the electrolyte, indicating an equivalent initial dissolved SnO_2 thickness of 10 nm. During operation of p^+-Si/SiO_x/SnO_x anodes, the concentration of Sn in the electrolyte initially decreased, and then increased over the first 22 h. Subsequently, SnO_x exhibited a dissolution rate of ~ 0.040 nm h^{-1} in 1.0 M KOH(aq) and ~ 0.028 nm h^{-1} in 1.0 M H_2SO_4(aq), implying > 1,000 h of continuous operation would be needed to produce a 50% loss of a 90 nm thick SnO_x film under these conditions.

5.2.2 Optical and Electronic Properties of SnO_x Films on Si

The band-edge positions, work function, and chemical properties of the ALD-deposited SnO_x film were determined using X-ray photoelectron spectroscopy (XPS). After correction for the relative sensitivity factors of Sn and O, integration of the Sn 3d and O 1s signals indicated that the surface stoichiometry of the SnO_x film was 1:1.47 ± 0.02 Sn:O (Figure S7). The Sn 3d XP spectra exhibited a Sn $3d_{5/2}$ peak at a binding energy of 486.7 ± 0.1 eV, whereas the O 1s spectra exhibited an asymmetric O 1s peak with a binding energy of 530.5 ± 0.1 eV. The binding energies of the observed Sn 3d and O 1s peaks are between those of SnO and SnO_2.[22-23]

n-Si/SiO_x/SnO_x samples exhibited an elemental Si $2p_{3/2}$ peak at a binding energy of 98.7 ± 0.1 eV (Figure S7c). The position of the Si $2p_{3/2}$ peak, at ~ 0.2 eV lower than the elemental binding energy of Si on n-Si(100)/SiO_x electrodes that had nominally the same doping density as the n-Si(100)/SiO_x/SnO_x samples, is consistent with an increase in band bending in the n-Si(100)/SiO_x/SnO_x devices relative to n-Si(100)/SiO_x.[24] The $2p_{3/2}$ binding-energy peak separation between elemental Si and silicon oxide was 4.1 ± 0.1 eV in n-Si(100)/SiO_x but was 2.9 ± 0.1 eV in n-Si(100)/SiO_x/SnO_x (Figure S7c). The $2p_{3/2}$ peak separation of Si and SiO_x is typically ~3.8 eV, and decreases in this separation are consistent with band bending within the SiO_x and/or changes in the chemical composition of the SiO_x layer due to the ALD process step.[24]

Secondary-electron measurements of n-Si(100)/SiO_x samples prepared using 850 ALD cycles of SnO_x indicated that the Fermi level was > 4.7 ± 0.1 eV below the vacuum energy (Figure S8b). The valence band was 3.2 ± 0.1 eV below the Fermi level, and a defect band

was observed at the Fermi level (Figure S8c). Hence, the conduction-band and valence-band edge of SnO_x are 3.5 eV ± 0.1 eV and 7.7 ± 0.1 eV, respectively, below the vacuum energy.

UV-Vis spectroscopy indicated that the optical band gap of the ALD-deposited SnO_x was 4.2 eV by (Figure S8a). In n-Si(100)/SiO_x/SnO_x devices, the ~ 90 nm thick SnO_x layer exhibited an average reflectance of 9.9% over the 400 – 1000 nm wavelength range, as compared to 35.3 % for n-Si(100)/SiO_x devices (Figure S5).

5.2.3 Electrochemical Properties of SnO_x Films on Si

Capacitance-voltage measurements of p^+-Si(100)/SiO_x anodes with 850 cycles of SnO_x indicated that the ALD-deposited SnO_x film was n-type, with a dopant concentration of 1.1×10^{19} cm^{-3}. In contact with $Fe(CN)_6^{3-/4-}$(aq) in the absence of illumination, p^+-Si(100)/SiO_x/SnO_x junctions exhibited a built-in voltage of 0.72 ± 0.01 V (Figure S6c). In contact with $Fe(CN)_6^{3-/4-}$(aq) under 100 mW cm^{-2} of simulated solar illumination, the fill factor of n-Si(100)/SiO_x/SnO_x electrodes decreased when > 100 ALD cycles of SnO_2 deposition were used (Figure S6a). Four-point probe measurements indicated that the SnO_x films prepared at 210 °C had a resistivity of 2.3×10^{-5} Ω m, which for 100 nm thick films would lead to a voltage drop of 2.3 nV at 100 mA cm^{-2}.

Compared to photoanodes without a Pt overlayer, photoanodes coated with 850 SnO_x ALD cycles exhibited an improved fill factor in contact with $Fe(CN)_6^{3-/4-}$(aq) when 2 nm of Pt was sputtered onto the SnO_x surface (Figure S6b). Sputter deposition of a Pt overlayer resulted in no observable n-type behavior in the capacitance-voltage measurements, indicating minimal band bending at the Si(100)/SnO_x surface (Figure S6d).

5.2.4 Photoelectrochemical Water Oxidation by Metallized SnO_x Films on Si

Electrocatalysts for the oxygen-evolution reaction (OER) were deposited onto n-Si(100)/SiO_x/SnO_x photoanodes prepared using 100 ALD cycles of SnO_x (details in Supplementary Information). Nickel-iron oxyhydroxide (NiFeOOH), cobalt oxide (CoO_x) and iridium oxide (IrO_x) provided representative OER catalysts that could be electrodeposited and subsequently used for the OER in either 1.0 M KOH(aq) or 1.0 M H_2SO_4(aq).[25-26] Figure S9 shows the effect of NiFeOOH, CoO_x, and IrO_x catalyst loading on the photoelectrochemical behavior of n-Si(100)/SiO_x/SnO_x anodes in contact with 1.0 M KOH(aq) or 1.0 M H_2SO_4(aq). In contact with 1.0 M KOH(aq), the ideal regenerative solar-to-O_2(g) efficiency, η_{IRC}, was 3.5% for n-Si(100)/SiO_x/SnO_x photoanodes coated with 5 mC cm-$^{-2}$ of electrodeposited NiFeOOH (Figure 2a).

The n-Si(100)/SiO_x/SnO_x electrodes were also coated with 1-2 μm long particles of electrodeposited NiFeOOH dispersed onto the electrode surface (Figure S10a,b). Further increases in NiFeOOH catalyst loading decreased the photocurrent density and fill factor of the photoanodes (Figure S9a). 5 mC cm^{-2} of photoanodically deposited CoO_x (Figure S10c) yielded η_{IRC} = 2.6% for n-Si/SiO_x/SnO_x photoanodes in contact with 1.0 M KOH(aq) (Figure 2a). Further increases in CoO_x loading led to more negative onset potentials for the OER but decreased the light-limited photocurrent density, and excessive CoO_x deposition decreased the light-limited photocurrent density as well as the fill factor (Figure S9b) of the resulting photoanodes. n-Si(100)/SiO_x/SnO_x photoanodes produced electrodeposition of IrO_x using 4 cyclic voltammetry scans to produce 50-500 nm of IrO_x nanoparticles (Figure S10d)

exhibited η_{IRC} = 3.1% in contact with 1.0 M H_2SO_4(aq) (Figure 2a). Further increases in IrO_x electrodeposition decreased the light-limited photocurrent density (Figure S9c).

Figure S11 shows high-resolution XPS data for SnO_x/catalyst interfaces after electrochemical deposition and short-term operation of the n-Si(100)/SiO_x/SnO_x photoelectrodes. The Ni 2p spectra of n-Si(100)/SiO_x/SnO_x electrodes coated with electrodeposited NiFeOOH are indicative of the presence of nickel hydroxide species (Figure S11b), consistent with previous reports of electrodeposited NiFeOOH catalysts and the reversible hydroxide/oxyhydroxide redox process at potentials relevant to the OER.[27] X-ray photoelectron spectra in the Fe 2p region could not be used to determine the oxidation state of Fe due to overlap with the Sn 3p signal. The percentage of the XPS spectra attributed to SnO_x, Sn/(Sn+Ni), was 92 ± 1%, consistent with the surface coverage observed by scanning-electron microscopy (Figure S10b, S11). The Co 2p peaks of the electrodeposited CoO_x catalyst indicated the presence of oxidized Co species, consistent with contributions from Co_3O_4 and $Co(OH)_2$ (Figure S11c). The Ir 4f spectra had an asymmetric doublet with a peak separation of 2.98 eV and an Ir $4f_{7/2}$ binding energy of 62.5 ± 0.1 eV, consistent with the X-ray photoelectron spectra of hydrated IrO_x species (Figure S11d).[28] Sn could not be detected with XPS on IrO_x coated electrodes, indicating complete coverage of the surface with the photo electrodeposited catalyst (Figure S10,S11). The SnO_x film was not markedly altered after electrochemical deposition of the water oxidation catalysts, as indicted by the Sn 3d spectra of the SnO_x films (Figure S11a).

5.2.5 Behavior of Si Microcone Photoanodes Coated with SnO_x

Figure S12 shows the photoelectrochemical behavior of n-Si μcone (μcn) arrays that had been chemically oxidized to form a conformal SiO_x layer and then coated with 100 ALD cycles of SnO_x (n-Si(μcn)/SiO_x/SnO_x). In contact with $Fe(CN)_6^{3-/4-}$(aq) under 100 mW cm^{-2} of simulated solar illumination, the n-Si(μcn)/SiO_x/SnO_x anodes exhibited a photovoltage of ~ 490 mV, which was comparable to the photovoltage exhibited by n-Si(μcn) array electrodes that contained a diffused np^+ junction (Figure S12a).

Water oxidation electrocatalysts (NiFeOOH, CoO_x, or IrO_x) were electrochemically or photoelectrochemically deposited on n-Si(μcn)/SiO_x/SnO_x using similar conditions to those used to prepare planar n-Si(100) photoanodes. A larger deposition cathodic current density (- 10 mA cm^{-2} instead of -1 mA cm^{-2}) was required to deposit NiFeOOH on n-Si (μcn) samples compared to planar n-Si(100) photoanodes. Figure S12 shows the effect of catalyst loading on the photoelectrochemical behavior of n-Si(μcn)/SiO_x/SnO_x. An increase in catalyst loading generally led to an improvement in the onset potential observed for water oxidation, until the optimal catalyst loading level (10 mC cm^{-2}, 10 mC cm^{-2}, and 4 CVs for NiFeOOH, CoO_x, and IrO_x, respectively) was obtained (Figure S12). Catalyst loadings beyond the optimal level led to a decrease in the light-limited photocurrent density, with the onset potential for water oxidation showing a negligible decrease for CoO_x and a substantial increase for NiFeOOH and IrO_x (Figure S12) as the catalyst loading increased. Scanning-electron microscopy images of n-Si(μcn) samples coated with optimal catalyst loadings indicated that relative to cathodic depositions (NiFeOOH), photoanodic deposition (CoO_x, IrO_x) led to preferential catalyst deposition on the tips of the μcones (Figure S13).

Figure 2b shows the photoelectrochemical behavior under 100 mW cm^{-2} of simulated solar illumination of n-Si(μcn)/SiO_x/SnO_x photoanodes with optimal NiFeOOH, CoO_x, and IrO_x loadings in contact with 1.0 M KOH(aq) or 1.0 M H_2SO_4(aq). The photoanodes coated with NiFeOOH or CoO_x exhibited an overpotential, η = -186 mV at 1 mA cm^{-2} in 1.0 M KOH(aq), and showed η = -167 mV in 1.0 M H_2SO_4(aq). n-Si(μcn)/SiO_x/SnO_x photoanodes coated with IrO_x exhibited η = -147 mV at 1 mA cm^{-2} in 1.0 M H_2SO_4(aq). The light-limited photocurrent density for n-Si(μcn)/SiO_x/SnO_x anodes coated with NiFeOOH, CoO_x, or IrO_x was 42.1, 41.7, and 43.0 mA cm^{-2}, respectively, as compared to the theoretical value of 43 mA cm-2 expected for unity external quantum yield for all photons in the 100 mW cm-2 Air Mass 1.5G solar spectrum having energies greater than the 1.12 eV band gap energy of Si. Under 100 mW cm^{-2} of simulated solar illumination, n-Si(μcn)/SiO_x/SnO_x electrodes coated with NiFeOOH, CoO_x, or IrO_x exhibited η_{IRC} = 1.3 %, 0.9 %, and 1.0 %, respectively.

Conformal coatings of amorphous TiO_2 were deposited on n-Si(μcn)/SiO_x/SnO_x and n-Si μW/SiO_x/SnO_x to improve the stability of the photoanodes in 1.0 M KOH(aq).[29] Electrodes consisting of n-Si(100)/SiO_x/SnO_x/TiO_2 with 2 nm of Ni exhibited photovoltages of ~ 602 mV in contact with $Fe(CN)_6^{3-/4-}$(aq) under 100 mW cm^{-2} of simulated solar illumination, whereas n-Si(μcn)/SiO_x/SnO_x/TiO_2 photoanodes exhibited photovoltages of ~ 490 mV (Figure S12a). Planar photoanodes with a layer of SnO_x/TiO_2 and 2 nm Ni initially exhibited η_{IRC} = 3.5% , with η_{IRC} = 3.4% after 50 h of operation under 100 mW cm^{-2} of illumination in 1.0 M KOH(aq) (Figure 4a). Figure S14b summarizes the band energetics of n-Si, SnO_x, and TiO_2 based on the data collected herein as well as previous results for amorphous TiO_2.[24]

Planar n-Si photoelectrodes coated with SnO_x/TiO_2/Ni exhibited a stable photocurrent in 1.0 M KOH(aq) for > 480 h (Figure 4b), whereas n-Si(μcn)/SiO_x/SnO_x/TiO_2 photoanodes with 2 nm of Ni did not exhibit stable photoelectrochemical behavior in 1.0 M KOH(aq). n-Si(μcn)/SiO_x/SnO_x/TiO_2 photoanodes with 4 nm of Ni exhibited photovoltages of ~ 490 mV in contact with $Fe(CN)_6^{3-/4-}$(aq) under 100 mW cm^{-2} of illumination (Figure S12a). The n-Si(μcn)/SiO_x/SnO_x/TiO_2 photoanodes with 4 nm Ni initially showed η_{IRC} ~ 0.5% with the efficiency increasing to η_{IRC} ~ 1.2% after 50 h, and exhibited a stable photocurrent for > 140 h of continuous operation (Figure 4).

5.3 Discussion

5.3.1 Properties of Atomic Layer Deposited SnO_x Coatings on Si

The conductivity through the SnO_x film is dependent on the degree of band-bending at the SnO_x/electrolyte interface. SnO_x films that were 90 nm thick exhibited slow charge-transfer kinetics to $Fe(CN)_6^{3-/4-}$(aq) (Figure S6a). Deposition of a thin metal film on SnO_x substantially improved the charge transfer kinetics to $Fe(CN)_6^{3-/4-}$(aq), as well as decreasing the thickness of the SnO_x film (Figure S6b). The resisitivity of the SnO_x film is 2.3×10^{-5} Ω m, which would lead to a voltage drop of < 2.3 nV at 100 mA cm^{-2} for < 100 nm thick films. This indicates that bulk conductivity cannot explain the slow interfacial charge transfer kinetics to $Fe(CN)_6^{3-/4-}$(aq) for 90 nm thick films.

Impedance measurements indicated that SnO_x exhibited a barrier height of V_b = 0.72 eV in contact with $Fe(CN)_6^{3-/4-}$(aq), consistent with the slow interfacial charge transter between SnO_x and $Fe(CN)_6^{3-/4-}$(aq) (Figure S6c). Deposition of a thin film of Pt on the surface of SnO_x led to negligible band-bending (Figure S6d). The amorphous to crystalline transition

observed with transmission-electron microscopy coupled with the electrochemical data in $Fe(CN)_6^{3-/4-}(aq)$ suggests that the amorphous SnO_x layer is insensitive to band bending at the surface/electrolyte interface, whereas the conductivity through the polycrystalline SnO_x layer is substantially affected by band bending at the surface/electrolyte interface.

5.3.2 Properties of Electrocatalysts on SnO_x

The high conductivity of thin SnO_x films allowed direct electrodeposition of active water oxidation electrocatalysts. The optocatalytic properties of electrodeposited catalysts have been shown to be favorable compared to compact pre-catalyst metal oxide films, as exemplified by electrodeposited NiFeOOH and sputter-deposited NiO_x.[25] Electrodeposition allows high utilization of all of the elements in the deposited film, whereas compact films result in a substantial portion of the film that does not interact with the electrolyte. The high ulitization of the film for catalysis results in a lower overpotential for the same optical transmission through the catalyst film. XPS indicates that the electrodeposited catalysts studied herein consist of oxides or hydroxides, with no apparent metal peaks that would lead to parasitic light absorption. These properties allow planar photoanodes with photocurrents ~ 30 mA cm^{-2} and μcone arrays with photocurrents ~ 42 mA cm^{-2} under simulated sunlight to be obtained. In contrast to the electrodeposited catalysts, sputtered catalysts exhibit properties that are not optimal for photoelectrochemical water splitting on μcone substrates. Thick metallic films substantially decrease the photovoltage observed on μcones arrays (Figure S14a). The decrease in photovoltage could be due to the formation of low-barrier height contacts or shunts in areas that were not completely covered by the SnO_x/TiO_2 coatings, which could be due to sample damage during processing.

5.3.3 Properties of Si Microcone Photoanodes

The conformal SnO_x coatings allow the construction of efficient three-dimension photoanodes for water oxidation in both strongly acidic and strongly alkaline electrolytes. Structured semiconductors, such as Si μcone arrays, allow the decoupling of light absorption paths and charge transfer paths. This decoupling can allow defective semiconductors with short diffusion lengths to be used efficiently, since charge collection occurs at the sides of the high-aspect structure, whereas light absorption occurs throughout the length of the μcone. The high aspect ratio tapered structure also minimizes reflection of incoming sunlight, which allows photocurrents ~ 42 mA cm^{-2} to be obtained with low loadings of catalyst.[6-7] While high-aspect ratio structures can improve the light-absorption properties, there is often a decrease in the open-circuit voltage (V_{oc}) of the device due to the increase in the diode saturation current due to the increase in junction area. The surface area of the μcone arrays studied herein is approximately 14.5 times higher than planar samples. The expected decrease in photovoltage is approximately 74 mV based on the ideality factor and diode current determined on planar samples. A decrease of about 110 – 130 mV is observed for n-Si μcones compared to planar samples, indicating that the majority of the decrease can be attributed to the increase in junction area. The ~ 50 mV of photovoltage unaccounted for by the surface area increase could be due to improper formation of the SiO_x layer during chemical oxidation, different junction properties for different surface terminations, or μcone damage during sample preparation. The overall decrease in photovoltage results in devices that are less efficient than planar samples. Further studies to address this issue could focus on developing junctions with significantly lower diode currents, which could provide

significant improvements in photovoltage for high-surface area structures. Alternatively, transparent and insulating passivation layers could be used to reduce the junction area on high-surface area structures, which could also improve the photovoltage of these devices.

5.3.4 Electrical Properties of SnO_x/TiO_2 Interfaces

The SnO_x layer is able to form an ohmic contact to TiO_2, allowing the construction of SnO_x/TiO_2 bi-layers that exhibit the rectifying properties of SnO_x, and the protective properties of TiO_2. Amorphous TiO_2 propective coatings have been used to protect n-Si, n-GaP, n-GaAs, and n-Si microwires from corrosion or passivation in 1.0 M KOH(aq) for 100-2,200 h of continuous operation.[19, 29] While TiO_2 can protect various semiconductors for significant periods of time, the band energetics at the n-Si/TiO_2 interface lead to a relative low photovoltage of ~ 360 mV under solar illumination, and a diffused np^+ junction is required to further increase the photovoltage. The SnO_x layers studied herein have favorable energetics for electron-hole pair separation and lead to photovoltages of ~ 620 mV under solar illumination, but exhibit thermodynamic instability in alkaline environments. SnO_x/TiO_2 bi-layers exhibit a similar photovoltage as SnO_x layers and an ohmic contact to each other as indicated by the photovoltage and fill factor observed for n-Si/SiO_x/SnO_x/TiO_2/Ni photoanodes in contact with $Fe(CN)_6^{3-/4-}$(aq) (Figure S14a). The work functions measured for SnO_x and TiO_2 indicate that negligible band-bending should occur at their interface (Figure S14b). The photoanodes coated with SnO_x/TiO_2 exhibit a photocurrent stability of ~ 480 h, which is comparable to that observed in other systems protected with TiO_2. The high photovoltage obtained for SnO_x/TiO_2 protected planar photanodes leads to an ideal regenerative solar-to-O_2(g) efficiency of ~ 3.5%. These results suggest that

SnO_x/TiO_2 layers could be utilized for efficient and stable photoelectrochemical water splitting devices in 1.0 M KOH(aq).

5.4 Conclusion

Conformal SnO_x coatings allow the formation of three-dimensional heterojunctions that exhibit diode currents of $1.3x10^{-11}$ A cm^{-2}, providing 620 mV and 490 mV of photovoltage on planar n-Si and n-Si μcone arrays, respectively. The SnO_x layer undergoes an amorphous to crystalline transition after ~ 18 nm of growth, and band-bending at the crystalline SnO_x/electrolyte junction has a strong influence on charge transfer to the electrolyte. The (photo)electrodeposition of OER catalysts such as NiFeOOH, CoO_x, and IrO_x on n-$Si/SiO_x/SnO_x$ μcone arrays places catalyst in regions that minimize parasitic light absorption, allowing light-limiting photocurrents of ~ 42 mA cm^{-2} under 100 mW cm^{-2} of simulated solar illumination in 1.0 M KOH(aq) and 1.0M H_2SO_4(aq). Planar n-Si photoanodes coated with a bi-layer of SnO_x and TiO_2 exhibit a comparable efficiency as observed in photoanodes with just SnO_x, while achieving stability similar to photoanodes coated with TiO_2 in 1.0 M KOH(aq).

5.5 Acknowledgements

This work was supported through the Office of Science of the U.S. Department of Energy (DOE) under award no. DE-SC0004993 to the Joint Center for Artificial Photosynthesis, a DOE Energy Innovation Hub, and in part by the National Science Foundation (NSF) and the Department of Energy (DOE) under NSF CA No. EEC-1041895. Any opinions, findings, and conclusions or recommendations expressed in this material are those of the author(s) and

do not necessarily reflect those of NSF or DOE. Fabrication was performed in Kavli Nanoscience Institute (KNI) at Caltech, and we thank KNI staff for their assistance during fabrication. I.M.H acknowledges a National Science Foundation Graduate Research Fellowship under Grant No. DGE-1144469. We thank C. Garland for assistance with transmission-electron microscopy measurements.

5.6 Supplementary Information

5.6.1 Chemicals

All chemicals were used as received, including potassium ferrocyanide trihydrate ($K_4Fe(CN)_6 \cdot 3H_2O$, Acros Organics, > 99%), potassium ferricyanide ($K_3Fe(CN)_6$, Fischer Scientific, Certified ACS), potassium chloride (KCl, Macron Chemicals, 99.6%), sulfuric acid (H_2SO_4, Fischer Scientific, TraceMetal Grade, 93-96%), potassium hydroxide (KOH, Sigma-Aldrich, Semiconductor Grade, 99.99%), hydrogen peroxide (H_2O_2, EMD Millipore Co., 30% aqueous solution), hydrochloric acid (HCl, EMD Millipore Co., 36-38% aqueous solution), potassium hexachloroiridate(IV) (K_2IrCl_6, Sigma-Aldrich, Technical Grade), nickel (II) nitrate hexahydrate ($Ni(NO_3)_2 \cdot 6H_2O$, Sigma-Aldrich, 99.999%), iron(II) sulfate heptahydrate ($FeSO_4 \cdot 7H_2O$, Sigma-Aldrich, ACS >99.0%), and gallium-indium eutectic (Alfa Aesar, 99.99%). A Barnsted Millipore system was used to obtain deionized water with 18.2 MΩ cm resistivity.

5.6.2 Silicon Oxide Layer Formation

Silicon wafers were chemically oxidized with a procedure similar to previous reports. Silicon polished in the (100) orientation of degenerately doped p-type conductivity (p+-Si, $\rho < 0.005$ Ω cm) or n-type conductivity (n-Si, $\rho = 0.1\text{-}1$ Ω cm) were etched in a BOE solution or HF(aq) for 1 min to remove the native silicon oxide layer, then rinsed with deionized water and dried under a flow of N_2(g). A controlled silicon oxide layer (SiO_x) was formed by placing the wafers in a 5:1:1 $H_2O/HCl/H_2O_2$ solution at 75 °C for 10 min. The samples were then rinsed with deionized water and dried under N_2(g).

5.6.3 Silicon Microcone Array Fabrication

Silicon wafers were coated with a 200 nm thick Al_2O_3 etch mask patterned into an array of 3 μm diameter circles with 7 μm pitch using standard photolithography procedures. The microcone arrays were etched in an Oxford Dielectric System 100 ICP/RIE. The etching procedure is similar to a previous report.[6-7] The etch was performed at a capacitive coupled power of 7 W, and inductively coupled power of 900 W. The etch was performed in three 30 min steps consisting 70 sccm of SF_6 with a O_2 flow rate of 6.0, 6.5, and 7.0 sccm. The chamber temperature and pressure were maintained at -130 °C and 10 mTorr, respectively.

5.6.4 Sample Preparation

Atomic layer deposition (ALD) was performed with a Cambridge Nanotech S200 ALD system. Tin oxide (SnO_x) films were deposited with alternating pulses of (tetrakis-dimethylamino)tin(IV) (TDMASn, Strem Chemicals, 99.99% Sn) and ozone (O_3). An ALD cycle consisted of a 0.3 s pulse of TDMASn, a 20 s purge under 20 sccm flow of N_2(g), a 0.1 s pulse of O_3, and a 30 s purge under 20 sccm flow of N_2(g). The samples were held at 210 °C during the SnO_x deposition unless otherwise specified. Titanium dioxide (TiO_2) films were deposited with a previously reported procedure.[29] An ALD TiO_2 deposition cycle consisted of a 0.1 s pulse of tetrakis-dimethylamidotitanium (TDMAT, Sigma-Aldrich), a 15 s purge under 20 sccm flow of N_2(g), a 0.015 s pulse of H_2O, and a 15 s purge under 20 sccm flow of N_2(g). The samples were held at 150 °C during the TiO_2 deposition. The TDMASn and TDMAT ALD cylinders were held at 60 °C and 75 °C with heating jackets.

An AJA Orion sputtering system was used to deposit metallic films of Ni or Pt. The films were sputtered from an Ar plasma with Ni (ACI Alloys) or Pt (ACI Alloys) metal targets.

The chamber pressure was < 10^{-7} Torr prior to sputter deposition. The Ar plasma was maintained during the deposition at a chamber pressure of 5 mTorr with an Ar flow rate of 20 sccm. The Ni and Pt films were deposited with RF target power of 100 W. Deposition rates were calibrated with approximately 100 nm thick films via profilometry (DektakXT Stylus profilometry) measurements. The duration of the sputtering was used to control the thickness of the metal films, and the samples were not intentionally heated during the deposition.

Electrodes were prepared with methods similar to previous work. [citation?] Si wafers were cleaved into ~ 0.25 cm^2 pieces, and ohmic contacts were made by either scribing In-Ga eutectic (Aldrich) on the back or thermally evaporating 50-100 nm of Al on the back prior to ALD depositions with an AJA Orion system equipped with a thermal evaporator. Tinned Cu wire was threaded through glass tubes, and Ag paint (SPI, Inc.) was used to make an electrical contact between the sample and the Cu wire, as well as to provide mechanical stability to the contact. The contact was dried for at least 2 h at room temperature. Epoxy (Hysol 9460) was used to insulate the back contact and to define the electrode area. The epoxy was cured for at least 12 h at room temperature prior to use. Electrode areas were determined by scanning the electrodes with an optical scanner (Epson perfection V360) and quantifying the area with ImageJ software. The electrode areas were between 5 and 20 mm^2 unless otherwise specified.

5.6.5 Materials Characterization

X-ray diffraction (XRD) analysis was performed with a Bruker D8 Discover instrument equipped with a Vantec-500 2-dimensional detector. Cu Kα radiation (1.54 Å) was generated at a tube current of 1000 μA and a tube voltage of 50 kV. The incident radiation was focused

with a 0.5 mm diameter mono-capillary collimator. The samples were placed at the correct position for diffraction measurements by adjusting the sample position until the diffuse reflectance of an aligned laser beam was in the correct position. Measurements were collected with a couple theta/2theta mode. The scattered radiation was collected with a Vantec-500 detector with an angular resolution < 0.04 °, which enabled the collection of diffraction from a 2θ range of 20° per scan. Four scans were collected in the range of 20° to 80° 2θ, and radiation was counted for a total duration of 4 h to obtain the XRD profile. The collected data were analyzed using Bruker EVA software. The diffraction data was compared to reference patterns for SnO_2.[30]

5.6.6 Surface Recombination Velocity Measurements

Carrier lifetime were determined with an instrument and procedure described in previous work.[31] Intrinsic 300 μm thick silicon wafers polished in the (111) orientation with a bulk lifetime > 1.5 ms were chemically oxidized to form a controlled SiO_x layer and coated with 100 SnO_x ALD cycles deposited at 210 °C with the same procedure that was used for n-type silicon wafers. Electron-hole pairs were generated in the i-Si/SiO_x/SnO_x sample by a 20 ns, 905 nm laser pulse from an OSRAM diode laser with an ETX-10A-93 driver. A PIN diode connected to an oscilloscope was used to measure the decay in reflected microwave intensity after each excitation. The lifetime was determined by fitting the average decay curve of 64 consecutive scans with an exponential function. The surface recombination velocity was determined from the following relationship:

$$\frac{1}{\tau_m} = \frac{1}{\tau_b} + \frac{2S}{d} \approx \frac{2S}{d}$$

where S is the surface recombination velocity, d is the thickness of the silicon wafer, τ_m is the bulk lifetime, and τ_m is the measured lifetime of the electron-hole pairs.

5.6.7 X-ray Photoelectron Spectroscopy

X-ray photoelectron spectroscopic (XPS) data were collected using a Kratos Axis NOVA (Katros Analytical, Manchester, UK) at a background pressure of < 10^{-9} Torr. A monochromatic Al Kα source at 1486.6 eV was used for excitation. High-resolution scans were collected at a resolution of 0.05 eV, and survey scans were collected at 1 eV resolution. All energies including peak energies, valence-band spectra, and work function measurements were calibrated against the binding energy of the adventitious C 1s peak, which was set at 284.8 eV. The bias of the sample was controlled by the XPS instrument for core-level peak energies and valence-band spectra, whereas for work function measurements the bias of the sample was controlled by an external power supply.

The Ni 2p spectra were fit with a previously reported procedure to determine the composition of the electrodeposited NiFeOOH film.[32] Due to the small projected area coverage of the catalyst on the n-Si/SiO_x/SnO_x electrode and the overlap of other elemental peaks, the Fe 2p spectra could not be used to quantify the Fe in the electrodeposited film. The Ni $2p_{3/2}$ spectra of n-Si/SiO_x/SnO_x/e-NiFeOOH electrodes operated for 3-5 cyclic voltammetry scans were fit with the reported peak separations, FWHM ratios, and relative peak areas for standard Ni samples. The absolute peak positions were allowed to vary within ±0.1 eV of the reported peak position to account for the precision of XPS measurements, but the reported peak separations were not adjusted. Only contributions from $Ni(OH)_2$ were required to adequately fit the collected XPS data for the electrodeposited films.

The Co 2p spectra were fit with a previously reported procedure to determine the amount of Co_3O_4 and $Co(OH)_2$ in the electrodeposited CoO_x film.[33] The Co $2p_{3/2}$ spectra of n-Si/SiO_x/SnO_x/CoO_x electrodes operated for 3-5 cyclic voltammetry scans were fit with the reported peak separations, FWHM ratios, and relative peak areas for standard Co samples. The absolute peak positions were allowed to vary within ±0.1 eV of the reported peak position to account for the precision of XPS measurements, but the reported peak separations were not adjusted. Contribution from both Co3O4 and $Co(OH)_2$ were required to adequately fit the collected XPS data for the electrodeposited films. The Ir 4f spectra were fit with based on the XPS spectra of previously reported experiments on Ir electrodes for water oxidation in sulfuric acid.[34]

5.6.8 Electrochemical Testing

X-ray photoelectron spectroscopic (XPS) data were collected using a Kratos Axis NOVA (Katros Analytical, Manchester, UK) at a background pressure of < 10^{-9} Torr. A monochromatic Al Kα source at 1486.6 eV was used for excitation. High-resolution scans were collected at a resolution of 0.05 eV, and survey scans were collected at 1 eV resolution. All energies including peak energies, valence-band spectra, and work function measurements were calibrated against the binding energy of the adventitious C 1s peak, which was set at 284.8 eV. The bias of the sample was controlled by the XPS instrument for core-level peak energies and valence-band spectra, whereas for work function measurements the bias of the sample was controlled by an external power supply.

The Ni 2p spectra were fit with a previously reported procedure to determine the composition of the electrodeposited NiFeOOH film.[32] Due to the small projected area

coverage of the catalyst on the n-Si/SiO_x/SnO_x electrode and the overlap of other elemental peaks, the Fe 2p spectra could not be used to quantify the Fe in the electrodeposited film. The Ni $2p_{3/2}$ spectra of n-Si/SiO_x/SnO_x/e-NiFeOOH electrodes operated for 3-5 cyclic voltammetry scans were fit with the reported peak separations, FWHM ratios, and relative peak areas for standard Ni samples. The absolute peak positions were allowed to vary within ±0.1 eV of the reported peak position to account for the precision of XPS measurements, but the reported peak separations were not adjusted. Only contributions from $Ni(OH)_2$ were required to adequately fit the collected XPS data for the electrodeposited films.

The Co 2p spectra were fit with a previously reported procedure to determine the amount of Co_3O_4 and $Co(OH)_2$ in the electrodeposited CoO_x film.[33] The Co $2p_{3/2}$ spectra of n-Si/SiO_x/SnO_x/CoO_x electrodes operated for 3-5 cyclic voltammetry scans were fit with the reported peak separations, FWHM ratios, and relative peak areas for standard Co samples. The absolute peak positions were allowed to vary within ±0.1 eV of the reported peak position to account for the precision of XPS measurements, but the reported peak separations were not adjusted. Contribution from both Co3O4 and $Co(OH)_2$ were required to adequately fit the collected XPS data for the electrodeposited films. The Ir 4f spectra were fit with based on the XPS spectra of previously reported experiments on Ir electrodes for water oxidation in sulfuric acid.[34]

5.6.9 Electrochemical Depositions

Nickel-iron oxyhydroxide (NiFeOOH) was electrochemically deposited without illumination with a cathodic current density of -1 mA cm^{-2} on planar electrodes and -10 mA cm^{-2} on microcones arrays from a 5×10^{-3} M $Ni(NO_3)_2$ and 5×10^{-3} M $FeSO_4$ stirred aqueous

solution using a two-electrode experiment with a single-compartment electrochemical cell using a carbon rod as a counter electrode. The $Ni(NO_3)_2$(aq) solution was purged with N_2(g) prior to the addition of $FeSO_4 \cdot 6H_2O$(s) to prevent Fe precipitation. Cobalt oxide (CoO_x) was photoelectrochemically deposited from a 0.01 M Co(II) nitrate/0.10 M sodium acetate aqueous solution under 100 mW cm^{-2} of simulated solar illumination with an anodic current density of 1 mA cm^{-2} using a two-electrode experiment with a single-compartment electrochemical cell using a carbon rod as a counter electrode. The NiFeOOH and CoO_x loading was controlled by changing the duration of the chronopotentiometric deposition. Iridium oxide (IrO_x) was photoelectrochemically deposited using a modified literature procedure.[26] Aqueous dark-brown solutions of 2×10^{-3} M K_2IrCl_6 and 2×10^{-3} M KOH were heated at 70 °C under continuous stirring until the solution became light-brown and slightly turbid. The solution was then placed in an ice bath to prevent precipitation of Ir species. The electrochemical cell consisted of one compartment with a SCE as a reference electrode and a carbon as a counter electrode. IrO_x was deposited with cyclic voltammetry scans from -0.2 to 1.2 V vs. SCE under 100 mW cm^{-2} of simulated solar illumination. The loading of the IrOx was controlled by changing the number of cyclic voltammetry scans.

5.6.10 Photovoltage Dependence on Surface Area

For junctions that have a constant surface-area normalized diode current that is independent of structure geometry, as is expected for well-formed junctions, the observed photovoltage scales with surface area increase, γ, based on equation 1.[1]

$$V_{oc} = \frac{nk_BT}{q} \ln\left(\frac{J_{ph}}{\gamma J_0}\right) \quad (1)$$

For the SnO_x heterojunction herein, the ideality factor was determined to be n = 1.07 and the diode current is $J_0 = 1.3*10^{-11}$ A cm^{-2} for photocurrents between 15 – 60 mA cm-2. Planar samples exhibit $\gamma = 1$, which results in a photovoltage of 596 mV at a photocurrent of 30 mA cm^{-2}, which is close to that observed in Figure S1a. The n-Si microcones studied herein have a pitch of 7 μm, a height of ~60 μm, and a base diameter of 3.5 μm. The surface area calculated from these dimensions leads to $\gamma \sim 13.3$. The photovoltage expected for n-Si microcones based on equation 1 is 524 mV, for $\gamma = 13.3$ at 30 mA cm^{-2} photocurrent, which is close to the experimentally observed photovoltage of 490 mV as shown on Figure S9a.

5.7 Supplementary Figures

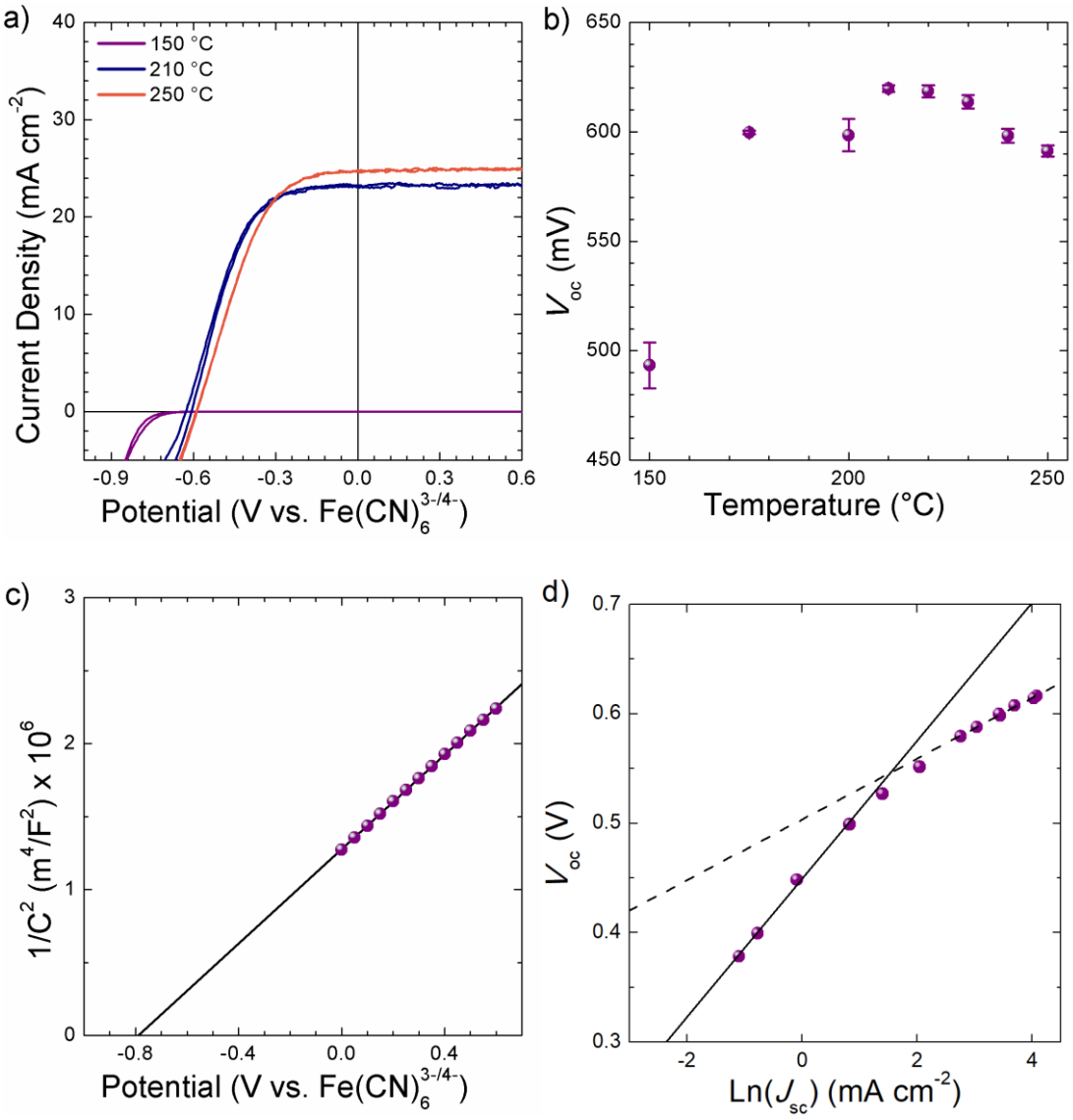

Figure S1. Electrochemical behavior of n-Si/SiO_x/SnO_x photoanodes coated with SnO_x deposited at temperatures between 150–250 °C in contact with $Fe(CN)_6^{3-/4-}$(aq). a) Photoelectrochemical behavior of n-Si/SiO_x/SnO_x photoanodes prepared with 100 SnO_x ALD cycles under 100 mW cm^{-2} of simulated solar illumination. b) Open-circuit voltage of n-Si/SiO_x/SnO_x photoanodes prepared with 100 or 500 SnO_x ALD cycles under 100 mW cm^{-}

^{2} of simulated solar illumination. c) Mott-Schottky plot of electrode capacitance versus voltage of n-Si/SiO_x/SnO_x photoanodes in the dark with a SnO_x layer that was deposited at 210 °C with 100 ALD cycles. d) Open-circuit voltage versus short-circuit current (V_{oc} vs J_{sc}) plot of -Si/SiO_x/SnO_x deposited at 210 °C in contact with $Fe(CN)_6^{3-/4-}$(aq) under 1 – 200 mW cm^{-2} of simulated solar illumination.

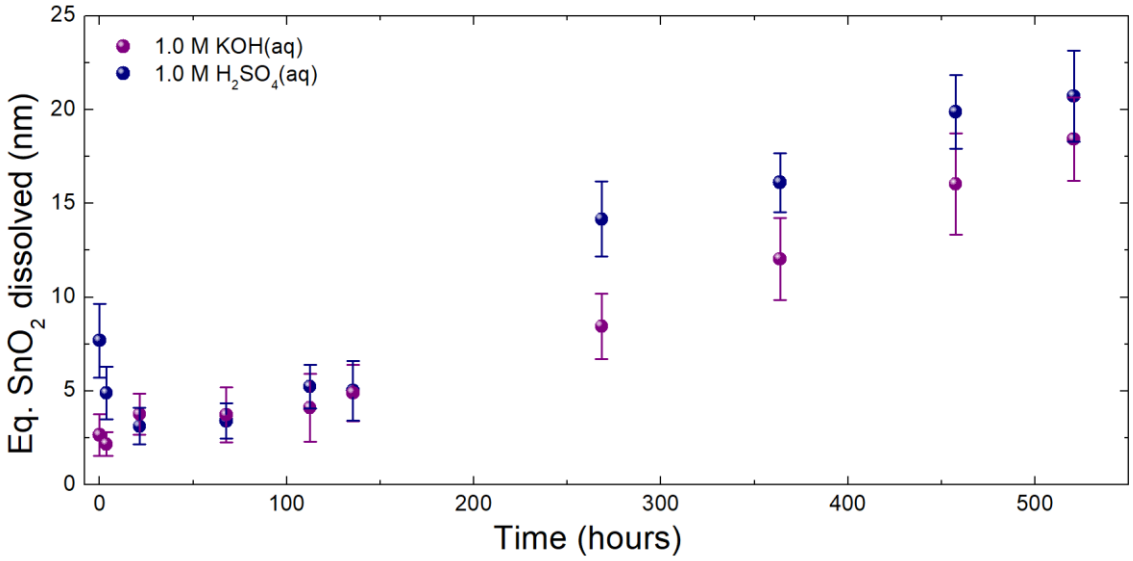

Figure S2. Dissolution of SnO_x film deposited at 210 °C with 850 ALD cycles on a p+-Si(100)/SiO_x substrate. Electrodes were held at 1.53 V vs. RHE in 1.0 M KOH(aq) and 1.0 M H_2SO_4(aq) eletrolytes.

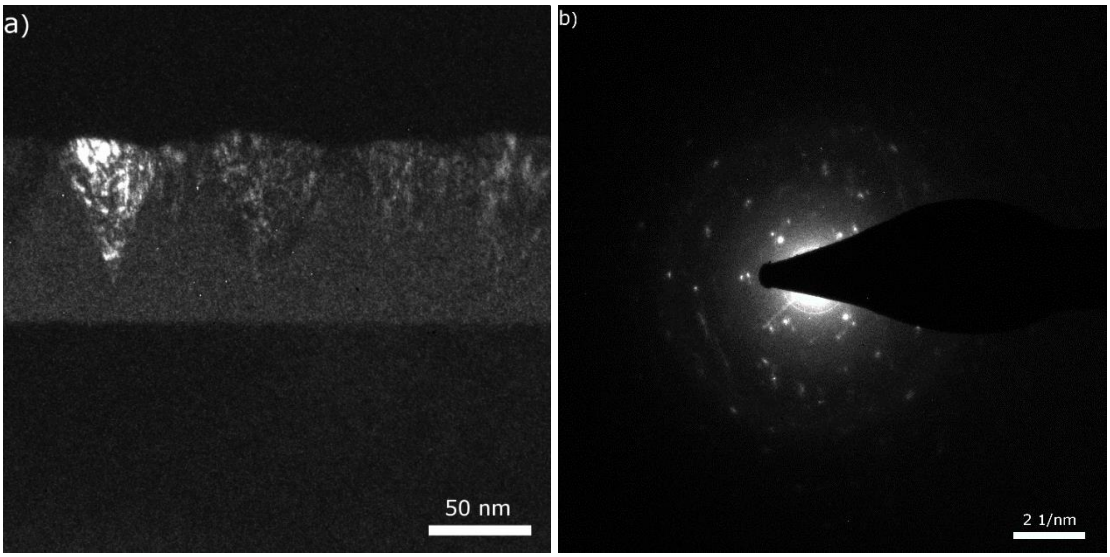

Figure S3. a) Dark field image of n-Si(100)/SiO_x coated with 850 cycles of SnO_x with image brightness corresponding to (002) SnO_2 diffraction signal collected through a 10 μm diemeter aperture. b) Electron diffraction pattern at 300 kV accelerating voltage of n-Si/SiO_x coated with 850 cycles of SnO_x.

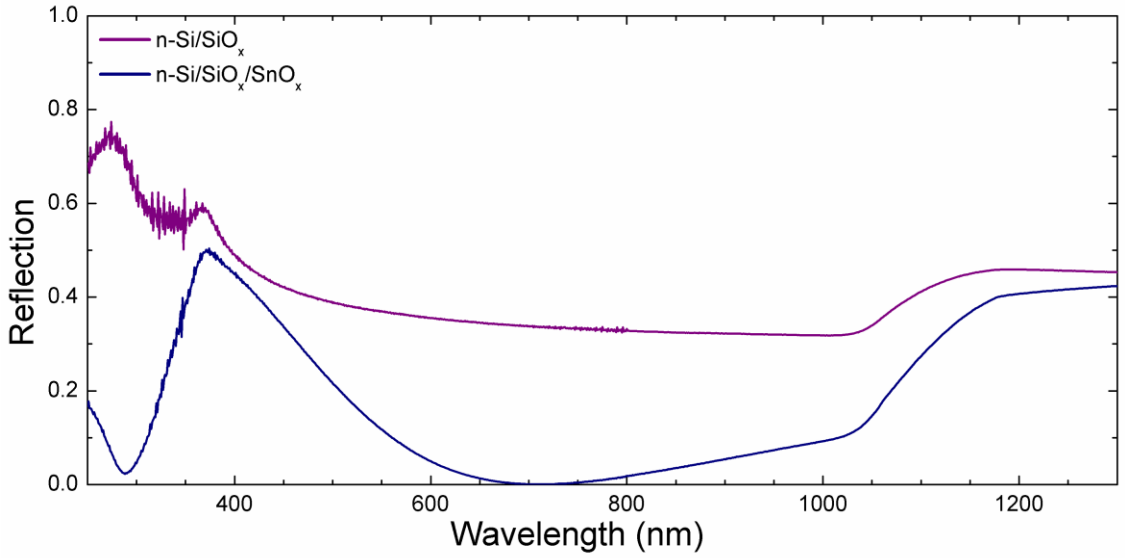

Figure S4. Optical reflectivity measurements at normal incidence of an n-Si/SiO_x/SnO_x wafer coated with SnO_x formed at 210 °C with 850 ALD cycles compared to an n-Si wafer with a native silicon oxide layer.

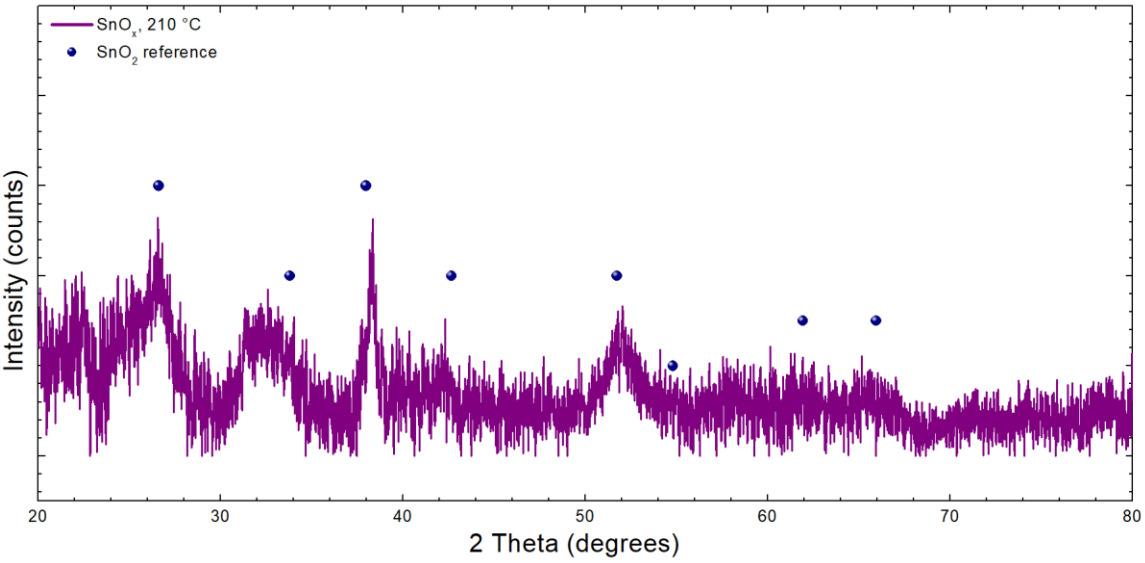

Figure S5. X-ray diffraction pattern for a SnO_x film deposited at 210 °C with 850 ALD cycles on an n-Si(100)/SiO_x substrate. Weak diffraction signals associated with SnO_2 could be observed.

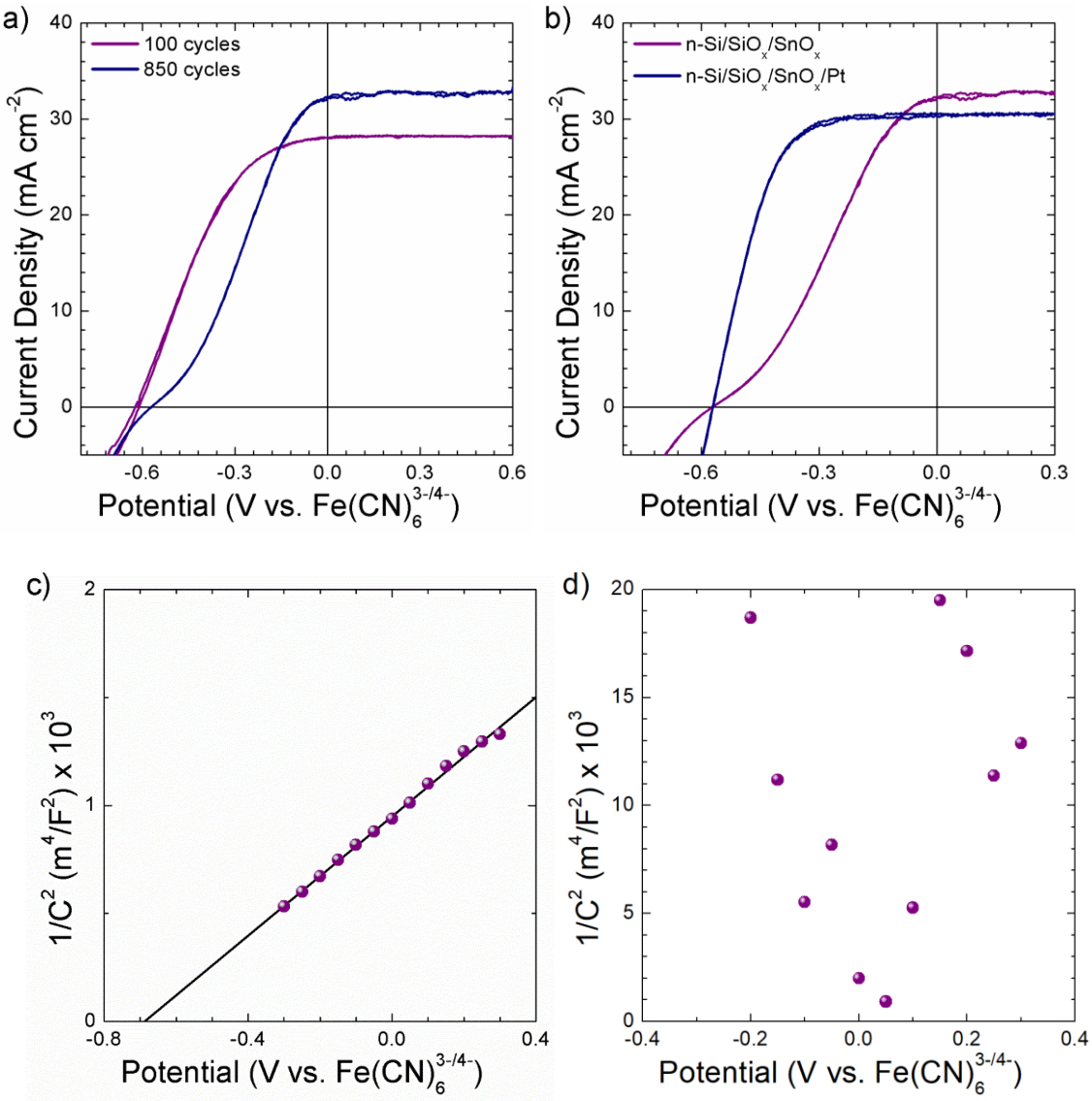

Figure S6. Electrochemical behavior of n-Si/SiO_x/SnO_x photoanodes coated with SnO_x deposited at 210 °C in contact with $Fe(CN)_6^{3-/4-}$(aq) under 100 mW cm^{-2} of simulated solar illumination. a) Photoelectrochemical behavior of n-Si/SiO_x/SnO_x photoanodes with 100 or 850 ALD SnO_x cycles. b) Photoelectrochemical behavior of n-Si/SiO_x photoanodes with 850 cycles of SnO_x with and without a sputter Pt overlayer. c) Mott-Schottky plot of electrode capacitance versus voltage of p^+-Si/SiO_x/SnO_x electrodes in the dark with a SnO_x layer deposited at 210 °C with 850 ALD cycles. d) Mott-Schottky plot of electrode capacitance

versus voltage of p^+-Si/SiO_x/SnO_x/Pt collected in the dark indicating no apparent band bending.

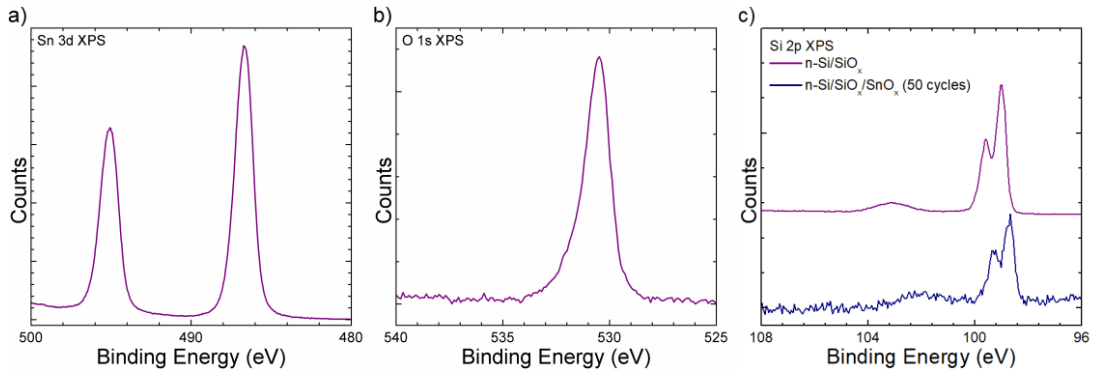

Figure S7. Chemical characterization of SnO_x film. a) High-resolution XPS spectra in the Sn 3d region of SnO_x deposited at 210 °C with 850 ALD cycles on a quartz substrate. b) High-resolution XPS spectra in the O 1s region of SnO_x deposited at 210 °C with 850 ALD cycles on a quartz substrate.

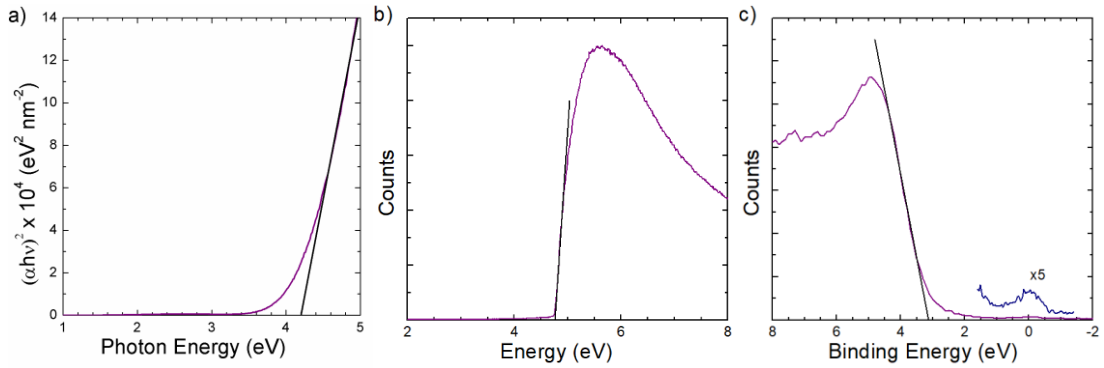

Figure S8. UV-Vis and XPS measurements of SnO_x deposited at 210 °C with 850 ALD cycles on a quartz substrate. a) Direct band gap determined with the Tauc plot method from transmission UV-Vis spectroscopy measurements. b) Fermi level position determined from the secondary-electron energy cut-off of a sample under bias within an XPS instrument. c) Valence-band spectrum of SnO_x.

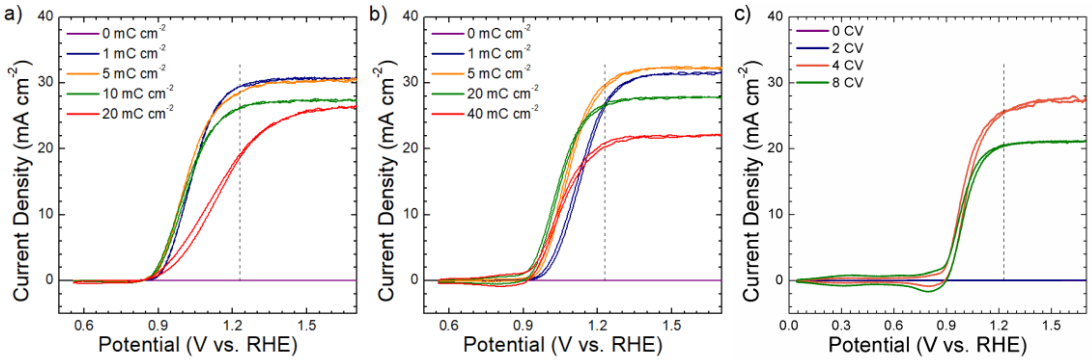

Figure S9. Photoelectrochemical behavior of planar n-Si/SiO_x photoanodes coated with 100 cycles of SnO_x and electrodeposited water oxidation catalysts in contact with 1.0 M KOH(aq) under 100 mW cm^{-2} of simulated solar illumination. a) Photoanodes with different amounts of NiFeOOH electrodeposited in the dark at a current density of 1 mA cm^{-2}. b) Photoanodes with different amounts of CoO_x photoelectrodeposited under 100 mW cm^{-2} of simulated solar illumination at a photocurrent density of 1 mA cm^{-2}. c) Photoanodes with different amounts of IrO_x photoelectrodeposited under 100 mW cm^{-2} of simulated solar illumination with a cyclic voltammetry procedure.

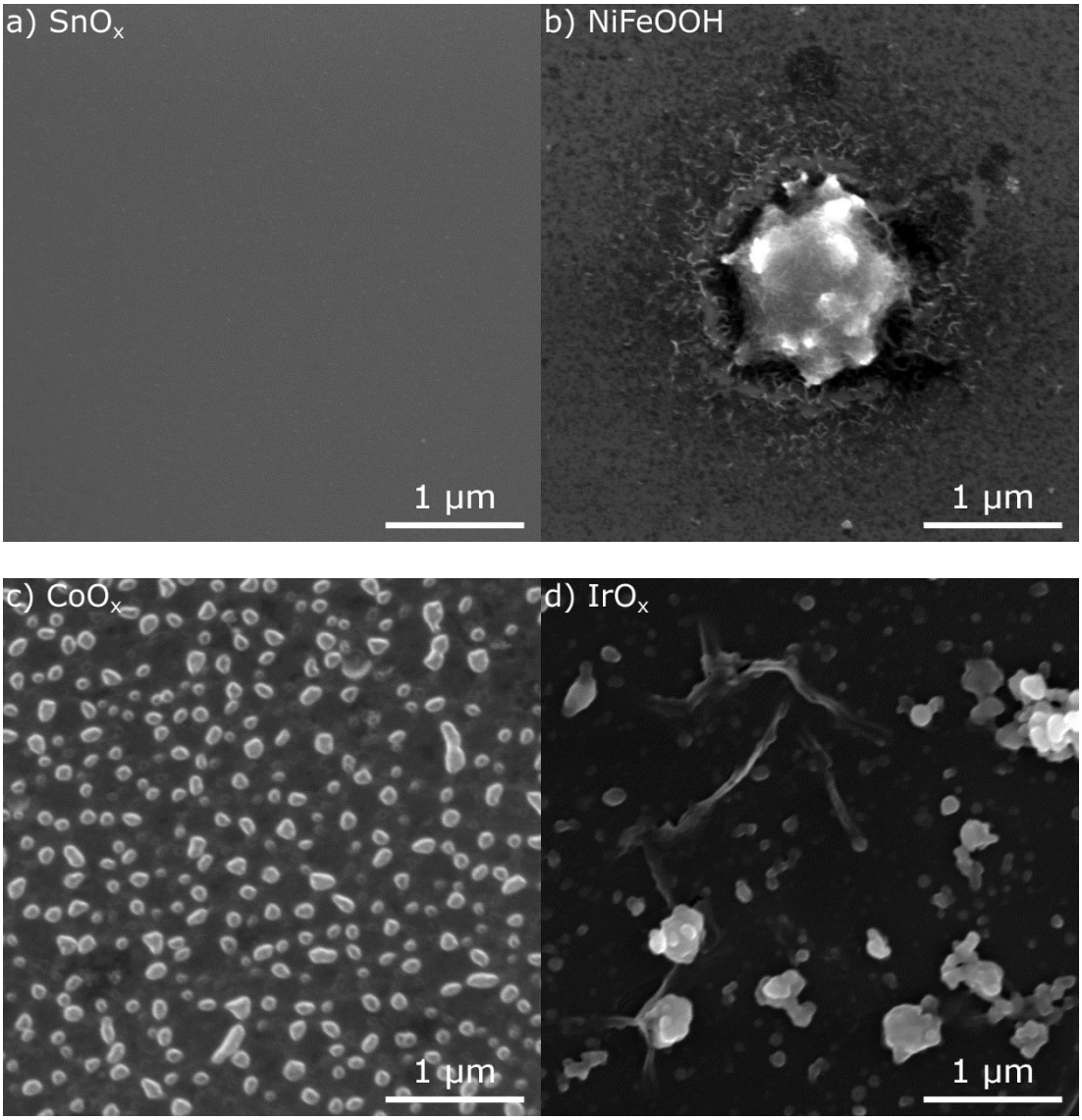

Figure S10. Scanning-electron miscroscopy images of n-Si/SiO_x photoanodes with 100 cycles of SnO_x and various electrodeposited water-oxidation catalysts. a) Bare SnO_x surface. b) SnO_x with electrodeposited 5 mC cm^{-2} of electrodeposited NiFeOOH. c) SnO_x with 5 mC cm^{-2} of electrodeposited CoO_x. d) SnO_x with IrO_x deposited with 4 CV scans.

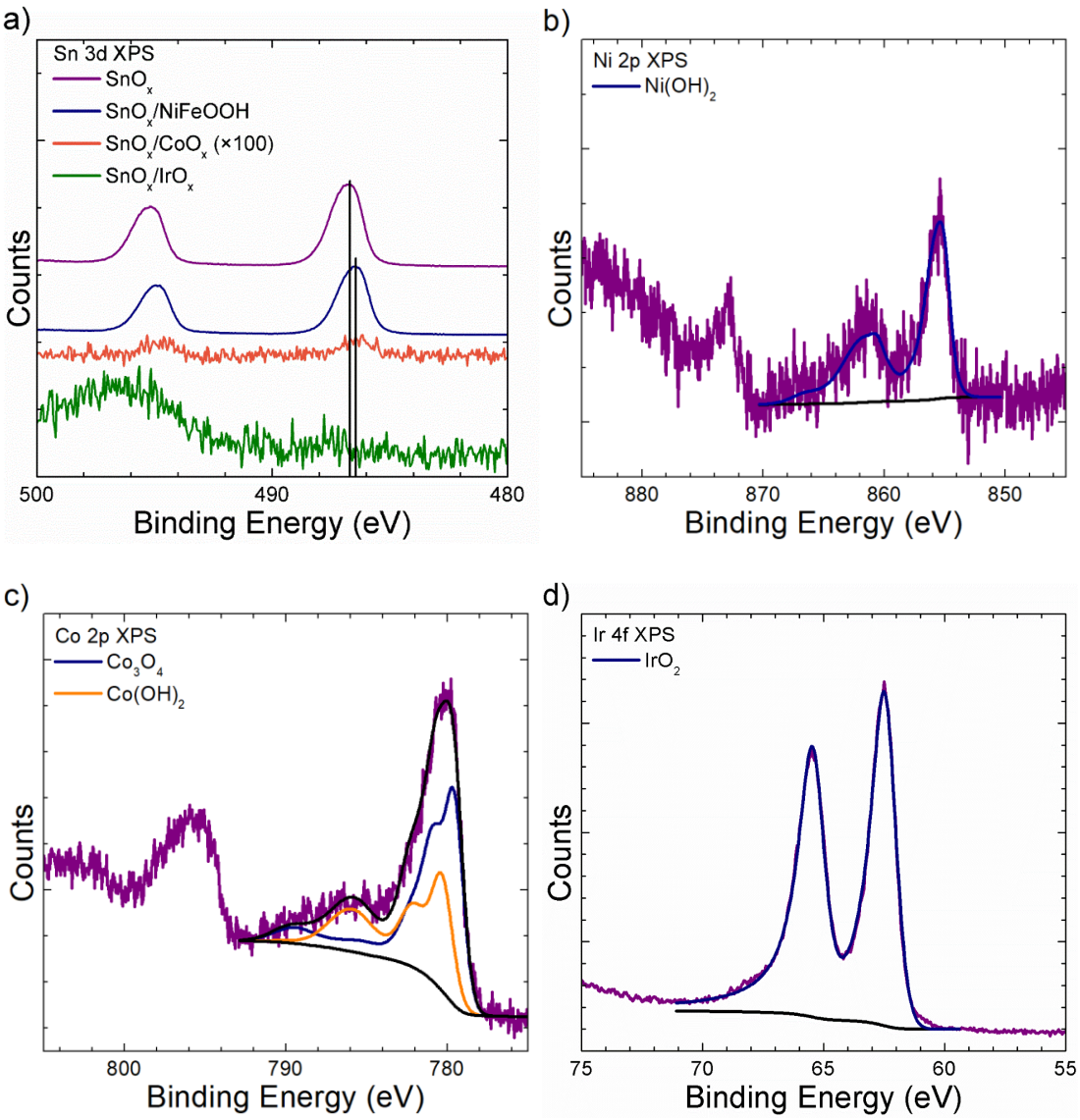

Figure S11. High-resolution XPS data of n-si/SiO_x photoanodes with 10 nm of SnO_x and various electrodeposited water oxidation catalysts after 3-5 cyclic voltammetry scans. a) Sn 3d spectra b) Ni 2p spectra. c) Co 2p spectra. d) Ir 4f spectra.

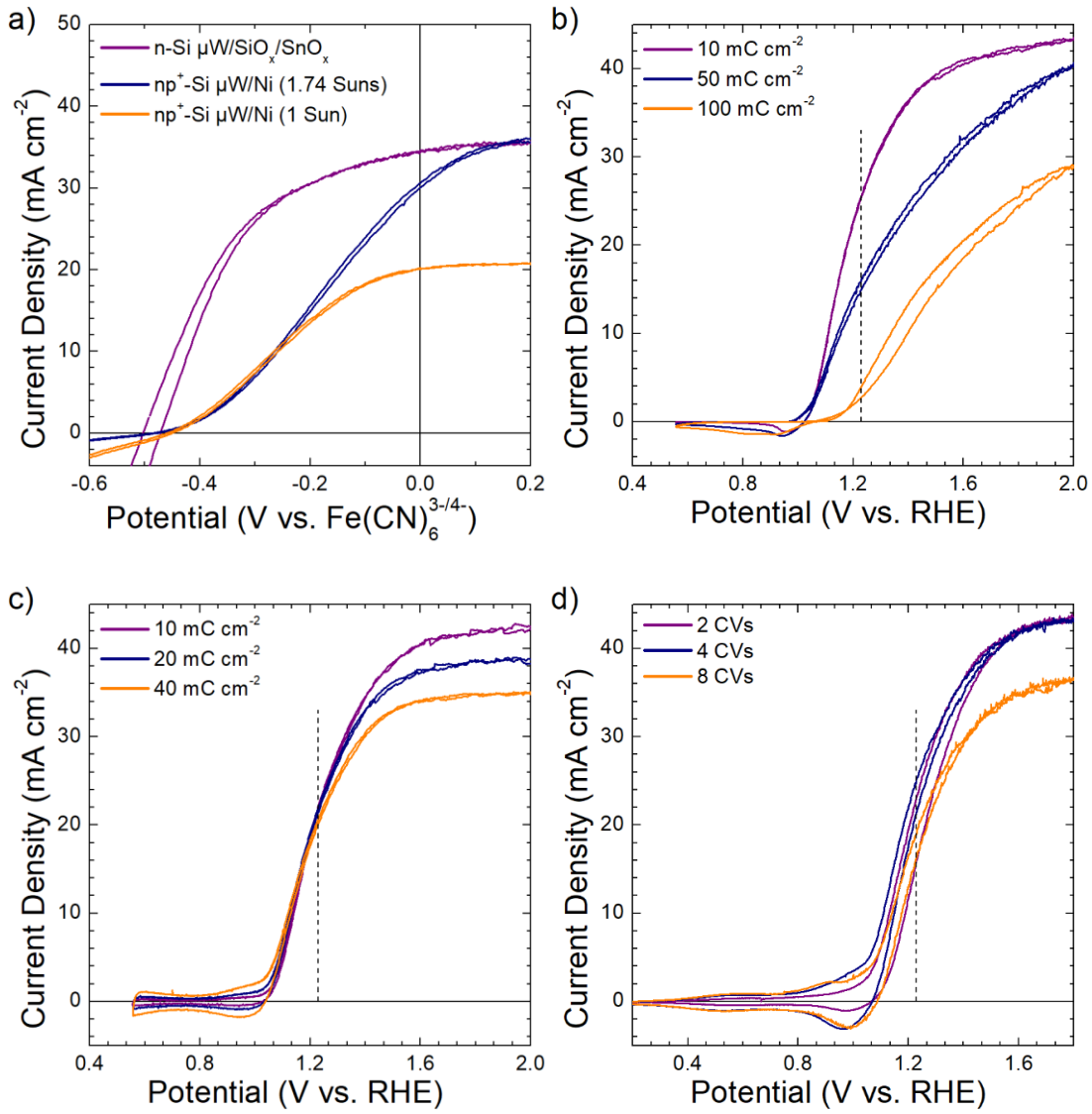

Figure S12. Photoelectrochemical behavior of. a) Photoelectrochemical behavior of n-Si μcones/SiO_x coated with 100 cycles of SnO_x in contact with $Fe(CN)_6^{3-/4-}$(aq) under 100 mW cm^{-2} of simulated solar illumination and np+-Si μcones/Ni under 100 mW cm^{-2} of illumination, and 174 mW cm^{-2} of illumination to obtain a photocurrent similar to n-Si μcone/SiO_x/SnO_x. b) Photoelectrochemical behavior under water oxidation conditions in 1.0 M KOH(aq) of n-Si μcone/SiO_x/SnO_x with different amounts of cathodically deposited

NiFeOOH. c) Photoelectrochemical behavior in 1.0 M KOH(aq) of n-Si μcone/SiO_x/SnO_x with different amounts of anodically deposited CoO_x. d) Photoelectrochemical behavior in 1.0 M H_2SO_4(aq) of n-Si μcone/SiO_x/SnO_x with different amounts of anodically deposited IrO_x.

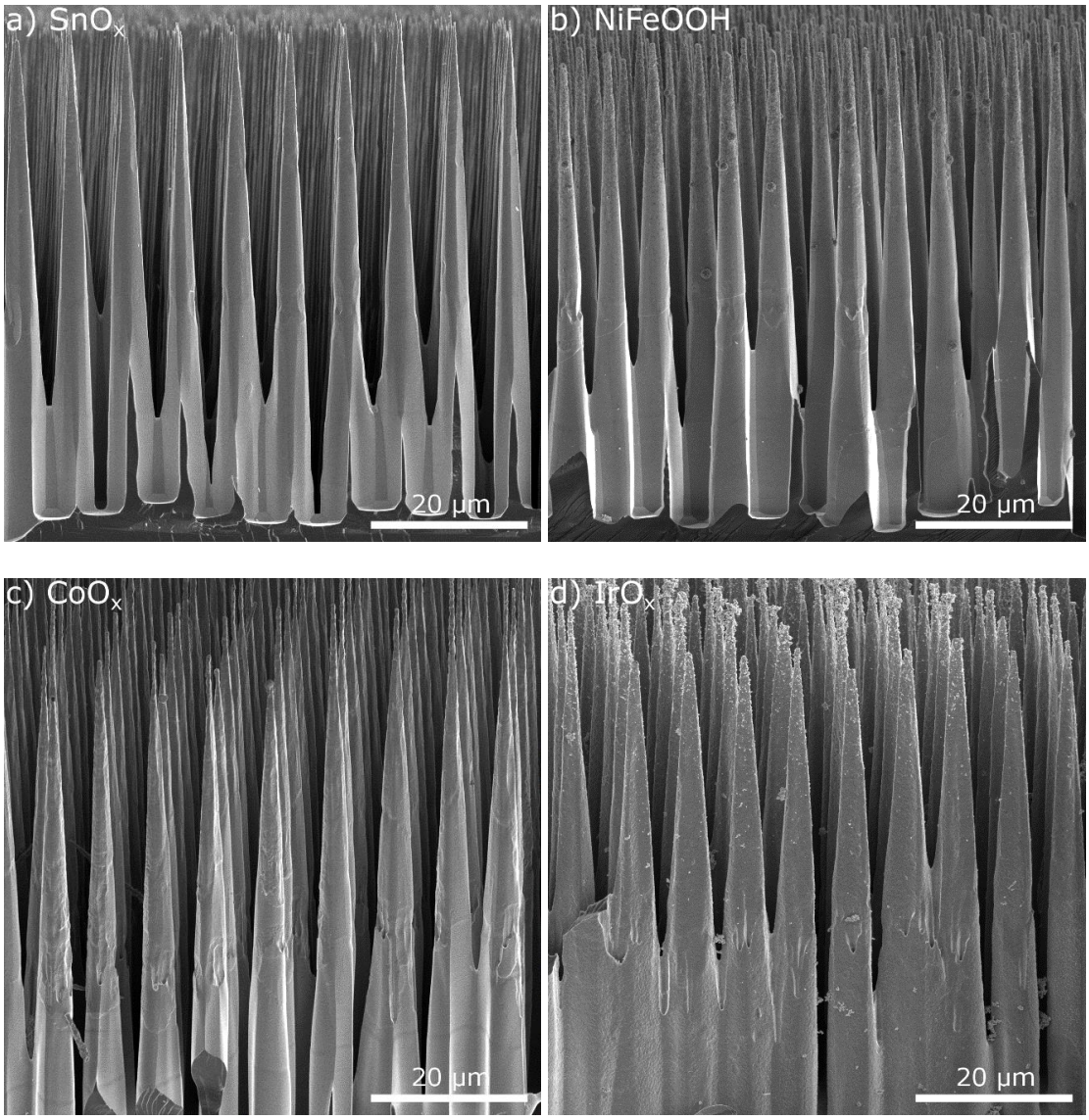

Figure S13. Scanning-electron miscroscopy images of n-Si μcones/SiO_x coated with 100 cycles of SnO_x and various (photo)electrodeposited catalysts. a) n-Si μcones prior to (photo)electrodeposition of catalysts, b) n-Si μcones with NiFeOOH electrochemically

deposited with 10 mC cm^{-2}, c) n-Si μcones with CoO_x photoelectrochemically deposited with 10 mC cm^{-2}, d) n-Si μcones with IrO_x photoelectrochemically deposited with 2 CVs.

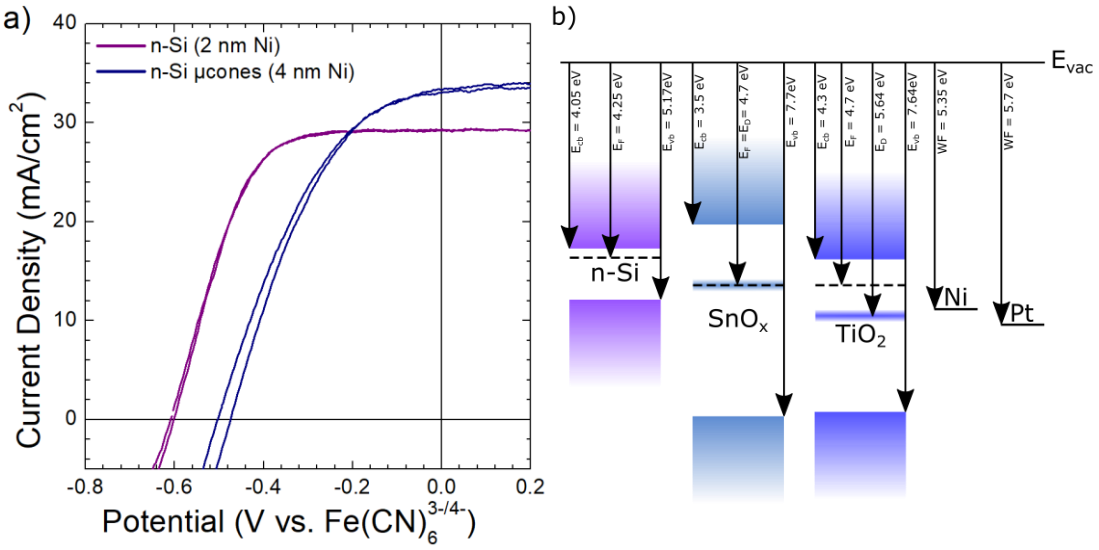

Figure S14. a) Photoelectrochemical behavior of n-Si/SiO_x and n-Si microcones/SiO_x photoanodes coated with 400 cycles of SnO_x, 900 cycles of TiO_2, and sputter deposited Ni in contact with $Fe(CN)_6^{3-/4-}$(aq) under 100 mW cm^{-2} of simulated solar illumination. b) Band energetics of n-Si, SnO_x, TiO_2, Ni, and Pt with respect to the vaccum energy. The band energetics of TiO_2, Ni, and Pt were obtained from previous reports.[24, 35]

5.8 References

1. Warren, E. L.; Atwater, H. A.; Lewis, N. S., Silicon Microwire Arrays for Solar Energy-Conversion Applications. *J. Phys. Chem. C* **2013,** *118* (2), 747-759.
2. Lewis, N. S., Developing a scalable artificial photosynthesis technology through nanomaterials by design. *Nat. Nanotech.* **2016,** *11* (12), 1010-1019.
3. Narkeviciute, I.; Chakthranont, P.; Mackus, A. J.; Hahn, C.; Pinaud, B. A.; Bent, S. F.; Jaramillo, T. F., Tandem Core-Shell Si-Ta_3N_5 Photoanodes for Photoelectrochemical Water Splitting. *Nano Lett.* **2016,** *16* (12), 7565-7572.
4. Shaner, M. R.; Fountaine, K. T.; Ardo, S.; Coridan, R. H.; Atwater, H. A.; Lewis, N. S., Photoelectrochemistry of core–shell tandem junction n–p^+-Si/n-WO_3 microwire array photoelectrodes. *Energy Environ. Sci.* **2014,** *7* (2), 779-790.
5. Chakthranont, P.; Hellstern, T. R.; McEnaney, J. M.; Jaramillo, T. F., Design and Fabrication of a Precious Metal-Free Tandem Core-Shell p^+n Si/W-Doped $BiVO_4$ Photoanode for Unassisted Water Splitting. *Adv. Energy Mater.* **2017,** *7* (22).
6. Yalamanchili, S.; Emmer, H. S.; Lewis, N. S.; Atwater, H. A. In *Highly absorbing and high lifetime tapered silicon microwire arrays as an alternative for thin film crystalline silicon solar cells*, 2016 IEEE 43rd Photovoltaic Specialists Conference (PVSC), 5-10 June 2016; 2016; pp 2999-3003.
7. Yalamanchili, S.; Emmer, H. S.; Fountaine, K. T.; Chen, C. T.; Lewis, N. S.; Atwater, H. A., Enhanced Absorption and <1% Spectrum-and-Angle-Averaged Reflection in Tapered Microwire Arrays. *ACS Photonics* **2016,** *3* (10), 1854-1861.

8. Dasog, M.; Carim, A. I.; Yalamanchili, S.; Atwater, H. A.; Lewis, N. S., Profiling Photoinduced Carrier Generation in Semiconductor Microwire Arrays via Photoelectrochemical Metal Deposition. *Nano Letters* **2016,** *16* (8), 5015-5021.
9. Lewis, N. S., Research opportunities to advance solar energy utilization. *Science* **2016,** *351* (6271), aad1920.
10. Bae, D.; Seger, B.; Vesborg, P. C.; Hansen, O.; Chorkendorff, I., Strategies for stable water splitting via protected photoelectrodes. *Chem. Soc. Rev.* **2017,** *46* (7), 1933-1954.
11. Lichterman, M. F.; Sun, K.; Hu, S.; Zhou, X.; McDowell, M. T.; Shaner, M. R.; Richter, M. H.; Crumlin, E. J.; Carim, A. I.; Saadi, F. H.; Brunschwig, B. S.; Lewis, N. S., Protection of inorganic semiconductors for sustained, efficient photoelectrochemical water oxidation. *Catal. Today* **2016,** *262*, 11-23.
12. Moreno-Hernandez, I. A.; Brunschwig, B. S.; Lewis, N. S., Tin Oxide as a Protective Heterojunction with Silicon for Efficient Photoelectrochemical Water Oxidation in Strongly Acidic or Alkaline Electrolytes. *Adv. Energy Mater.* **2018,** *8* (24), 1801155.
13. Chen, Y. W.; Prange, J. D.; Duhnen, S.; Park, Y.; Gunji, M.; Chidsey, C. E.; McIntyre, P. C., Atomic layer-deposited tunnel oxide stabilizes silicon photoanodes for water oxidation. *Nat. Mater.* **2011,** *10* (7), 539-44.
14. Yang, J.; Walczak, K.; Anzenberg, E.; Toma, F. M.; Yuan, G.; Beeman, J.; Schwartzberg, A.; Lin, Y.; Hettick, M.; Javey, A.; Ager, J. W.; Yano, J.; Frei, H.; Sharp, I. D., Efficient and sustained photoelectrochemical water oxidation by cobalt oxide/silicon photoanodes with nanotextured interfaces. *J. Am. Chem. Soc.* **2014,** *136* (17), 6191-4.

15. Yao, T.; Chen, R.; Li, J.; Han, J.; Qin, W.; Wang, H.; Shi, J.; Fan, F.; Li, C., Manipulating the Interfacial Energetics of n-type Silicon Photoanode for Efficient Water Oxidation. *J. Am. Chem. Soc.* **2016,** *138* (41), 13664-13672.

16. Mei, B.; Pedersen, T.; Malacrida, P.; Bae, D.; Frydendal, R.; Hansen, O.; Vesborg, P. C. K.; Seger, B.; Chorkendorff, I., Crystalline TiO_2: A Generic and Effective Electron-Conducting Protection Layer for Photoanodes and -cathodes. *J. Phys. Chem. C* **2015,** *119* (27), 15019-15027.

17. Mei, B.; Seger, B.; Pedersen, T.; Malizia, M.; Hansen, O.; Chorkendorff, I.; Vesborg, P. C., Protection of p^+-n-Si Photoanodes by Sputter-Deposited Ir/IrO_x Thin Films. *J. Phys. Chem. Lett.* **2014,** *5* (11), 1948-52.

18. Kenney, M. J.; Gong, M.; Li, Y.; Wu, J. Z.; Feng, J.; Lanza, M.; Dai, H., High-performance silicon photoanodes passivated with ultrathin nickel films for water oxidation. *Science* **2013,** *342* (6160), 836-40.

19. Shaner, M. R.; Hu, S.; Sun, K.; Lewis, N. S., Stabilization of Si microwire arrays for solar-driven H_2O oxidation to O_2(g) in 1.0 M KOH(aq) using conformal coatings of amorphous TiO_2. *Energy Environ. Sci.* **2015,** *8* (1), 203-207.

20. Yu, Y.; Zhang, Z.; Yin, X.; Kvit, A.; Liao, Q.; Kang, Z.; Yan, X.; Zhang, Y.; Wang, X., Enhanced photoelectrochemical efficiency and stability using a conformal TiO_2 film on a black silicon photoanode. *Nat. Energy* **2017,** *2* (6).

21. Choi, D.-w.; Park, J.-S., Highly conductive SnO_2 thin films deposited by atomic layer deposition using tetrakis-dimethyl-amine-tin precursor and ozone reactant. *Surf. Coat. Technol.* **2014,** *259*, 238-243.

22. Stranick, M. A.; Moskwa, A., SnO by XPS. *Surf. Sci. Spectra* **1993,** *2* (1), 45-49.

23. Stranick, M. A.; Moskwa, A., SnO_2 by XPS. *Surf. Sci. Spectra* **1993,** *2* (1), 50-54.

24. Hu, S.; Richter, M. H.; Lichterman, M. F.; Beardslee, J.; Mayer, T.; Brunschwig, B. S.; Lewis, N. S., Electrical, Photoelectrochemical, and Photoelectron Spectroscopic Investigation of the Interfacial Transport and Energetics of Amorphous TiO_2/Si Heterojunctions. *Journal of Physical Chemistry C* **2016,** *120* (6), 3117-3129.

25. Sun, K.; Moreno-Hernandez, I. A.; Schmidt, W. C.; Zhou, X.; Crompton, J. C.; Liu, R.; Saadi, F. H.; Chen, Y.; Papadantonakis, K. M.; Lewis, N. S., A Comparison of the Chemical, Optical and Electrocatalytic Properties of Water-Oxidation Catalysts for Use in Integrated Solar-Fuels Generators. *Energy Environ. Sci.* **2017,** *10*, 987-1002.

26. Zhao, Y.; Vargas-Barbosa, N. M.; Hernandez-Pagan, E. A.; Mallouk, T. E., Anodic deposition of colloidal iridium oxide thin films from hexahydroxyiridate(IV) solutions. *Small* **2011,** *7* (14), 2087-93.

27. Trotochaud, L.; Young, S. L.; Ranney, J. K.; Boettcher, S. W., Nickel-iron oxyhydroxide oxygen-evolution electrocatalysts: the role of intentional and incidental iron incorporation. *J. Am. Chem. Soc.* **2014,** *136* (18), 6744-6753.

28. Freakley, S. J.; Ruiz-Esquius, J.; Morgan, D. J., The X-ray photoelectron spectra of Ir, IrO_2 and $IrCl_3$ revisited. *Surf. Interface Anal.* **2017,** *49*, 794–799.

29. Hu, S.; Shaner, M. R.; Beardslee, J. A.; Lichterman, M.; Brunschwig, B. S.; Lewis, N. S., Amorphous TiO_2 coatings stabilize Si, GaAs, and GaP photoanodes for efficient water oxidation. *Science* **2014,** *344* (6187), 1005-9.

30. Baur, W. H.; Khan, A. A., Rutile-Type Compounds. IV. SiO_2, GeO_2 and a Comparison with other Rutile-Type Structures. *Acta Cryst.* **1971,** *B27*, 2133-2139.

31. Plymale, N. T.; Kim, Y.-G.; Soriaga, M. P.; Brunschwig, B. S.; Lewis, N. S., Synthesis, Characterization, and Reactivity of Ethynyl- and Propynyl-Terminated Si(111) Surfaces. *J. Phys. Chem. C* **2015,** *119* (34), 19847-19862.
32. Biesinger, M. C.; Payne, B. P.; Lau, L. W. M.; Gerson, A.; Smart, R. S. C., X-ray photoelectron spectroscopic chemical state quantification of mixed nickel metal, oxide and hydroxide systems. *Surf. Interface Anal.* **2009,** *41* (4), 324-332.
33. Biesinger, M. C.; Payne, B. P.; Grosvenor, A. P.; Lau, L. W. M.; Gerson, A. R.; Smart, R. S. C., Resolving surface chemical states in XPS analysis of first row transition metals, oxides and hydroxides: Cr, Mn, Fe, Co and Ni. *Appl. Surf. Sci.* **2011,** *257* (7), 2717-2730.
34. Hall, H. Y.; Sherwood, P. M. A., X-Ray Photoelectron Spectroscopic Studies of the Iridium Electrode System. *J. Chem. Soc., Faraday Trans. 1* **1984,** *80*, 135-152.
35. Skriver, H. L.; Rosengaard, N. M., Surface energy and work function of elemental metals. *Phys. Rev. B* **1992,** *46* (11), 7157-7168.